Functional Catalytic Surfaces for Environmental Sustainability

WILSON, MATTHEW

Functional Catalytic Surfaces for Environmental Sustainability

Matthew Wilson

PhD Thesis

Department of Chemistry
Durham University

2018

DECLARATION

The work contained within this thesis was carried out at the Department of Chemistry, University of Durham between September 2012 and September 2016. It is the original work of this author (except when otherwise stated) and has not been submitted for a degree at this or any other higher education establishment.

S. N. Barrientos-Palomo, N. L. Mitchell and P. C. Stevens (Department of Chemistry, University of Durham) synthesised the MOF films used in Chapter 5. C. Y. C. Cheng (Department of Chemistry, University of Durham) carried out the initial work that inspired Chapter 6. R. K. Chellappan (Department of Chemistry, University of Durham) synthesised a number of P25-TiO_2 macrosphere samples used in Chapter 7. R. C. Fraser (Department of Chemistry, University of Durham) carried out all NKD film thickness measurements and analyses. In all cases G. Oswald (Department of Chemistry, University of Durham) carried out XRD data collection and analysis. Carbon-carbon coupling reactions in Chapter 3 were partly carried out by R. Kore (Department of Chemistry, Indian Institute of Technology Ropar). All ICP analysis in Chapters 3 and 4 was carried out by Medac Ltd. Some sample preparation and photocatalytic data in Appendix 1 was conducted in collaboration with J. Dawson. All contributions from the above to data within figures are credited in the respective figure captions throughout this thesis.

STATEMENT OF COPYRIGHT

ACKNOWLEDGEMENTS

Many thanks to all the following: Professor Jas Pal Badyal, my supervisor for more years than he signed up for, whose advice and guidance has made this thesis possible; all those who have made up Lab 98 — Tom, Phil, James, Rebekah, Andrea, Hannah, Matt, Samantha, Isaias, Angus, Rajesh, Jenny, Charles, Natalie, Peter, Rowan, Michael, Barnie — for their constructive discussions, support and humour; Neil, Paul, Kelvin, Bryan, and Omer in the workshops, for the dedicated way in which they made and fixed equipment; Malcolm and Aaron, for making and repairing many glass plasma reactors; Simon Beaumont for assistance with GC, as well as discussions on catalysis and general advice; Professor Rajendra Srivastava (Indian Institute of Technology, Ropar) for research collaboration; Jackie Mosely and Durham Mass Spectrometry Group for use of their GC-MS; Tracey Davey at the University of Newcastle for training me on the SEM; and Tim Hawkins of the University of Durham Biology Department for use of the optical microscope.

To my family, for their support. To Jen, for her tireless patience.

.

LIST OF PUBLICATIONS

ARISING FROM THESIS

Work in this thesis has been published as follows:

1. “Recyclable Palladium Catalyst Cloths for Carbon-Carbon Coupling Reactions” Wilson, M.; Kore, R.; Fraser, R. C.; Beaumont, S. K.; Srivastava, R.; Badyal, J. P. S. *Colloids Surf., A* **2017**, *520*, 788–795.
2. “Palladium–Poly(Ionic Liquid) Membranes for Permselective Sonochemical Flow Catalysis” Wilson, M.; Kore, R.; Ritchie, A. W.; Fraser, R. C.; Beaumont, S. K.; Srivastava, R.; Badyal, J. P. S. *Colloids Surf., A* **2018**, *545*, 78–85.
3. “Substrate-Independent Epitaxial Growth of the Metal–Organic Framework MOF-508a” Wilson, M.; Barrientos-Palomo, S. N.; Stevens, P. C.; Mitchell, N. L.; Oswald, G.; Nagaraja, C. M.; Badyal, J. P. S. *ACS Appl. Mater. Interfaces* **2018**, *10*, 4057–4065.
4. “Magnetic Recyclable Microcomposite Silica-Steel Core with TiO_2 Nanocomposite Shell Photocatalysts for Sustainable Water Purification” Wilson, M.; Cheng, C. Y. C.; Oswald, G.; Srivastava, R.; Beaumont, S. K.; Badyal. J. P. S. *Colloids Surf., A* **2017**, *523*, 27–37.

COLLABORATIVE PUBLICATIONS

1. “Smart Water Channelling Through Dual Wettability by Leaves of the Bamboo Phyllostachys Aurea” Wigzell J. M.; Racovita, R. C.; Stentiford, B. G.; Wilson, M.; Harris, M. T.; Fletcher, I. W.; Mosquin, D. P. K.; Justice, D.; Beaumont, S. K.; Jetter, R.; Badyal, J. P S. *Colloids Surf., A* **2016**, *506*, 344–355.
2. “Plasmachemical Double Click Thiol–ene Reactions for Wet Electrical Barrier” Fraser, R. C.; Carletto, A.; Wilson, M.; Badyal, J. P. S. *ACS Appl. Mater. Interfaces* **2016**, *8*, 21832–21838.

ABSTRACT

Functional surfaces are of crucial importance to both fundamental and applied science. Many phenomena are driven by the properties of interfaces: catalysis, corrosion and adhesion to name a few. These properties can be modified using surface functionalisation, which in this thesis is applied to three areas of environmental concern: sustainable catalytic carbon-carbon coupling, atmospheric CO_2 sequestration and photocatalytic water purification. Chapter 1 provides an introduction to these three areas and Chapter 2 summarises the common experimental techniques used throughout this thesis.

Chapters 3 and 4 describe the application of pulsed plasma deposition for production of palladium functionalised catalysts for common carbon-carbon coupling reactions. For low loading palladium catalyst cloths in Chapter 3, high product yields and selectivities have been measured in conjunction with environmentally friendly solvents. In Chapter 4, palladium - poly(ionic liquid) catalyst membranes are described, which demonstrate selective permeation (separation) of the product species through the underlying membrane support. Both low loading palladium catalyst cloths and palladium - poly(ionic liquid) catalyst membranes display low levels of metal leaching allowing them to be recycled multiple times.

Chapter 5 extends the use of pulsed plasma deposited imidazole moieties to the directed liquid-phase epitaxial (layer-by-layer) growth of metal-organic frameworks (MOFs). The MOF-508 functionalised surface displays CO_2 gas capture behaviour at atmospheric concentrations proportional to the number of MOF-508 layers.

Finally, Chapters 6 and 7 describe the preparation of separable P25 TiO_2 based photocatalysts. Micron-sized silica-steel microcomposite core with TiO_2 nanocomposite shell photocatalysts were prepared using sol-gel chemistry in Chapter 6. Their application to degradation of waterborne organic pollutants during UV illumination has been demonstrated, along with recycling via magnetic separation. Chapter 7 describes photocatalytic P25-TiO_2 composite macrospheres, which possess both UV and visible light photocatalytic activity depending on the synthesis conditions. These macrospheres have been demonstrated for their use in flat bed reactors under visible light irradiation, for application to point of use solar driven removal of water borne contaminants. Additionally, Appendix 1 outlines work carried out on the fundamentals of P25 TiO_2 photocatalysts, using XRD and photocatalytic degradation studies.

TABLE OF CONTENTS

LIST OF SCHEMES

LIST OF FIGURES

LIST OF TABLES

Chapter 1 Introduction

1.1 Why Catalysts?

Catalysts are found in a wide variety of industrial processes, facilitating the production of fertilisers, plastics and pharmaceuticals to name a few. Through catalyst design, there are opportunities to ensure that demand for such materials is met in an efficient way with minimal environmental impact. To promote progression towards a more environmentally sustainable approach to catalysis, twelve principles of "green chemistry" have been outlined,[1] which briefly comprise reducing toxicity, minimising waste and increasing use of renewable feedstocks. Based on these principles, the use of catalysts that deliver high yields and a high degree of selectivity, preferentially those that do so in aqueous media, are an attractive route to sustainability for industrial processes.

However, catalysts find roles not only within synthesis of commercially significant products, but also in life saving applications such as purification of drinking water. Undoubtedly, the acquisition of clean drinking water is of paramount importance in developing countries, reducing the prevalence of water borne diseases and improving quality of life. It is therefore vital that cheap, simple solutions are developed which can be easily used by those in greatest need. This can be achieved using a functional surface approach to tailor the catalyst to the specific application.

1.1.1 Palladium Catalysed Carbon-Carbon Coupling Reactions

Carbon-carbon coupling reactions are highly prevalent in fine chemical and pharmaceutical production,[2] being used in about 14% of all bulk organic synthesis good manufacturing practices (GMP).[3] As such, the development of catalytic materials to facilitate the formation of new carbon-carbon bonds is of significant importance, as recognised by the awarding of the 2010 Nobel Prize in Chemistry to Heck, Negishi, and Suzuki for their pioneering metal catalysed reactions.[4]

The earliest reports of carbon-carbon coupling reactions involved the use of reagents such as Grignards and organolithiums,[5,6] which do not fit the ethos of green chemistry and sustainability due to the specialist handling required and their hazardous nature. To this end, the development of metal catalysed coupling reactions posed a pivotal moment in the move towards more environmentally friendly synthesis. The most

commonly utilised metal catalysed carbon-carbon coupling reactions are the Sonogashira,[7] Mizoroki-Heck,[8,9] Suzuki-Miyaura,[10] Stille,[11] Negishi,[12] and Kamuda[13] carbon-carbon coupling reactions, Figure 1.1. These allow for the synthesis of a variety of aryl and biaryl compounds, without consumption of the metal centre.

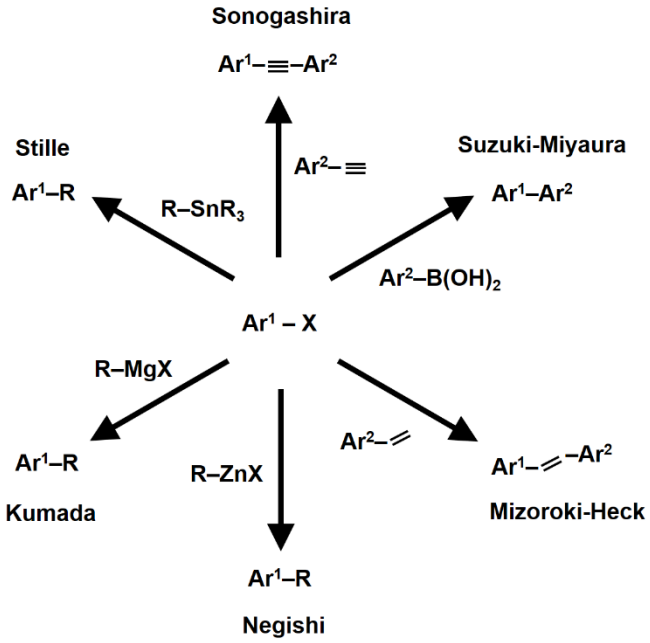

Figure 1.1: Key carbon-carbon coupling reactions involving aryl halides.

In each of the listed reactions, a palladium centre (typically with associated ligands) undergoes an oxidation reduction cycle between palladium(II) and palladium(0) during the catalytic process,[14] Figure 1.2. The active Pd^0L_2 catalyst can be formed via dissociation of a Pd^0L_4 complex such as $Pd(PPh_3)_4$,[15] or via activation of a palladium(II) pre-catalyst such as $Pd(OAc)_2$.[16] After formation of the active catalyst, oxidative addition of the aryl halide to the catalyst yields a *trans* complex,[17] followed by transmetallation, *cis-trans* isomerisation, and finally reductive elimination to yield the coupled product and regeneration of the active catalyst.[14] The rate limiting step is generally oxidative addition, most notably for aryl chlorides and deactivated aryl bromides, with reactivity decreasing I > Br > Cl.[18]

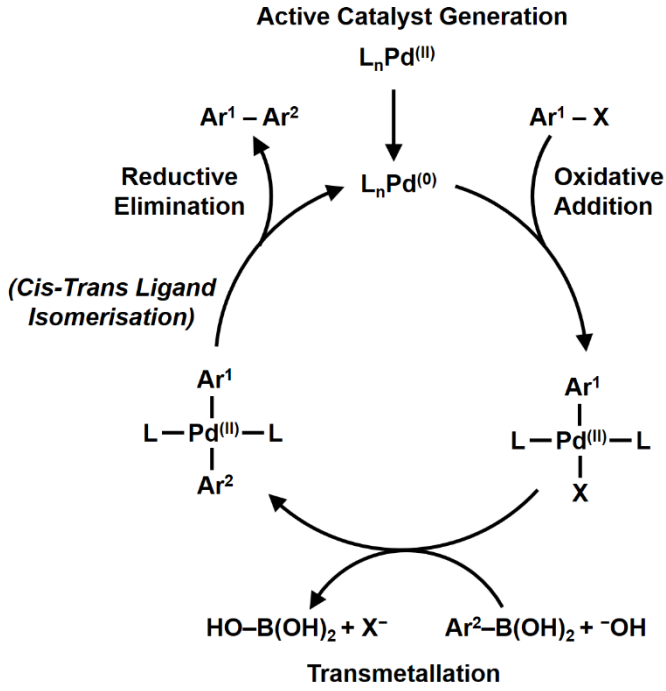

Figure 1.2: The Suzuki-Miyaura carbon-carbon coupling reaction using PdL_2.

1.1.2 The Use of Heterogeneous Palladium Catalysts

In solution, homogeneous catalysts can provide extremely high turn-over frequencies (TOFs) (defined as the number of moles of product per mole of palladium per second[19]), often in the order of 10^7 h^{-1}.[20,21] This high reactivity comes at the cost of the necessity for post reaction separation of the catalyst and reactant solution, leading to problems with public health regulation compliance for metal contaminants in active pharmaceutical ingredients.[22]

Heterogeneous catalysts offer significant benefits over homogeneous catalysts with regards to the aforementioned challenges. Comparable TOFs to those of homogeneous catalysts have been documented on dispersed zeolite-supported palladium catalysts,[23] whilst offering improved separation through filtration. Palladium on carbon (Pd/C) is commonly used as a model heterogeneous system, as it displays high TOFs (10^6 h^{-1}) and meets many of the criteria for an environmentally friendly catalyst due to its simple preparation.[24,25,26,27] Many alternative support materials such as inorganic solids,[28] thin polymer films,[29,30,31] cellulose paper,[32] wool,[33] and loose polymer fibres,[34,35] have been

envisaged for heterogeneous carbon-carbon coupling reactions. Each of these has the benefit of improved post reaction separation and reusability over homogeneous catalysts.

Despite the reduced rates of carbon-carbon coupling observed for aryl chloride reactants, the development of catalysts which achieve comparable rates with chloro derivatives has attracted attention due to the reduced costs (about five times lower cost relative to iodobenzene).[36,37] High TOFs for a range of homogeneous carbon-carbon coupling reactions have been achieved using ligands such as oximes,[38] phosphanes,[39,40,41,42] and carbenes,[43,44] signifying progression towards more sustainable catalysts. Although heterogeneous catalysts are currently unable to display comparable TOFs for aryl chloride, significant progress has been made in this respect.

Immobilisation of palladium clusters within the top surface of cobalt oxide-based films as been demonstrated to couple activated aryl chlorides with TOFs similar to non-activated aryl bromides.[45] Similarly, mixed magnesium-aluminium oxides also show good total conversion of aryl chlorides when palladium clusters are attached to the surface during synthesis.[46] This type of catalyst allows for the benefits of separation to be combined with utilisation of cheaper reagents. In reality, heterogeneous catalysts would not need to achieve the same rates as a homogeneous catalyst; economic viability may be achieved at lower TOFs due to the ease of separation of solid supported catalysts.

Despite the considerable benefits, heterogenous palladium catalysts are not without fault. The exact role and nature of the palladium active species is still unclear, with the potential for leaching of palladium into the reactant solution due to comparatively weak coordination bonding in some materials.[47] In addition, generation of the active catalyst (via in-situ formation of Pd^0)[48,49] may result in the formation of palladium nanoparticles during catalytic use,[50,51,52] indicating that the observed catalytic activity of many heterogeneous systems may, in part, be due to palladium nanoparticles formed in situ. Such nanoparticles may facilitate catalysis in several ways: by direct reaction bound to the supports' surface,[53] by diffusion into solution and readsorption upon reaction completion,[52,54] or by acting as reservoirs for reactive molecular palladium species.[55,56]

1.1.3 A Functional Surface Approach

Despite the reduced TOFs and potential palladium leaching of heterogeneous systems, the lack of solvent-based post reaction catalyst separation and excellent potential recyclability makes heterogeneous palladium carbon-carbon coupling a rewarding area

for development. Crucially, moving away from powdered heterogeneous catalysts allows for the development of continuous rather than batch catalytic processes.

1.2 Carbon Sequestration

Large scale industrial processes involved in bulk chemical synthesis produce a range of airborne pollutants, either directly through emitted exhaust gas, or indirectly through the use of fossil fuel generated electricity. In developing environmentally sustainable catalytic processes it is therefore vital to ensure proper treatment or control of any emitted gaseous waste.

One of the major sources of pollution from combustion engines is CO_2; the atmospheric concentrations of which have been increasing rapidly since the industrial revolution (ca. 1760–1840) from 280 ppm, to >400 ppm in 2017.[57,58] These are the highest levels recorded in the past 650000 years,[59] therefore despite the apparent controversy over the cause of such a significant rise, little argument can be made for not addressing global CO_2 emissions. The effects of a net increase in CO_2 concentration on the environment include climate change and associated temperature related effects,[60] ocean acidification,[61] and changes in plant ecology and nutritional density,[62] outcomes which may not be reversible.[60] Many efforts to reduce emission have already been taken worldwide, with treaties such as the Paris climate agreement attempting to unite nations over a global initiative.[63] Given the ever increasing energy demand, production of CO_2 will likely continue from combustion engines and power plants for many years to come.

Carbon sequestration is the capture of CO_2 from a system, followed by permanent storage in geological formations such as depleted oil and gas seams.[64] In natural systems this occurs via carbon sinks such as the formation of carbonate in oceans and the growth of long lived plants.[57,61] By designing systems to capture and store large amounts of CO_2 at the point of emission, we can relieve the pressure on environmental systems, reducing the global net CO_2 production. Most importantly, any material for carbon capture and sequestration must itself have a low environmental impact.

Typically, point of source carbon capture in fossil fuel driven power plants (electrical and heat production accounted for 25% of global CO_2 emissions in 2010)[65] can take the form of either post-combustion or pre-combustion capture steps, Figure 1.3.[66] Post-combustion is attractive due to the relative ease in which it can be applied to current power stations, however the concentration of CO_2 in typical flue gas is low and at ambient

pressure. Comparatively, pre-combustion systems can provide better total uptake due to concentrated CO_2 levels and increased pressure in the gas stream but cannot be easily retrofitted to existing systems. No matter which route an industrial process chooses to capture CO_2, the active storage material must have sufficient CO_2 uptake levels and acceptable reusability to ensure economic and environmental sustainability.

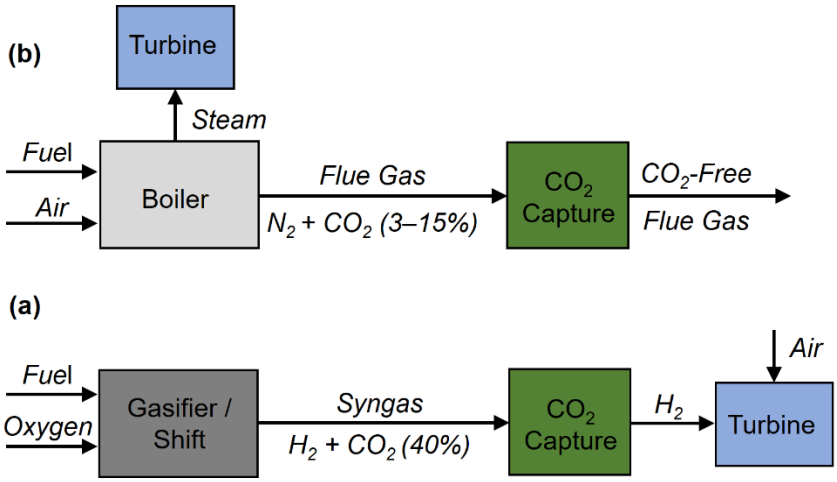

Figure 1.3: Examples of: (a); pre-combustion and (b) post-combustion CO_2 capture systems in coal-driven power generation. Figure adapted from reference 66.

1.2.1 Current Materials for Carbon Sequestration

One of the oldest methods for CO_2 removal from gas flows entails the use of an aqueous solution of amines, which react with CO_2 to form a carbamate.[67] Originally developed in 1930 for separation of natural gas streams,[68] this technology was later assessed for use in scrubbing CO_2 from flue gas.[69] One of the main concerns with the use of amine solutions is the large amount of heat required to regenerate the amine and compress the evolved CO_2 for sequestration, which results in a high cost of the process.[69] These costs can be somewhat mitigated by intelligent design of the turbine and stripping system for retention of energy.[70,71,72]

Given the viability of amine absorption, reducing the energy barrier for desorption of the CO_2 is highly sought after. One option is the use of a carbonic anhydrase (CA) enzyme, which can act as a promoter to reduce the energy demand of desorption.[73,74] Membrane immobilization has been used to stabilise the enzyme, however there is potential for mass transfer limitations through the amine liquid phase to the membranes

which could reduce the overall rate of uptake.[73] Small scale testing of CA enzyme-based systems has shown that 85% removal of CO_2 from a concentrated feed stream can be achieved.[74]

Increased temperature ranges for absorption compared to aqueous amine systems can be achieved using alkali metal oxides, which demonstrate CO_2 capture from <100 ºC up to 700 ºC depending on the oxide composition.[75] Of all the alkali metal oxides, calcium oxide yields the highest CO_2 adsorption (~70 wt%). However, instability towards sintering hinders its application for repeated industrial adsorption-desorption cycles.[76] This can be partially resolved by the formation of binary oxides,[75] although the total absorption capacity per cycle is reduced.

Alternative solid sorbents include carbonaceous materials such as activated carbon,[77] carbon nanotubes,[78] and zeolitic frameworks.[79] A major drawback of these capture materials is that CO_2 is weakly physisorbed onto the material, yielding poor selectivity and high temperature sensitivity. Zeolites containing alkali metals show improvements in operable temperature range,[80] however water adsorption competes with CO_2 adsorption,[81] limiting the applicability to flue gases which typically have a high water content.

Another popular industrial system is the hot carbonate system, which relies on the adsorption of CO_2 into the carbonate to form a bicarbonate. Normally this would then need to be regenerated separately, however the Benfield process has reduced the downtime associated with this by including an on-line method of regeneration. To achieve this, a separate regeneration reactor is added, into which the bicarbonate is continuously transferred and stripped on the excess CO_2.[82] The regenerated carbonate is then recycled back into the absorption reactor. The main drawback is its high cost due to the engineering demands of adding a Benfield system to a plant.

One of the main drawbacks of all the aforementioned processes is the limited total absorption, which is typically a 1:1 molar ratio of CO_2 to reagent. At high pressures, metal organic frameworks (MOFs) have demonstrated incredibly high absorption capacities, exceeding 280 wt% CO_2 uptake at 50 bar.[83] Despite atmospheric absorption capacities being lower than those measured at high pressure, MOFs have the potential to outperform other CO_2 capture materials (4.4 wt% possible in simulated air mixtures[84]). Saturated adsorption levels of CO_2 in MOFs can be correlated to the total surface area of the

material,[85] which explains the high weight percent captures possible with MOF materials given that surface areas exceeding 10^3 m^2 g^{-1} have been reported.[86]

1.2.2 Surface Bound Capture Materials

MOFs have been shown to give the highest capture by mass of all CO_2 capture materials, making them ideal candidates for sequestration of atmospheric CO_2. Their drawbacks lie in synthesis from linkers that are often not commonly available, along with the nanoscale size of the solvothermally synthesised particles. This limits the applicability of MOFs to many industrial processes, which would suffer from large pressure drops over packed beds of such small particles. Whilst pelleting may overcome these problems, the risk of reduced surface area arising from MOF framework damage due to sintering and pore blocking during the pelleting process may render this an unsuitable option.

A functional surface approach could allow for anchoring of MOFs to a support that suited a specific application. In addition, captured CO_2 may then be used for catalytic processes such as the formation of syngas and hydrogenation of CO_2 to methanol through multifunctional surface design.[87,88] Such a system would not only remove CO_2 from the atmosphere, but also provide an environmentally friendly source of reagents for industrial processes.

1.3 The World Water Shortage

Water is without a doubt one of the most important resources this planet has to offer. Only 2.5% of the planet's water is found as freshwater and access to clean water and sanitation has seen only slight improvements in the last decade.[89,90] However, the full scale of the water crisis in many developing countries is difficult to discern from the collated data available.

For example, the readily quoted 2.5% freshwater statistic does not consider the proportion of freshwater that is accessible at the surface at any one point in time. To this end, the annual discharge of rivers and other waterways into the oceans can be considered, which gives a reduced figure of 45,500 km^3 per year.[91] However, it is estimated that up to 10% of this is lost through subterranean run-off;[92] as well as additional losses through evapotransipration. All these effects contribute to an ever-diminishing amount of available freshwater.

Gross volume of freshwater is but one element that needs to be considered when assessing water scarcity. Water contamination is one of the biggest factors affecting health in areas where water crises occur. The three countries with the highest diarrhoea mortality rates are India, Nigeria and Pakistan, with mortality rates at 402,200, 119,700 and 103,300 deaths per year respectively.[93,94,95] To take India as an example, the total available renewable water resources total 1,911 km^3 per year.[96] 56 km^3 per year is used for municipal purposes, which correlates to 45 m^3 per capita per year.[96] In the UK, municipal water usage stands at 118 m^3 per capita per year.[97] On the face of it, in terms of gross water usage, the figures belie that the water crisis is not nearly as severe as it is commonly believed to be. However, the high diarrhoea mortality rates demonstrate that much of this water is unsuitable for human consumption and the division of clean water is anything but even.

Similar trends are observed in the data for Nigeria, where municipal water usage stands at 89 m^3 per capita per year,[98] yet the mortality rate for diarrhoea in terms of percentage population stands at more than twice that of India. Therefore, the biggest challenge facing these countries when addressing the water crisis is that of purification, rather than just acquisition.

1.3.1 Sources of Drinking Water

The source of drinking water in countries such as India remains a problem; the cleaner the source, the easier it is to purify. To this end it is worth considering the most common methods employed in countries such as India to collect drinking water (as well as methods still in development) to assess the application of water purification.

Ground water is a common source of drinking water for much of India when brought to the surface via wells. However, it is susceptible to contamination in the form of nitrates from agricultural run-off,[99,100] pharmaceutical effluent,[101] fluoride and arsenic.[102,103] Recently, there have also been reports of organochloride pesticides present in groundwater,[104] however these are found at lower concentrations than in surface water.[105] Despite these sources of contamination, ground water provides a vital source of drinking water for those fortunate enough to have access to a well. Unfortunately, in many cases other water sources are being used, which possess higher contamination levels.

Surface water (such as lakes and rivers) is by the far the most accessible source of water in areas where there is not an inherent shortage of water in the local environment.

However, unlike water from wells it is often considerably more contaminated by bacteria from faecal matter.[106] Anthropogenic activity is a major source of contamination of waterways in India. Mining, tanneries, steel plants and thermal power plants all produce effluent streams that can be rich in heavy metals,[107] along with pharmaceutical industries that can introduce a variety of aromatic organic compounds into waterways.[101] However, their effect is somewhat dwarfed by the inefficient management of human effluent and the resulting contamination of drinking water sources. Whilst early efforts have curbed the spread of pathogens such as typhoid and cholera, many other bacteria originating from human waste are still prevalent in surface water.[108]

Where rainfall is plentiful, collection and subsequent storage of rainwater offers a safe alternative source of drinking water. In areas of low atmospheric pollution where collection methods are sanitised, rainwater may be used immediately as drinking water. However, pollution and storage often results in the need for further purification.[109] There are also health concerns over the lack of dissolved minerals in rain water when it is used as a primary drinking water source alongside a diet poor in minerals.[109] The concept of rainwater harvesting is far from new, with evidence of anthropological features associated with rainwater harvesting from as far back as 2600 BC in India.[110]

Many arid areas that lack regular rainfall (particularly those near coastlines) see frequent fog episodes.[111] Harvesting water from fog is becoming an active area of research, particularly in biomimetics. There are examples where nature has devised ingenious surfaces for capture of water from saturated air and fog droplets.[112] Fog harvesting was demonstrated at a relatively simplistic level by utilising polypropylene mesh supported perpendicular to the fog stream, known as the “standard fog collector” or SFC.[113,114] One of the main advantages to fog harvesting is the potential for a low cost solution to the water crisis in arid areas with the right environmental conditions. To this end, the first application of a fog harvesting system to supply a community with water was a scaled-up version of the SFC in El Tofo in northern Chile.[115] However, as with all water collection methods, there is not a ‘one size fits all’ method, so effective application of the aforementioned techniques must be carefully considered for each region or community in need.

1.3.2 Purification by Filtration

Filtration of water, whether collected from rain, fog or rivers, is quite often the least costly method for purification. Effluent flows are often treated by filtration before they pass to water systems or municipal applications. For heavily soiled effluent flows such as municipal waste, a multistage process is required, with each stage providing sequential purification. Primary treatment is often a sedimentation step, allowing large particulate matter to be removed from the effluent stream. Secondary treatment removes the bulk of the biological matter by degradation utilising bacterial cultures developed within the treatment units. At this point the effluent flow may be discharged into non-sensitive water systems. Tertiary purification (such as filtration) provides the necessary quality of water for unrestricted irrigation or municipal use, removing the pathogenic species that remain after secondary treatment.[116]

Membrane filtration units are often used as modular systems, with each type of membrane offering different rejection parameters, Figure 1.4.[117] Microfiltration and ultrafiltration have attracted the most interest with regards to water purification of effluent streams and production of potable water due to higher flux at lower operating pressures. One of the main drawbacks to membrane-based systems is the increase in required operating pressures (or the decrease in flux at a set pressure) over time due to fouling. This results in the requirement for regular cleaning, increased operating costs and replacement of the membrane units if they become irreversibly fouled.

Biofouling is by far one of the most problematic causes of reduced flux for filtration elements.[118,119,120,121] At the membrane surface there is a strong flow of water, acting as an anchoring force for biomolecules, along with a potential for increased nutrient flow and biomass; it is therefore unsurprising that biofilm formation is a common occurrence. Ideally, control of biofilm formation would be achieved without the use of biocides, reducing costs and preventing the need for removal of any biocidal agent if it enters the filtrate. This could be achieved by preventing the initial bioadhesion that leads to biofilm formation. Surface functionalisation may provide the answer through modification of surface roughness and other properties, which can reduce bioadhesion.

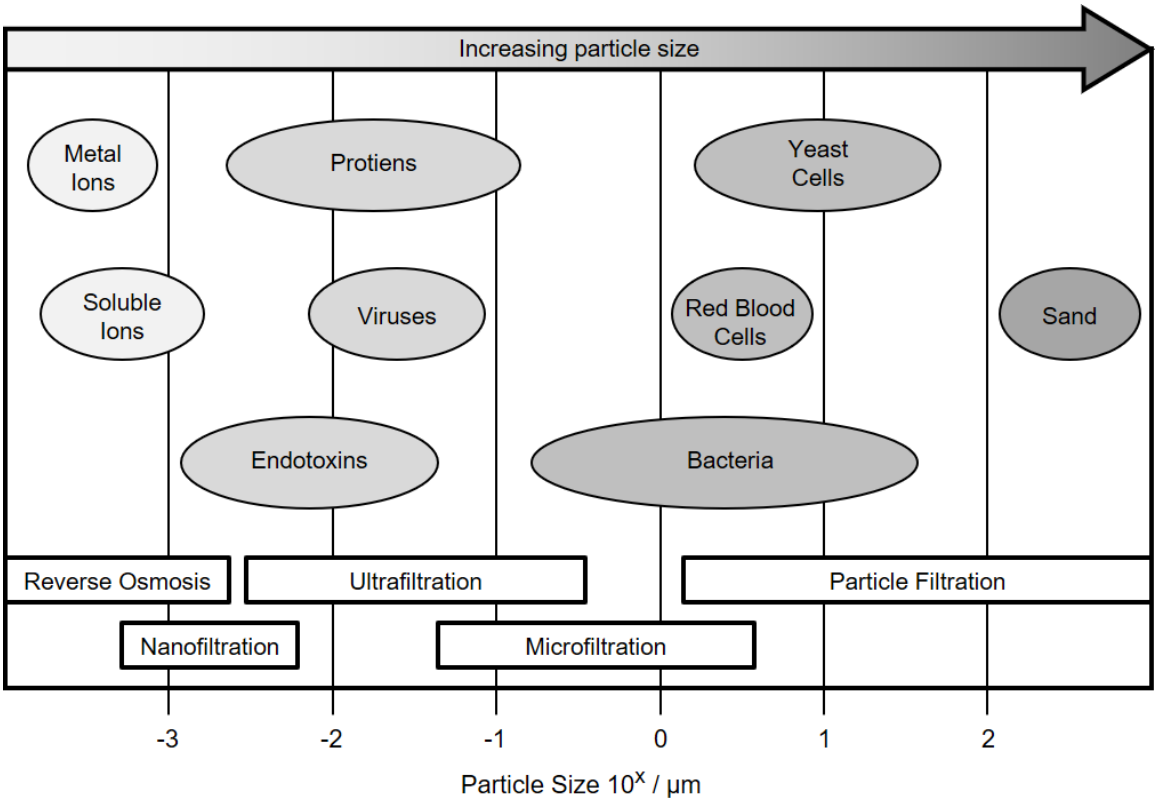

Figure 1.4: Schematic diagram of different types of particles and the appropriate filtration type for each size range.

1.3.3 Ultraviolet Sterilisation

Ultraviolet (UV) light in the 280–315 nm range (UVB) has well documented sterilisation effects. Although known since the late 1800s, the true nature of UV sterilisation was not discussed until 1928.[122] Unfortunately only a small fraction of the sun's output falls within this region, which limits the efficiency of solar UV sterilisation methods. Therefore, either a synthetic form of UV light must be used, or concentration of the sun's UVB output must be achieved through reactor design. The former option is used in many industrial and domestic applications, whereas the latter offers a much more sustainable system for developing countries. So popular is the concept of solar water disinfection, that the term 'SODIS' was coined (a contraction of **So**lar **Dis**infection).

There has been a drive over the last 10 years to make SODIS accessible to communities where it is needed most. At its simplest, the SODIS initiative (from the Swiss Federal Institute of Aquatic Sciences and Technology) has provided plastic bottles in 15

countries spanning Africa, Asia and Latin America for simple rooftop SODIS.[123] The bottle is filled with water from the available water source, followed by placement of the bottle in full sun (often on a rooftop) for the recommended time of 6 h for a 1 L bottle.

Although particulate matter, dissolved salts and heavy metals are unaffected by SODIS, the main water borne pathogenic species are. *Escherichia coli* is often used as an indicator for the presence of faecal coliform, therefore studies into the effect of UV on this bacterial species are common.[124,125] It is the effect of UV light on DNA which causes inactivation of the bacteria,[126] manifesting itself in disruption of normal cellular functions such as ATP synthesis.[125] In addition, there is a degree of cell wall damage which also dictates the amount of inactivation, which is dependent on several factors. The presence of dissolved oxygen greatly increases the rate of photo-inactivation, with the increase dependent on the bacterial species.[127] Salt concentration and pH also play a key role.[128] Viral pathogens are considerably more variable in their response to photo-inactivation. For example, whilst bovine rotavirus and polio can be completely inactivated in 6 h of illumination with strong natural sunlight,[129,130] encephalomyocarditis viruses and a range of coliphage viruses require significantly longer exposure times at normal solar photon flux.[129,131] Whilst SODIS has proven to be effective against a range of pathogens, protozoa have proven to be much more resilient to the treatment.[130,132,133]

SODIS efficiency is greatly dependent on the reactor type. The aforementioned studies considered the effects of natural sunlight on pathogens at radiative fluxes similar to that experienced in many equatorial countries. It stands to reason that increased pathogenic inactivation can be achieved by concentrating solar irradiation, not only through increased UV irradiation, but also through elevated temperatures which have been shown to increases pathogenic cyst inactivation.[130,132] However, almost counterintuitively, the inactivation of bacteria is dependent on the uninterrupted total energy per unit area irradiated, rather than the peak irradiance.[134] For *E. Coli* this equates to >108 kJ m^{-2}, which explains why batch reactors are often more effective then continuous flow reactors for inactivation of pathogens.[134] Nevertheless, continuous flow reactors have shown some success via the application of compound parabolic collectors, or CPCs, schematically shown in Figure 1.5. These curved mirrors allow concentration of light onto a central point independent of the direction of illumination. A reactor of this type was piloted in rural Kenya to purify surface water from a local dam;[135] capable of an output flow of 10 L min^{-1}, this reactor showed complete removal of coliform after a 20 min pass time.

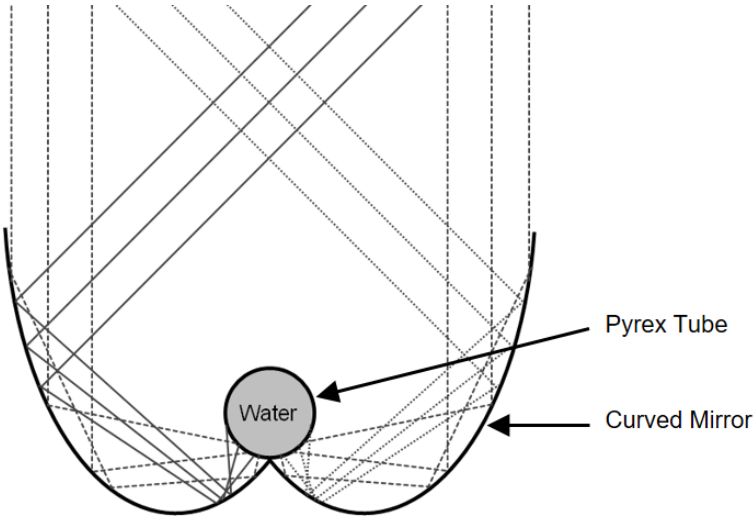

Figure 1.5: Schematic of a compound parabolic collector (CPC) for water purification. Through careful design, solar light can be directed into a central Pyrex tube (through which contaminated water is flowed) independent of the illumination angle**.**

1.3.4 Metal Oxide Photocatalysis

Inorganic oxides are used in a wide variety of applications, such as solid-state gas sensors,[136,137] memory applications,[138,139] photocleaning surfaces,[140] light emitting diodes and solar cells.[141,142] As with photocatalysis, many of these applications rely on energy generated from the harvesting of light, therefore increasing the efficiency of this process is paramount in developing new materials and enhancing productivity.

From a molecular orbital description, the splitting of valence orbitals into bonding, non-bonding and antibonding orbitals for polyatomics produces a set of discreet energy levels, equal in number to those of the valence orbitals that were combined to create them. As a molecule increases in size, the number of molecular orbitals increases until discreet levels can no longer be defined. At this point the orbitals can be described as crystal orbitals that extend through the solid and are referred to as bands. The variation in energy of the bands as a function of the wavenumber k ($2\pi/\lambda$) forms the basis of band structure diagrams. A transition can only occur between orbitals with the same value of k (this is not strictly true for relaxations, when phonons can cause a shift in k).[143] Therefore, the band gap is defined as the energy difference between the maximum of the valence band and

the minimum of the conduction band. Band minima and maxima may not correspond to the same value of *k*, thus band gaps are termed direct if they align, and indirect if not.

Defect sites break the regular periodicity causing perturbations of the electronic structure. Point defects are common in one form or another in solids. They can mainly be classified as lattice vacancies, interstitial atoms, Schottky defects or Frenkel defects. The former two are self-explanatory. Schottky defects are the formation of a cation and anion vacancy, Frenkel defects are where a vacancy is balanced by an interstitial ion. An alternative way a defect can be charge-balanced is by additional electrons or holes in the lattice. An example is the *F*-centre in alkali halides, where anion vacancies trap electrons, which have a defined set of electronic transitions resulting in colour (hence their more common name of colour centres).[144] Similar effects can be seen when atoms are substituted for dopant species. For example, if a lattice position which normally is occupied by a species with *n* valence electrons is substituted for a species with *n* – 1 electrons, an acceptor level is introduced into the band structure producing holes in the valence band (VB). Similarly, if it is exchanged for a species with *n* + 1 electrons, a donor level is introduced which can donate an electron into the conduction band (CB).

By far the most studied photocatalytic inorganic oxide is titanium dioxide (TiO_2). Possessing a wide band gap of 3.2 eV for anatase and 3.0 eV for rutile,[145] photoexcitation by UV light causes the formation of electron-hole pairs. The presence of adsorbed oxygen at the surface causes trapping of these photo excited electrons as $O_2^{-}{}_{(ads)}$ species;[146,147,148,149] this results in an electrostatic repulsion between the surface and the remaining CB electrons, self-limiting the concentration of $O_2^{-}{}_{(ads)}$. The negatively charged surface attracts holes in the valence band, and the combination with $O_2^{-}{}_{(ads)}$ leads to dissociation of O_2 and formation of surface vacancies.[148,150,151] The equilibrium between dissociation and re-adsorption of O_2 dictates the concentration of electrons in the CB.[150]

Photodegradation of small organic molecules, such as pesticides, has shown to be very effective over TiO_2. There are numerous reports on the photocatalytic power of the UV-TiO_2 system, spanning oxygen and nitrogen containing compounds,[152,153,154,155,156,157] as well as chlorinated and aromatic molecules which often make up the building block of pesticides.[158,159,160,161,162] Crucially for water purification, TiO_2 has shown to have high bactericidal activity towards *E. coli*,[163,164] as well as other common bacteria.[165,166] Direct comparison with non-catalysed SODIS demonstrated that TiO_2 inclusion improves oocyst destruction,[132] an area where SODIS is normally insufficient.

As with the degradation of small organic molecules, the exact mechanism of bactericidal activity is not well established. Several theories have been proposed, the first suggests that photochemical oxidation of coenzyme A (CoA) was occurring, producing a dimeric form.[166,167] CoA is present in all living organisms, functioning as an acyl carrier group and carbonyl activating group in many biochemical pathways such as respiration. Thus, it was thought that CoA inactivation was limiting respiratory activity leading to cell death. A potential theory is that direct disruption of the cell wall is occurring; although the exact mechanism is unclear, it manifests as leakage of K^+ ions that parallels cell death.[165] Another mechanism may be the photooxidative destruction of membranous endotoxins integral to the cell wall.[168] It is also possible that the photogenerated reactive species attack polyunsaturated phospholipids, causing a peroxidation reaction resulting in the breakdown of the cell membrane.[169] Of course it is unlikely that only one pathway exists. Different bacterial species may be susceptible to different modes of attack, possibly reflected in the various mechanisms proposed, which often study different bacteria. However, in all cases, the inclusion of hydroxide, peroxide and oxygen species seems to be a prerequisite.[170,171]

1.3.5 Putting Theory into Practice

TiO_2 is a widely studied photocatalyst that shows huge potential for water purification via SODIS. Whilst powdered material (which is a common form for photocatalytic materials) offers an excellent tool for research purposes, it is not a cost-effective method for water purification due to the requirement for post reaction separation effectively making the addition of photocatalyst more costly than ultrafiltration alone. Therefore, any treatment applied must be transferable to an immobilised form for ease of separation.

1.4 Scope of Thesis

Consideration is given to how functional catalytic surfaces can be employed for development of sustainable technology with regards to carbon-carbon coupling reactions, CO_2 sequestration and photocatalysis.

Carbon-carbon coupling reactions are widely used in the industrial synthesis of fine chemicals and pharmaceuticals. Homogeneous catalysts for this process require post reaction separation, limiting their application to batch processes. Heterogeneous catalysts

offer potential for continuous flow reactors, reducing the environmental and economic cost associated with separation steps. Easily separable palladium catalysts are designed, through surface functionalisation using plasma deposition of polymers with tailored surface moieties. These are prepared by surface complexation of palladium(II) chloride with plasmachemical imidazole functionalised non-woven polypropylene cloth and by complexation of palladium(II) chloride to ionic liquid functionalised flexible porous substrates. For Sonogashira, Mizoroki-Heck, and Suzuki-Miyaura carbon-carbon coupling reactions in conjunction with environmentally friendly solvents, high product yields (54%, 82%, and 99%, respectively) and selectivities (99%, 93%, and greater than 99% respectively) have been measured for palladium catalyst cloths. Palladium-poly(ionic liquid) membranes are demonstrated to have a high yield and selectivity (77% and greater than 99%, respectively) for the Suzuki-Miyaura reaction, which could also be conducted sonochemically at room temperature in conjunction with selective separation of product and reagents from the reaction solution. Both these materials display low levels of metal leaching allowing them to be recycled multiple times.

Increased industrial production of bulk and fine chemicals alongside population expansion have resulted in rising atmospheric CO_2 levels, making offsetting emissions through CO_2 sequestration (capture and permanent storage) a world-wide concern. Point of emission control of CO_2 has been applied to industrial plants through amine and carbonate reactors, however these are themselves typically power intensive due to the regeneration step. The practical application of metal organic frameworks (MOFs) for CO_2 capture has not yet been fully realised, despite their excellent gas capture properties. Surface functionalisation is demonstrated to provide a tailored route for promoting the growth of CO_2 capture MOFs on inorganic and polymeric substrates. Pulsed plasma deposited poly(1-allylimidazole) films are herein shown to initiate the growth of microporous [Zn (benzene-1,4-dicarboxylate)-(4,4'-bipyridine)0.5] (MOF-508). The liquid phase epitaxy synthesis of the MOF-508a polymorph contains two interpenetrating crystal lattice frameworks which undergo orientated Volmer–Weber growth. CO_2 capture is demonstrated at atmospheric concentrations (0.2 Torr), with a total uptake of 6 mmol g^{-1}.

With demands for freshwater divided between industrial and municipal uses, access to clean water is of vital importance; unfortunately, many lack this most basic resource. Contamination from agriculture and industry is a major source of poor water quality in countries such as India, Nigeria and Pakistan, making affordable photocatalysts

crucial for supporting development in these regions. TiO_2 is a photocatalytically active semiconductor which is currently used for water purification applications. Although highly effective in a dispersed form, filtration requirements make this challenging to adopt on a large scale. TiO_2 is herein shown to be made separable through attachment to magnetic particles and encapsulation into macro scale spheres. The synthesised materials are investigated for their UV and visible light photocatalytic activity through degradation of methylene blue organic dye.

The results of this thesis will then be discussed with respect to future work that could expand on the proof of concept studies outlined in the following chapters.

1.4 References

[1] Anastas, P. T.; Warner, J. C. Green Chemistry: Theory and Practice, Oxford University Press: New York, 1998, pp.30.

[2] Shien, H. C. Selected Applications of Transition Metal-Catalyzed Carbon Carbon Cross-Coupling Reactions in the Pharmaceutical Industry. In *Applications of Transition Metal Catlysis in Drug Discovery and Development: An Industrial Perspective*; Crawley, M. L.; Trost, B. M. John Wiley & Sons, Inc., Hoboken, New Jersey 2012; p 25–95.

[3] Dugger, R. W.; Ragan, J. A.; Ripin, D. H. B. Survey of GMP Bulk Reactions Run in a Research Facility between 1985 and 2002. *Org. Process Res. Dev.* **2005**, *9*, 253–258.

[4] Wu, X.-F.; Anbarasan, P.; Neumann, H.; Beller, M. From Noble Metal to Nobel Prize: Palladium-Catalyzed Coupling Reactions as Key Methods in Organic Synthesis. *Angew. Chemie Int. Edn.* **2010**, *49*, 9047–9050.

[5] Yamamura, M.; Moritani, I.; Murahashi, S.-I. The Reaction of σ-Vinylpalladium Complexes with Alkyllithiums. Stereospecific Syntheses of Olefins from Vinyl Halides and Alkyllithiums. *J. Organomet. Chem.* **1975**, *91*, C39–C42.

[6] Tamura, M.; Kochi, J. K. Copper-Catalyzed Coupling of Grignard Reagents and Akyl Halides in Tetrahydrofuran Solutions. *J Organomet. Chem.* **1972**, *42*, 205–228.

[7] Sonogashira, K.; Tohda, Y.; Hagihara, N. Convenient Synthesis of Acetylenes: Catalytic Substitutions of Acetylenic Hydrogen with Bromoalkenes, Iodoarenes, and Bromopyridines. *Tetrahedron Lett.* **1975**, *16*, 4467–4470.

[8] Heck, R. F.; Nolley, J. P. Jr. Palladium-Catalyzed Vinylic Hydrogen Substitution Reactions with Aryl, Benzyl, and Styryl Halides. *J.Org. Chem.* **1972**, *37*, 2320–2322.

[9] Mizoroki, T.; Mori, K.; Ozaki, A. Arylation of Olefin with Aryl Iodide Catalyzed by Palladium. *Bull. Chem. Soc. Japan* **1971**, *44*, 581.

[10] Miyaura, N.; Yanagi, T.; Suzuki, A. The Palladium-Catalyzed Cross-Coupling Reaction of Phenylboronic Acid with Haloarenes in the Presence of Bases. *Synth. Commun.* **1981**, *11*, 513–519.

[11] Milstein, D.; Stille, J. K. Palladium-Catalyzed Coupling of Tetraorganotin Compounds with Aryl and Benzyl Halides. Synthetic Utility and Mechanism. *J. Am. Chem. Soc.* **1978**, *100*, 3636–3638.

[12] Negishi, E.; Baba, S. Novel Stereoselective Alkenyl–Aryl Coupling via Nickel-Catalysed Reaction of Alkenylanes with Aryl Halides. *J. Chem. Soc., Chem*. *Commun*. **1976**, 596b–597b.

[13] Tamao, K.; Kiso, Y.; Sumitani, K.; Kumada, M. Alkyl Group Isomerization in the Cross-Coupling Reaction of Secondary Alkyl Grignard Reagents with Organic Halides in the Presence of Nickel-Phosphine Complexes as Catalysts. *J. Am. Chem. Soc*. **1972**, *94*, 9268–9269.

[14] Yin, L.; Liebscher, J. Carbon-Carbon Coupling Reactions Catalyzed by Heterogeneous Palladium Catalysts. *Chem. Rev*. **2006**, *107*, 133–173.

[15] Smith, G. B.; Dezeny, G. C.; Hughes, D. L.; King, A. O.; Verhoeven, T. R. J. Mechanistic Studies of the Suzuki Cross-Coupling Reaction. *Org. Chem.* **1994**, *59*, 8151–8156.

[16] Amatore, C.; Carre, E.; Jutand, A.; M'Barki, M. A. Evidence for the Ligation of Palladium(0) Complexes by Acetate Ions: Consequences on the Mechanism of Their Oxidative Addition with Phenyl Iodide and $PhPd(OAc)(PPh_3)_2$ as Intermediate in the Heck Reaction. *Organometallics* **1995**, *14*, 1818–1826.

[17] Aliprantis, A. O.; Canary, J. W. Observation of Catalytic Intermediates in the Suzuki Reaction by Electrospray Mass Spectrometry. *J. Am. Chem. Soc.* **1994**, *116*, 6985–6986.

[18] Fitton, P.; Rick, E. A. The Addition of Aryl Halides to Tetrakis(triphenylphosphine)palladium(0). *J. Organomet. Chem.* **1971**, *28*, 287–291

[19] Boudart, M. Turnover Rates in Heterogeneous Catalysis. *Chem. Rev.* **1995**, *95*, 661–665.

[20] Beller, M.; Fischer, H.; Herrmann, W. A.; Öfele, K.; Brossmer, C. Palladacycles as Efficient Catalysts for Aryl Coupling Reactions. *Angew. Chem. Int. Ed.* **1995**, *34*, 1848–1849.

[21] Feuerstein, M.; Laurenti, D.; Bougeant, C.; Doucet, H.; Santelli, M. Palladium–Tetraphosphine Catalysed Cross Coupling of Aryl Bromides with Arylboronic Acids: Remarkable Influence of the Nature of the Ligand. *Chem. Commun.* **2001**, *4*, 325–326.

[22] European Medicines Agency, ICH Guideline Q3D on Elemental Impurities http://www.ema.europa.eu/docs/en_GB/document_library/Scientific_guideline/2015/00/WC500180284.pdf (accessed Apr 5, 2016).

[23] Okumura, K.; Tomiyama, T.; Okuda, S.; Yoshida, H.; Niwa, M. Origin of the Excellent Catalytic Activity of Pd Loaded on Ultra-Stable Y Zeolites in Suzuki-Miyaura Reaction. *J. Catal.* **2010**, *273*, 156–166.

[24] Felpin, F. X.; Ayad, T.; Mitra, S. Pd/C: An Old Catalyst for New Applications - Its Use for the Suzuki-Miyaura Reaction. *Eur. J. Org. Chem.* **2006**, *12*, 2679–2690.

[25] Mateos, C.; Rincón, J. A.; Martín-Hidalgo, B.; Villanueva, J. Green and Scalable Procedure for Extremely Fast Ligandless Suzuki–Miyaura Cross-Coupling Reactions in Aqueous IPA Using Solid-Supported Pd in Continuous Flow. *Tetrahedron Lett.* **2014**, *55*, 3701–3705.

[26] Glasnov, T. N.; Findenig, S.; Kappe, C. O. Heterogeneous Versus Homogeneous Palladium Catalysts for Ligandless Mizoroki–Heck Reactions: A Comparison of Batch/Microwave and Continuous-Flow Processing. *Chem. - Eur. J.* **2009**, *15*, 1001–1010.

[27] Phan, N. T. S.; Khan, J.; Styring, P. Polymer-Supported Palladium Catalysed Suzuki–Miyaura Reactions in Batch and a Mini-Continuous Flow Reactor System. *Tetrahedron* **2005**, *61*, 12065–12073.

[28] Yin, L.; Liebscher, J. Carbon−Carbon Coupling Reactions Catalyzed by Heterogeneous Palladium Catalysts. *Chem. Rev.* **2007**, *107*, 133–173.

[29] Zhao, X.; Zhang, J.; Zhao, Y; Li, X. Pd- and Ni-Pyridyl Complexes Deposited as Films for Suzuki-Miyaura and Mizoroki-Heck Cross Coupling Reactions. *Catal. Lett.* **2015**, *145*, 2010–2019

[30] Zhao, X.; Zhao, Y.; Zhang, J.; Li, X. A Highly Active Multi-Usable Palladium Pyridylfluorene Film-Based Catalyst for C-C Cross-Coupling Reactions. *Appl. Organometal. Chem.* **2015**, *29*, 840–845

[31] Li, X.; Zhao, X.; Zhang, J.; Zhao, Y. Assembly of a Multilayer Film and Catalytic Application in Suzuki Cross-Coupling Reaction Based on Synergistic Effects of a Conjugated Organometallic Pyridyl $Pt(C{\equiv}C)_2$ Moiety with Palladium. *Chem. Commun.* **2013**, *49*, 10004–10006.

[32] Zheng, G.; Kaefer, K.; Mourdikoudis, S.; Polavarapu, L.; Vaz, B.; Cartmell, S. E.; Bouleghlimat, A.; Buurma, N. J.; Yate, L.; de Lera, Á. R.; Liz-Marzán, L. M.; Pastoriza-Santos, I.; Pérez-Juste, J. Palladium Nanoparticle-Loaded Cellulose Paper: A Highly Efficient, Robust, and Recyclable Self-Assembled Composite Catalytic System. *J. Phys. Chem. Lett.* **2015**, *6*, 230–238.

[33] Wu, S.; Ma, H.; Jia, X.; Zhong, Y.; Lei, Z. Biopolymer-Metal Complex Wool-Pd as a Highly Active Heterogeneous Catalyst for Heck Reaction in Aqueous Media. *Tetrahedron* **2011**, *67*, 250–256.

[34] Colacot, T. J.; Gore, E. S.; Kuber, A. High-Throughput Screening Studies of Fiber-Supported Catalysts Leading to Room-Temperature Suzuki Coupling. *Organometallics* **2002**, *21*, 3301–3304.

[35] Colacot, T. J.; Carole, W. A.; Neide, B. A.; Harad, A. Tunable Palladium-FibreCats for Aryl Chloride Suzuki Coupling with Minimal Metal Leaching. *Organometallics* **2008**, *27*, 5605–5611.

[36] Sigma Aldrich Co. http://www.sigmaaldrich.com/catalog/product/aldrich/i7632?lang=en&region=GB (accessed May 19, 2016).

[37] Sigma Aldrich Co http://www.sigmaaldrich.com/catalog/product/sial/319996?lang=en&region=GB (accessed May 19, 2016).

[38] Alonso, D. A.; Nájera, C.; Pacheco, M. C. Highly Active Oxime-Derived Palladacycle Complexes for Suzuki-Miyaura and Ullmann-Type Coupling Reactions. *J. Org. Chem.* **2002**, *67*, 5588–5594.

[39] Feuerstein, M.; Doucet, H.; Santelli, M. Palladium Catalysed Cross-Coupling of Aryl Chlorides with Arylboronic Acids in the Presence of a New Tetraphosphine Ligand. *Synlett.* **2001**, *9*, 1458–1460.

[40] Old, D. W.; Wolfe, J. P.; Buchwald, S. L. A Highly Active Catalyst for Palladium-Catalyzed Cross-Coupling Reactions: Room-Temperature Suzuki Couplings and Amination of Unactivated Aryl Chlorides. *J. Am. Chem. Soc*. **1998**, *120*, 9722–9723.

[41] Zapf, A.; Ehrentraut, A.; Beller, M. A. New Highly Efficient Catalyst System for the Coupling of Nonactivated and Deactivated Aryl Chlorides with Arylboronic Acids. *Angew. Chem. Int. Ed.* **2000**, *39*, 4153–4155.

[42] Littke, A. F.; Fu, G. C. The First General Method for Stille Cross-Couplings of Aryl Chlorides. *Angew. Chem. Int. Ed.* **1999**, *38*, 2411–2413.

[43] Grasa, G. A.; Hillier, A. C.; Nolan, S. P. Convenient and Efficient Suzuki−Miyaura Cross-Coupling Catalyzed by a Palladium/Diazabutadiene System. *Org. Lett*. **2001**, *3*, 1077–1080.

[44] Herrmann, W. A.; Reisinger, C.-P.; Spiegler, M. Chelating N-Heterocyclic Carbene Ligands in Palladium-Catalyzed Heck-Type Reactions. *J. Organomet. Chem.* **1998**, *1*, 93–96.

[45] Duan, L.; Fu, R.; Xiao, Z.; Zhao, Q.; Wang, J.-Q.; Chen, S.; Wan, Y. Activation of Aryl Chlorides in Water under Phase-Transfer Agent-Free and Ligand-Free Suzuki Coupling by Heterogeneous Palladium Supported on Hybrid Mesoporous Carbon. *ACS Catal.* **2015**, *5*, 575–586.

[46] Choudary, B. M.; Madhi, S.; Chowdari, N. S.; Kantam, M. L.; Sreedhar, B. Layered Double Hydroxide Supported Nanopalladium Catalyst for Heck-, Suzuki-, Sonogashira-, and Stille-Type Coupling Reactions of Chloroarenes. *J. Am. Chem. Soc.* **2002**, *124*, 14127–14136.

[47] Dioos, B.M.; Vankelecom, I. F.; Jacobs, P. Aspects of Immobilisation of Catalysts on Polymeric Supports. *Adv. Synth. Catal.* **2006**, *348*, 1413–1446.

[48] Rosner, T.; Bars, J. L.; Pfaltz, A.; Blackmond, D. G. Kinetic Studies of Heck Coupling Reactions Using Palladacycle Catalysts: Experimental and Kinetic Modeling of the Role of Dimer Species. *J. Am. Chem. Soc.* **2001**, *123*, 1848–1855.

[49] Consorti, C. S.; Flores, F. R.; Dupont, J. Kinetics and Mechanistic Aspects of the Heck Reaction Promoted by a CN-Palladacycle. *J. Am. Chem. Soc.* **2005**, *127*, 12054–12065.

[50] Han, W.; Liu, C.; Jin, Z.-L. In Situ Generation of Palladium Nanoparticles: A Simple and Highly Active Protocol for Oxygen-Promoted Ligand-Free Suzuki Coupling Reaction of Aryl Chlorides. *Org. Lett.* **2007**, *9*, 4005–4007.

[51] Rocaboy, C.; Gladysz, J. A. Thermomorphic Fluorous Imine and Thioether Palladacycles as Precursors for Highly Active Heck and Suzuki Catalysts; Evidence for Palladium Nanoparticle Pathways. *New J. Chem.* **2003**, *27*, 39–49.

[52] de Vries, A. H. M.; Mulders, J. M. C. A.; Mommers, J. H. M.; Henderick, H. J. W.; de Vries, J. G. Homeopathic Ligand-Free Palladium as a Catalyst in the Heck Reaction. A Comparison with a Palladacycle. *Org. Lett.* **2003,** *5*, 3285–3288.

[53] Ellis, P.; Fairlamb, I.; Hackett, S.; Wilson, K.; Lee, A. Evidence for the Surface-Catalyzed Suzuki–Miyaura Reaction over Palladium Nanoparticles: An Operando XAS Study. *Angew. Chem. Int. Ed.* **2010**, *49*, 1820–1824.

[54] Conlon, D. A.; Pipik, B.; Ferdinand, S.; LeBlond, C. R.; Sowa, Jr., J. R.; Izzo, B.; Collins, P.; Ho, G.-J.; Williams, M.; Shi, Y.-J.; Sun, Y. Suzuki-Miyaura Cross-Coupling with Quasi-Heterogeneous Palladium. *Adv. Synth. Catal.* **2003**, *345*, 931–935.

[55] Phan, S. N.; Van der Sluys, M.; Jones, C. W. On the Nature of the Active Species in Palladium Catalyzed Mizoroki–Heck and Suzuki–Miyaura Couplings – Homogeneous or Heterogeneous Catalysis, A Critical Review. *Adv. Synth. Catal.* **2006**, *348*, 609–678.

[56] Cassol, C. C.; Umpierre, A. P.; Machado, G.; Wolke, S. I.; Dupont, J. The Role of Pd Nanoparticles in Ionic Liquid in the Heck Reaction. *J. Am. Chem. Soc.* **2005**, *127*, 3298–3299.

[57] Canadell, J. G.; Le Quéré, C.; Raupach, M. R.; Field, C. B.; Buitenhuis, E. T.; Ciais, P.; Conway, T. G.; Gillett, N. P.; Houghton, R. A.; Marland, G. Contributions to Accelerating Atmospheric CO_2 Growth from Economic Activity, Carbon Intensity, and Efficiency of Natural Sinks. *PNAS* **2007**, *104*, 18866–18870.

[58] NOAA/ESRL Global Monitoring Division. https://www.esrl.noaa.gov/gmd/ccgg/trends/#mlo (accessed June 15, 2017).

[59] Siegenthaler, U.; Stocker, T. F.; Monnin, E.; Lüthi, D.; Schwander, J.; Stauffer, B.; Raynaud, D.; Barnola, J. M.; Fischer, H.; Masson-Delmotte, V.; Jouzel, J. Stable Carbon Cycle-Climate Relationship During the Late Pleistocene. *Science* **2005**, *25*, 1313–1317.

[60] Solomon, S.; Plattner, G.-K.; Knutti, R.; Friedlingstein, P. Irreversible Climate Change Due to Carbon Dioxide Emissions. *PNAS* **2009**, *106*, 1704–1709.

[61] Doney, S. C.; Fabry, V. J.; Feely, R. A.; Kleypas, J. A. Ocean Acidification: The Other CO_2 Problem. *Annu. Rev. Mar. Sci.* **2009**, *1*, 169–92.

[62] Taub, D. R.; Miller, B.; Allen, H. Effects of Elevated CO_2 on the Protein Concentration of Food Crops: A Meta-Analysis. *Global Change Biol.* **2008**,*14*, 565–575.

[63] Schreurs, M. A. The Paris Climate Agreement and the Three Largest Emitters: China, the United States, and the European Union. *Politics and Governance* **2016**, *4*, 219–223.

[64] White, C. M.; Strazisar, B. R.; Granite, E. J.; Hoffman, J. S.; Pennline, H. W. Separation and Capture of CO_2 from Large Stationary Sources and Sequestration in Geological Formations--Coalbeds and Deep Saline Aquifers. *J. Air Waste Manage. Assoc.* **2003**, *53*, 645–715.

[65] United States Environmental Protection Agency. https://www.epa.gov/ghgemissions/global-greenhouse-gas-emissions-data (accessed June 20, 2017)

[66] Figueroa, J. D.; Fout, T.; Plasynski, S.; McIlvried, H.; Srivastava, R. D. Advances in CO_2 capture technology—The U.S. Department of Energy's Carbon Sequestration Program. *Int. J. Greenhouse Gas Control* **2008**, *2*, 9–20.

[67] Caplow, M. Kinetics of Carbamate Formation and Breakdown. *J. Am. Chem. Soc*. **1968**, *90*, 6795–6803.

[68] Bottoms, R. R. Separating acid gases. U.S. Patent 1783901, Oct 7th 1930.

[69] Rochelle, G. T. Amine Scrubbing for CO_2 Capture. *Science* **2009**, *325*, 1652–1654.

[70] Mimura, T.; Simayoshi, H.; Suda, T.; Iijima, M.; Mituoka, S. Development of Energy Saving Technology for Flue Gas Carbon Dioxide Recovery in Power Plant by Chemical Absorption Method and Steam System*. Energy Convers. Manage.* **1997**, *38*, S57–S62.

[71] Desideri, U.; Paolucci, A. Performance Modelling of a Carbon Dioxide Removal System for Power Plants. *Energy Convers. Manage.* **1999**, *40*, 1899–1915.

[72] Singh, D.; Croiset, E.; Douglas, P. L.; Douglas, M. A. Techno-Economic Study of CO_2 Capture from an Existing Coal-Fired Power Plant: MEA Scrubbing vs. O_2/CO_2 Recycle Combustion. *Energy Convers. Manage.* **2003**, *44*, 3073–3091.

[73] Yong, J, K. J.; Stevens, G. W.; Caruso, F.; Kentis, S. E. The use of Carbonic Anhydrase to Accelerate Carbon Dioxide Capture Processes. *J. Appl. Chem. Biotechnol.* **2015**, *90*, 3–10.

[74] Trachtenberg, M. C.; Cowan, R. M.; Smith, D. A.; Horazak, D. A.; Jensen, M. D.; Laumb, J. D.; Vucelic, A. P.; Chen, H.; Wang, L.; Wu, X. Membrane-Based, Enzyme-Facilitated, Efficient Carbon Dioxide Capture. *Energy Procedia* **2009**, *1*, 353–360.

[75] Wang, S.; Yan, S.; Ma, X.; Gong, J. Recent Advances in Capture of Carbon Dioxide using Alkali-Metal-Based Oxides. *Energy Environ. Sci.* **2011**, *4*, 3805–3819.

[76] Abanades, J. C.; Anthony, E. J.; Lu, D. Y.; Salvador, C.; Alvarez, D. Capture of CO_2 from Combustion Gases in a Fluidized Bed of CaO. *AIChE J.* **2004**, *50*, 1614–1622.

[77] Himeno, S.; Komatsu, T.; Fujita, S. High-Pressure Adsorption Equilibria of Methane and Carbon Dioxide on Several Activated Carbons. *J. Chem. Eng. Data* **2005**, *50*, 369–376.

[78] Cinke, M.; Li, J.; Bauschlicher, C. W.; Ricca, A.; Meyyappan, M. CO_2 Adsorption in Single-Walled Carbon Nanotubes. *Chem. Phys. Lett.* **2003**, *376*, 761–766.

[79] Izzaouihda, S.; El Makarim, H. S.; Benoit, D. M.; Komiha, N. Theoretical Study of the CO_2 Adsorption by Zeolitic Imidazolate Frameworks (ZIFs). J*. Phys. Chem. C* **2017**, *121*, 20259–20265.

[80] Walton, K. S.; Abney, M. B.; LeVan, M. D. CO_2 Adsorption in Y and X Zeolites Modified by Alkali Metal Cation Exchange. *Microporous Mesoporous Mater.* **2006**, *91*, 78–84.

[81] Gallei, E.; Stumpf, G. Infrared Spectroscopic Studies of the Adsorption of Carbon Dioxide and the Coadsorption of Carbon Dioxide and Water on CaY- and NiY-Zeolites. *J. Colloid Interface Sci.* **1976**, *55*, 415–420.

[82] UOP. https://www.uop.com/?document=benfield-process-datasheet&download=1 (accessed December 1, 2017).

[83] Furukawa, H.; Ko, N.; Go, Y. B.; Aratani, N.; Choi, S. B.; Choi, E.; Yazaydin, A. O.; Snurr, R. Q.; O'Keeffe, M.; Kim, J.; Yaghi, O. M. Ultrahigh Porosity in Metal-Organic Frameworks. *Science* **2010**, *329*, 424–428.

[84] McDonald, T. M.; Lee, W. R.; Mason, J. A.; Wiers, B. M.; Hong, C. S.; Long, J. R. Capture of Carbon Dioxide from Air and Flue Gas in the Alkylamine-Appended Metal–Organic Framework mmen-Mg2(dobpdc). *J. Am. Chem. Soc.* **2012**, *134*, 7056–7065.

[85] Millward, A. R.; Yaghi, O. M. Metal−Organic Frameworks with Exceptionally High Capacity for Storage of Carbon Dioxide at Room Temperature. *J. Am. Chem. Soc*. **2005**, *127*, 17998–17999.

[86] Farha, O. K.; Eryazici, I.; Jeong, N. C.; Hauser, B. G.; Wilmer, C. E.; Sarjeant, A. A.; Snurr, R. Q.; Nguyen, S.-B. T.; Yazaydın, A. O.; Hupp, J. T. Metal–Organic Framework Materials with Ultrahigh Surface Areas: Is the Sky the Limit? *J. Am. Chem. Soc.* **2012**, *134*, 15016–15021.

[87] Song. C.; Pan, W. Tri-Reforming of Methane: A Novel Concept for Catalytic Production of Industrially Useful Synthesis Gas with Desired H_2/CO Ratios. *Catal. Today* **2004**, *98*, 463–484.

[88] Zhang, Q.; Zuo, Y. Z.; Han, M. H.; Wang, J. F.; Jin, Y.; Wei, F. Long Carbon Nanotubes Intercrossed Cu/Zn/Al/Zr Catalyst for CO/CO_2 Hydrogenation to Methanol/Dimethyl Ether. *Catal. Today* **2010**, *150*, 55–60.

[89] The World Bank statistics. http://data.worldbank.org/indicator/SH.H2O.SAFE.ZS (accessed May 22, 2013)

[90] The World Bank statistics. http://data.worldbank.org/indicator/SH.STA.ACSN (accessed May 22, 2013)

[91] Oki, T.; Kanae, S. Global Hydrological Cycles and World Water Resources. *Science* **2006**, *313*, 1068–1072.

[92] Church T. M. An Underground Route for the Water Cycle. *Nature* **1996**, *380*, 579–580.

[93] World Health Organisation. http://www.who.int/quantifying_ehimpacts/countryprofilessearo.pdf (accessed May 22, 2013)

[94] World Health Organisation. http://www.who.int/quantifying_ehimpacts/countryprofilesafro.pdf (accessed May 22, 2013)

[95] World Health Organisation. http://www.who.int/quantifying_ehimpacts/countryprofilesemro.pdf (accessed May 22, 2013)

[96] Food and Agriculture Organisation of the United Nations. http://www.fao.org/nr/water/aquastat/data/factsheets/aquastat_fact_sheet_ind_en.pdf (accessed May 22, 2013)

[97] Food and Agriculture Organisation of the United Nations. http://www.fao.org/nr/water/aquastat/data/factsheets/aquastat_fact_sheet_gbr_en.pdf (accessed May 22, 2013)

[98] Food and Agriculture Organisation of the United Nations. http://www.fao.org/nr/water/aquastat/data/factsheets/aquastat_fact_sheet_nga_en.pdf (accessed May 22, 2013)

[99] Almasri, M. N. Nitrate Contamination of Groundwater: A Conceptual Management Framework. *Environ. Impact Asses.* **2007**, *27*, 220–342.

[100] Jeevanandam, M.; Kannan, R.; Srinivasalu, S.; Rammohan, V. Hydrogeochemistry and Groundwater Quality Assessment of Lower Part of the Ponnaiyar River Basin, Cuddalore District, South India. *Environ. Monit. Assess.* **2006**, *132*, 263–274.

[101] Fick, J.; Söderström, H.; Lindberg, R. H.; Pham, C.; Tysklind, M.; Larsson, D. G. Contamination of Surface, Ground, and Drinking Water from Pharmaceutical Production. *Environ. Toxic. Chem*. **2009**, *28*, 2522–2527.

[102] Raju, N. J.; Dey, S.; Das, K. Fluoride Contamination in Groundwaters of Sonbhadra District, Uttar Pradesh, India. *Curr. Sci*. **2009**, *96*, 979–985.

[103] Seddique, A. A.; Masuda, H.; Mitamura, M.; Shinoda, K.; Yamanaka T.; Itai, T.; Maruoka, T.; Uesugi, K.; Ahmed, K. M.; Biswas, D. K. Arsenic Release from Biotite into a Holocene Groundwater Aquifer in Bangladesh. *Appl. Geochem.* **2008**, *23*, 2236–2248.

[104] Akhil, P. S.; Sujatha, C. H. Prevalence of Organochlorine Pesticide Residues in Groundwaters of Kasargod District, India. *Toxicol. Environ. Chem*. **2012**, *94*, 1718–1725.

[105] Kumari, B.; Madan, V. K.; Kathpal, T. S. Status of Insecticide Contamination of Soil and Water in Haryana, India. *Environ. Monit. Assess.* **2008**, *136*, 239–244.

[106] Dash, R. R.; Mehrotra, I.; Kumar, P.; Grischek, T. Lake Bank Filtration at Nainital, India: Water-Quality Evaluation. *Hydrogeol. J.* **2008**, *16*, 1089–1099.

[107] Kar, D.; Sur, P.; Mandal, K.; Saha, T.; Kole, R. K. Assessment of Heavy Metal Pollution in Surface Water. *Int. J. Environ. Sci. Tech.* **2008**, *5*, 119–124.

[108] Szewzyk, U.; Szewzyk, R.; Manz, W.; Schleifer, K. H. Microbiological Safety of Drinking Water. *Annu. Rev. Microbiol.* **2000**, *54*, 81–127.

[109] World Health Organisation. http://www.who.int/water_sanitation_health/gdwqrevision/rainwater.pdf (accessed May 23, 2013)

[110] Pandey, D. N.; Gupta, A. K.; Anderson, D. M. Rainwater Harvesting as an Adaptation to Climate Change. *Curr. Sci.* **2003**, *85*, 46–59.

[111] Schemenauer, R. S.; Cereceda, P. Fog-Water Collection in Arid Coastal Locations. *Ambio* **1991**, *20*, 303–308.

[112] Parker, A. R.; Lawrence, C. R. Water Capture by a Desert Beetle. *Nature* **2001**, *414*, 33–34.

[113] Al-Jayyousi, O. R.; Mohsen, M. S. Evaluation of Fog Collection in Jordan. *Water Environ. J.* **1999**, *13*, 195–199.

[114] Prada, S.; da Silva, M. Fog Precipitation on the Island of Madeira (Portugal). *Environ. Geol*, **2001**, *41*, 384–389.

[115] Schemenauer, R. S.; Cereceda, P. Fog Collection's Role in Water Planning for Developing Countries. *Nat. Resour. Forum* **1994**, *18*, 91–100.

[116] Blumenthal, U. J.; Mara, D. D.; Peasey, A.; Ruiz-Palacios, G.; Stott, R. Guidelines for the Microbiological Quality of Treated Wastewater Used in Ariculture: Recommendations for Revising WHO Guidelines. *Bull. World Health Organ.* **2000**, 78, 1104–1116.

[117] DOW Water and Process Solutions. http://msdssearch.dow.com/PublishedLiteratureDOWCOM/dh_0042/0901b80380042dd2.pdf?filepath=liquidseps/pdfs/noreg/609-02002.pdf&fromPage=GetDoc (accessed May 23, 2013)

[118] Mo, L.; Huanga, X. Fouling Characteristics and Cleaning Strategies in a Coagulation-Microfiltration Combination Process for Water Purification. *Desalination* **2003**, *159*, 1–9.

[119] Zularisam, A. W.; Ismail, A. F.; Salim, R. Behaviours of Natural Organic Matter in Membrane Filtration for Surface Water Treatment - A Review. *Desalination* **2006**, *194*, 211–231.

[120] Howe, K. J.; Clark, M. M. Fouling of Microfiltration and Ultrafiltration Membranes by Natural Waters. *Environ. Sci. Technol.* **2002**, *36*, 3571–3576.

[121] Vrijenhoek, E. M.; Hong, S.; Elimelech, M. Influence of Membrane Surface Properties on Initial Rate of Colloidal Fouling of Reverse Osmosis and Nanofiltration Membranes. *J. Membrane Sci.* **2001**, *188*, 115–128.

[122] Gates, F. L. On Nuclear Derivatives and the Lethal Action of Ultra-Violet Light. *Science* **1928**, *68*, 479–480.

[123] SODIS. http://www.sodis.ch/projekte/index_EN (accessed May 29, 2013)

[124] McGuigan, K. G.; Joyce, T. M.; Conroy, R. M.; Gillespie, J. B.; Elmore-Meegan, M. Solar Disinfection of Drinking Water Contained in Transparent Plastic Bottles: Characterizing the Bacterial Inactivation Process. *J. Appl. Microbiol.* **1998**, 84, 1138–1148.

[125] Berney, M.; Weilenmann, H. U.; Egli, T. Flow-Cytometric Study of Vital Cellular Functions in Escherichia Coli During Solar Disinfection (SODIS). *Microbiology* **2006**, *152*, 1719–1729.

[126] Eisenstark, A. Mutagenic and Lethal Effects of Near-Ultraviolet Radiation (290-400 nm) on Bacteria and Phage. *Environ Mol. Mutagen.* **1987**, *10*, 317–337.

[127] Reed, R. H. Solar Inactivation of Faecal Bacteria in Water: The Critical Role of Oxygen. *Lett. Appl. Microbiol.* **1997**, *24*, 276–280.

[128] Moss, S. H.; Smith, K. C. Membrane Damage can be a Significant Factor in the Inactivation of Escherichia Coli by Near-Ultraviolet Radiation. *Photochem. Photobiol.* **1981**, *33*, 203–210.

[129] Wegelin, M.; Canonica, S.; Mechsner, K.; Fleischmann, T.; Pesaro, F.; Metzler, A. Solar water Disinfection: Scope of the Process and Analysis of Radiation Experiments. *J. Water SRT – Aqua* **1994**, *43*, 154–169.

[130] Heaselgrave, W.; Patel, N.; Kehoe, S. C.; Kilvington, S.; McGuigan, K. G. Solar Disinfection of Poliovirus and Acanthamoeba Polyphaga Cysts in Water - A Laboratory Study Using Simulated Sunlight. *Lett. Appl. Microbiol.* **2006**, *43*, 125–130.

[131] Dejung, S.; Fuentes, I.; Almanza, G.; Jarro, R.; Navarro, L.; Arias, G.; Urquieta, E.; Torrico, A.; Fenandez, W.; Iriarte, M.; Birrer, C.; Stahel, W. A.; Wegelin, M. *J. Water SRT – Aqua* **2007**, *56*, 245–256.

[132] Lonnen, J.; Kilvington, S.; Kehoe, S. C.; Al-Touati, F.; McGuigan, K. Solar and Photocatalytic Disinfection of Protozoan, Fungal and Bacterial Microbes in Drinking Water. *Water Res.* **2005**, *39*, 877–883.

[133] Méndez-Hermida, F.; Ares-Mazás, E.; McGuigan, K. G.; Boyle, M.; Sichel, C.; Fernández-Ibáñez, P. Disinfection of Drinking Water Contaminated with Cryptosporidium Parvum Oocysts Under Natural Sunlight and Using the Photocatalyst TiO_2. *J. Photochem. Photobiol.* **2007**, *88*, 105–111.

[134] Ubomba-Jaswa, E.; Navntoft, C.; Polo-López, M. I.; Fernández-Ibáñez, P. *J.*; McGuigan, K. G. Solar Disinfection of Drinking Water (SODIS): An Investigation of the Effect of UV-A Dose on Inactivation Efficiency. *Photochem. Photobiol. Sci.* **2009**, *8*, 587–595.

[135] Gill, L.; Price, C. Preliminary Observations of a Continuous Flow Solar Disinfection System for a Rural Community in Kenya. *Energy* **2010**, *35*, 4607–4611.

[136] Eranna, G.; Joshi, B. C.; Runthala, D. P.; Gupta, R. P. Oxide Materials for Development of Integrated Gas Sensors—A Comprehensive Review. *Crit. Rev. Solid State* **2004**, *29*, 111–188.

[137] Mitra, P.; Chatterjee, A. P.; Maiti, H. S. Chemical Deposition of ZnO Films for Gas Sensors. *J. Mater. Sci.-Mater. El.* **1998**, *9*, 441–445.

[138] Beck, A.; Bednorz, J. G.; Gerber, C.; Rossel, C.; Widmer, D. Reproducible Switching Effect in Thin Oxide Films for Memory Applications. *App. Phys. Lett.* **2000**, *77*, 139–141.

[139] Somani, P. R.; Radhakrishnan, S. Electrochromic Materials and Devices: Present and Future. *Mater. Chem. Phys.* **2003**, *77*, 117–133.

[140] Wood, T. J.; Hurst, G. A.; Schofield, W. C. E.; Thompson, R. L.; Oswald, G.; Evans, J. S. O.; Sharples, G. J.; Pearson, G.; Petty, M. C.; Badyal, J. P. S. Electroless Deposition of Multi-Functional Zinc Oxide Surfaces Displaying Photoconductive, Superhydrophobic, Photowetting, and Antibacterial Properties. *J. Mater. Chem.* **2012**, *22*, 3859–3867.

[141] Bolink, H. J.; Brine, H.; Coronado, E.; Sessolo, M. Hybrid Organic-Inorganic Light Emitting Diodes: Effect of the Metal Oxide. *J. Mater. Chem.* **2010**, *20*, 4047–4049.

[142] Granqvist, C. G. Transparent Conductors as Solar Energy Materials: A Panoramic Review. *Sol. Enrerg. Mat. Sol. Cells* **2007**, *91*, 1529–1598.

[143] Cox P. A. *The Electronic Structure and Chemistry of Solids*. Oxford University Press, New York, **1987**

[144] Inui, T.; Uemura, Y. Theory of Color Centers in Ionic Crystals I: Electronic States of F-Centers in Alkali Halides. *Prog. Theor. Phys.* **1950**, *5*, 252–265.

[145] Ji, P.; Takeuchi, M.; Cuong, T. M.; Zhang, J. L.; Matsuoka, M.; Anpo, M. Recent Advances in Visible Light-Responsive Titanium Oxide-Based Photocatalysts. *Res. Chem. Intermediat.* **2010**, *36*, 327–347.

[146] Morrison, S. R. Surface Barrier Effects in Adsorption, Illustrated by Zinc Oxide. *Adv. Catal.* **1955**, *7*, 259–301.

[147] Tench, A. J.; Lawson, T. Oxygen Species Adsorbed on Zinc Oxide. *Chem. Phys. Lett.* **1971**, *8*, 177–178.

[148] Hirschwald, W. H. Zinc Oxide: An Outstanding Example of a Binary Compound Semiconductor. *Acc. Chem. Res.* **1985**, *18*, 228–234.

[149] Thompson, T. L.; Yates, J. T. Jr. Surface Science Studies of the Photoactivation of TiO_2 - New Photochemical Processes. *Chem. Rev.* **2006**, *106*, 4428–4453.

[150] Melnick, D. A. Zinc Oxide Photoconduction, an Oxygen Adsorption Process. *J. Chem. Phys.* **1957**, 26, 1136–1146.

[151] Barry, T. I.; Stone, F. S. The Reactions of Oxygen at Dark and Irradiated Zinc Oxide Surfaces. *Proc. R. Soc. London, Ser. A* **1960**, *255*, 124–144.

[152] Matthews, R. W.; Abdullah, M.; Low, G. K.-C. Photocatalytic Oxidation for Total Organic Carbon Analysis. *Anal. Chim. Acta.* **1990**, *223*, 171–179.

[153] Matthews, R. W. Purification of Water with Near—U.V. Illuminated Suspensions of Titanium Dioxide. *Water Res.* **1990**, *24*, 653–660.

[154] Low, G. K.-C.; McEvoy, S. R.; Matthews, R. W. Formation of Ammonium and Nitrate Ions from Photocatalytic Oxidation of Ring Nitrogenous Compounds over Titanium Dioxide. *Chemosphere* **1989**, *19*, 1611–1621.

[155] Low, G. K.-C.; McEvoy, S. R.; Matthews, R. W. Formation of Nitrate and Ammonium Ions in Titanium Dioxide Mediated Photocatalytic Degradation of Organic Compounds Containing Nitrogen Atoms. *Environ. Sci. Technol.* **1991**, *25*, 460–467.

[156] Pelizzetti, E.; Minero, C.; Pramauro, E.; Barbeni, M.; Maurino, V.; Tosato, M. Photocatalytic Degradation of Atrazine at PPB Levels Under Solar Light and in the Presence of TiO_2 Particles. *Chim. Ind.* **1987**, *69*, 88–89.

[157] Augugliaro, V.; Palmisano, L.; Schiavello, M.; Sclafani, A. Photocatalytic Degradation of Nitrophenols in Aqueous Titanium Dioxide Dispersion. *Appl. Catal.* **1991**, *69*, 323–340.

[158] Barbeni, M.; Pramauro, E.; Pelizzetti, E.; Borgarello, E.; Serpone, N. Photodegradation of Pentachlorophenol Catalyzed by Semiconductor Particles. *Chemosphere* **1985**,*14*, 195–208

[159] Matthews, R. W. Photo-Oxidation of Organic Material in Aqueous Suspensions of Titanium Dioxide. *Water Res.* **1986,** *20*, 569–578.

[160] Okatomo, K.; Yamamoto, Y.; Tanaka, H.; Tanaka, M.; Itaya, A. Heterogeneous Photocatalytic Decomposition of Phenol over TiO_2 Powder. *Bull. Chem. Soc. Jpn.* **1985**, *58*, 2015–2022.

[161] Matthews, R. W. Solar-Electric Water Purification Using Photocatalytic Oxidation with TiO_2 as a Stationary Phase. *Solar Energy* **1987,** *38*, 405–413.

[162] Augugliaro, V.; Palmisano, L.; Sclafani, A.; Minero, C.; Pelizzetti, E. Photocatalytic Degradation of Phenol in Aqueous Titanium Dioxide Dispersions. *Toxicol. Enuiron. Chem.* **1988**,*16* ,89–109.

[163] Jacoby, W. A.; Maness, P. C.; Wolfrum, E. J.; Blake, D. M.; Fennel, J. A. Mineralization of Bacterial Cell Mass on a Photocatalytic Surface in Air. *Environ. Sci. Technol.* **1998**, *32*, 2650–2653.

[164] Ireland, J. C.; Klostermann, P.; Rice, E. W.; Clark, R. M. Inactivation of Escherichia Coli by Titanium Dioxide Photocatalytic Oxidation. *Appl. Environ. Microbiol.* **1993**, *59*, 1668–1670.

[165] Saito, T.; Iwase, T.; Horie, J.; Morioka, T. Mode of Photocatalytic Bactericidal Action of Powdered Semiconductor TiO_2 on Mutans Streptococci. *J. Photochem. Photobiol. B.* **1992**, 14, 369–379.

[166] Matsunaga, T.; Tomoda, R.; Nakajima, T.; Wake, H. Photoelectrochemical Sterilization of Microbial Cells by Semiconductor Powders. *FEMS Microbiol. Lett.* **1985**, *29*, 211–214.

[167] Matsunaga, T.; Tomoda, R.; Nakajima, Y.; Nakamura, N.; Komine, T. Continuous-Sterilization System That Uses Photosemiconductor Powders. *Appl. Environ. Microbiol.* **1988**, *54*, 1330–1333.

[168] Sunada, K.; Kikuchi, Y.; Hashimoto, K.; Fujishima, A. Bactericidal and Detoxification Effects of TiO(2) Thin Film Photocatalysts. *Environ. Sci. Technol.* **1998**, *32*, 726–728.

[169] Maness, P.-C.; Smolinski, S.; Blake, D.; Huang, Z.; Wolfrum, E. J.; Jacoby, W. A. Bactericidal Activity of Photocatalytic TiO_2 Reaction: Toward an Understanding of its Killing Mechanism. *Appl. Environ. Microbiol.* **1999**, *65*, 4094–4098.

[170] Kikuchi, Y.; Sunada, K.; Iyoda, T.; Hashimoto, K.; Fujishima, A. Photocatalytic Bactericidal Effect of TiO_2 Thin Films: Dynamic View of the Active Oxygen Species Responsible for the Effect. *J. Photochem. Photobiol. A.* **1997**, *106*, 51–56.

[171] Cho, M.; Chung, H.; Choi, W.; Yoon, J. Linear Correlation Between Inactivation of E-coli and OH Radical Concentration in TiO_2 Photocatalytic Disinfection. *Water Res.* **2004**, *38*, 1069–1077.

Chapter 2 Experimental Methods

Throughout this thesis, a wide range of analytical techniques are utilised for the characterisation of the prepared functional catalytic materials and the products of catalytic reactions. This chapter briefly summarises the experimental methods, along with pulsed plasma deposition, which is the major surface preparation technique used throughout.

2.1 Pulsed Plasma Deposition

Commonly referred to as the fourth state of matter,[1] plasma is used to describe a gas comprising ionised particles such as charged ions, electrons, and metastables, as well as a neutral fraction of non-ionised gas. Plasma discharge is induced by the application of an electric field, which accelerates electrons resulting in collisions causing ionisation. Subsequently, the electrons produced in the ionisation process undergo further collisions resulting in a cascade and formation of a plasma. Use of a non-polymerising gas such as CF_4, O_2 or H_2 can modify the chemical properties of a surface by etching, oxidizing or reducing surface functionality. The surface nature of this technique allows for retention of the bulk properties of the material.

Alternatively, polymerisable gaseous precursors can be used to produce a polymer film. Continuous wave deposition typically yields films that have a high degree of fragmentation and poor functional group retention.[2] This can be avoided by using pulsed plasma deposition, which comprises modulating an electrical discharge in the presence of gaseous precursors containing polymerisable carbon-carbon double bonds.[2,3] Mechanistically, there are two distinct reaction regimes corresponding to the plasma duty cycle on and off periods (typical timescales are of the order of microseconds and milliseconds respectively).[4] Namely, monomer activation and reactive site generation at the substrate surface occur during each short burst of plasma (via VUV irradiation, ion, or electron bombardment) followed by conventional carbon-carbon double bond polymerization proceeding in the subsequent extended off-time (in the absence of any VUV-, ion-, or electron-induced damage to the growing film). High levels of precursor structural retention within the deposited nanolayer can be achieved, thereby yielding specific functionalities at the surface (as confirmed by ToF-SIMS[5] and NMR spectroscopy[6]). Furthermore, by programming the pulsed plasma duty cycle, it is possible to control the surface density of desired chemical groups. The covalent attachment of the

functional films to the underlying substrate occurs via free radical sites created at the interface during the onset of plasma exposure. Other distinct advantages include the fact that the plasmachemical approach is quick (single-step), solventless, energy-efficient, and the reactive gaseous nature of the electrical discharge provides conformality to a whole host of substrate materials and complex geometries (e.g. powders, fibres, tubes, cloths, etc.).[7,8] Surface functionalities devised in the past include: anhydride,[4] carboxylic acid,[9] amine,[10] cyano,[11] epoxide,[5] hydroxyl,[12] halide,[13] thiol,[14] furfuryl,[15] perfluoroalkyl,[16] perfluoromethylene,[17] and trifluoromethyl[18] groups.

2.2 Infrared Spectroscopy

The vibrational modes of a molecule can be probed by light of the correct wavelength for excitation of vibrational energy levels. Transitions that result in a change in dipole moment can be studied using infrared light, producing absorbances at specific wavelengths that result in a 'fingerprint' of the molecule. The wavelength of light that is absorbed is dependent on the amount of energy required to produce a vibration of the covalent bond, which is related to the spring constant and the reduced mass of the bond.[19] Smaller masses and stronger bonds result in higher frequency absorbance bands.

Dispersive infrared spectroscopy acquires spectra of the absorbance bands by scanning across a range of wavelengths and comparing the input intensity with the output,[20] resulting in long scan times. Fourier transform infrared spectroscopy (FTIR) allows for much faster spectral acquisition by concurrently scanning the whole wavelength range. In doing so it allows for spectral averaging of larger numbers of spectra, resulting in better signal to noise ratios and increased sensitivities in a shorter period of time. In addition, the resolution is improved over dispersive infrared spectroscopy as it is not limited by the step size of gratings for beam splitting.

Deconvolution of the signal intensity at different wavelengths is achieved using an interferometer. The broad-spectrum infrared light source is passed through a beam splitter which directs one beam over a fixed mirror and the second across a movable mirror. The two beams are recombined before being passed through the sample, which produces interference patterns due to the differing path lengths induced by the movable mirror. The signal intensity is plotted as a function of optical path difference; a Fourier transform is applied to the data resulting in an absorption spectrum as a function of wavelength.[20]

Whilst FTIR is commonly performed in transmission mode with either a transparent sample cell or potassium bromide disc,[20] there are more practical methods for performing surface sensitive infrared spectroscopy on thin films. Reflection-absorption infrared spectroscopy (RAIRS) involves the deposition of a thin film onto an infrared reflective surface, such as silicon wafer or gold coated substrate. The infrared beam is directed onto the sample coated substrate at a grazing angle, where the beam is reflected to a collection mirror at the specular reflection angle. Part of the beam will reflect off the thin film, however the remaining portion will pass through the sample and be reflected off the substrate, resulting in two passes through the sample, giving increased path lengths over a simple transmission method. By subtracting the spectrum of the bare substrate, the sample spectrum is obtained.

Alternatively, thicker films and a range of other solid and liquid samples can be analysed using attenuated total reflectance infrared spectroscopy (ATR IR). The sample is compressed against the surface of an infrared transparent crystal such as diamond, through which the infrared beam is passed at a set angle. The beam undergoes total internal reflection at the surface of the crystal due to the large difference in refractive indices of the crystal and sample. At the points of reflection, an evanescent wave is formed which propagates into the sample (typically 2.5–25 μm for mid infrared),[20] producing an infrared spectrum of the sample after background subtraction from the crystal spectrum.

2.3 Raman Microscopy

Similar to infrared spectroscopy, Raman spectroscopy techniques can be used to study the vibrational modes of a molecular species. Whilst in infrared spectroscopy the absorption of light is measured as a function of incident wavelength, in Raman spectroscopy the sample is irradiated with light of a single frequency and the wavelength and intensity of the scattered light is measured.[19] The scattered light comprises two types of signal, Rayleigh scattering and Raman scattering. Rayleigh scattering is light of the same frequency as the incident beam and is very intense, Raman scattering contains Stokes and anti-Stokes lines which are comparatively weak in intensity.

When the incident beam strikes the sample, the light (which is of lower energy than the energy gap to the first electronic excitated state) excites the molecules into a ‘virtual’ vibrational level, which is higher in energy than the vibrational levels in the ground electronic state, Figure 2.1. From this ‘virtual’ level, the molecule relaxes to vibrational

levels in the ground electronic state, releasing photons. The molecule can relax to the original vibrational level (Rayleigh scattering), a higher vibrational level (Stokes), or a lower vibrational level (anti-Stokes). Anti-stokes lines are by far the weakest of the Raman signals, as they require the excitation from a vibrational level above the ground state, of which the population is considerably lower (as per a Maxwell-Boltzmann distribution).

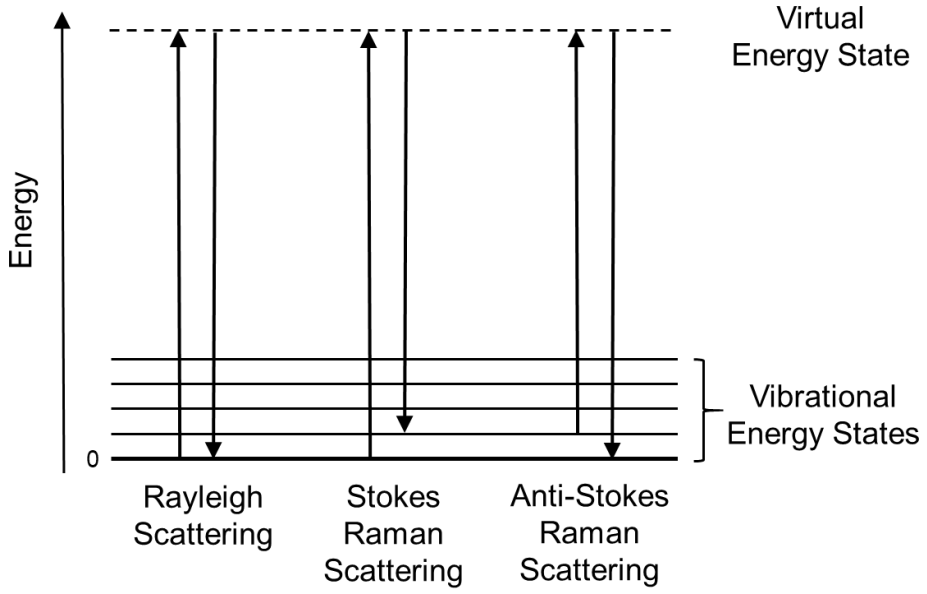

Figure 2.1: Schematic representation of Raman scattering.

Raman spectroscopy can be carried out in a variety of ways for the study of gases, liquids and solids. It can be combined with an optical microscope to allow for Raman mapping of a sample and spatial sampling in the plane parallel to the surface, known as Raman microscopy. This is achieved by focusing an optical microscope onto the surface of a sample and passing a laser through the lens instead of a broad-spectrum light source. The laser light is partially reflected by the sample, and the returning signal contains the Rayleigh and Raman scattering. Rayleigh scattering is removed by a notch or edge filter, leaving only the Raman scattering to pass to the detector. Raman microscopy can also be confocal, allowing for spatial resolution in the plane perpendicular to the sample surface, using a confocal slit or filter in the beam path. This allows a confocal Raman microscope to study surface treatment and films at micron thicknesses.[21]

2.4 UV-Vis Spectroscopy

When light of the correct wavelength for electronic transitions of the target molecule is passed through the sample, a proportion of the light is absorbed resulting in excitation of electrons to higher energy levels. The proportion of absorbed light is the absorbance and is defined as the negative log of the final intensity (I) over the initial intensity (I_0), Equation 2.1. The flux absorbed is proportional to the path length (L), concentration of the target molecule (c) and the molar absorption coefficient (ε), as shown in Equation 2.2, the Beer-Lambert law. The latter is an experimentally derived constant which is a measure of a molecules ability to absorb light at a given wavelength.

$$A = -\log_{10}\left(\frac{I}{I_0}\right) \qquad \text{Eq. 2.1}$$

$$A = \varepsilon c L \qquad \text{Eq. 2.2}$$

2.4.1 Absorbance Measurements

Photocatalytic destruction of pollutants can be tracked using a dye molecule that contains aromaticity typically found in the structures of many organic pollutants such as pesticides and textile dyes. Methylene blue is ideally suited for such photocatalytic measurements, having absorbance peaks at 610 nm and 660 nm,[22] allowing simple determination of concentration via the Beer-Lambert law.

2.4.2 Diffuse Reflectance

UV-Vis spectroscopy can also be used to characterise the absorbance of opaque diffuse materials such as powders and rough films using diffuse reflectance spectroscopy. An integrating sphere made of diffusely reflecting material is used to collect the scattered light from the sample, Figure 2.2. Multiple internal reflections within the integrating sphere produce homogeneous illumination of the integrating sphere wall, which is sampled using a spectrophotometer. Larger integrating spheres allow for smaller ratios between the sample ports and the undisrupted sphere wall reducing uncertainties associated with imperfect junctions. Two sphere designs are typically employed, the first exchanges part of the sphere wall with the sample after background collection which allows for smaller, low cost spheres to be used. However, the introduction of the sample after background collection results in a substitution error; this error arises from the absorption of light by the

sample during multiple reflections around the sphere, which in the first design differs between the background and sample spectrum. Therefore, this technique tends to produce erroneous results with strongly absorbing samples.

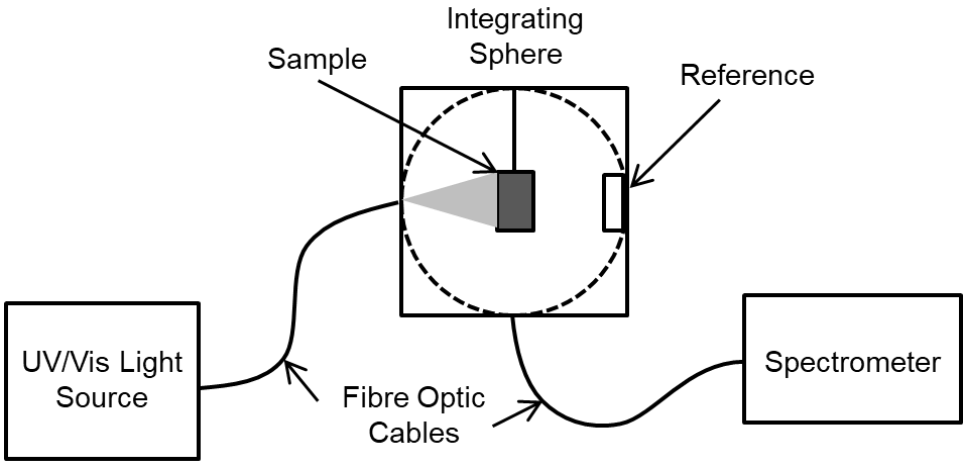

Figure 2.2: Schematic diagram of the integrating sphere setup used in this work.

The second design holds the sample in the center of the sphere on a movable mount. The sample is moved to a position away from the incident light beam during background collection, followed by interruption of the beam during sample collection. This removes the substitution error associated with sample port based designs at the cost of larger, more expensive integrating spheres. The integrating sphere system used herein is comprised of a low-density optical PTFE (Berghof Products and Instruments GmbH) sphere with an internal diameter of 100 mm connected to an optical fiber coupled halogen deuterium dual light source and spectrophotometer, Figure 2.2. The sample holder and ports were manufactured from the same low-density PTFE as the sphere walls.

2.5 X-Ray Photoelectron Spectroscopy

X-Ray photoelectron spectroscopy (XPS) is a surface sensitive technique that allows for characterisation of the atomic composition of a sample. Sample depths vary with a range of conditions including the element of interest and sample composition but are typically in the order of nanometers.[23,24,25] Through appropriate calibration, XPS can yield quantitative atomic composition making it a powerful tool for the characterisation of thin films and surface-modified materials.

XPS involves irradiation of the samples with soft X-rays of sufficient energy to cause emission of electrons from core levels, Figure 2.3. These emitted photoelectrons have kinetic energies that are a function of the input photon energy and the binding energy of the electron:

$$E_K = hv - E_B - \phi_s \qquad \text{Eq. 2.3}$$

where E_K is the kinetic energy of the emitted photoelectron, hv is the energy of the X-rays, E_B is the binding energy of the emitted electron and ϕ_s is the spectrometer work function. The kinetic energy of emitted photoelectrons is typically 5–2000 eV, which corresponds to an inelastic mean free path of a few nanometres, resulting in surface sensitivity.

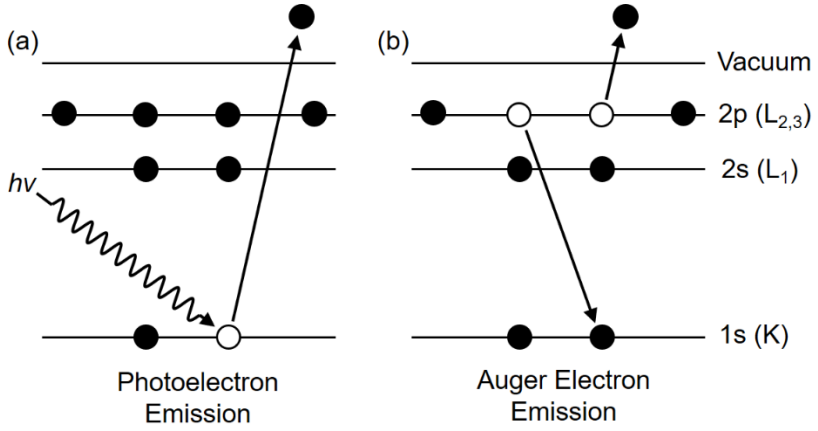

Figure 2.3: Schematic diagram of the XPS emission processes for a model atom: (a) incident photon causes the emission of a photoelectron from a core level; and (b) relaxation process resulting in emission of a $KL_{2,3}L_{2,3}$ Auger electron.

The binding energy of emitted photoelectrons is characteristic to both the element and the binding environment. Therefore, photoelectron peaks in XPS spectra consist of binding envelopes which may contain multiple peaks characteristic of the different binding environments within the sample. Peak intensities are related to the cross section of the ionisation process; once corrected using appropriate sensitivity factors the peak areas can be used for quantification of the surface composition.

There are often additional lines associated with photoelectron binding envelopes, including Auger lines, secondary electron peaks when using non-monochromated X-ray sources and shake-up lines from aromaticity. The former arise from the relaxation of electrons from higher energy levels into the hole formed by the initial ionization, Figure 2.3.

2.6 Powder X-Ray Diffraction

The regularly repeating structure of crystalline solids allows diffraction of radiation when it correlates with interatomic distances, i.e. wavelengths in the order of 1 Å. Therefore, X-ray diffraction (XRD) is a powerful tool in determining the crystal structure of solids. A diffracted photon of light is intensified if other photons exiting the material are in phase. This occurs if the distance travelled by the second photon is a multiple of the wavelength of the first photon. The geometric restriction of this results in Braggs' law, which is defined as:

$$n\lambda = 2d_{hkl}\sin\theta \qquad \text{Eq. 2.4}$$

where n is a positive integer, λ is the wavelength of incident light and θ is the scattering angle.

In this report the source of X-rays was a Cu X-ray tube, which produced Cu $k\alpha$ radiation at a wavelength of 1.5418 Å. Generation of X-ray wavelength photons proceeds via bombardment of the copper anode with high energy electrons, causing removal of core level, 1s electrons from copper. Radiative relaxation from the 2p to 1s levels produces $k\alpha$ radiation, which is one of a number of fixed wavelengths among a background of white radiation arising due to lost energy through collisions. The incident beam was monochromated with a Ge(111) monochromator, and the detector was a linear position-sensitive detector. As the detector is scanned through a range of angles relative to the incidence beam (quoted as 2θ values), the intensity of the diffracted light is measured as a function of 2θ, producing a diffraction trace. The lattice constants (a, b and c) can be related to the Miller indices (h, k and l) for an orthorhombic lattice by:

$$\frac{1}{d_{hkl}} = \frac{h^2}{a^2} + \frac{k^2}{b^2} + \frac{l^2}{c^2} \qquad \text{Eq. 2.5}$$

Therefore h, k, and l can be determined for each peak in the diffraction trace from the value of d_{hkl}.

2.7 BET Surface Area

The catalytic activity of a solid material is often dependent on the number of active sites available for a given reaction. For heterogeneous catalysts, high specific surface areas are typically associated with high turn-over frequencies due to the increased number of

active sites. Therefore, determination of the specific surface area of a material is vital in understanding the factors governing the activity of a heterogeneous catalyst. Determination of this can be achieved using the BET theory,[26] which models the physisorption of an inert gas on a solid surface according to an extension of the Langmuir theory of monolayer adsorption. The BET model assumes that gas molecules are physisorbed on a solid surface in layers infinitely, the Langmuir theory is applicable to each layer and that molecules in each physisorbed layer interact only with adjacent layers. The resulting BET equation can be expressed as:

$$\frac{P}{V(P_0-P)} = \frac{1}{CV_m} + \left(\frac{C-1}{CV_m}\right)\left(\frac{P}{P_0}\right) \qquad \text{Eq. 2.6}$$

where V is the adsorption capacity at equilibrium pressure P, V_m is the monolayer capacity, P_0 is the saturation pressure and C is the BET constant (which comprises terms for the heat of adsorption of the first monolayer and of subsequent multilayers).

The interactions between an inert gas and a solid surface are weak, so to achieve multilayer adsorption the sample must be cooled to below the boiling point of the probe inert gas (usually nitrogen at 77 K). This allows for the introduced gas to adsorb to the surface. By measuring the pressure of the sample chamber when differing known volumes of gas are added, a series of equilibrium and saturation pressures can be calculated. A plot of $P/1(P_0-P)$ against P/P_0 between $0.05< P/P_0 <0.35$ will yield a straight line with a gradient S and intercept I:

$$S = \frac{C-1}{CV_m} \qquad \text{Eq. 2.7}$$

$$I = \frac{1}{CV_m} \qquad \text{Eq. 2.8}$$

$$V_m = \frac{1}{S+I} \qquad \text{Eq. 2.9}$$

which allows us to calculate V_m. From this, the BET total surface area S_T (units of area^2) and specific surface area S_{BET} (typically units of area^2 mass^{-1}) can be calculated:

$$S_T = \frac{V_m N s}{M_V} \qquad \text{Eq. 2.10}$$

$$S_{BET} = \frac{S_T}{a} \qquad \text{Eq. 2.11}$$

where N is Avagadro's number, s is the adsorption cross-section, M_V is the molar volume and a is the mass of the sample. The mass can be substituted in some cases for other units that allow for meaningful comparison, such as flat area or length.

Although care must be taken in interpreting results of specific surface areas of different sample types, between similar materials the BET method allows for comparison between heterogeneous catalysts that would otherwise not be possible.

2.8 Scanning Electron Microscopy

Scanning electron microscopy (SEM) provides topographical analysis of the sample at higher resolutions than optical microscopy. A beam of high energy electrons (typically 10–40 keV) is focused onto the surface of the sample, ionising the atoms on the surface, which emit lower energy secondary electrons. The secondary electrons are accelerated through a positively biased grid adjacent to the surface and passed to a photomultiplier. Micrographs are generated from the distribution of the secondary electrons as the electron beam is scanned across the surface. The ionisation process results in a charged surface unless a conductive layer such as gold is added prior to analysis, typically applied via sputtering.

2.9 Film Thickness Measurements

For thin films deposited onto flat substrates, spectrophotometry provides a means for determination of optical constants such as refractive index and adsorption coefficients as well as film thickness.

A deposited film will have a different refractive index to the underlying substrate, meaning a single film will have two interfaces: one with the ambient gas (typically air) and one with the underlying substrate. When light passes through these two interfaces, a portion is specularly reflected, a portion is transmitted and a portion is absorbed. Whether the light from two interfaces interacts constructively or destructively in the emergent beam depends on the path length difference, which is a function of the incident angle, film thickness and refractive indices. The total intensity of the emergent beam is also a function of the absorption coefficient of the material, which will vary as a function of wavelength. The interference pattern measured by recording the intensity of the reflected light across a range of incident beam wavelengths (typically 350–1000 nm) can by fitted using a

Cauchy material model using a modified Levenberg Marquardt algorithm to yield the optical constants and film thickness.[27]

2.10 Quartz Crystal Microbalance

Real-time detection of the adsorption of sub-microgram levels of material onto solid surfaces provides a challenge for those wishing to study absorption properties of thin films. One route to achieving this is by using a quartz crystal microbalance (QCM), which is capable of detecting mass changes to nanogram accuracy. Quartz crystals display the piezoelectric effect, where an applied voltage can induce a mechanical deformation and applying mechanical stress can induce a voltage. By applying an alternating voltage, a standing shear wave can be induced within the crystal, with a stable well-defined resonance frequency. In QCM systems, the quartz crystal is attached to gold electrodes and exposed to the analyte or adsorbate molecules, Figure 2.4. When the mass of the crystal changes due to adsorption or deposition, the resonant frequency changes, which is related to the mass change by the Sauerbrey equation.[28]

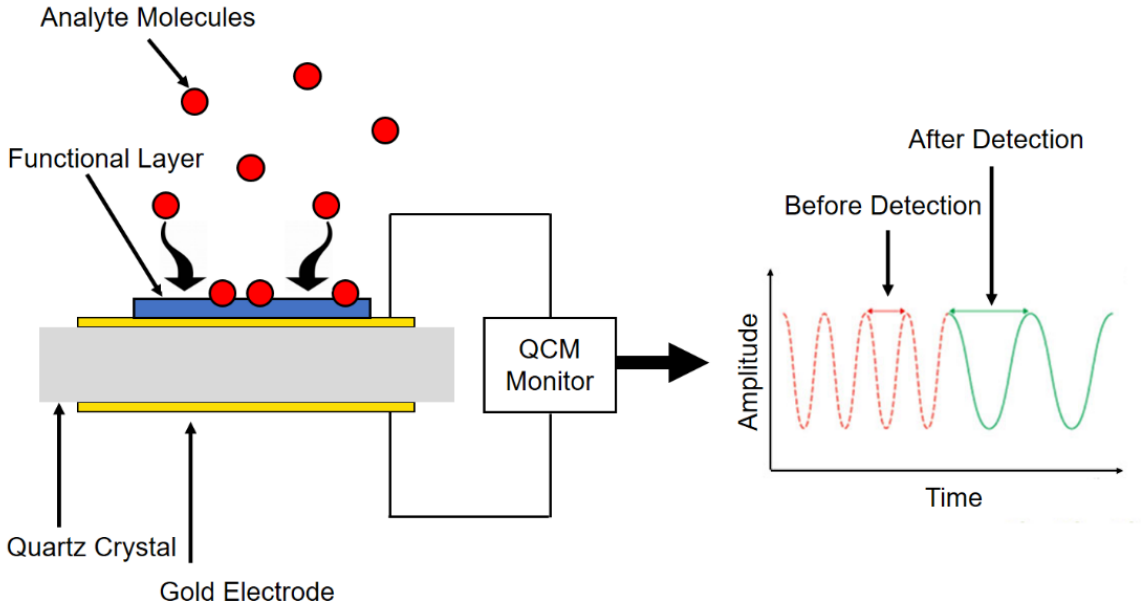

Figure 2.4: Schematic representation of the detection mode of a QCM system.

For the detection of gas phase analytes, a custom vacuum system was built to house the QCM, Figure 2.5. This comprised a dry nitrogen / oxygen air mix (with ratio flow control), moisture monitor, analyte line with leak valve, low and medium vacuum gauges,

glass QCM chamber and vacuum line to a rotary vane pump with a liquid nitrogen cold trap. For a standard test, the system was evacuated to base pressure before the analyte was added to the desired partial pressure. The glass chamber was topped up to atmospheric pressure with the dry nitrogen / oxygen mix.

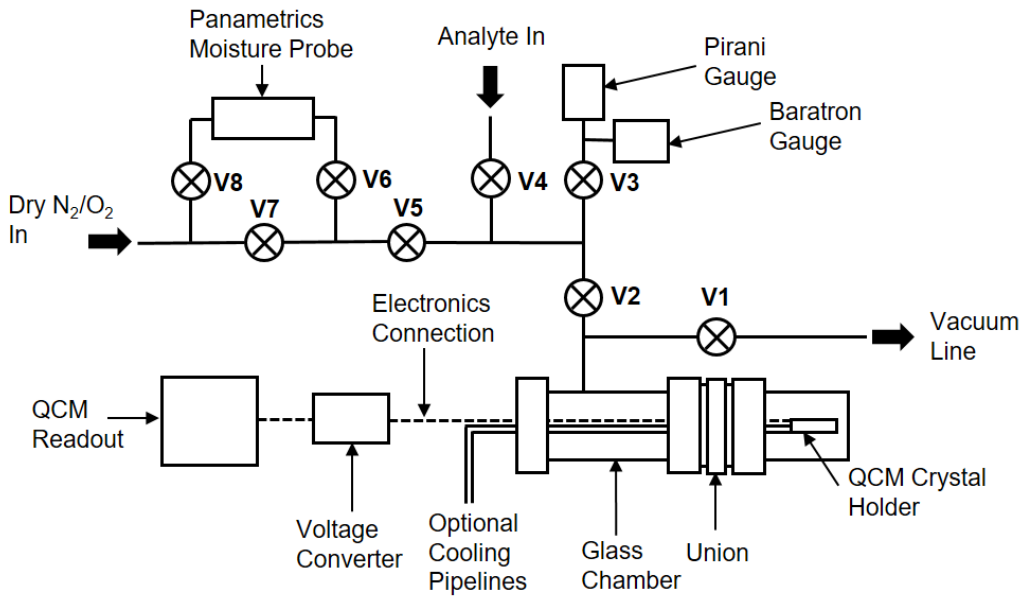

Figure 2.5: Diagram of the QCM system used for detection of gas phase analytes.

2.11 Gas Chromatography

Gas chromatography (GC) provides a quick method for separating complex mixtures of components with similar solubilities and functional groups, providing they can be vapourised without decomposition. In GC, a mobile phase of an inert gas such as helium is used as a carrier of the vapourised analyte. This is passed through a stationary phase with which the analyte interacts, resulting in different elution times for the components of the mixture. The stationary phase may be either a packed column, where the stationary phase is coated onto a particulate inert support, or a capillary column, the walls of which have been coated with the stationary phase.

Temperature of the system affects the elution times and thus the resolution of the final chromatograph. Higher temperatures will result in fast vapourisation of the analyte, however this may result in overlapping signals. Lower temperatures and highly precise, slow temperature ramps tend to give better resolution at the expense of experimental time.

Combining GC with a mass spectrometer (GC-MS) allows for identification of the different components in the analyte mixture, which is not otherwise possible with mass spectrometry alone. The components of the analyte are introduced to the mass spectrometer as they are eluted from the column, where they are ionized and passed through the quadrupole of the mass spectrometer to separate fragments by molecular weight. The final chromatograph therefore contains not only elution times (which can be compared to standard data for the column type and conditions), but also information about the fragmentation of the molecule allowing for identification of the analyte components.

2.12 References

[1] Langmuir, I. The Interaction of Electron and Positive Ion Space Charges in Cathode Sheaths. *Phys. Rev.* **1929**, *33*, 954–989.

[2] Yasuda, H.; Hsu, T. Some Aspects of Plasma Polymerization Investigated by Pulsed R.F. Discharge. *J. Polym. Sci. Chem.* **1977**, *15*, 81–97.

[3] Savage, C. R.; Timmons, R. B.; Lin, J. W. Molecular Control of Surface Film Compositions Via Pulsed Radio-Frequency Plasma Deposition of Perfluoropropylene Oxide. *Chem. Mater.* **1991**, *3*, 575–577.

[4] Ryan, M. E.; Hynes, A. M.; Badyal, J. P. S. Pulsed Plasma Polymerization of Maleic Anhydride. *Chem. Mater.* **1996**, *8*, 37–42.

[5] Tarducci, C.; Kinmond, E. J.; Brewer, S. A.; Willis, C.; Badyal, J. P. S. Epoxide-Functionalized Solid Surfaces. *Chem. Mater.* **2000**, *12*, 1884–1889.

[6] Kinmond, E. J.; Coulson, S. R.; Brewer, S. A.; Willis, C.; Badyal, J. P. S. High Structural Retention During Pulsed Plasma Polymerization of 1H,1H,2H-perfluorododecene: an NMR and TOF-SIMS Study. *Polymer* **2005**, *46*, 6829–6835.

[7] Yasuda, H. Plasma Polymerization; Academic Press: New York, 1985.

[8] Akhavan, B.; Jarvis, K.; Majewski, P. Plasma Polymer-Functionalized Silica Particles for Heavy Metals Removal. *ACS Appl. Mater. Interfaces* **2015**, *7*, 4265–4274.

[9] Hutton, S. J.; Crowther, J. M.; Badyal, J. P. S. Complexation of Fluorosurfactants to Functionalized Solid Surfaces: Smart Behaviour. *Chem. Mater.* **2000**, *12*, 2282–2286.

[10] Harris, L. G.; Schofield, W. C. E.; Doores, K. J.; Davis, B. G. ; Badyal, J. P. S. Rewritable Glycochips. *J. Am. Chem. Soc.* **2009**, *131*, 7755–7761.

[11] Tarducci, C.; Schofield, W. C. E.; Brewer, S. A.; Willis, C.; Badyal, J. P. S. Cyano-Functionalized Solid Surfaces. Chem. Mater. **2001**, *13*, 1800–1803.

[12] Tarducci, C.; Schofield, W. C. E.; Brewer, S. A.; Willis, C.; Badyal, J. P. S. Monomolecular Functionalization of Pulsed Plasma Deposited Poly(2-hydroxyethyl methacrylate) Surfaces. *Chem. Mater*. **2002**, *14*, 2541–2545.

[13] Teare, D. O. H.; Barwick, D. C.; Schofield, W. C. E.; Garrod, R. P.; Ward, L. J.; Badyal, J. P. S. Substrate-Independent Approach for Polymer Brush Growth by Surface Atom Transfer Radical Polymerization. *Langmuir* **2005**, *21*, 11425–11430.

[14] Schofield, W. C. E.; McGettrick, J.; Bradley, T. J.; Przyborski, S.; Badyal, J. P. S. Re-Writable DNA Microarrays. *J. Am. Chem. Soc.* **2006**, *128*, 2280–2285.

[15] Tarducci, C.; Brewer, S. A.; Willis, C.; Badyal, J. P. S. Diels-Alder Chemistry at Furan Functionalized Solid Surfaces. *Chem. Commun.* **2005**, 406–408.

[16] Coulson, S. R.; Woodward, I. S.; Brewer, S. A.; Willis, C.; Badyal, J. P. S. Ultra-Low Surface Energy Plasma Polymer Films. *Chem. Mater.* **2000**, *12*, 2031–2038.

[17] Limb, S. J.; Gleason, K. K.; Edell, D. J.; Gleason, E. F. Flexible Fluorocarbon Wire Coatings by Pulsed Plasma Enhanced Chemical Vapor Deposition*. J. Vac. Sci. Technol.*, *A* **1997**, *15*, 1814–1818.

[18] Wang, J.-H.; Chen, J.-J.; Timmons, R. B. Plasma Synthesis of a Novel CF3-Dominated Fluorocarbon Film. *Chem. Mater.* **1996**, *8*, 2212–2214.

[19] Lin-Vien, D.; Colthrup, N. B.; Fateley, W. G.; Grasselli, J. G. The Handbook of Infrared and Raman Characteristic Frequencies of Organic Molecules; Academic Press: Boston, 1991

[20] Stuart, B. H. Infrared Spectroscopy: Fundamentals and Applications; John Wiley & Sons Ltd.: Chichester, U.K., 2004

[21] Everall, N. Depth Profiling with Confocal Raman Microscopy, Part I. *Spectroscopy* [Online] **2004**, *19*, http://alfresco.ubm-us.net/alfresco_images/pharma/2014/08/22/5285a034-fa62-4025-b0d8-b160bfc3ab5f/article-128007.pdf (accessed Jan 15, 2018).

[22] Spencer, W.; Sutter, J. R. Kinetic Study of the Monomer-Dimer Equilibrium of Methylene Blue in Aqueous Solution. *J. Phys. Chem*. **1979**, *83*, 1573–1576.

[23] Moulder, J. F.; Stickle, W. F.; Sobol, P. E.; Bomben, K. D. Handbook of X-Ray Photoelectron Spectroscopy: A Reference Book of Standard Spectra for Identification and Interpretation of XPS data; Perkin-Elmer Corp.: Eden Prarie, MN, 1992

[24] Beamson, G.; Briggs, D. High-Resolution XPS of Organic Polymers, The Scienta ESCA 300 Database; John Wiley & Sons, Ltd: Chichester, 1992.

[25] Banwell, C. N.; McCash, E. M. Fundamentals of Molecular Spectroscopy, 4th ed, McGraw-Hill: London, 1994.

[26] Brunauer, S.; Emmett, P. H.; Teller, E. Adsorption of Gases in Multimolecular Layers. *J. Am. Chem. Soc.* **1938**, *60*, 309–319.

[27] Lovering, D. NKD-6000 Technical Manual; Aquila Instruments: Cambridge, U.K., 1998.

[28] Sauerbrey, G. Verwendung von Schwingquarzen zur Wägung dünner Schichten und zur Mikrowägung. *Zeitschrift für Physik* **1959**, *155*, 206–222.

Chapter 3 Palladium Catalyst Cloths for Carbon-Carbon Coupling Reactions

3.1 Introduction

Heterogeneous (supported) catalysts can potentially address many of the drawbacks associated with homogeneous palladium catalyst carbon-carbon coupling reactions as discussed in Chapter 1. Existing commercially available materials include Pd/C, Pd/Al_2O_3, and loose polymer fibre anchored palladium(II) centres,[1,2] however these all require post-reaction filtration steps. There also exist dip catalysts for carbon-carbon coupling reactions (which do not require post-reaction filtration). For instance, palladium and nickel composite silica films dip coated onto glass supports rely on the sacrificial role of nickel, which ultimately limits the useable catalyst lifetime.[3] In the case of palladium nanoparticles supported on thin cellulose acetate polymer membranes, catalyst activity only lasts about 3 h.[4] Longer life catalysts have been reported for palladium nanoparticles incorporated into spin coated poly(vinyl alcohol);[5] however, these free standing multilayer films of just 1 μm thickness are difficult to handle for industrial scale processing. In the case of palladium nanoparticles incorporated onto cellulose paper and wool only 5–6 recycles are feasible,[6,7] whilst incorporation of palladium(II) species within a polymer film as an alternative to palladium nanoparticles suffers from high levels of metal leaching contributing towards homogeneous (rather than heterogeneous) catalysis.[8,9,10,11]

Although imidazole-based ligands for palladium catalysis are extensively used in homogeneous Mizoroki-Heck[12,15] and Suzuki-Miyaura[13,14,15,16] coupling reactions, their application on solid surfaces to anchor palladium catalysts has not been previously reported. In this chapter, we describe the anchoring of palladium catalyst sites through surface imidazole groups formed by pulsed plasma deposition of poly(1-allylimidazole) onto a cheap non-woven polypropylene support, Scheme 3.1. Palladium catalyst cloths prepared using surface imidazole groups have been evaluated for Sonogashira, Mizoroki-Heck, and Suzuki-Miyaura carbon-carbon coupling reactions, as well as recycling studies, Scheme 3.2.

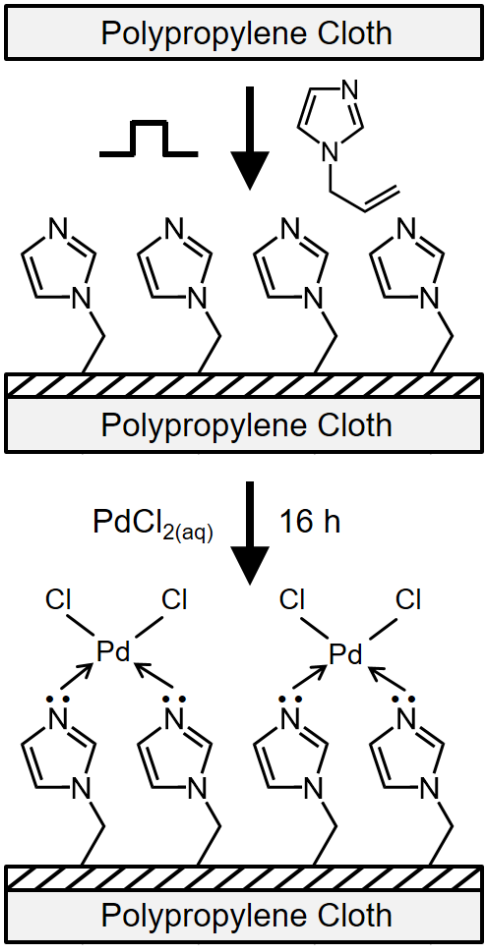

Scheme 3.1: Pulsed plasmachemical deposition of poly(1-allylimidazole) onto polypropylene cloth followed by surface tethering of palladium pro-catalyst species.

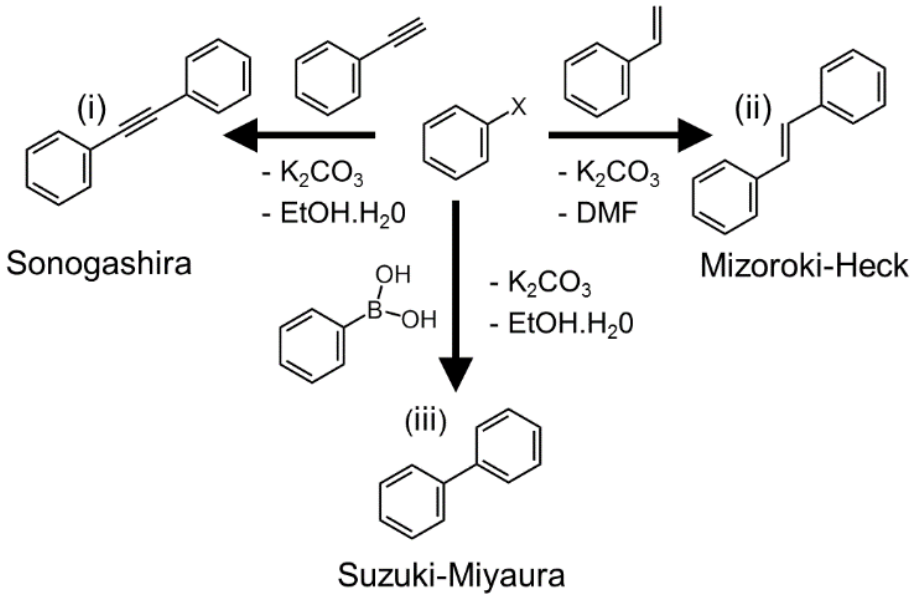

Scheme 3.2: Carbon-carbon coupling reactions of haloarene using palladium catalyst cloth: (i) Sonogashira coupling reaction with phenylacetylene; (ii) Mizoroki-Heck coupling reaction with styrene; and (iii) Suzuki-Miyaura coupling reaction with phenylboronic acid. Where X is a halogen atom.

3.2 Experimental Section

3.2.1 Pulsed Plasma Deposition of Poly(1-Allylimidazole)

A cylindrical glass reactor (5.5 cm diameter, 475 cm^3 volume) housed within a Faraday cage was used for plasmachemical deposition. This was connected to a 30 L min^{-1} rotary pump (E2M2, Edwards Vacuum Ltd.) via a liquid nitrogen cold trap (base pressure less than 2 x 10^{-3} mbar and air leak rate better than 6 x 10^{-9} mol s^{-1}).[17] A copper coil wound around the reactor (4 mm diameter, 10 turns, located 10 cm downstream from the gas inlet) was connected to a 13.56 MHz radio frequency (RF) power supply via an L-C matching network. A signal generator (model TG503, Thurlby Thandar Instruments Ltd.) was used to trigger the RF power supply. Prior to film deposition, the whole apparatus was thoroughly scrubbed using detergent and hot water, rinsed with propan-2-ol (+99.5 wt%, Fisher Scientific UK Ltd.), oven dried at 423 K, and further cleaned using a 50 W continuous wave air plasma at 0.2 mbar for 30 min. Silicon substrate preparation comprised successive sonication in propan-2-ol and cyclohexane (+99.7 wt%, Sigma-

Aldrich Co.) for 15 min prior to insertion into the centre of the chamber. Further cleaning entailed running a 50 W continuous wave air plasma at 0.2 mbar for 30 min prior to film deposition. Non-woven polypropylene cloth (middle layer of disposable surgical face masks, SDMedical50pk, Security Direct, PO Box 1269) was used as provided. 1-Allylimidazole (97 wt%, Acros Organics b.v.b.a.) precursor was loaded into a sealable glass tube, degassed via several freeze-pump-thaw cycles, and then attached to the reactor. Monomer vapour was then allowed to purge the apparatus at a pressure of 0.15 mbar for 15 min prior to electrical discharge ignition. Pulsed plasma deposition was performed using a duty cycle on-period (t_{on}) of 20 µs and a duty cycle off-period (t_{off}) of 1200 µs in conjunction with a RF generator power output (P_{on}) of 30 W.[18] Upon plasma extinction, the precursor vapour was allowed to continue to pass through the system for a further 15 min, and then the chamber was evacuated to base pressure followed by venting to atmosphere. The equivalent of 1.69 ± 0.09 µm pulsed plasma deposition onto silicon wafers either side of the much higher surface area non-woven polypropylene material was sufficient to ensure that all the individual cloth fibres had a conformal coating (as confirmed by XPS which corresponds to a fibre coating thickness at least of the order of nanometres).

3.2.2 Surface Tethering of Palladium

The pulsed plasma deposited poly(1-allylimidazole) surfaces were immersed for 16 h into an aqueous catalyst solution comprising 2 mM palladium(II) chloride (+99.999 wt%, Alfa Aesar Co. Ltd.), 3.0 M sodium chloride (+99.5 wt%, Sigma-Aldrich Co.), and 0.5 M sodium citrate dihydrate (+99 wt%, Sigma-Aldrich Co.) in high purity water (BS 3978 Grade 1) adjusted to pH 4.5 with citric acid monohydrate (+99 wt%, Sigma-Aldrich Co.)[19]. The surfaces were then rinsed in high purity water for 20 min.

3.2.3 Film Characterisation

Reflection-absorption infrared (RAIRS) spectra of pulsed plasma poly(1-allylimidazole) deposited onto silicon wafers were acquired using a FTIR spectrometer (Spectrum One, Perkin-Elmer Inc.) fitted with a liquid nitrogen cooled MCT detector operating at 4 cm^{-1} resolution across the 400–4000 cm^{-1} range. The instrument included a variable angle reflection-absorption accessory (Specac Ltd.) set to a grazing angle of 66° for silicon wafer substrates and adjusted for p-polarization. Attenuated total reflectance (ATR) infrared

spectra of 1-allylimidazole precursor were obtained using a Golden Gate accessory (Specac Ltd.)

Film thickness values of pulsed plasma poly(1-allylimidazole) deposited onto silicon wafers were measured using a spectrophotometer (nkd-6000, Aquila Instruments Ltd.). Transmittance-reflectance curves (350–1000 nm wavelength range) were acquired for each sample and fitted to a Cauchy model for dielectric materials[20] using a modified Levenberg-Marquardt algorithm.[21] This was used to check for uniform deposition rate onto the non-woven polypropylene cloth material.

Surface elemental compositions of pulsed plasma poly(1-allylimidazole) deposited onto silicon wafers and non-woven polypropylene cloth were measured by X-ray photoelectron spectroscopy (XPS) using a VG ESCALAB II electron spectrometer equipped with a non-monochromated Mg $K\alpha_{1,2}$ X-ray source (1253.6 eV) and a concentric hemispherical analyser. Photoemitted electrons were collected at a take-off angle of 20° from the substrate normal, with electron detection in the constant analyser energy mode (CAE, pass energies of 20 and 50 eV for high resolution and survey spectra, respectively). Experimentally determined instrument sensitivity factors were C(1s) : O(1s) : N(1s) : Cl(2p) : Pd(3d) equals 1.00 : 0.35 : 0.70 : 0.37 : 0.06 respectively. The core level binding energy envelopes were fitted with a linear background and Gaussian peak shape.[22,23] A least squares regression was used for peak fitting, with a fixed full-width-half-maximum (FWHM) for all environments within a binding envelope. All binding energies were referenced to the C(1s) -$\underline{C}_xH_y$ hydrocarbon peak at 285.0 eV.[24]

3.2.4 Carbon-Carbon Coupling Reactions

Sonogashira Coupling Reaction

For single use palladium cloth studies, new B14 borosilicate sample flasks were thoroughly scrubbed using detergent and hot water, rinsed with acetone and oven dried at 373 K for 12 h. This cleaning procedure was followed before every reaction in order to remove any impurity. For single run studies on the palladium catalyst cloth, 0.50 ± 0.01 mmol of iodobenzene (98 wt%, Sigma-Aldrich Co.), 0.74 ± 0.01 mmol of phenylacetylene (98 wt%, Sigma-Aldrich Co.), and 0.99 ± 0.01 mmol of K_2CO_3 (98 wt%, Sigma-Aldrich Co.) were weighed out into a borosilicate flask. 3 mL of a solution comprising ethanol and high purity water in a 2 : 1 volume ratio was added, the flask was agitated to dissolve the K_2CO_3, and then the catalyst cloth was added (7.9 ± 2.6 mg catalyst cloth, with 0.50 ± 0.17 µmol

of palladium(II) or 0.68 wt% (53.7 ± 17.9 µg) initial palladium loading as measured by ICP-OES analysis). The B14 flask was fitted to a B14 water cooled condenser and immersed in a water bath at 343 K for 12 h for the reaction to proceed using a PTFE coated stirrer bar agitated at 500 rpm. Afterwards, the flask was removed from the water bath and allowed to cool to room temperature, after which the catalyst cloth was removed and the solution decanted. The flask was then rinsed twice with 2.5 mL of chloroform (99.8 wt%, Merck KGaA) and the washings were added to the decanted solution. The combined solution was washed twice with 3 mL of water, and the organic portion was dried over anhydrous sodium sulphate (99 wt%, SD-Fine Chem Ltd.) before analysis by GC and GC-MS without further dilution.

In the case of palladium cloth recycling studies, B10 borosilicate sample flasks (Scientific Glass Laboratories Ltd.) were rinsed with ethanol (+99.8 wt%, Fisher Scientific UK Ltd.), thoroughly scrubbed using detergent and hot water, followed by immersion for 10 h in a solution comprising sodium hydroxide (99.2 wt%, Fisher Scientific UK Ltd.), propan-2-ol, and high purity water in a mass ratio 1 : 20 : 5 in order to remove any organic residue. The flasks were then thoroughly scrubbed using detergent and hot water, rinsed in propan-2-ol, and oven dried at 423 K. A final wash step consisted of immersion for 1 h in a 1 wt% nitric acid bath (70 wt% in water, Fisher Scientific UK Ltd., further diluted in high purity water), followed by thorough rinsing with high purity water and oven drying at 423 K, to ensure that no palladium transfer occurred between solutions. This rigorous cleaning procedure was undertaken before each reaction. 0.50 ± 0.01 mmol of iodobenzene, 0.74 ± 0.01 mmol of phenylacetylene, and 0.99 ± 0.01 mmol of K_2CO_3 were weighed out into a borosilicate flask. 3 mL of a solution comprising ethanol and high purity water in a 2 : 1 volume ratio was added, the flask was agitated to dissolve the K_2CO_3, and then the catalyst cloth was added (5.8 ± 0.5 mg catalyst cloth, with 0.11 ± 0.01 µmol palladium(II) or 0.21 wt% (12 ± 1 µg) initial palladium loading as measured by ICP-OES analysis (Vista MPX, Varian Inc.)). The B10 flask was fitted to a B10 water cooled condenser and immersed in a water bath at 343 K for 12 h for the reaction to proceed. For these recycling studies, the stirrer was not included in order to prevent abrasive damage to the cloth material over sequential recycling runs. Afterwards, the flask was removed from the water bath and allowed to cool to room temperature, after which the catalyst cloth was removed and the solution decanted. The flask was then rinsed twice with 1 mL of chloroform (99.8 wt%, Fisher Scientific UK Ltd.) and the washings were added to the

decanted solution. Solutions for GC analysis were extracted three times with 3 mL of chloroform, spiked with 4 mg mL^{-1} decane (0.1 g, +99 wt%, Sigma-Aldrich Co.), and made up to 25 mL with dichloromethane (99.99 wt%, Fisher Scientific UK Ltd.). Solutions for ICP-OES analysis were sealed in screw topped borosilicate glass vials fitted with a PTFE/silicone slit septum (J.G Finneran Associates Inc. part no. 603570-08). The catalyst cloths were dried in air at 293 K for a minimum of 1 h before reuse in recycling studies with a fresh reactant solution each time.

Mizoroki-Heck Coupling Reaction

A PTFE lined autoclave 15 mL was thoroughly scrubbed using detergent and hot water, rinsed with acetone and oven dried at 373 K for 12 h. This cleaning procedure was followed before every reaction. 0.50 ± 0.01 mmol of iodobenzene (98 wt%, Sigma-Aldrich Co.), 0.75 ± 0.01 mmol of styrene (99 wt%, Sigma-Aldrich Co.), and 0.99 ± 0.005 mmol of K_2CO_3 (98 wt%, Loba Chemie Pvt. Ltd.) were weighed out into a PTFE lined autoclave. 3 mL of acetonitrile (99.8 wt%, S D Fine-Chem Ltd.) was added, the autoclave was agitated and the catalyst cloth was added (7.9 ± 2.6 mg catalyst cloth, with 0.50 ± 0.17 µmol of palladium(II) or 0.68 wt% (53.7 ± 17.9 µg) initial palladium loading as measured by ICP-OES analysis). The autoclave was fitted with a PTFE coated magnetic stirrer, agitated at 500 rpm, and heated to 413 K for 6 h for the reaction to proceed. Afterwards, the autoclave was left to cool to room temperature, after which the catalyst was removed and the solution decanted. The autoclave was rinsed twice with 1 mL of acetonitrile and twice with 1 mL of ethyl acetate (99.5 wt%, S D Fine-Chem Ltd). The washings were added to the decanted solution before analysis by GC and GC-MS without further dilution.

Suzuki-Miyaura Coupling Reaction

For single use palladium cloth studies, new B14 borosilicate sample flasks were thoroughly scrubbed using detergent and hot water, rinsed with acetone and oven dried at 373 K for 12 h. This cleaning procedure was followed before every reaction. 0.50 ± 0.05 mmol of iodobenzene (98 wt%, Sigma-Aldrich Co.), 0.75 ± 0.01 mmol of phenylboronic acid (95 wt%, Sigma-Aldrich Co.), and 0.99 ± 0.01 mmol of K_2CO_3 (98 wt%, Sigma-Aldrich Co.) were weighed out into a borosilicate flask. 3 mL of a solution comprising ethanol and high purity water in a 2 : 1 volume ratio was added, the flask was agitated to dissolve the K_2CO_3, and then the catalyst cloth was added (7.9 ± 2.6 mg catalyst cloth, with 0.50 ± 0.17 µmol of palladium(II) or 0.68 wt% (53.7 ± 17.9 µg) initial

palladium loading as measured by ICP-OES analysis) Alternatively, the iodobenzene reagent was substituted for bromobenzene (>99.5 wt%, Sigma-Aldrich Co.) or chlorobenzene (99.8 wt%, Sigma-Aldrich Co.). The B14 flask was fitted to a B14 water cooled condenser and immersed in a water bath at 343 K for 30 min for the reaction to proceed using a PTFE coated stirrer bar agitated at 500 rpm. Afterwards, the flask was removed from the water bath and allowed to cool to room temperature, after which the catalyst cloth was removed and the solution decanted. The flask was then rinsed twice with 2.5 mL of chloroform and the washings were added to the decanted solution. The combined solution was washed twice with 3 mL of water, and the organic portion was dried over anhydrous sodium sulphate before analysis by GC and GC-MS without further dilution.

In the case of palladium cloth recycling studies, B10 borosilicate sample flasks were rinsed with ethanol, thoroughly scrubbed using detergent and hot water, followed by immersion for 1 h in a solution comprising sodium hydroxide, propan-2-ol, and high purity water in a mass ratio 1 : 20 : 5 in order to remove any organic residue. The flasks were then thoroughly scrubbed using detergent and hot water, rinsed in propan-2-ol, and oven dried at 423 K. A final wash step consisted of immersion for 1 h in a 1 wt% nitric acid bath, followed by thorough rinsing with high purity water and oven drying at 423 K, to ensure that no palladium transfer occurred between solutions. This rigorous cleaning procedure was undertaken before each reaction. 0.50 ± 0.05 mmol of iodobenzene, 0.75 ± 0.01 mmol of phenylboronic acid, and 0.99 ± 0.01 mmol of K_2CO_3 were weighed out into a borosilicate flask. 3 mL of a solution comprising ethanol and high purity water in a 2 : 1 volume ratio was added, the flask was agitated to dissolve the K_2CO_3, and then the catalyst cloth was added (7.9 ± 2.6 mg catalyst cloth, with 0.50 ± 0.17 µmol of palladium(II) or 0.68 wt% (53.7 ± 17.9 µg) initial palladium loading as measured by ICP-OES analysis). Alternatively, 0.50 ± 0.05 mmol of 4-methoxyiodobenzene (98 wt%, Sigma-Aldrich Co.) was substituted for iodobenzene to rule out homocoupled by-product formation. The flask was fitted to a water cooled condenser and immersed in a water bath at 343 K for 30 min for the reaction to proceed. For these recycling studies, the stirrer was not included in order to prevent abrasive damage to the cloth material over sequential recycling runs. Afterwards, the flask was removed from the water bath and allowed to cool to room temperature, after which the catalyst cloth was removed and the solution decanted. The flask was then rinsed twice with 1 mL of chloroform and the washings were added to the

decanted solution. Solutions for GC analysis were extracted three times with 3 mL of chloroform, spiked with 4 mg mL^{-1} decane (0.1 g), and made up to 25 mL with dichloromethane. Solutions for ICP-OES analysis were sealed in screw topped borosilicate glass vials fitted with a PTFE/silicone slit septum. Catalyst cloths were dried in air at 293 K for a minimum of 1 h before reuse in recycling studies with a fresh reactant solution each time.

3.2.5 Product Analysis

Mizoroki-Heck, Suzuki-Miyaura, and Sonogashira Single Use Coupling Reactions

Gas chromatography (GC) (Young Lin Instrument Co. YL6100 gas chromatograph with a flame ionization detector (FID) fitted with a siloxane capillary column (5% phenyl / 95% dimethylpolysiloxane BP-5), length of 30 m, internal diameter of 0.25 mm, coating thickness of 0.25 µm), a starting temperature of 353 K, a hold time of 5 min, a ramp rate 5 K min^{-1}, and a final temperature of 573 K, with a hold time of 10 min. Product yield was calculated from GC as the percentage conversion of haloarene to desired coupled product in the recovered reaction solution, all other reagents were used in excess. Product selectivity was calculated as the percentage of desired product molecules produced per molecule of haloarene consumed. Gas chromatography mass spectrometry analysis (GC-MS) (Schimadzu Europa Gmbh, GCMS-QP2010 Ultra fitted with an Rxi®-5Sil column, length of 30 m, internal diameter of 0.25 mm, coating thickness of 0.25 µm) was conducted with a starting temperature of 353 K, a hold time of 5 min, a ramp rate 5 K min^{-1}, and a final temperature of 573 K with a hold time of 10 min. Coupling reaction products were confirmed using authentic samples of biphenyl (99 wt%, Aldrich Chemical Co. Inc.), diphenylacetylene (98 wt%, Aldrich Chemical Co. Inc.), and trans-stilbene (96 wt%, Aldrich Chemical Co. Inc.).

Sonogashira and Suzuki-Miyaura Coupling Recycling Experiments

GC (Bruker Corp. Scion 456 gas chromatograph with a flame ionization detector (FID) fitted with a siloxane capillary column (5% phenyl / 95% dimethylpolysiloxane BP-5), length of 30 m, internal diameter of 0.25 mm, coating thickness of 0.25 µm) was conducted using high-performance liquid chromatography (HPLC) autosampler vials with a PTFE/silicone slit septum at a starting temperature of 373 K, a hold time of 4 min, a ramp rate of 20 K min^{-1}, and a final temperature of 473 K with a hold time of 9 min. Product yield

was calculated from GC as the percentage conversion of haloarene to desired coupled product in the recovered reaction solution, all other reagents were used in excess. GC-MS (Shimadzu Europa Gmbh, GCMS-QP2010 Ultra fitted with an Rxi®-5Sil column, length of 10 m, internal diameter of 0.15 mm, column coating thickness of 0.15 µm) was conducted at a starting temperature of 303 K and a hold time of 1 min, a ramp rate of 50 K min^{-1}, and a final temperature of 573 K, with a hold time of 5 min.

3.2.6 Palladium Catalyst Loading

Palladium loading on the catalyst cloth and amount leached during recycling studies was measured by ICP-OES (Vista MPX CCD Simultaneous axial ICP-OES, Varian Inc.). Calibration of detected palladium signal intensity to actual palladium content in solution was carried out to an accuracy of 0.01 ppm using reference samples at 1, 2, and 5 ppm, prepared from a 1000 ppm stock solution (26 X 1-Pd(a), MBH Analytical Ltd.) diluted in high purity water (resistance of 18.2 MΩ). Analyte solutions and palladium catalytic cloths were digested in 5 mL of sulphuric and perchloric acids (95 wt% Normapur®, and 65 wt% Normatom® respectively, VWR International Ltd.) by a wet ashing method followed by dilution to 25 mL in high purity water. The detection limit of palladium in these catalysis experiment analyte solutions was 0.1 ppm on a mass basis.

3.3 Results

3.3.1 Surface Tethering of Palladium

Infrared spectroscopy of pulsed plasma deposited poly(1-allylimidazole) films confirmed a high level of imidazole functional group structural retention,[18] Figure 3.1. Characteristic imidazole ring absorbances include: C=C–H ring stretch (3107 cm^{-1}), C=N ring stretch (1504 cm^{-1}), and N=C–H ring in-plane bend vibration (1107 cm^{-1}).[25] Bands present in the 1560–1700 cm^{-1} range can be attributed to a low level of plasma fragmented imidazole group C=N stretches,[26] and carbonyl stretches from adducts formed through atmospheric carbon dioxide adsorption.[27,28] Disappearance of the monoalkyl vinyl CH_2 wag (906 cm^{-1}) associated with the precursor molecule confirmed selective polymerisation of the vinyl group during pulsed plasma deposition.[29]

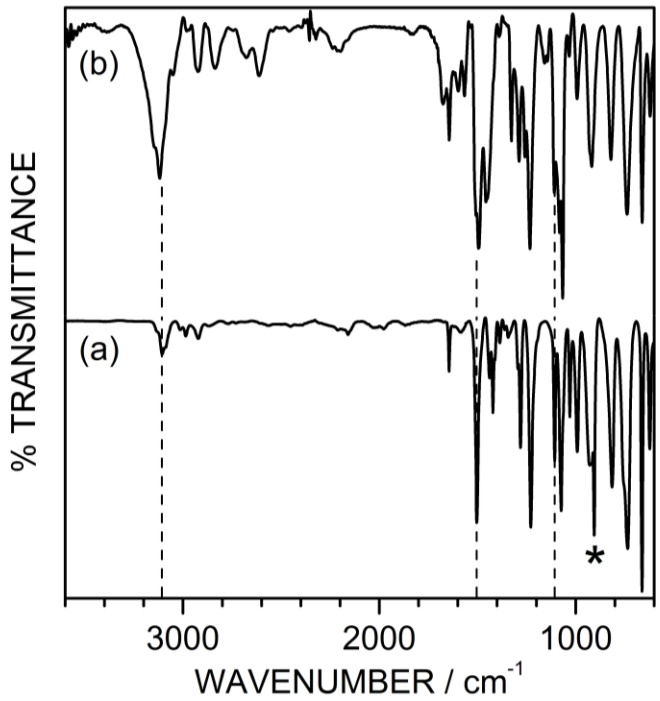

Figure 3.1: (a) ATR infrared spectra of 1-allylimidazole liquid precursor; and (b) RAIRS infrared spectra of pulsed plasma deposited poly(1-allylimidazole) (t_{on} = 20 µs, t_{off} = 1200 µs, P_{on} = 30 W, thickness = 1.69 ± 0.09 µm). Dashed lines denote characteristic imidazole ring absorbances at 3107 cm^{-1}, 1504 cm^{-1}, and 1107 cm^{-1}. * Denotes monoalkyl vinyl CH_2 wag at 906 cm^{-1}. Overall relative intensity differences between the two spectra are due to the use of ATR versus RAIRS infrared spectroscopy techniques.

XPS analysis of pulsed plasma poly(1-allylimidazole) deposited onto non-woven polypropylene cloth detected carbon, nitrogen, and a small amount of oxygen, Figure 3.2 and Table 3.1. The N(1s) binding envelope could be fitted to two different nitrogen environments at 398.7 eV and 400.5 eV, corresponding to the imidazole ring C=N and C-N nitrogen centres respectively,[30] Figure 3.3. Their slight deviation away from the theoretical 1 : 1 peak area ratio stems from a small amount of precursor fragmentation within the electrical discharge.[26] Immersing the imidazole functionalised cloth into palladium(II) chloride containing aqueous solution followed by rinsing in water gave rise to the appearance of palladium and chlorine XPS signals, signifying surface complex formation, Figure 3.2 and Scheme 3.1. This was accompanied by the relative attenuation in the 398.7 eV C=N environment, which is consistent with metal complexation to imidazole ligand C=N centres entailing nitrogen lone pair donation to the positively

charged metal centre causing a decrease in electron density around the complexing nitrogen atom (increase in N(1s) XPS binding energy[19,31]), Figure 3.3. The detection of some oxygen signal can be attributed to factors such as water absorption and the formation of adducts through atmospheric carbon dioxide adsorption.[26,27,28]

Table 3.1: XPS elemental relative atomic compositions at each stage of palladium catalyst cloth preparation and for a control sample in which polypropylene cloth without pulsed plasma poly(1-allylimidazole) functionalization was exposed to $PdCl_2$ solution.

Sample	C / %	N / %	O / %	Pd / %	Cl / %
Polypropylene cloth	100	-	-	-	-
Control polypropylene cloth exposed to palladium(II) chloride solution	93	-	7	-	-
Pulsed plasma poly(1-allylimidazole) coated polypropylene cloth	74 ± 1	24 ± 1	3 ±1	-	-
Palladium catalyst cloth	64 ± 5	13 ± 2	16 ± 4	2 ± 1	5 ± 2

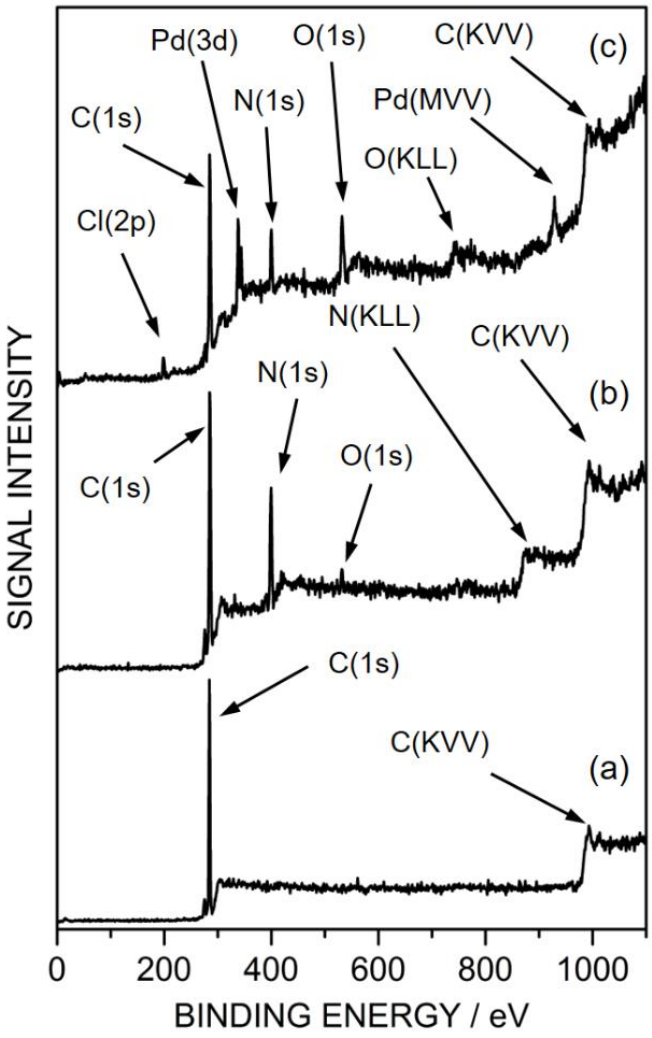

Figure 3.2: Wide scan XPS spectra of: (a) untreated polypropylene cloth; (b) pulsed plasma poly(1-allylimidazole) deposited onto polypropylene cloth (t_{on} = 20 µs, t_{off} = 1200 µs, P_{on} = 30 W); and (c) following palladium(II) chloride complexation to imidazole-functionalised cloth.

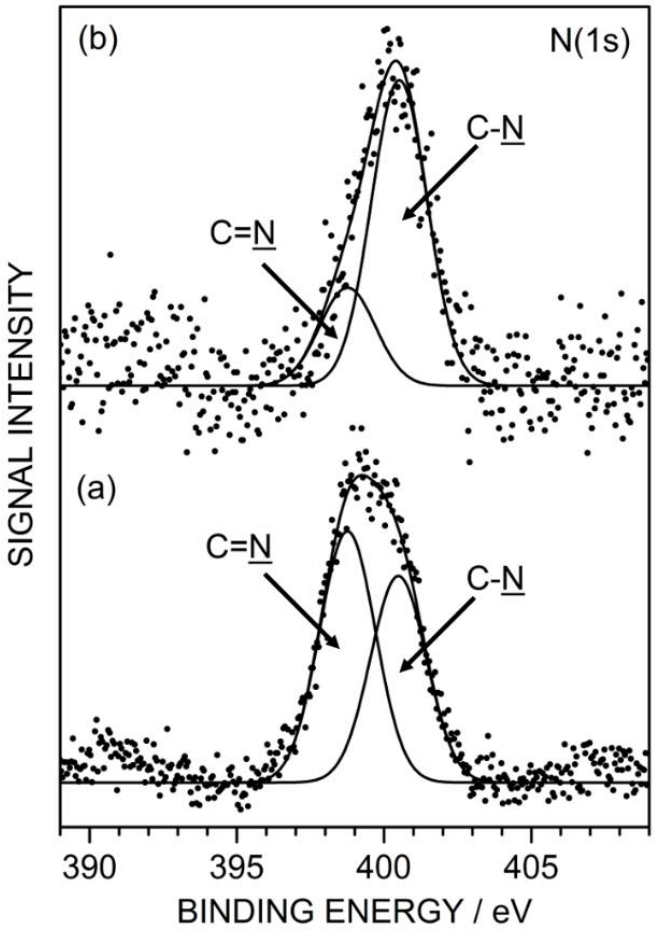

Figure 3.3: N(1s) XPS spectra: (a) pulsed plasma poly(1-allylimidazole) deposited onto polypropylene cloth (t_{on} = 20 µs, t_{off} = 1200 µs, P_{on} = 30 W); and (b) following palladium(II) chloride complexation to cloth.

3.3.2 Carbon-Carbon Coupling Reactions

The prepared low loading (0.68 wt%) palladium catalyst cloths were found to give very good product yields and high selectivities for Sonogashira, Mizoroki-Heck, and Suzuki-Miyaura coupling reactions of iodobenzene, Table 3.2. It was noted that bromobenzene displayed a small drop in catalytic performance compared to iodobenzene, whilst chlorobenzene gave rise to much lower catalytic coupling yields. This is consistent with the known attenuated activity of bromo and chlorobenzene towards oxidative addition reactions.[32] For chlorobenzene, raising the reaction temperature from 343 K to 383 K led to an improvement in turn over frequency, Table 3.2.

Table 3.2: Cross-coupling reactions for halobenzene reagents (0.50 ± 0.05 mmol, stirred) using 0.50 ± 0.17 µmol palladium(II) catalyst cloths (7.9 ± 2.6 mg catalyst cloth with 0.68 wt% palladium loading), Scheme 3.2. Yield is defined as the amount of desired product as a molar percentage of the initial limiting reagent. Turn over frequency (TOF) is defined as the number of moles of product per mole of palladium per second,[33] assuming each palladium atom is an active site. [Coupling reactions and GC conducted by R. Kore]

Coupling Reaction	**Reagent 1**	**Reagent 2**	**Conditions**	**Yield / %**	**Selectivity / %**	**TOF / h^{-1}**
Sonogashira	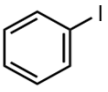	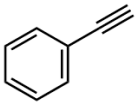	Ethanol-water, 12 h, 343 K	54 ± 3	99 ± 1	45 ± 2
Mizoroki-Heck	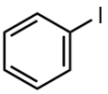	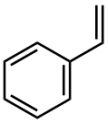	Acetonitrile, 0.5 h, 413 K	82 ± 7	93 ± 1	1640 ± 131
Suzuki-Miyaura	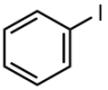	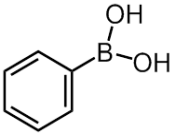	Ethanol-water, 0.5 h, 343 K	99 ± 1	>99	1980 ± 20
Suzuki-Miyaura	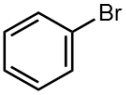	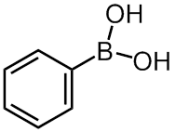	Ethanol-water, 5 h, 343 K	87 ± 6	>99	175 ± 17
Suzuki-Miyaura	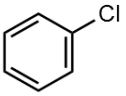	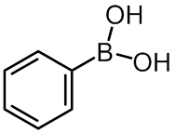	Ethanol-water, 18 h, 343 K	10 ± 2	>99	6 ± 1
Suzuki-Miyaura	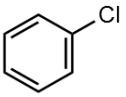	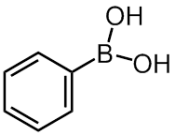	Ethanol-water, 18 h, 383 K	25	>99	14

The Suzuki-Miyaura coupling reaction was further investigated by running a control experiment using 4-methoxyiodobenzene as a reactant with phenylboronic acid under similar reaction conditions in order to rule out the possibility of homocoupled by-product formation; GC-MS analysis of the resulting products showed the presence of only 4-methoxybiphenyl and biphenyl was not observed.

3.3.3 Recycling of Palladium Catalyst Cloth

Any possibility of palladium leaching from the catalyst cloths leading to predominantly homogeneous catalysis was checked by ICP-OES of the solution phase over 16 Suzuki-Miyaura and Sonogashira reaction cycles (i.e. 15 repeat cycles) in tandem with measurement of product yields, Figure 3.4 and Figure 3.5. Lower initial product yields were observed for both Suzuki-Miyaura and Sonogashira reactions during recycling studies when compared to single use studies, Table 3.2, this was due to the absence of stirring in the former case. The Suzuki-Miyaura coupling reaction for iodobenzene reactant showed minimal leaching (1.3 ± 0.4% per cycle of the starting 0.68 wt% palladium cloth loading). The expected product yield trend over repeat cycles for a purely surface bound heterogeneous reaction was determined by scaling the product yield to the percentage palladium loading remaining on the cloth (i.e. 80% palladium remaining would give 80% of the product yield measured for the fresh catalyst cloth). The expected product yield trend for a purely homogeneous solution-based reaction was estimated to remain constant as the percentage loading on the cloth decreased, due to the measured constant leaching level. The observed decreasing trend in activity likely rules out purely homogeneous catalytic behaviour because the very low palladium leaching rate remains steady throughout the recycling studies. However, the formation of palladium nanoparticles on the surface may result in reserviors of active species that can diffuse into the solution and readsorb upon reaction completion.[34] This may result in a slow decline in activity and a low leaching rate, as observed for the studied catalytic cloths.

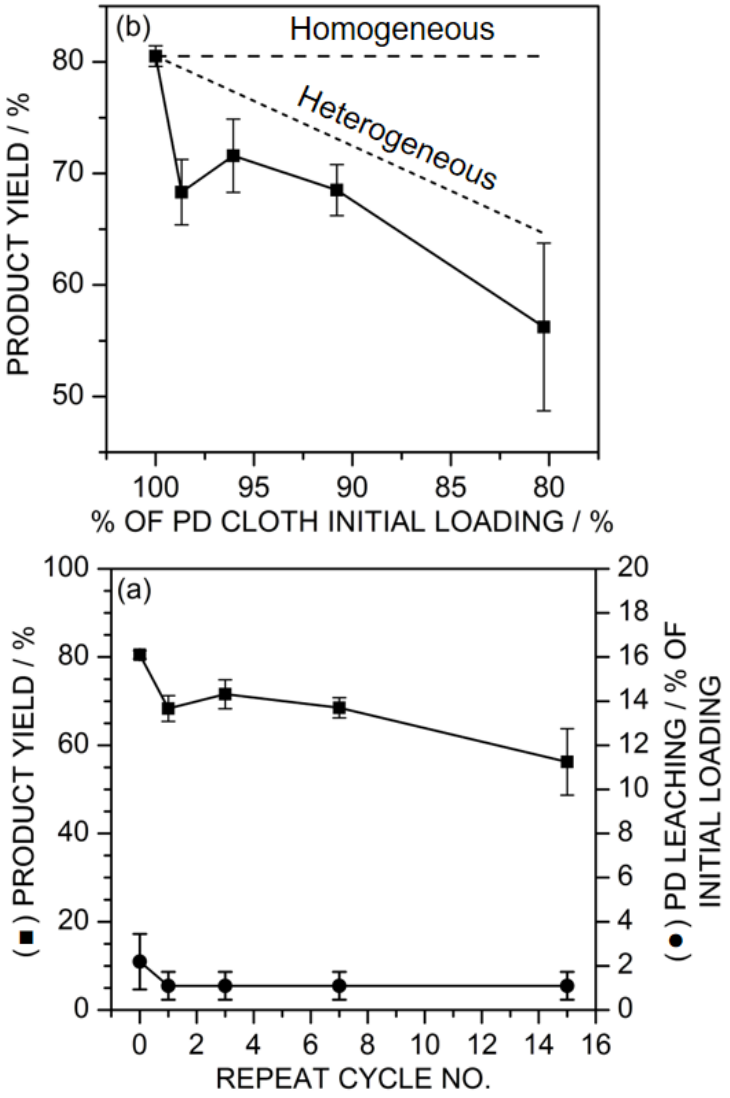

Figure 3.4: Recycling Suzuki-Miyaura coupling reaction of iodobenzene (0.50 ± 0.05 mmol iodobenzene, 343 K, 0.5 h per reaction, unstirred) using the same palladium catalyst cloth (7.9 ± 2.6 mg catalyst cloth, with 0.50 ± 0.17 µmol palladium(II) or 0.68 wt% initial palladium loading as measured by ICP-OES): (a) percentage product yield (■) and percentage palladium leaching of initial cloth loading per cycle (●) as a function of repeat cycle number; (b) percentage product yield as a function of the palladium loading remaining on the cloth (■) (calculated from the measured constant absolute value of palladium leaching per cycle of 1.3 ± 0.4% of the starting cloth loading i.e. repeat cycle no. 0). Dashed lines represent theoretical product yields for exclusively homogeneous and heterogeneous catalyst reaction pathways. Error bars are the standard deviation of three repeat experiments. [ICP analysis carried out by Medac Ltd.]

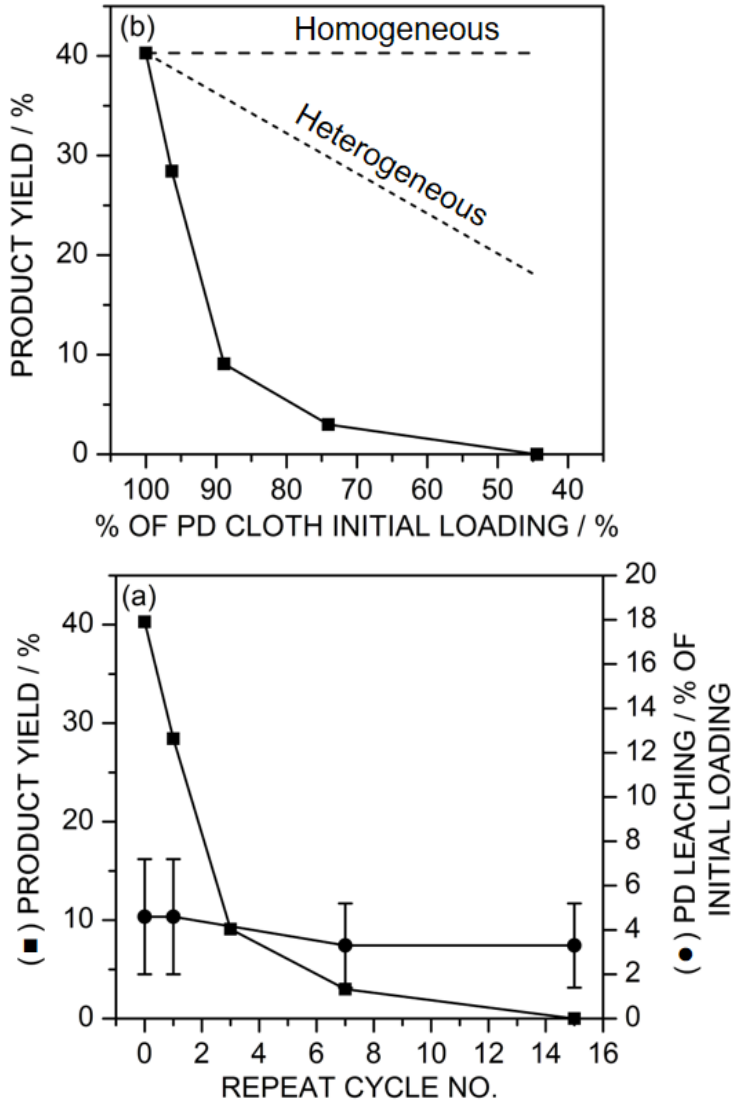

Figure 3.5: Recycling Sonogashira coupling reaction of iodobenzene (0.50 ± 0.05 mmol iodobenzene, 343 K, 12 h per reaction, unstirred) using the same palladium catalyst cloth (5.8 ± 0.5 mg catalyst cloth, with 0.11 ± 0.01 μmol palladium(II) or 0.21 wt% initial palladium loading as measured by ICP-OES): (a) percentage product yield (■) and percentage palladium leaching of initial cloth loading per cycle (●) as a function of repeat cycle number; (b) percentage product yield as a function of the palladium loading remaining on the cloth (■) (calculated from the measured constant absolute value of palladium leaching per cycle of 3.7 ± 1.1% of the starting cloth loading i.e. repeat cycle no. = 0). Dashed lines represent theoretical product yields for exclusively homogeneous and heterogeneous catalyst reaction pathways. Error bars are the standard deviation of three repeat experiments. [ICP analysis carried out by Medac Ltd.]

The aforementioned palladium cloth recycling trend observed for the Suzuki-Miyaura coupling reaction was confirmed for Sonogashira reactions over a much longer time period by lowering the catalyst loading on the cloth (0.21 wt% initial palladium loading equivalent to 0.11 ± 0.01 μmol) and extending the reaction time (12 h per reaction) so as to allow monitoring over the full catalyst lifetime. The level of palladium leaching from the catalyst cloths remained low at 3.7 ± 1.1% of starting cloth palladium loading (i.e. repeat cycle no. 0) per 12 h cycle throughout the overall Sonogashira reaction operational time of 192 h, at which point the cloth reached complete exhaustion, Figure 3.5. Again, the low level of palladium leaching remains steady in absolute terms, which rules out exclusive homogeneous palladium catalysis due to metal leaching because the product yield does not remain constant between consecutive recycles. Furthermore, the non-linearity of product yield with remaining palladium cloth loading suggests that either aggregation of metal atoms to form less active palladium clusters or poisoning is occurring on the cloth surface, Figure 3.5.

3.4 Discussion

Pulsed plasmachemical functionalisation of solid surfaces using polymerisable functional precursors is a well-established solventless, single-step, conformal, and substrate-independent technique, which offers the advantage of high levels of functional group retention,[35] thus making it well-suited for the preparation of cloth supported heterogeneous catalysts. Infrared and XPS analyses have shown that there is a high level of imidazole ring retention during pulsed plasma deposition of 1-allylimidazole precursor, thereby facilitating palladium(II) ion complexation onto the surface, Scheme 3.1, Figure 3.1, and Table 3.1. The analogous [$PdCl_2$(allylimidazole)$_2$] compound is reported to be stable at room temperature.[36] XPS analysis has shown that the measured N : Pd : Cl ratio of 6.5 : 1 : 2.5 is consistent with the formation of surface tethered [$PdCl_2(im)_2$], with the excess nitrogen content most likely arising from a combination of uncoordinated imidazole rings and a small degree of imidazole ring fragmentation during the pulsed plasma deposition process.[26]

Sonogashira, Mizoroki-Heck, and Suzuki-Miyaura coupling reactions of iodobenzene have demonstrated the practical viability of these palladium catalyst cloths. The palladium cloth loadings used for the Suzuki-Miyaura coupling reaction (for the reaction solution equivalent to 0.10 ± 0.04 mol% or 18 ± 6 ppm on a mass basis) are lower

than most previously reported dip catalysts (which range from 0.2 mol % to 2.0 mol%,[3,4,6,7] with a single instance of 0.06 mol%)[5] and are comparable to many dispersed solid supported heterogeneous catalysts.[37,38,39,40,41,42,43,44] Low palladium loading and high product yields for the Suzuki-Miyaura coupling of iodobenzene equates to a TOF of 1980 ± 20 h^{-1} (TON = 990 ± 10), which surpasses the TOFs reported for all but one palladium dip catalyst (TOF = 5808 h^{-1});[6] however, the higher reaction temperatures and shorter reaction times used in that example (403 K and 5 min, compared to the present 343 K and 30 min) are conducive to higher TOFs. Whilst very high TOFs of up to 10^7 h^{-1} are achievable with dispersed solid supported palladium catalysts and homogeneous catalysts in both organic solvents and water, such catalysts require post reaction separation.[37,45,46,47] Palladium catalyst cloths were also active for the Suzuki-Miyaura coupling of bromo and chloro benzene, indicating that this material can catalyse cheaper feedstocks.

The robustness of the catalyst cloths towards palladium leaching has been exemplified by following Sonogashira coupling over extended reaction times lasting days (choosing the lower than 99% reaction yield provided a meaningful check on monitoring yield changes). Palladium leaching over the total 192 h of catalyst cloth use was found to be less than 3.3 ± 0.7 ppb h^{-1} cm^{-3} when using an initial cloth equivalent reaction solution loading of 4.0 ± 0.4 ppm (on a mass basis or 0.022 ± 0.003 mol%), thereby demonstrating the prolonged stability of the palladium catalyst cloth. This compares favourably with previously reported studies where the palladium catalyst leaching rate ranges from less than 1 ppb h^{-1} cm^{-3} to over 100 ppb h^{-1} cm^{-3}.[5,37,39,40,42,43,48] The observed drop in product yield with extended reaction time may be due to aggregation of palladium bound to the imidazole moieties,[49] or catalyst poisoning. No breakdown point (characterised by a large rise in palladium leaching) was observed, highlighting the scope for far better reusability compared to existing state-of-the-art Fibrecat® commercial catalysts (which typically release increasing amounts of palladium after just three catalytic cycles[35]). The absence of any correlation between product yield and palladium leaching rules out the possibility of leached palladium species being primarily responsible for the observed catalysis, Figure 3.5.

Compared to conventional dispersed solid supported palladium catalysts, which require post-reaction filtration or complicated chemical synthesis in the case of magnetic separation, the envisaged benefits for the use of such cloth catalysts includes scope for

environmentally friendly solvents, lower costs, ease of use, and recyclability.[2,38,39,40,41,42,43,44,50]

3.5 Conclusions

Plasmachemical surface functionalisation with imidazole groups offers a cheap and quick approach for preparing low loading palladium catalyst cloths. These have been evaluated for Sonogashira, Mizoroki-Heck, and Suzuki-Miyaura carbon-carbon coupling reactions, and shown to exhibit high product yields (54%, 82%, and 99% respectively) and selectivities (99%, 93%, and greater than 99% respectively), whilst retaining catalytic activity over extended periods of usage (including recycling).

3.7 References

[1] Colacot, T. J.; Gore, E. S.; Kuber, A. High-Throughput Screening Studies of Fiber-Supported Catalysts Leading to Room-Temperature Suzuki Coupling. *Organometallics* **2002**, *21*, 16, 3301–3304.

[2] Colacot, T. J.; Carole, W. A.; Neide, B. A.; Harad, A. Tunable Palladium-FibreCats for Aryl Chloride Suzuki Coupling with Minimal Metal Leaching. *Organometallics*, **2008**, *27*, 5605–5611.

[3] Saha, J.; Bhowmik, K.; Das, I.; De, G. Pd–Ni Alloy Nanoparticle Doped Mesoporous SiO2 Film: The Sacrificial Role of Ni to Resist Pd-Oxidation in the C–C Coupling Reaction. *Dalton Trans.* **2014**, *43*, 13325–13332.

[4] Faria, V. W.; Oliveira, D. G. M.; Kurz, M. H. S.; Gonçalves, F. F.; Scheeren, C. W.; Rosa, G. R. Palladium Nanoparticles Supported in a Polymeric Membrane: An Efficient Phosphine-Free “Green” Catalyst for Suzuki-Miyaura Reactions in Water. *RSC Adv.* **2014**, *4*, 13446–13452.

[5] Hariprasad, E.; Radhakrishnan, T. P. Palladium Nanoparticle-Embedded Polymer Thin Film “Dip Catalyst” for Suzuki−Miyaura Reaction. *ACS Catal.* **2012**, *2*, 1179–1186.

[6] Zheng, G.; Kaefer, K.; Mourdikoudis, S.; Polavarapu, L.; Vaz, B.; Cartmell, S. E.; Bouleghlimat, A.; Buurma, N. J.; Yate, L.; de Lera, Á. R.; Liz-Marzán, L. M.; Pastoriza-Santos, I.; Pérez-Juste, J. Palladium Nanoparticle-Loaded Cellulose Paper: A Highly Efficient, Robust, and Recyclable Self-Assembled Composite Catalytic System. *J. Phys. Chem. Lett.* **2015**, *6*, 230–238.

[7] Wu, S.; Ma, H.; Jia, X.; Zhong,Y.; Lei, Z. Biopolymer-Metal Complex Wool–Pd as a Highly Active Heterogeneous Catalyst for Heck Reaction in Aqueous Media. *Tetrahedron*, **2011**, *67*, 250–256.

[8] Zhao, X.; Zhang, J.; Zhao, Y; Li, X. Pd- and Ni-Pyridyl Complexes Deposited as Films for Suzuki–Miyaura and Mizoroki–Heck Cross Coupling Reactions. *Catal. Lett.* **2015**, *145*, 2010–2019.

[9] Zhao, X.; Zhao, Y.; Zhang, J.; Li, X. A Highly Active Multi-Usable Palladium Pyridylfluorene Film-Based Catalyst for C-C Cross-Coupling Reactions. *Appl. Organometal. Chem.* **2015**, *29*, 840–845.

[10] Li, X.; Zhao, X.; Zhang, J.; Zhao, Y. Assembly of a Multilayer Film and Catalytic Application in Suzuki Cross-Coupling Reaction Based on Synergistic Effects of a Conjugated Organometallic Pyridyl Pt(C≡C)2 Moiety with Palladium. *Chem. Commun.* **2013**, *49*, 10004–10006.

[11] Zhang, J.; Li, T.; Zhao, X.; Zhao, Y.; Li, F.; Li, X. High Catalytic Active Palladium Nanoparticles Gradually Discharged from Multilayer Films to Promote Suzuki, Heck and Sonogashira Cross Coupling Reactions. *J. Colloid Interface Sci.* **2016**, *463*, 13–21.

[12] Haneda, S.; Ueba, C.; Eda, K.; Hayashi, M. Imidazole and Imidazoline Derivatives as *N*-Donor Ligands for Palladium-Catalyzed Mizoroki–Heck Reaction. *Adv. Synth. Catal.* **2007**, *349*, 833–835.

[13] Mathews, C. J.; Smith, P. J.; Welton, T. Novel Palladium Imidazole Catalysts for Suzuki Cross-Coupling Reactions. *J. Mol. Catal. A: Chem.* **2003**, *206*, 77–82.

[14] Szulmanowicz, M. S.; Zawartka, W.; Gniewek, A.; Trzeciak, A. M. Structure, Dynamics and Catalytic Activity of Palladium(II) Complexes with Imidazole Ligands. *Inorg. Chim. Acta* **2010**, *363*, 4346–4354.

[15] Trivedi, M.; Singh, G.; Nagarajan, R.; Rath, N.P. Imidazole Containing Palladium(II) Complexes as Efficient Pre-Catalyst Systems for Heck and Suzuki Coupling Reaction: Synthesis, Structural Characterization and Catalytic Properties. *Inorg. Chim. Acta* **2013**, *394*, 107–116.

[16] Borah, G.; Boruah, D.; Sarmah, G.; Bharadwaj, S. K.; Bora, U. The Development of Phosphinoamine–Pd(II)–Imidazole Complexes: Implications in Room-Temperature Suzuki–Miyaura Cross-Coupling Reaction. *Appl. Organomet. Chem.* **2013**, *27*, 688–694.

[17] Ehrlich, C. D.; Basford J. A. Recommended Practices for the Calibration and Use of Leaks. *J. Vac. Sci. Technol. A* **1992**, *10,* 1–17.

[18] Wood, T. J.; Schofield, W. C. E.; Lund, P.; Larsen, M. J.; Badyal, J. P. S. Highly Ion-Conducting Poly(Ionic Liquid) Layers. *Chem. Commun.* **2012**, *48*, 10201–10203.

[19] Bradley, T. J.; Schofield, W. C. E.; Garrod, R. P.; Badyal, J. P. S. Electroless Metallization onto Pulsed Plasma Deposited Poly(4-vinylpyridine) Surfaces. *Langmuir* **2006**, *22*, 7552.

[20] Diebold, A. C.; Chism, W. W. Characterisation and Metrology of Medium Dielectric Constant Gate Dielectric Films. In *High Dielectric Constant Materials: VSLI MOSFET Applications*; Huff, H. R.; Gilmer, D. C., Eds. Springer-Verlag, Berlin Heidelberg 2005, p 486.

[21] Lovering, D. *NKD-6000 Technical Manual*; Aquila Instruments: Cambridge, U.K. 1998.

[22] Evans, J. F.; Gibson, J.H.; Moulder, J. F.; Hammond, J. S.; Goretzki, H. Angle resolved ESCA analysis of plasma modified polystyrene. *Fresenius Z Anal. Chem*. **1984**, *319*, 841–844.

[23] Friedman, R. M.; Hudis, J.; Perlman, M. L. Chemical Effects on Linewidths Observed in Photoelectron Spectroscopy. *Phys. Rev. Lett.* **1972**, *29*, 692.

[24] Johansson, G.; Hedman, J.; Berndtsson, A.; Klasson, M.; Nilsson, R. Calibration of Electron Spectra. *J. Electron Spectrosc.* **1973**, *2*, 295–317.

[25] Kumagai, M.; Tsuchida, K.; Ogino, Y.; Hansen, J.; Ishida, H. Radical Copolymerization of 1-Vinylimidazole and Methacryl- or Styryl-Functional Silane Coupling Agents. *Polymer* **1995**, *36*, 3, 535–542.

[26] Han, L. M.; Timmons, R. B.; Bogdal, D.; Pielichowski, J. Ring Retention via Pulsed Plasma Polymerization of Heterocyclic Aromatic Compounds. *Chem. Mater.* **1998**, *10*, 1422–1429.

[27] Battjes, K. P.; Barolo, A. M.; Dreyfuss, P. New Evidence Related to Reactions of Aminated Silane Coupling Agents with Carbon Dioxide. *J. Adhesion Sci. Technol.* **1991**, *5*, 785–799.

[28] Morris, W.; Leung, B.; Furukawa, H.; Yaghi, O. K.; He, N.; Hayashi, H.; Houndonougbo, Y.; Asta, M.; Laird, B. B.; Yaghi, O. M. A Combined Experimental–Computational Investigation of Carbon Dioxide Capture in a Series of Isoreticular Zeolitic Imidazolate Frameworks. *J. Am. Chem. Soc.* **2010**, *132*, 11006–11008.

[29] Lin-Vien, D.; Colthup, N. B.; Fateley, W. G.; Grasselli, J. G. The Handbook of Infrared and Raman Characteristic Frequencies of Organic Molecules; Academic Press, Inc., San Diego, 1991; pp 74.

[30] Luo, X. F.; Goh, S. H.; Lee, S. Y.; Huan, C. H. A. Spectroscopic Studies of Interactions in Complexes of Poly(1-Vinylimidazole) with Poly(Styrenesulfonic Acid) or the Zinc Salt of Poly(Styrenesulfonate). *Macromol. Chem. Phys.* **1999**, *200*, 874–880.

[31] Drolet, D. P.; Manuta, D. M.; Lees, A. J. FT-IR and XPS Study of Copper(II) Complexes of Imidazole and Benzimidazole. *Inorg. Chim. Acta* **1988**, *146*, 173–180.

[32] Fitton, P.; Rick, E. A. The Addition of Aryl Halides to Tetrakis(Triphenylphosphine)Palladium(0). *J. Organomet. Chem.* **1971**, *28*, 287–291.

[33] Boudart, M. Turnover Rates in Heterogeneous Catalysis. *Chem. Rev.* **1995**, *95*, 661–665.

[34] de Vries, A. H. M.; Mulders, J. M. C. A.; Mommers, J. H. M.; Henderickx, H. J. W.; de Vries, J. G. Homeopathic Ligand-Free Palladium as a Catalyst in the Heck Reaction. A Comparison with a Palladacycle. *Org. Lett.* **2003**, *5*, 3285–3288.

[35] Badyal, J. P. S. Beyond the Surface. *Chem. Br.* **2001**, *37*, 45–46.

[36] Kurdziel, K.; Olejniczak, S.; Okruszek, A.; Głowiak, T.; Kruszyński, R.; Materazzi, S.; Potrzebowski, M. J. Search of Structure and Ligands Exchange for Palladium(II) Complexes with *N*-allylimidazole; X-Ray and Solid-State/Solution NMR Studies. *J. Organomet. Chem.* **2006**, *691*, 869–878.

[37] Scheuermann, G. M.; Rumi, L.; Steurer, P.; Bannwarth, W.; Mülhaupt, R. Palladium Nanoparticles on Graphite Oxide and Its Functionalized Graphene Derivatives as Highly Active Catalysts for the Suzuki-Miyaura Coupling Reaction. *J. Am. Chem. Soc.* **2009**, *131*, 8262–8270.

[38] Yuan, B.; Pan, Y.; Lee, Y.; Yin, B.; Jiang, H. A Highly Active Heterogeneous Palladium Catalyst for the Suzuki-Miyaura and Ullmann Coupling of Aryl Chlorides in Aqueous Media. *Angew. Chem. Int. Ed.* **2010**, *49*, 4054–4058.

[39] Yamada, Y. M. A.; Sarker, S. M.; Uozumi, Y. Self-Assembled Poly(Imidazole-Palladium): Highly Active, Reusable Catalyst at Parts per Million to Parts per Billion Levels. *J. Am. Chem. Soc.* **2012**, *134*, 3190–3198.

[40] Choudary, B. M.; Madhi, S.; Chowdari, N. S.; Kantam, M. L.; Sreedhar, B. Layered Double Hydroxide Supported Nanopalladium Catalyst for Heck-, Suzuki-, Sonogashira, and Stille-Type Coupling Reactions of Chloroarenes. *J. Am. Chem. Soc.* **2002**, *124*, 14127–14136.

[41] Lakshmi Kantam, M.; Roy, S.; Roy, M.; Sreedhar, B.; Choudary, B. M. Nanocrystalline Magnesium Oxide-Stabilized Palladium(0): An Efficient and Reusable Catalyst for Suzuki and Stille Cross-Coupling of Aryl Halides. *Adv. Synth. Catal.* **2005**, *347*, 2002–2008.

[42] Zhang, L.; Su, Z.; Jiang, F.; Zhou, Y.; Xu, W.; Hong, M. Catalytic Palladium Nanoparticles Supported on Nanoscale MOFs: A Highly Active Catalyst for Suzuki–Miyaura Cross-Coupling Reaction. *Tetrahedron*, **2013**, *69*, 9237–9244

[43] LeBlond, C. R.; Andrews, A. T.; Sun, Y.; Sowa, J. R. Jr. Activation of Aryl Chlorides for Suzuki Cross-Coupling by Ligandless, Heterogeneous Palladium. *Org. Lett.* **2001**, *3*, 1555–1557.

[44] Duan, L.; Fu, R.; Xiao, Z.; Zhao, Q.; Wang, J.-Q.; Chen, S.; Wan, Y. Activation of Aryl Chlorides in Water under Phase-Transfer Agent-Free and Ligand-Free Suzuki Coupling by Heterogeneous Palladium Supported on Hybrid Mesoporous Carbon. *ACS Catal.* **2015**, *5*, 575–586.

[45] Okumura, K.; Tomiyama, T.; Okuda, S.; Yoshida, H.; Niwa, M. Origin of the Excellent Catalytic Activity of Pd Loaded on Ultra-Stable Y Zeolites in Suzuki-Miyaura Reaction. *J. Catal.* **2010**, *273*, 156–166.

[46] Beller, M.; Fischer, H.; Herrmann, W. A.; Öfele, K.; Brossmer, C. Palladacycles as Efficient Catalysts for Aryl Coupling Reactions. *Angew. Chem. Int. Ed.* **1995**, *34*, 1848–1849.

[47] Feuerstein, M.; Laurenti, D.; Bougeant, C.; Doucet, H.; Santelli, M. Palladium–Tetraphosphine Catalysed Cross Coupling of Aryl Bromides with Arylboronic Acids: Remarkable Influence of the Nature of the Ligand. *Chem. Commun.* **2001**, *4*, 325–326.

[48] Frindy, S.; Primo, A.; Lahcini, M.; Bousmina M.; Garcia, H.; El Kadib, A. Pd Embedded in Chitosan Microspheres as Tunable Soft-Materials for Sonogashira Cross-Coupling in Water–Ethanol Mixture. *Green Chem.* **2015**, *17*, 1893–1898.

[49] Hu, J.; Liu, Y. Pd Nanoparticle Aging and Its Implications in the Suzuki Cross-Coupling Reaction. *Langmuir* **2005**, *21*, 2121–2123.

[50] Okumura, K. High-Turnover Heterogeneous Palladium Catalysts in Coupling Reactions: The Case of Pd Loaded on Dealuminated Y Zeolites. In *Palladium-Catalyzed Coupling Reactions - Practical Aspects and Future Developments*; Molnár, Á., Eds. Wiley-VCH, Weinheim 2013, p 31–56.

Chapter 4 Sonicated Palladium – Poly(Ionic Liquid) Membrane Flow Catalysis

4.1 Introduction

Ionic liquids are used for a wide range of applications including catalysis.[1,2,3] In the case of the Suzuki-Miyaura carbon-carbon coupling reaction, palladium species immobilised within ionic liquids have been shown to be highly effective catalyst systems.[4,5,6,7,8,9,10,11,12,13,14,15,16] For instance, ionic liquid imidazolium cations can coordinate palladium catalyst centres.[4,5,6,7,8,9,10,11,12,13,14,15] The covalent attachment of ionic liquids to conventional polymer backbones such as poly(vinylbenzyl)[7,12] and poly(divinylbenzene)[13] has also been reported. Whilst such homogeneous systems can produce high yields and reaction selectivities,[4,5,6,7,8,9,10,11,12,13,14,15,16] the inherent requirement for elution of the product limits them to batch processing. Other disadvantages include the need for high metal catalyst loadings, metal loss due to leaching, or catalyst breakdown; all of which can lead to additional processing steps and extra costs being incurred (e.g. post-reaction metal recovery in order to comply with public health regulations for pharmaceutical active ingredients[17]).

In the case of heterogeneous catalyst Suzuki-Miyaura carbon-carbon coupling reaction systems, palladium dispersed onto carbon (Pd/C) provides ease of product recovery, a relatively high reaction rate, lower cost, and integration into packed bed reactors or columns.[18,19,20,21] However, not only are high temperatures and loadings necessary to achieve adequate yields, significant levels of metal leaching are observed. Lower palladium loadings have been reported for ionic liquids covalently attached to solid support materials for packed bed reactors (these include metal phosphates,[22] metal oxides,[23] and organic polymers[24]). Despite such heterogeneous systems displaying reduced palladium leaching compared to conventional Pd/C systems, elevated temperatures or microwave heating are still needed to achieve high product yields. Microchannel and capillary reactors are alternatives to packed bed reactor systems, benefiting from lower loadings, high turnover frequencies (TOFs), and low levels of catalyst leaching.[25,26] Their drawback is the small active catalytic areas available in such devices limiting the overall reaction product capacity compared to conventional larger-scale packed bed flow reactors.

Hybrid catalyst - membrane systems can potentially address the aforementioned limitations. Ionic liquids supported onto membranes have been prepared by photo-initiated grafting of imidazolium groups onto polyethersulfone membranes.[27] The resulting membrane supported palladium - poly(ionic liquid) catalysts yield rapid TOFs (147 h^{-1}, moles of product per mole of palladium per hour), but operate at above ambient temperatures (333 K). In this chapter, a continuous flow anisotropic palladium - poly(ionic liquid) catalyst membrane system containing the above advantages of low Pd loading is described, which operates at low temperatures (293 K) and delivers comparable performance (TOF = 154 h^{-1}) to previously reported poly(ionic liquid) catalysts. Its fabrication comprises pulsed plasma deposition of a poly(vinylbenzyl chloride) layer onto a membrane to generate surface benzyl chloride groups followed by the Menshutkin reaction to form surface tethered quaternised N-butylimidazole moieties which are subsequently used to complex palladium chloride catalyst to the imidazolium cations,[28] Scheme 4.1. The fabricated palladium - poly(ionic liquid) catalyst membranes have been employed for the Suzuki-Miyaura carbon-carbon coupling reaction, Scheme 4.2.

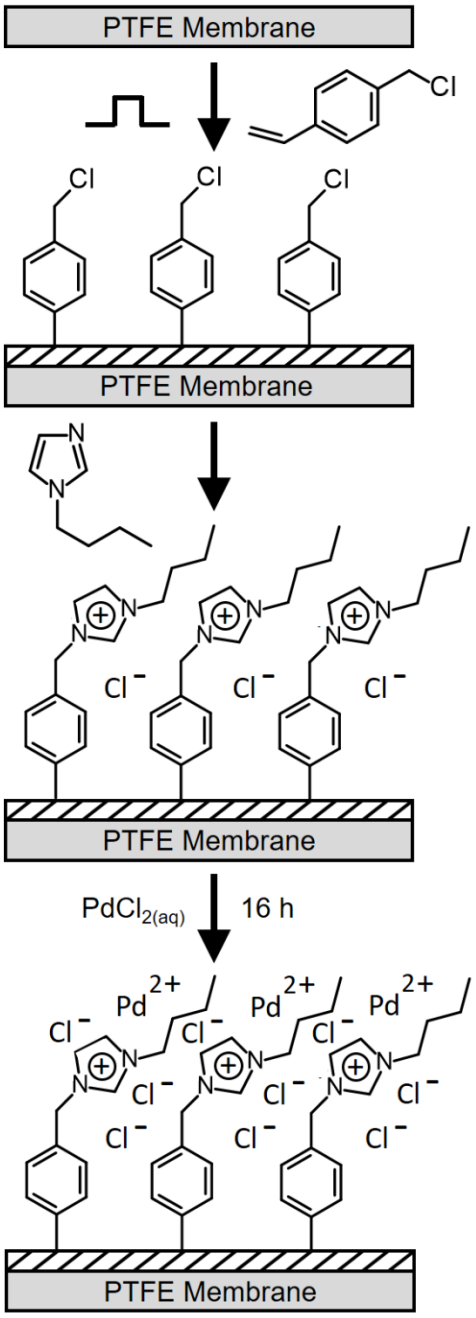

Scheme 4.1: Preparation of anisotropic palladium - poly(ionic liquid) catalyst membrane by pulsed plasma deposition of poly(vinylbenzyl chloride) layer (diagonally hatched shading) onto PTFE membrane followed by solution phase quaternisation with N-butylimidazole and then complexation to palladium(II) pro-catalyst**.**

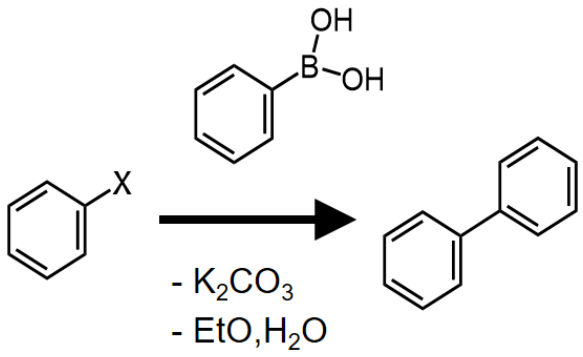

Scheme 4.2: Suzuki-Miyaura carbon-carbon coupling reaction of iodobenzene with phenylboronic acid using palladium - poly(ionic liquid) catalyst membrane.

4.2 Experimental Section

4.2.1 Preparation of Palladium - Poly(Ionic Liquid) Catalyst Membrane

A cylindrical glass reactor (5.5 cm diameter, 475 cm^3 volume) housed within a Faraday cage was used for plasmachemical deposition. This was connected to a 30 L min^{-1} rotary pump (model E2M2, Edwards Vacuum Ltd.) via a liquid nitrogen cold trap (base pressure less than 2 x 10^{-3} mbar and air leak rate better than 6 x 10^{-9} mol s^{-1}).[29] A copper coil wound around the reactor (4 mm diameter, 10 turns, located 10 cm downstream from the gas inlet) was connected to a 13.56 MHz radio frequency (RF) power supply via an L-C matching network. A signal generator (model TG503, Thurlby Thandar Instruments Ltd.) was used to trigger the RF power supply. Prior to film deposition, the whole apparatus was thoroughly scrubbed using detergent and hot water, rinsed with propan-2-ol (+99.5 wt%, Fisher Scientific UK Ltd.), oven dried at 423 K, and further cleaned using a 50 W continuous wave air plasma at 0.2 mbar for 30 min. Silicon substrate preparation comprised successive sonication in propan-2-ol and cyclohexane (+99.7 wt%, Sigma-Aldrich Co.) for 15 min prior to insertion into the centre of the chamber. Further cleaning entailed running a 50 W continuous wave air plasma at 0.2 mbar for 30 min prior to film deposition. Polytetrafluoroethylene (PTFE) membrane film (36B(1), 180 ± 10 μm thickness, 5 ± 2 μm surface pore size (determined by SEM), Mupor Ltd) was used as provided. Vinylbenzyl chloride (mixture of 3- and 4- isomers, 97 wt%, Sigma-Aldrich Co.) precursor was loaded into a sealable glass tube, degassed via several freeze-pump-thaw

cycles, and then attached to the reactor. Monomer vapour was then allowed to purge the apparatus at a pressure of 0.15 mbar for 15 min prior to electrical discharge ignition. Pulsed plasma deposition was performed using a duty cycle on-period (t_{on}) of 100 μs and a duty cycle off-period (t_{off}) of 4 ms in conjunction with a RF generator power output (P_{on}) of 30 W.[30] Upon plasma extinction, the precursor vapour was allowed to continue to pass through the system for a further 15 min, and then the chamber was evacuated to base pressure followed by venting to atmosphere. Deposited layer thicknesses were approximately 2.3 ± 0.2 μm (deposition rate 160 ± 10 nm min^{-1}).

For conversion to a supported ionic liquid layer, the pulsed plasma poly(vinylbenzyl chloride) coated substrate was immersed for 120 h into a 1 : 6 by volume solution of N-butylimidazole (98 wt%, Sigma-Aldrich Co.) in dimethylformamide (DMF, 99.5 wt%, Fisher Scientific UK Ltd.), followed by rinsing in DMF for 16 h. The quaternised surfaces were then immersed for 16 h into an aqueous solution comprising 2 mM palladium(II) chloride (+99.999 wt%, Alfa Aesar Co. Ltd.), 3.0 M sodium chloride (+99.5 wt%, Sigma-Aldrich Co.), and 0.5 M sodium citrate dihydrate (+99 wt%, Sigma-Aldrich Co.) in high purity water (BS 3978 Grade 1) adjusted to pH 4.5 with citric acid monohydrate (+99 wt%, Sigma-Aldrich Co.).[31] The surfaces were then rinsed in high purity water for 20 min.

4.2.2 Characterisation

Film thickness values of pulsed plasma poly(vinylbenzyl chloride) deposited onto silicon wafers were measured using a spectrophotometer (model nkd-6000, Aquila Instruments Ltd.). Transmittance-reflectance curves (350–1000 nm wavelength range) were acquired for each sample and fitted to a Cauchy model for dielectric materials[32] using a modified Levenberg-Marquardt algorithm.[33]

Reflection-absorption infrared (RAIRS) spectra of pulsed plasma poly(vinylbenzyl chloride) deposited onto silicon wafers were acquired using a FTIR spectrometer (Spectrum One, Perkin-Elmer Inc.) fitted with a liquid nitrogen cooled MCT detector operating at 4 cm^{-1} resolution across the 400–4000 cm^{-1} range. The instrument included a variable angle reflection-absorption accessory (Specac Ltd.) set to a grazing angle of 66° for silicon wafer substrates and adjusted for p-polarization. Attenuated total reflectance (ATR) infrared spectra of vinylbenzyl chloride precursor were obtained using a Golden Gate accessory (Specac Ltd.).

Surface elemental compositions of pulsed plasma poly(vinylbenzyl chloride) deposited onto silicon wafers and PTFE membrane were measured by X-ray photoelectron spectroscopy (XPS) using a VG ESCALAB II electron spectrometer equipped with a non-monochromated Mg $K\alpha_{1,2}$ X-ray source (1253.6 eV) and a concentric hemispherical analyser. Photoemitted electrons were collected at a take-off angle of 20° from the substrate normal, with electron detection in the constant analyser energy mode (CAE, pass energies of 20 and 50 eV for high resolution and survey spectra respectively). Experimentally determined instrument sensitivity factors were C(1s) : O(1s) : N(1s) : Cl(2p) : Pd(3d) : F(1s) equals 1.00 : 0.35 : 0.70 : 0.37 : 0.06 : 0.25 respectively. The core level binding energy envelopes were fitted using Gaussian peak shapes and linear backgrounds.[34,35] A least squares regression was used for peak fitting, with a fixed-full-width-half maximum (FWHM) for all environments within a binding envelope. All binding energies were referenced to the C(1s) $-\underline{C}_xH_y$ hydrocarbon peak at 285.0 eV.[36]

Palladium loading on the catalyst membrane, and amount leached during recycling studies was measured by ICP-OES (Vista MPX CCD Simultaneous axial ICP-OES, Varian Inc.). Calibration of detected palladium signal intensity to actual palladium content in solution was carried out to an accuracy of 0.01 ppm using reference samples at 1, 2, and 5 ppm, prepared from a 1000 ppm stock solution (26 X 1-Pd(a), MBH Analytical Ltd.) diluted in high purity water (resistance of 18.2 MΩ). Analyte solutions were digested in 5 mL of sulphuric and perchloric acids (95 wt% Normapur®, and 65 wt% Normatom® respectively, VWR International Ltd.) using a wet digestion method followed by dilution to 25 mL in high purity water. The detection limit of palladium in these catalysis experiment analyte solutions was 0.1 ppm on a mass basis. Palladium membranes were treated in the same manner to remove the palladium containing poly(ionic liquid) - plasma polymer layer from the PTFE membrane substrate.

4.2.3 Suzuki-Miyaura Carbon-Carbon Coupling Reaction

For palladium - poly(ionic liquid) catalyst membrane heated batch reactor studies of catalysis and recycling, B10 borosilicate sample flasks were rinsed with ethanol, thoroughly scrubbed using detergent and hot water, followed by immersion for 1 h in a solution comprising sodium hydroxide (99.2 wt%, Fisher Scientific UK Ltd.), propan-2-ol (+99.5 wt%, Fisher Scientific UK Ltd.), and high purity water (mass ratio 1 : 20 : 5) in order to remove any organic residue. The flasks were then thoroughly scrubbed using detergent

and hot water, rinsed in propan-2-ol, and oven dried at 423 K. A final wash step consisted of immersion for 1 h in a 1 wt% nitric acid bath (70 wt% in water, Fisher Scientific UK Ltd., further diluted in high purity water), followed by thorough rinsing with high purity water and oven drying at 423 K, to ensure that no palladium transfer occurred between solutions. This rigorous cleaning procedure was undertaken before each reaction. 0.50 ± 0.05 mmol of iodobenzene (98 wt%, Sigma-Aldrich Co.), 0.75 ± 0.01 mmol of phenylboronic acid (95 wt%, Sigma-Aldrich Co.), and 0.99 ± 0.01 mmol of potassium carbonate (98 wt%, Sigma-Aldrich Co.) were weighed out into a borosilicate flask. 3 mL of a solution comprising ethanol (+99.8 wt%, Fisher Scientific UK Ltd.) and high purity water in a 2 : 1 volume ratio was added, the flask was agitated to dissolve the potassium carbonate, and then the catalyst membrane was added (47.9 ± 3.4 mg catalyst membrane, with 0.304 ± 0.022 µmol of palladium(II) or 0.067 wt% (32.3 ± 2.3 µg) initial palladium loading as measured by ICP-OES analysis). As a control experiment, 0.50 ± 0.05 mmol of 4-methoxyiodobenzene (98 wt%, Sigma-Aldrich Co.) was substituted for iodobenzene to rule out homocoupled by-product formation. The flask was fitted to a water cooled condenser and immersed in a water bath at 343 K for 30 min for the reaction to proceed. The reaction solutions were not stirred in order to prevent abrasive damage to the membrane material over consecutive recycling runs. Afterwards, the flask was removed from the water bath and allowed to cool to room temperature, followed by removal of the catalyst membrane and the solution decanted. The flask was then rinsed twice with 1 mL of chloroform (99.8 wt%, Fisher Scientific UK Ltd.) and the washings were added to the decanted solution. Solutions for gas chromatography (GC) analysis were extracted three times with 3 mL of chloroform, spiked with 4 mg mL^{-1} decane (0.1 g, +99 wt%, Sigma-Aldrich Co.), and made up to 25 mL with dichloromethane (99.99 wt%, Fisher Scientific UK Ltd.). Solutions for ICP-OES analysis were sealed in screw topped borosilicate glass vials fitted with a PTFE/silicone slit septum. Catalyst membranes were dried in air at 293 K for a minimum of 1 h before reuse in recycling studies with a fresh reactant solution each time.

For Suzuki-Miyaura carbon-carbon coupling reactions under sonicated flow conditions, a custom gravity-fed flow cell was used, Figure 4.1. 1.0 ± 0.1 mmol of iodobenzene, 1.50 ± 0.01 mmol of phenylboronic acid, and 2.00 ± 0.01 mmol of K_2CO_3 were added to the reactor along with 6 mL of a solution comprising ethanol and high purity water in a 2 : 1 volume ratio (the area of exposed catalyst was 3.6 cm^2, with 0.61 µmol of

palladium(II) (64.6 ± 2.3 µg) initial palladium loading as measured by ICP-OES analysis). The reactor was then immersed in an ultrasonic bath (Clifton Ultrasonic Bath, Serial No. 41212, Nickel-Electro Ltd.) at 20 ± 2 ºC for 1 h. Afterwards, the reactor was removed from the ultrasonic bath, the product solutions and residual reaction solutions were decanted and stored separately. As reported in the Results and Discussion sections, the membrane setup preferential separates biphenyl product and some remaining iodobenzene reactant from the phenylboronic acid reactant and reaction solvents, such that the product solution contains only biphenyl product and some iodobenzene reactant. The product solution glassware was rinsed twice with 1 mL of chloroform and the washings were added to the decanted product solution. Residual reaction solutions were extracted for GC analysis three times with 3 mL of chloroform, spiked with 4 mg mL^{-1} decane (0.1 g), and made up to 25 mL with dichloromethane. Product solutions (which did not require extraction) were spiked with 4 mg mL^{-1} decane (0.1 g) and made up to 25 mL with dichloromethane.

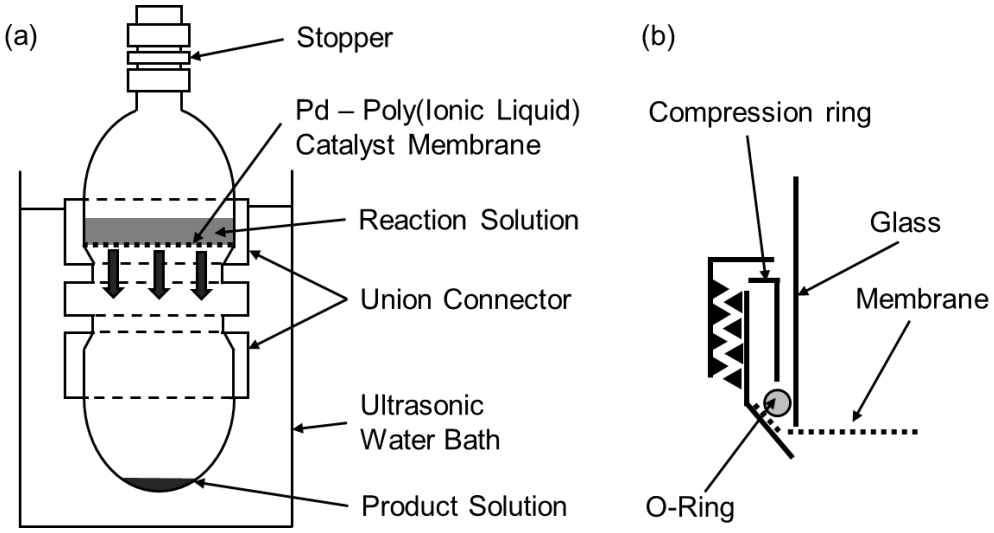

Figure 4.1: (a) Sonicated catalyst membrane reactor for room temperature Suzuki-Miyaura coupling reaction; and (b) detail of the sealing method within the union connector.

GC (Bruker Corp. Scion 456 gas chromatograph with a flame ionization detector (FID) fitted with a siloxane capillary column (5% phenyl / 95% dimethylpolysiloxane BP-5), length of 30 m, internal diameter of 0.25 mm, coating thickness of 0.25 µm) was conducted using high-performance liquid chromatography (HPLC) autosampler vials with a PTFE/silicone slit septum at a starting temperature of 373 K, a hold time of 4 min, a ramp rate of 20 K min^{-1}, and a final temperature of 473 K with a hold time of 9 min. Product

yield was calculated from GC traces as the percentage conversion of haloarene to desired coupled product in the recovered reaction solution, all other reagents were used in excess. GC-MS (Shimadzu Europa Gmbh, GCMS-QP2010 Ultra fitted with an Rxi®-5Sil column, length of 10 m, internal diameter of 0.15 mm, column coating thickness of 0.15 μm) was conducted using high-performance liquid chromatography (HPLC) autosampler vials with a PTFE/silicone slit septum at a starting temperature of 303 K and a hold time of 1 min, a ramp rate of 50 K min^{-1}, and a final temperature of 573 K, with a hold time of 5 min.

4.3 Results

4.3.1 Pulsed Plasma Deposited Poly(Vinylbenzyl Chloride)

Infrared spectroscopy of pulsed plasma deposited poly(vinylbenzyl chloride) films confirmed a high level of benzyl chloride functional group structural retention,[37,38,39] Figure 4.2. Disappearance of the monoalkyl vinyl $=CH_2$ wag vibration mode (906 cm^{-1}) associated with the precursor molecule confirmed selective vinyl group polymerisation during pulsed plasma deposition.[40] Characteristic para-substituted benzene ring absorbances can be found at 1603 cm^{-1}, and 1490 cm^{-1}.[40] The band at 1263 cm^{-1} for both the precursor and plasma deposited polymer corresponds to the $Cl–CH_2–$ wag mode.[40] This halogen-containing group is a prerequisite for quaternisation leading to the formation of a poly(ionic liquid) layer.

XPS analysis of pulsed plasma poly(vinylbenzyl chloride) deposited onto PTFE membrane detected carbon, chlorine, and low levels of oxygen (attributed to a small amount of atmospheric water absorption[41]), Table 4.1 and Figure 4.3. The absence of fluorine signal confirmed complete coverage of the underlying PTFE membrane (no pinholes).

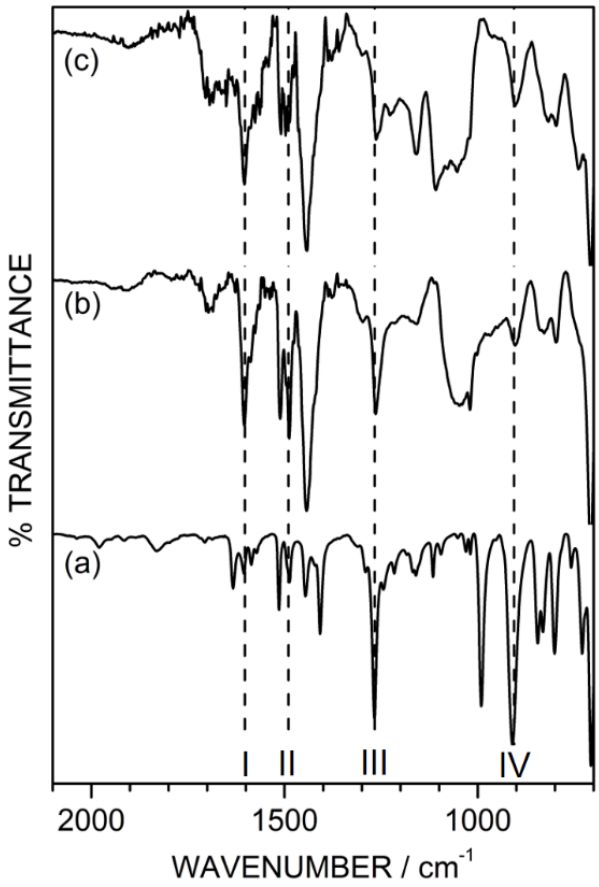

Figure 4.2: Infrared spectra of: (a) vinylbenzyl chloride liquid precursor; (b) pulsed plasma deposited poly(vinylbenzyl chloride); and (c) pulsed plasma deposited poly(vinylbenzyl chloride) quaternised with N-butylimidazole. I and II denote characteristic para-substituted benzene ring stretches at 1603 cm^{-1} and 1490 cm^{-1} respectively. III denotes characteristic Cl–CH_2– wag mode at 1263 cm^{-1}. IV denotes precursor monoalkyl vinyl =CH_2 wag at 906 cm^{-1}.

Table 4.1: XPS relative atomic compositions at each stage of palladium - poly(ionic liquid) catalyst membrane preparation, and for a control sample comprising non-quaternised poly(vinylbenzyl chloride) functionalised PTFE membrane exposed to $PdCl_2$ solution and then rinsed in high purity water.

PTFE Membrane	**C / %**	**N / %**	**O / %**	**Cl / %**	**Pd / %**	**F / %**
Untreated	29.2	-	-	-	-	70.8
Pulsed Plasma Poly(Vinylbenzyl Chloride) Functionalised	90.4 ± 0.5	-	0.4 ± 0.8	9.2 ± 0.3	-	-
Pulsed Plasma Poly(Vinylbenzyl Chloride) Functionalised + Quaternised	83.7 ± 0.7	7.9 ± 0.4	4.1 ± 0.3	4.3 ± 0.3	-	-
Pulsed Plasma Poly(Vinylbenzyl Chloride) Functionalised + Quaternised + $PdCl_{2(aq)}$	78.6 ± 2.2	6.4 ± 0.6	9.8 ± 2.4	4.3 ± 0.6	0.9 ± 0.1	-
Control Pulsed Plasma Poly(Vinylbenzyl Chloride) Functionalised + $PdCl_{2(aq)}$	80.7	-	12.9	6.4	0.0	-

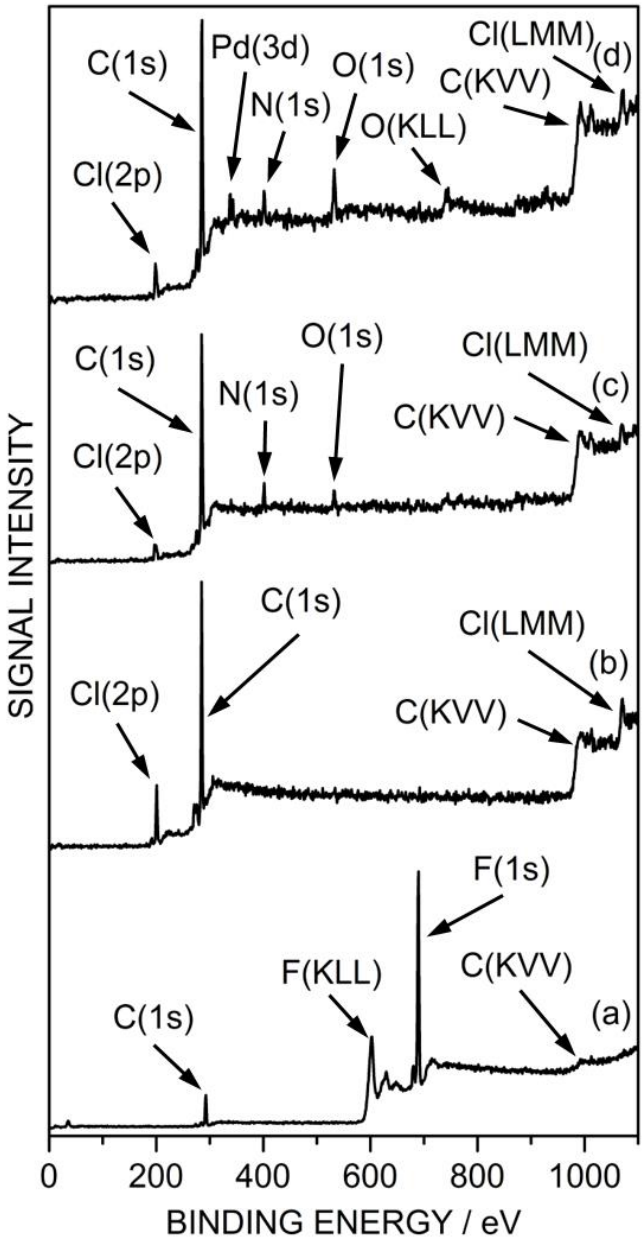

Figure 4.3: Wide scan XPS spectra of PTFE membrane: (a) untreated; (b) pulsed plasma deposited poly(vinylbenzyl chloride); (c) following quaternisation of (b) with N-butylimidazole; and (d) following palladium(II) chloride complexation to (c).

4.3.2 Palladium - Poly(Ionic Liquid) Catalyst Membrane

Quaternisation of the pulsed plasma deposited poly(vinylbenzyl chloride) films with N-butylimidazole resulted in the appearance of nitrogen XPS signal at the surface, Table 4.1 and Figure 4.3. The N(1s) binding envelope of the quaternised films could be fitted to a main nitrogen environment at 401.9 ± 0.1 eV corresponding to two equivalent nitrogen centres in positively charged imidazolium rings,[42,43,44] Figure 4.4 and Scheme 4.1. The slight shoulder towards lower N(1s) binding energy can be attributed to the reaction of N-butylimidazole with trapped free radicals contained within the plasma deposited layer.[45,46] The N(1s) environment at 401.9 ± 0.1 eV could be used to trace the degree of quaternisation as a function of treatment time, Figure 4.5, showing that after 5 days (120 h) the quaternisation reaction was complete.

The Cl(2p) peak envelope could be fitted to two different chlorine atom environments with Cl($2p_{3/2}$) binding energy values of 197.3 ± 0.1 eV and 200.6 ± 0.2 eV corresponding to chloride anions and non-quaternised unreacted benzyl chloride groups respectively,[47] Figure 4.6. Based on these two Cl($2p_{3/2}$) binding energy environments, the level of surface quaternisation was calculated to be 52 ± 9% after 5 days of reaction (Cl^-:Cl ratio of 1:1, Figure 4.5). Infrared spectroscopy of the quaternised membranes did not detect any contributions from characteristic positively charged imidazolium ring absorbances at 1350 cm^{-1} and 1180 cm^{-1},[48] thereby indicating that only near-surface quaternisation had occurred (i.e. very low concentration relative to the bulk underlying pulsed plasma deposited poly(vinylbenzyl chloride) layer), Figure 4.2.

Immersion of the quaternised films into aqueous palladium(II) chloride solution gave rise to the appearance of Pd(3d) XPS signals on the quaternised films characteristic of palladium(II), signifying surface complexation, Table 4.1. No significant change in binding energy was observed in the N(1s) XPS signal at 401.9 ± 0.1 eV, Figure 4.4, which is consistent with previous studies for palladium(II) containing ionic liquids.[49] This was accompanied by the relative Cl($2p_{3/2}$) chloride anion peak component at 197.3 ± 0.1 eV within the overall Cl(2p) envelope increasing due to the incorporation of additional chloride anions accompanying the palladium(II) catalyst complexation process, Figure 4.6.

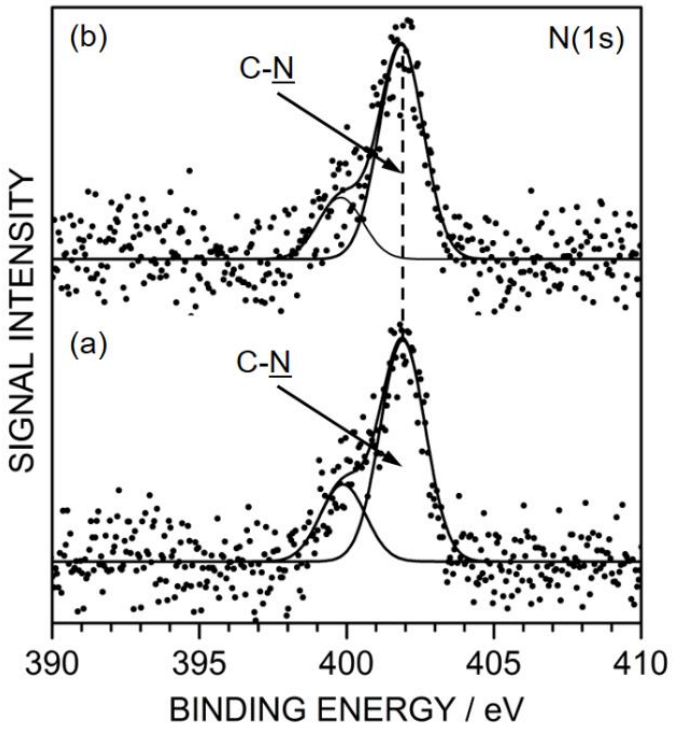

Figure 4.4: N(1s) XPS spectra: (a) pulsed plasma poly(vinylbenzyl chloride) deposited onto PTFE membrane and quaternised with N-butylimidazole; and (b) following palladium(II) chloride complexation to (a).

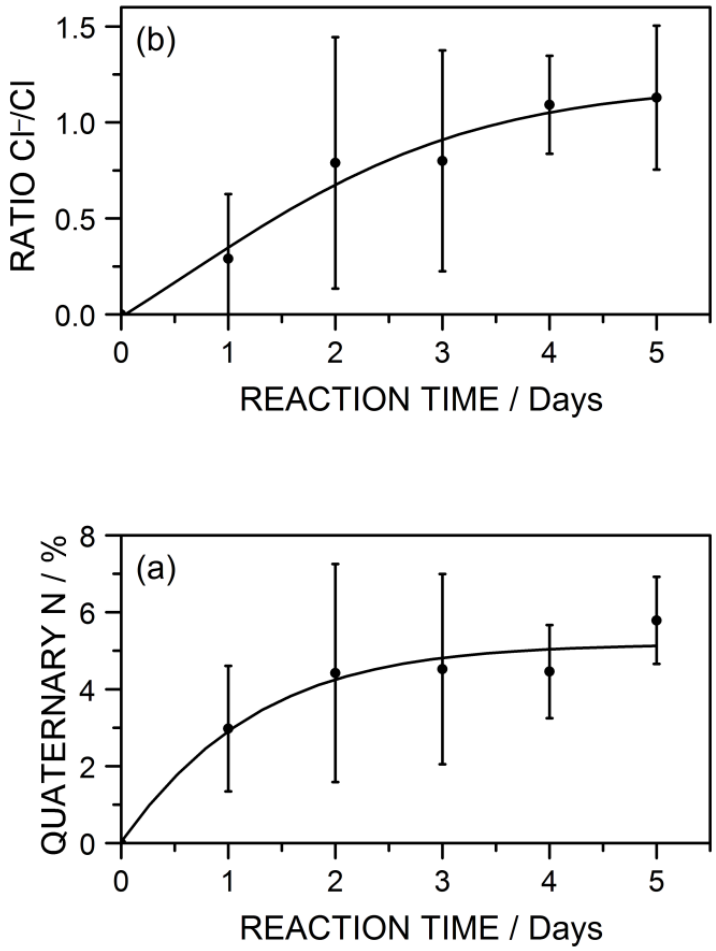

Figure 4.5: Quaternisation of pulsed plasma deposited poly(vinylbenzyl chloride) with N-butylimidazole measured by XPS: (a) relative atomic composition of quaternised nitrogen as a percentage of all elemental species on the surface; and (b) ratio of relative atomic composition of chloride to C-Cl species. Error bars are the standard deviation of three repeat experiments. Tend lines have been added only as a guide.

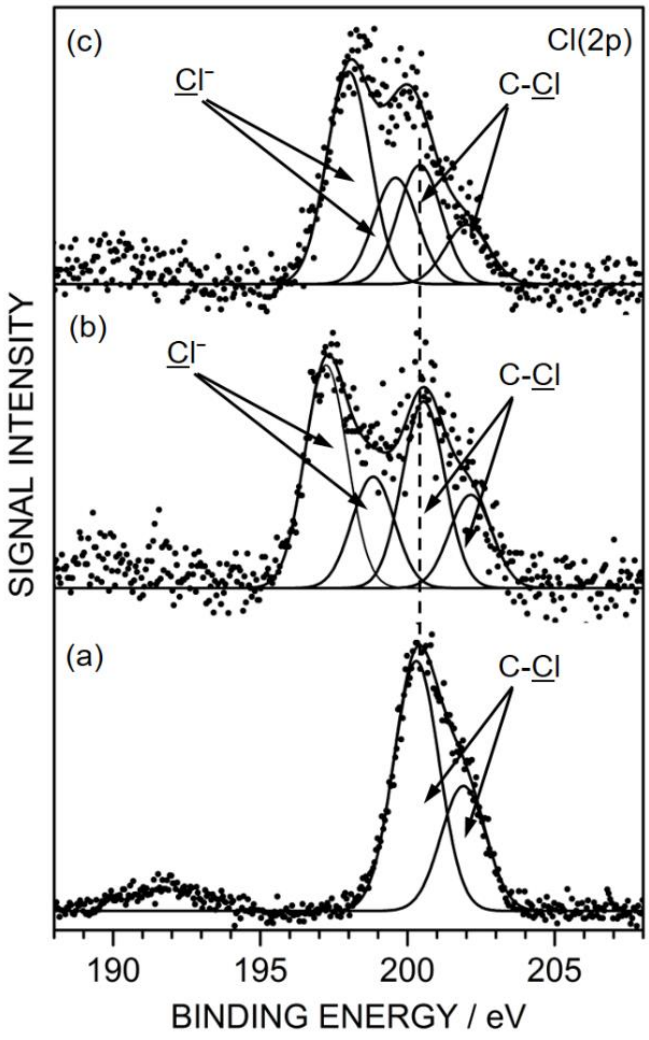

Figure 4.6: Cl(2p) XPS spectra: (a) pulsed plasma poly(vinylbenzyl chloride) deposited onto PTFE membrane; (b) following quaternisation with N-butylimidazole; and (c) following palladium(II) chloride complexation to (b). Due to spin-orbit coupling, Cl($2p_{1/2}$) components are shifted by 1.6 eV to higher binding energy relative to the Cl($2p_{3/2}$) components, with a Cl($2p_{3/2}$):Cl($2p_{1/2}$) peak area ratio equal to 2:1.[47]

4.3.3 Suzuki-Miyaura Carbon-Carbon Coupling Reaction

Heated Batch Catalysis

The catalytic activity and stability of the prepared palladium - poly(ionic liquid) catalyst membranes were monitored over 3 repeat cycles (4 cycles in total) for the Suzuki-Miyaura carbon-carbon coupling reaction at 343 K, Figure 4.7 and Scheme 4.2. Product yield remained constant throughout (77 ± 7%, only iodobenzene and phenylboronic compounds exceeded 1% of the GC biphenyl product peak area) under the given experimental conditions, with a turnover frequency of 3097 ± 323 h^{-1} (TOF, moles of product per mole of palladium per hour). Palladium leaching into the reaction solution was found to be 83 ± 33 ppb h^{-1} cm^{-3} (for the initial membrane equivalent reaction solution loading of 11.1 ± 8 ppm on a mass basis, or 0.061 ± 0.004 mol% - this is equivalent to ~1% of the Pd present leaching from an already sub 0.1 mol% catalyst during one reaction cycle at 343 K).

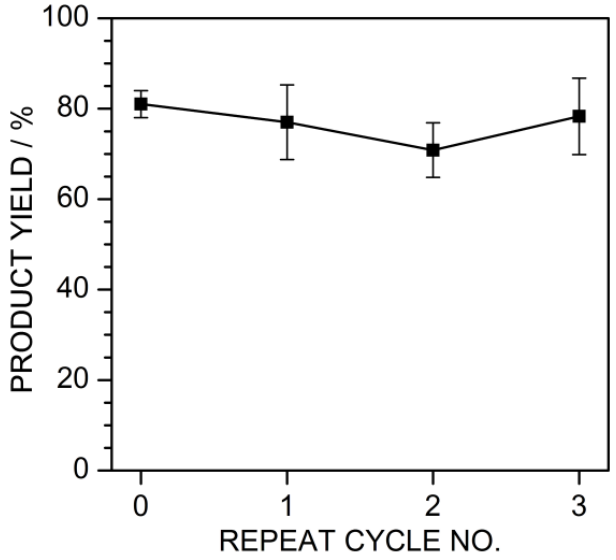

Figure 4.7: Product yield for Suzuki-Miyaura carbon-carbon coupling reaction of iodobenzene with phenylboronic acid as a function of recycle number using the same piece of palladium - poly(ionic liquid) catalyst membrane. 47.9 ± 3.4 mg catalyst membrane, with 32.3 ± 2.3 µg palladium(II) loading (or 674 ppm initial palladium content in the catalyst membrane as measured by ICP-OES), 0.5 h per reaction cycle, at 343 K, unstirred. Palladium leaching was measured after each repeat cycle. Error bars are the standard deviation of three repeat experiments.

As a control, the Suzuki-Miyaura coupling reaction was run using 4-methoxyiodobenzene and phenylboronic acid reactants under similar reaction conditions in order to rule out the possibility of homocoupled by-product formation. GC-MS analysis of the obtained products showed the presence of only 4-methoxybiphenyl, and an absence of homocoupled biphenyl by-product.

Room Temperature Sonicated Membrane Flow Catalysis

The practical viability of these palladium - poly(ionic liquid) catalyst membranes for continuous flow Suzuki-Miyaura carbon-carbon coupling reactions was demonstrated by allowing the reaction solution to permeate into the membrane during sonication at room temperature. After 1 h of reaction time, 17 mol% (0.17 mmol of 1.0 mmol) of the iodobenzene reactant present in the starting solution had been transported through the catalytic membrane as either product or unreacted iodobenzene. The collected solution contained only aromatic organic compounds (54 mol% biphenyl product, 42 mol% iodobenzene, and 4 mol% phenylboronic acid – no other components exceeded 3% of the GC biphenyl product peak area). This indicates that iodobenzene (either unreacted or as carbon-carbon coupled biphenyl product) preferentially passes through the membrane relative to phenylboronic acid. The TOF for biphenyl product formation was 154 h^{-1}.

4.4 Discussion

Pulsed plasmachemical functionalisation of solid surfaces using polymerisable functional precursors is a well-established, solventless, single-step, conformal, and substrate-independent technique, which offers the advantage of high levels of functional group retention,[50] thus making it well-suited for the preparation of membrane-supported poly(ionic liquid) catalysts. Infrared spectroscopy and XPS analyses have shown that there is a high level of chloro group and benzene ring retention during pulsed plasma deposition of vinylbenzyl chloride precursor, thereby facilitating the subsequent step of quaternisation with N-butylimidazole to form a poly(ionic liquid) layer, Scheme 4.1, Figure 4.2, Figure 4.3, Figure 4.4 and Figure 4.6. Complexation of this surface to palladium chloride yields a palladium containing poly(ionic liquid) catalyst membrane.

Although high TOFs are achievable with conventional dispersed homogeneous and heterogeneous palladium catalyst systems,[51,52,53,54] such materials suffer from the drawback of requiring post reaction recovery of the palladium catalyst. The practical

viability of the palladium - poly(ionic liquid) catalyst membranes in the present study has been demonstrated for the Suzuki-Miyaura reaction of iodobenzene. The measured TOF value of 3097 ± 323 h^{-1} for heated (343 K) batch reaction mode is comparable with previously reported homogeneous ionic liquid catalysts (TOFs of 10^2–10^5 h^{-1})[4,5,7,9,10] and other heterogeneous poly(ionic liquid) catalysts (TOFs of 10^1–10^3 h^{-1}).[12,13,14,15]

The palladium membrane loadings used for the Suzuki-Miyaura coupling reaction (a reaction solution equivalent of 0.061 ± 0.004 mol% or 11.1 ± 8 ppm on a mass basis) are lower than most previously reported ionic liquid catalysts (homogeneous and heterogeneous) which range between 0.1–18 mol%.[5,7,8,9,10,11,12,14,15,16,21] A palladium leaching value of 83 ppb h^{-1} cm^{-3} at 343 K compares favourably with previously reported solid support heterogeneous catalysts, where leaching rates exceed 100 ppb h^{-1} cm^{-3}.[55,56]

In the case of the flow membrane reactor mode of operation, ambient temperature sonicated Suzuki-Miyaura reactions gave a calculated TOF value for biphenyl product formation of 154 h^{-1}. This is comparable with previously reported Suzuki-Miyaura flow reactors (TOF 10^1 to 10^4 h^{-1}),[23,25,26,27,57] however such systems require high pressures or elevated temperatures. The beneficial preferential separation of iodobenzene reactant and biphenyl product from the phenylboronic acid and reaction solvents in the present study can be ascribed to the selective solubility of the prepared membrane system, Scheme 4.3. Ionic liquids tend to solvate a wide range of species including benzene and haloarenes,[58,59] therefore iodobenzene can diffuse directly through the poly(ionic liquid) layer, accounting for its high concentration in the product solution. Comparatively, phenylboronic acid is insoluble in some imidazolium ionic liquids and will predominantly remain behind in the reactant ethanol:water solvent phase.[60] The absence of water and ethanol reaction mixture transportation through the catalyst membrane is most probably due to the immiscibility of ethanol and water with imidazole containing ionic liquids and the pulsed plasma deposited poly(vinylbenzyl chloride) at ambient temperature,[61,62,63] as well as liquid repellency from the underlying PTFE membrane (surface tension of water = 72.8 mN m^{-1},[64] surface tension of ethanol = 22.3 mN m^{-1},[64] and surface energy of PTFE = 20.0 mN m^{-1},[65]). Therefore, the outlined approach not only allows for the palladium-catalysed Suzuki-Miyaura carbon-carbon coupling reaction to proceed at room temperature under flow conditions, but also concurrently separates the solvent mixture from the aromatic product phase, thereby eliminating any need for post reaction separation of product from reaction solvents.

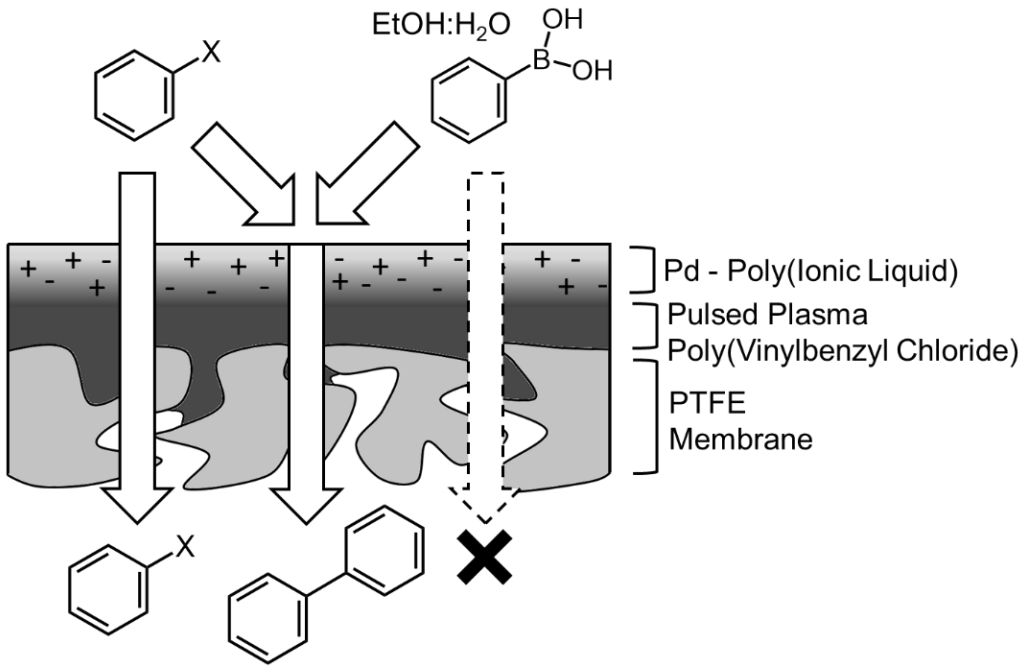

Scheme 4.3: Selective separation of iodobenzene and biphenyl product from phenylboronic acid and solvent mixture using palladium - poly(ionic liquid) membranes.

4.5 Conclusions

Plasmachemical surface functionalisation with benzyl chloride groups provides a quick, low cost approach for fabricating anisotropic palladium - poly(ionic liquid) catalyst membrane systems. This comprises pulsed plasma deposition of a poly(vinylbenzyl chloride) layer onto a membrane to generate surface benzyl chloride groups followed by quaternisation with N-butylimidazole to form a surface tethered poly(ionic liquid) which subsequently is complexed to palladium(II) catalyst. These coated substrates have been evaluated in a heated batch reactor for the Suzuki-Miyaura carbon-carbon coupling reaction, and shown to exhibit 77 ± 7% product yield (343 K, 0.5 h, 0.06 mol % Pd) and >99% selectivity, as well as retaining catalytic activity over extended periods of usage (including recycling), and low levels of palladium catalyst leaching. In the case of a sonochemical anisotropic membrane flow reactor setup operating at ambient temperature, it has been shown that selective separation of the Suzuki-Miyaura carbon-carbon coupling reaction biphenyl product (and some remaining iodobenzene reactant) from phenylboronic acid and solvent mixture can be achieved.

4.7 References

[1] Wasserscheid, P.; Keim, W. Ionic Liquids—New “Solutions” for Transition Metal Catalysis. *Angew. Chem., Int. Ed.* **2000**, *39*, 3772–3789.

[2] Pârvulescu, V. I.; Hardacre, C. Catalysis in Ionic Liquids. *Chem. Rev.* **2007**, *107*, 2615−2665.

[3] Hallett, J. P.; Welton, T. Room-Temperature Ionic Liquids: Solvents for Synthesis and Catalysis. 2. *Chem. Rev.* **2011**, *111*, 3508–3576.

[4] Durand, J.; Teuma, E.; Malbosc, F.; Kihn, Y.; Gómez, M. Palladium Nanoparticles Immobilized in Ionic Liquid: An Outstanding Catalyst for the Suzuki C–C Coupling. *Catal. Commun.* **2008**, *9*, 273–275.

[5] Meriç, N.; Aydemir, N. M.; Işik, U.; Ocak, Y. S.; Rafikova, K.; Paşa, S.; Kayan, C.; Dura, F.; Zazybin, A.; Temel, H. Cross-Coupling Reactions in Water Using Ionic Liquid-Based Palladium(II)–Phosphinite Complexes as Outstanding Catalysts. *Appl. Organomet. Chem.* **2014**, *28*, 818–825.

[6] Cotugno, P.; Casiello, M.; Nacci, A.; Mastrorilli, P.; Dell’Anna, M. M.; Monopoli, A. Suzuki Coupling of Iodo and Bromoarenes Catalyzed by Chitosan-Supported Pd-Nanoparticles in Ionic Liquids. *J. Organometal. Chem.* **2014**, *752*, 1–5.

[7] Yang, X.; Fei, Z.; Zhao, D.; Ang, W. H.; Li, Y.; Dyson, P. J. Palladium Nanoparticles Stabilized by an Ionic Polymer and Ionic Liquid: A Versatile System for C-C Cross-Coupling Reactions. *Inorg. Chem.* **2008**, *47*, 3292–3297.

[8] McLachlan, F.; Mathews, C. J.; Smith, P. J.; Welton, T. Palladium-Catalyzed Suzuki Cross-Coupling Reactions in Ambient Temperature Ionic Liquids: Evidence for the Importance of Palladium Imidazolylidene Complexes. *Organometallics* **2003**, *22*, 5350–5357.

[9] Mathews, C. J.; Smith, P. J.; Welton, T. Palladium Catalysed Suzuki Cross-Coupling Reactions in Ambient Temperature Ionic Liquids. *Chem. Commun.* **2000**, *14*, 1249–1250.

[10] Grasa, G. A.; Viciu, M. S.; Huang, J.; Zhang, C.; Trudell, M. L.; Nolan, S. P. Suzuki-Miyaura Cross-Coupling Reactions Mediated by Palladium/Imidazolium Salt Systems. *Organometallics* **2002**, *21*, 2866–2873.

[11] Xiao, J.-C.; Shreeve, J. M. Synthesis of 2,2’-Biimidazolium-Based Ionic Liquids: Use as a New Reaction Medium and Ligand for Palladium-Catalyzed Suzuki Cross-Coupling Reactions. *J. Org. Chem.* **2005**, *70*, 3072–3078.

[12] Ghazali-Esfahani, S.; Păunescu, E.; Bagherzadeh, M.; Fei, Z.; Laurenczy, G.; Dyson, P. J. A Simple Catalyst for Aqueous Phase Suzuki Reactions Based on Palladium Nanoparticles Immobilized on an Ionic Polymer. *Sci. China: Chem.* **2016**, *59*, 482–486.

[13] Yu, Y.; Hu, T.; Chen, X.; Xu, K.; Zhang, J.; Huang, J. Pd Nanoparticles on a Porous Ionic Copolymer: A Highly Active and Recyclable Catalyst for Suzuki–Miyaura Reaction under Air in Water. *Chem. Commun*. **2011**, *47*, 3592–3594.

[14] Wang, J.; Xu, B.; Sun, H.; Song, G. Palladium Nanoparticles Supported on Functional Ionic Liquid Modified Magnetic Nanoparticles as Recyclable Catalyst for Room Temperature Suzuki Reaction. *Tetrahedron Lett.* **2013**, *54*, 238–241.

[15] Borkowski, T.; Dobosz, J.; Tylus, W.; Trzeciak, A. M. Palladium Supported on Al2O3–CeO2 Modified with Ionic Liquids as a Highly Active Catalyst of the Suzuki–Miyaura Cross-Coupling. *J. Catal.* **2014**, *319*, 87–94.

[16] Zhao, D.; Fei, F.; Geldbach, T. J.; Scopelliti, R.; Dyson, P. J. Nitrile-Functionalized Pyridinium Ionic Liquids: Synthesis, Characterization, and Their Application in Carbon Carbon Coupling Reactions. *J. Am. Chem. Soc*. **2004**, *126*, 15876–15882.

[17] European Medicines Agency, ICH Guideline Q3D on Elemental Impurities http://www.ema.europa.eu/docs/en_GB/document_library/Scientific_guideline/2015/00/WC500180284.pdf (accessed Apr 5, 2016).

[18] Felpin, F. X.; Ayad, T.; Mitra, S. Pd/C: An Old Catalyst for New Applications - Its Use for the Suzuki-Miyaura Reaction. *Eur. J. Org. Chem.* **2006**, *12*, 2679–2690.

[19] Mateos, C.; Rincón, J. A.; Martín-Hidalgo, B.; Villanueva, J. Green and Scalable Procedure for Extremely Fast Ligandless Suzuki–Miyaura Cross-Coupling Reactions in Aqueous IPA Using Solid-Supported Pd in Continuous Flow. *Tetrahedron Lett.* **2014**, *55*, 3701–3705.

[20] Glasnov, T. N.; Findenig, S.; Kappe, C. O. Heterogeneous Versus Homogeneous Palladium Catalysts for Ligandless Mizoroki–Heck Reactions: A Comparison of Batch/Microwave and Continuous-Flow Processing. *Chem. - Eur. J.* **2009**, *15*, 1001–1010.

[21] Phan, N. T. S.; Khan, J.; Styring, P. Polymer-Supported Palladium Catalysed Suzuki–Miyaura Reactions in Batch and a Mini-Continuous Flow Reactor System. *Tetrahedron* **2005**, *61*, 12065–12073.

[22] Petrucci, C.; Cappelletti, M.; Piermatti, O.; Nocchetti, M.; Pica, M.; Pizzoa, F.; Vaccaro, L. Immobilized Palladium Nanoparticles on Potassium Zirconium Phosphate as an Efficient Recoverable Heterogeneous Catalyst for a Clean Heck Reaction in Flow. *J. Mol. Catal. A: Chem.* **2015**, *401*, 27–34.

[23] Lichtenegger, G. J.; Maier, M.; Khinast, J. G.; Gruber-Wölfler, H. Continuous Suzuki–Miyaura Reactions with Novel Ce–Sn–Pd Oxides and Integrated Crystallization as Continuous Downstream Protocol. *J. Flow Chem.* **2016**, *6*, 244–251.

[24] Baxendale, I. R.; Griffiths-Jones, C. M.; Ley, S. V.; Tranmer, G. K. Microwave-Assisted Suzuki Coupling Reactions with an Encapsulated Palladium Catalyst for Batch and Continuous-Flow Transformations. *Chem. - Eur. J.* **2006**, *12*, 4407–4416.

[25] Uozumi, Y.; Yamada, Y. M. A.; Beppu, T.; Fukuyama, N.; Ueno, M.; Kitamori, T. Instantaneous Carbon-Carbon Bond Formation Using a Microchannel Reactor with a Catalytic Membrane. *J. Am. Chem. Soc.* **2006**, *128*, 15994–15995.

[26] Jones, R. C.; Canty, A. J.; Deverell, J. A.; Gardiner, M. G.; Guijt, R. M.; Rodemann, T.; Smith, J. A.; Tolhurst, V.-A. Supported Palladium Catalysis Using a Heteroleptic 2-Methylthiomethylpyridine–N,S–Donor Motif for Mizoroki–Heck and Suzuki–Miyaura

Coupling, Including Continuous Organic Monolith in Capillary Microscale Flow-Through Mode. *Tetrahedron* **2009**, *65*, 7474–7481.

[27] Gu, Y.; Favier, I.; Pradel, C.; Gin, D. L.; Lahitte, J.-F.; Noble, R. D.; Gómez, M.; Remigy, J.-C. High Catalytic Efficiency of Palladium Nanoparticles Immobilized in a Polymer Membrane Containing Poly(Ionic Liquid) in Suzuki–Miyaura Cross-Coupling Reaction. *J. Membrane Sci.* **2015**, *492*, 331–339.

[28] Lee, C. K.; Peng, H. H.; Lin, I. J. B. Liquid Crystals of N,N′ -Dialkylimidazolium Salts Comprising Palladium(II) and Copper(II) Ions. *Chem. Mater.* **2004**, *16*, 530–536.

[29] Ehrlich, C. D.; Basford J. A. Recommended Practices for the Calibration and Use of Leaks. *J. Vac. Sci. Technol., A* **1992**, *10,* 1–17.

[30] Wood, T. J.; Schofield, W. C. E.; Lund, P.; Larsen, M. J.; Badyal, J. P. S. Highly Ion-Conducting Poly(Ionic Liquid) Layers. *Chem. Commun.* **2012**, *48*, 10201–10203.

[31] Bradley, T. J.; Schofield, W. C. E.; Garrod, R. P.; Badyal, J. P. S. Electroless Metallization onto Pulsed Plasma Deposited Poly(4-Vinylpyridine) Surfaces. *Langmuir* **2006**, *22*, 7552–7555.

[32] Diebold, A. C.; Chism, W. W. Characterisation and Metrology of Medium Dielectric Constant Gate Dielectric Films. In *High Dielectric Constant Materials: VSLI MOSFET Applications*; Huff, H. R.; Gilmer, D. C., Eds. Springer-Verlag, Berlin Heidelberg 2005, pp 486.

[33] Lovering, D. *NKD-6000 Technical Manual*; Aquila Instruments: Cambridge, U.K. 1998.

[34] Evans, J. F.; Gibson, J.H.; Moulder, J. F.; Hammond, J. S.; Goretzki, H. Angle resolved ESCA analysis of plasma modified polystyrene. *Fresen. Z Anal. Chem*. **1984**, *319*, 841–844.

[35] Friedman, R. M.; Hudis, J.; Perlman, M. L. Chemical Effects on Linewidths Observed in Photoelectron Spectroscopy. *Phys. Rev. Lett.* **1972**, *29*, 692.

[36] Johansson, G.; Hedman, J.; Berndtsson, A.; Klasson, M.; Nilsson, R. Calibration of Electron Spectra. *J. Electron Spectrosc. Relat. Phenom.* **1973**, *2*, 295–317.

[37] Morsch, S.; Schofield, W. C. E.; Badyal, J. P. S. Surface Actuation of Smart Nanoshutters. *Langmuir* **2010**, *26*, 12342–12350.

[38] Morsch, S.; Schofield, W. C. E.; Badyal, J. P. S. Tailoring the Density of Surface-Tethered Bottlebrushes. *Langmuir* **2011**, *27*, 14151–14159.

[39] Morsch, S.; Wood, T. J. Schofield, W. C. E.; Badyal, J. P. S. A Combined Plasmachemical and Emulsion Templating Approach for Actuated Macroporous Scaffolds. *Adv. Funct. Mater.* **2012**, *22*, 313–322.

[40] Lin-Vien, D.; Colthup, N. B.; Fateley, W. G.; Grasselli, J. G. The Handbook of Infrared and Raman Characteristic Frequencies of Organic Molecules; Academic Press, Inc., San Diego, 1991.

[41] Han, L. M.; Timmons, R. B.; Bogdal, D.; Pielichowski, J. Ring Retention via Pulsed Plasma Polymerization of Heterocyclic Aromatic Compounds. *Chem. Mater.* **1998**, *10*, 1422–1429.

[42] Cremer, T.; Kolbeck, C.; Lovelock, K. R. J.; Paape, N.; Wölfel, R.; Schulz, P. S.: Wasserscheid, P.; Weber, H.; Thar, J.; Kirchner, B.; Maier, F.; Steinrück, H.-P. Towards a Molecular Understanding of Cation–Anion Interactions—Probing the Electronic Structure of Imidazolium Ionic Liquids by NMR Spectroscopy, X-ray Photoelectron Spectroscopy and Theoretical Calculations. *Chem. - Eur. J.* **2010**, *16*, 9018–9033.

[43] Luo, X. F.; Goh, S. H.; Lee, S. Y.; Huan, C. H. A. Spectroscopic Studies of Interactions in Complexes of Poly(1-Vinylimidazole) with Poly(Styrenesulfonic Acid) or the Zinc Salt of Poly(Styrenesulfonate). *Macromol*. *Chem. Phys.* **1999**, *200*, 874–880.

[44] Wood, T. J.; Schofield, W. C. E.; Lund, P.; Larsen, M. J.; Badyal, J. P. S. Highly Ion-Conducting Poly(Ionic Liquid) Layers. *Chem. Commun*. **2012**, *48*, 10201–10203.

[45] Akhavan, B.; Jarvis, K.; Majewski, P. Plasma Polymer-Functionalized Silica Particles for Heavy Metals Removal. *ACS Appl. Mater. Interfaces* **2015**, *7*, 4265–4274.

[46] Teare, D. O. H.; Schofield, W. C. E.; Garrod, R. P.; Badyal, J. P. S. Rapid Polymer Brush Growth by TEMPO-Mediated Controlled Free-Radical Polymerization From Swollen Plasma Deposited Poly(Maleic Anhydride) Initiator Surfaces. *Langmuir* **2005**, *21*, 10818–10824.

[47] Moulder, J. F.; Stickle, W. F.; Sobol, P. E.; Bomden, K. D. In Handbook of X-ray Photoelectron Spectroscopy; Chastain, J., Eds.; Perkin-Elmer Corporation: Minnesota, 1992.

[48] Noack, K.; Schulz, P. S.; Paape, N.; Kiefer, J.; Wasserscheid, P.; Leipertz, A. The Role of the C2 Position in Interionic Interactions of Imidazolium Based Ionic Liquids: A Vibrational and NMR Spectroscopic Study. *Phys. Chem. Chem. Phys*. **2010**, *12*, 14153–14161.

[49] Maier, F.; Gottfried, J. M.; Rossa, J.; Gerhard, D.; Schulz, P. S.; Schwieger, W.; Wasserscheid, P.; Steinrück, H.-P. Surface Enrichment and Depletion Effects of Ions Dissolved in an Ionic Liquid: An X-ray Photoelectron Spectroscopy Study. *Angew. Chem., Int. Ed.* **2006**, *45*, 7778–7780.

[50] Badyal, J. P. S. Beyond the Surface. *Chem. Br.* **2001**, *37*, 45–46.

[51] Scheuermann, G. M.; Rumi, L.; Steurer, P.; Bannwarth, W.; Mülhaupt, R. Palladium Nanoparticles on Graphite Oxide and Its Functionalized Graphene Derivatives as Highly Active Catalysts for the Suzuki-Miyaura Coupling Reaction. *J. Am. Chem. Soc.* **2009**, *131*, 8262–8270.

[52] Okumura, K.; Tomiyama, T.; Okuda, S.; Yoshida, H.; Niwa, M. Origin of the Excellent Catalytic Activity of Pd Loaded on Ultra-Stable Y Zeolites in Suzuki-Miyaura Reaction. *J. Catal.* **2010**, *273*, 156–166.

[53] Beller, M.; Fischer, H.; Herrmann, W. A.; Öfele, K.; Brossmer, C. Palladacycles as Efficient Catalysts for Aryl Coupling Reactions. *Angew. Chem., Int. Ed.* **1995**, *34*, 1848–1849.

[54] Feuerstein, M.; Laurenti, D.; Bougeant, C.; Doucet, H.; Santelli, M. Palladium–Tetraphosphine Catalysed Cross Coupling of Aryl Bromides with Arylboronic Acids: Remarkable Influence of the Nature of the Ligand. *Chem. Commun.* **2001**, *4*, 325–326.

[55] Choudary, B. M.; Madhi, S.; Chowdari, N. S.; Kantam, M. L.; Sreedhar, B. Layered Double Hydroxide Supported Nanopalladium Catalyst for Heck-, Suzuki-, Sonogashira-, and Stille-Type Coupling Reactions of Chloroarenes. *J. Am. Chem. Soc.* **2002**, *124*, 14127–14136.

[56] Frindy, S.; Primo, A.; Lahcini, M.; Bousmina M.; Garcia, H.; El Kadib, A. Pd Embedded in Chitosan Microspheres as Tunable Soft-Materials for Sonogashira Cross-Coupling in Water–Ethanol Mixture. *Green Chem.* **2015**, *17*, 1893–1898.

[57] Hagiwara, H.; Sugawara, Y.; Isobe, K.; Hoshi, T.; Suzuki, T. Immobilization of Pd(OAc)2 in Ionic Liquid on Silica: Application to Sustainable Mizoroki−Heck Reaction. *Org. Lett*. **2004**, *6*, 2325–2328.

[58] Shiflett, M. B.; Niehaus, A. M. S.; Yokozeki, A. Liquid-Liquid Equilibria in Binary Mixtures Containing Chlorobenzene, Bromobenzene, and Iodobenzene with Ionic Liquid 1-Ethyl-3-methylimidazolim Bis(trifluoromethylsulfonyl)imide. *J. Chem. Eng. Data* **2009**, *54*, 2090–2094.

[59] Huddleston, J. G.; Willauer, H. D.; Swatloski, R. P.; Visser, A. E.; Rogers, R. D. Room Temperature Ionic Liquids as Novel Media for 'Clean' Liquid–Liquid Extraction. *Chem. Commun.* **1998**, *16*, 1765–1766.

[60] Singh, R.; Sharma, M.; Mamgain, R.; Rawat, D. S. Ionic Liquids: A Versatile Medium for Palladium-Catalyzed Reactions. *J. Braz. Chem. Soc.* **2008**, *19*, 357–379.

[61] Najdanovic-Visak, V.; Esperanc¸ J. M. S. S.; Rebelo, L. P. N.; da Ponte, M. N.; Guedes, H. J. R.; Seddon, K. R.; de Sousa, H. C.; Szydlowski, J. Pressure, Isotope, and Water Co-Solvent Effects in Liquid-Liquid Equilibria of (Ionic Liquid + Alcohol) Systems. *J. Phys. Chem. B* **2003**, *107*, 12797-12807.

[62] Polymer Source Inc. www.polymersource.com/Resources/Solubility.pdf (accessed May 29, 2017).

[63] Alfa Aesar, Thermo Fisher Scientific. www.alfa.com/en/content/msds/english/43067.pdf (accessed May 29, 2017).

[64] Vázquez, G.; Alvarez, E.; Navaza, J. M. Surface Tension of Alcohol + Water from 20 to 50 ºC. *J. Chem. Eng. Data* **1995**, *40*, 611–614.

[65] Chen, J. -R.; Wakida, T. Studies on the Surface Free Energy and Surface Structure of PTFE Film Treated with Low Temperature Plasma. *J. Appl. Polym. Sci.* **1997**, *63*, 1733–1739.

Chapter 5 Substrate Independent Epitaxial Growth of a Metal-Organic Framework

5.1 Introduction

In Chapter 3, pulsed plasma deposited poly(1-allylimidazole) was demonstrated to provide imidazole moieties that could bind palladium to form a catalytic functional surface. In this chapter, it is applied to CO_2 sequestration for reduction in the environmental impact of industrial processes.

Reticular synthesis of metal-organic frameworks (MOFs) entails the coordination bonding of metal ion to organic ligand building blocks via self-assembly leading to the formation of one-, two-, or three-dimensional structures. Some of these can be highly porous (several 1,000s $m^2\ g^{-1}$), and they have been developed for a variety of applications including hydrogen storage,[1] gas and liquid separations,[2,3] catalysis,[4,5] and supercapacitors[6]. The wide range of organic linkers and metal cations available allows for the fine tuning of pore sizes,[7,8] and chemical reactivity.[9] To this end, MOFs have been found to be promising candidates for CO_2 gas capture materials due to their pore size selective adsorption combined with high internal surface areas.[10]

However, MOFs are mainly synthesised as particulate bulk materials, which can be difficult to handle or incorporate into specific device architectures. An alternative strategy is to grow MOFs directly onto a solid surface using liquid phase epitaxy (layer-by-layer). Previously, such surface-grown MOFs have been limited to specific substrate materials, including: metals,[11,12,13,14] metal oxides,[14,15,16,17,18,19] self-assembled monolayers (SAMs),[20,21,22,23,24] and organic polymers.[25,26,27,28,29] The major drawback for each of these systems is that in each case the deposition technique needs to be tailored for the chosen substrate. Langmuir-Blodgett deposition of pre-synthesised MOF particles directly onto substrates has also been explored for CO_2 capture, but this approach lacks robustness due to the absence of any direct chemical coordination between the deposited MOF particles and the underlying substrate material.[30]

A particularly interesting MOF is [Zn (benzene-1,4-dicarboxylate)-(4,4'-bipyridine)$_{0.5}$] (MOF-508) which is reported to display high levels of CO_2 capture and separation of linear alkanes.[31,32] Its bulk form can be solvothermally synthesised by reacting benzene-1,4-dicarboxylic acid (terephthalic acid), 4,4'-bipyridine, and zinc nitrate

in an organic solvent such as dimethylformamide at elevated temperatures (363 K).[31] The product MOF crystallites are built of zinc-terephthalate primitive square frameworks, separated by 4,4'-bipyridine pillars, Scheme 5.1. In its bulk form, the MOF framework is interpenetrated with a second identical framework (catenation) leading to a reduced pore size (4.0 Å diameter) and forming one of two polymorphs, MOF-508a and MOF-508b (which are the solvent inclusive and solvent free materials respectively).[31,32,33] Such a reduction in MOF network pore size improves CO_2 adsorption due to greater interactions with the MOF channel walls.[34]

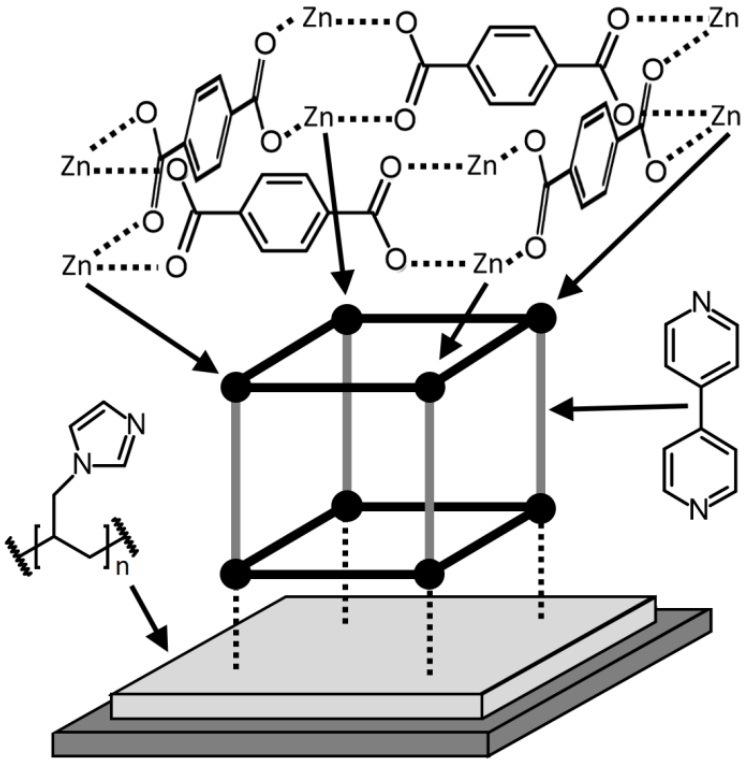

Scheme 5.1: Layer-by-layer growth of MOF-508 onto pulsed plasma deposited poly(1-allylimidazole) linker layer.

Self-assembled monolayer liquid phase epitaxy of MOF-508 growth onto gold substrates is reported to give rise to the loss of MOF framework interpenetration leading to only the large pores (reduced CO_2 capture efficiency as well as higher water contamination in humid environments).[20,33] In this chapter, a methodology for the surface growth of MOF-508 materials by liquid phase epitaxy is described, which leads to the formation of an interpenetrated MOF-508 network with reduced pore size (akin to MOF-

508a as evidenced by X-ray diffraction and infrared spectroscopy), and therefore better suited to CO_2 capture and stability towards humidity. This comprises pulsed plasma deposition of a poly(1-allylimidazole) layer onto either quartz crystal microbalance (QCM) discs or PTFE membranes to generate surface linker imidazole groups, followed by liquid phase epitaxial growth of MOF-508 using zinc acetate as the metal ion source in association with terephthalic acid and 4,4'-bipyridine as secondary building units, Scheme 5.1. The MOF-508 layers grown by liquid phase epitaxy onto pulsed plasma deposited poly(1-allylimidazole) functionalised materials in this chapter have been tested for CO_2 capture in both pure CO_2 atmospheres and diluted to atmospheric concentrations.

5.2 Experimental Section

5.2.1 Pulsed Plasma Deposition of Poly(1-Allylimidazole) Linker Layer

A cylindrical glass reactor (5.5 cm diameter, 475 cm^3 volume) housed within a Faraday cage was used for plasmachemical deposition. This was connected to a 30 L min^{-1} rotary pump (E2M2, Edwards Vacuum Ltd.) via a liquid nitrogen cold trap (base pressure less than 1.5 x 10^{-3} Torr and air leak rate better than 6 x 10^{-9} mol s^{-1}).[35] A copper coil wound around the reactor (4 mm diameter, 10 turns, located 10 cm downstream from the gas inlet) was connected to a 13.56 MHz radio frequency (RF) power supply via an L-C matching network. A signal generator (model TG503, Thurlby Thandar Instruments Ltd.) was used to trigger the RF power supply. Prior to film deposition, the whole apparatus was thoroughly scrubbed using detergent and hot water, rinsed with propan-2-ol (+99.5 wt%, Fisher Scientific UK Ltd.), oven dried at 423 K, and further cleaned using a 50 W continuous wave air plasma at 0.15 Torr pressure for 30 min.

Quartz crystal microbalance disk (14 mm diameter, gold coated, INFICON GmbH) and silicon substrate (Silicon Valley Microelectronics Inc.) preparation comprised successive sonication in propan-2-ol and cyclohexane (+99.7 wt%, Sigma-Aldrich Co.) for 15 min before insertion into the centre of the chamber. Further cleaning entailed running a 50 W continuous wave air plasma at 0.15 Torr pressure for 15 min followed by plasmachemical film deposition. PTFE membrane (180 ± 10 μm thickness, 5 ± 2 μm surface pore size determined by SEM, Mupor Ltd.) was used as a flexible substrate.

A layer of tetramethylsilane plasma polymer was deposited first in order to provide an organosilicon network for good adhesion to the substrate of the pulsed plasma

deposited poly(1-allylimidazole) film.[36] Tetramethylsilane precursor (99.9 wt%, Alfa Aesar, Thermo Fisher Scientific Inc.) was loaded into a sealable glass tube, degassed via several freeze-pump-thaw cycles, and then attached to the reactor. This was followed by purging the chamber with tetramethylsilane vapour at a pressure of 0.15 Torr for 15 min prior to electrical discharge ignition. Plasma deposition was performed in continuous wave mode using a RF generator power output of 3 W for 120 s. Upon plasma extinction, the tetramethylsilane vapour was allowed to continue to pass through the system for a further 15 min, and then the chamber was evacuated to base pressure followed by venting to atmosphere.

The tetramethylsilane plasma polymer coated substrates were then inserted into a cleaned chamber for pulsed plasma polymer deposition of the MOF linker layer. 1-allylimidazole (+97 wt%, Acros Organics B.V.B.A.) precursor was loaded into a sealable glass tube, degassed via several freeze-pump-thaw cycles, and then attached to the reactor. Precursor vapour was then allowed to purge the apparatus at a pressure of 0.11 Torr for 15 min prior to electrical discharge ignition. Pulsed plasma deposition was performed using a duty cycle on-period (t_{on}) of 20 µs and a duty cycle off-period (t_{off}) of 1200 µs in conjunction with a RF generator power output (P_{on}) of 30 W for 15 min (thicker films were deposited for 1 h in order to match infrared spectroscopy RAIRS sampling depth).[37] Upon plasma extinction, the precursor vapour was allowed to continue to pass through the system for a further 15 min, and then the chamber was evacuated to base pressure followed by venting to atmosphere.

5.2.2 Growth of MOF-508 Layers

MOF-508 growth onto pulsed plasma deposited poly(1-allylimidazole) coated substrates was carried out by liquid phase epitaxy.[20,38] A 1.0 mM zinc acetate (99.99 wt%, Sigma-Aldrich Co.) in tetrahydrofuran (99.8 wt%, Fisher Scientific UK Ltd.) solution was sonicated for 30 min prior to use. A second solution comprising 0.2 mM terephthalic acid (97 wt%, Sigma-Aldrich Co.) and 0.2 mM 4,4'-bipyridine (98 wt%, Sigma-Aldrich Co.) in tetrahydrofuran was also sonicated for 30 min prior to use. The coated substrates were first immersed into the zinc acetate solution for 5 min, then rinsed in fresh tetrahydrofuran for 10 s and dried in air for 1 min (PTFE substrates used a 2 min drying period). Once dry, the coated substrates were immersed into the terephthalic acid-4,4'-bipyridine solution for 5 min, followed by rinsing in fresh tetrahydrofuran for 10 s and drying in air. This is

designated as one complete liquid phase epitaxy cycle and corresponds to one layer of MOF; the cycle was repeated multiple times to build up the required number of layers. This procedure led to solvent incorporation to give MOF-508a (as determined by X-ray diffraction). Activation of this material (solvent removal) was achieved by employing a low boiling point solvent (tetrahydrofuran) during the MOF synthesis, which readily desorbs out of the MOF lattice under vacuum to leave behind open cavities available for CO_2 capture.[39]

5.2.3 Film Characterisation

Infrared spectra were acquired using a FTIR spectrometer (Spectrum One, Perkin-Elmer Inc.) fitted with a liquid nitrogen cooled MCT detector operating at 4 cm^{-1} resolution across the 400–4000 cm^{-1} range. For reflection-absorption infrared (RAIRS) spectra of pulsed plasma deposited poly(1-allylimidazole) and grown MOF layers, the instrument included a variable angle reflection-absorption accessory (Specac Ltd.) set to a grazing angle of 66° for silicon wafer substrates and adjusted for p-polarization. Attenuated total reflectance (ATR) infrared spectra of 1-allylimidazole liquid precursor were obtained using a Golden Gate accessory (Specac Ltd.)

Surface elemental compositions were measured by X-ray photoelectron spectroscopy (XPS) using a VG ESCALAB II electron spectrometer equipped with a non-monochromated Mg $K\alpha_{1,2}$ X-ray source (1253.6 eV) and a concentric hemispherical analyser. Photoemitted electrons were collected at a take-off angle of 20° from the substrate normal, with electron detection in the constant analyser energy mode (CAE, pass energies of 20 and 50 eV for high resolution and survey spectra respectively). Experimentally determined instrument sensitivity factors were C(1s) : O(1s) : N(1s) equals 1.00 : 0.35 : 0.70 respectively. The core level binding energy envelopes were fitted using Gaussian peak shapes with fixed full-width-half-maxima and linear backgrounds.[40,41] All binding energy values are referenced to the C(1s) $-\underline{C}_xH_y$ hydrocarbon peak at 285.0 eV.[42]

X-ray diffractograms were acquired across 5°–80° 2θ range using 0.02° step size with a powder diffractometer (model d8, Bruker Corp.). The copper anode X-ray source (Cu Kα 1.5418 Å wavelength radiation) was operated at 40 kV and 40 mA.

Scanning electron microscopy (SEM) analysis was undertaken using secondary electron detection mode, in conjunction with 25 kV accelerating voltage (model VEGA3 LMU SEM, Tescan Orsay Holding, a.s.).

5.2.4 CO_2 Capture

CO_2 adsorption onto coated quartz crystal microbalance substrates (Front Load Single Sensor, INFICON GmbH) housed inside a glass chamber was carried out at 293 K. The sensor was connected to a thin film deposition monitor (model XTM/2, INFICON GmbH). Each coated quartz crystal microbalance disc was loaded into the chamber and evacuated at 4 x 10^{-2} Torr for 24 h at 293 K leading to the desorption of entrapped MOF-508a lattice solvent molecules.[39] CO_2 gas (99.995 vol%, BOC Ltd.) was introduced to the system at 0.2 Torr pressure, followed by dry 80 : 20 O_2 (99.5 vol%, BOC Ltd.) : N_2 (99.998 vol%, BOC Ltd.) gas mixture (<60 ppm H_2O, Series 3 moisture monitor, GE Panametrics Ltd.) to make up to 760 Torr. Adsorbed CO_2 gas mass readings were taken at set intervals over a 456 h period and normalised to the flat area of the quartz crystal microbalance disc (1.54 cm^2). Control experiments using 760 Torr of dry oxygen-nitrogen gas mix (no CO_2) showed no mass change.

Volumetric CO_2 gas adsorption for flexible PTFE supported MOF layers was carried out in a sorptometer (model BET-201, Porous Materials Inc.). Samples were loaded into a glass tube of known volume and degassed at <1 x 10^{-2} Torr for 24 h to remove any adsorbed moisture. CO_2 gas was introduced into a calibrated volume at 1000 ± 2 Torr at 293 K, followed by equilibration with the sample chamber to provide an initial CO_2 pressure over the sample of 720 ± 2 Torr. Pressure readings were taken at fixed intervals over a period of 480 h in order to follow the pressure drop as a function of time. The number of moles of adsorbed gas was calculated from the pressure drop in the system (for which the volume is known), then converted to mass of adsorbed CO_2 gas, and normalised to the size of the flat area of the PTFE membrane (40.5 cm^2). The sample volume was calculated by gas pycnometry using N_2 gas and was subtracted from the sample cell volume for CO_2 adsorption experiments.

5.3 Results

5.3.1 Pulsed Plasma Deposition of Poly(1-allylimidazole) Linker Layer

Infrared spectroscopy of pulsed plasma deposited poly(1-allylimidazole) films confirmed a high level of precursor imidazole functional group structural retention,[37] Figure 5.1. Characteristic imidazole ring absorbances include: C=C–H ring stretch (3107 cm^{-1}), C=N

ring stretch (1504 cm^{-1}), and N=C–H ring in-plane bend (1107 cm^{-1}) vibrations.[43] Disappearance of the monoalkyl vinyl $=CH_2$ wag vibration mode (906 cm^{-1}) associated with the 1-allylimidazole precursor molecule confirmed selective polymerisation of the vinyl group during pulsed plasma deposition.[44] Absorbance bands visible in the 1560–1700 cm^{-1} spectral range can be attributed to a small amount of electrical discharge fragmented imidazole group C=N stretches,[45] and carbonyl stretches belonging to adducts formed through atmospheric carbon dioxide adsorption following exposure to air of the deposited film.[46,47]

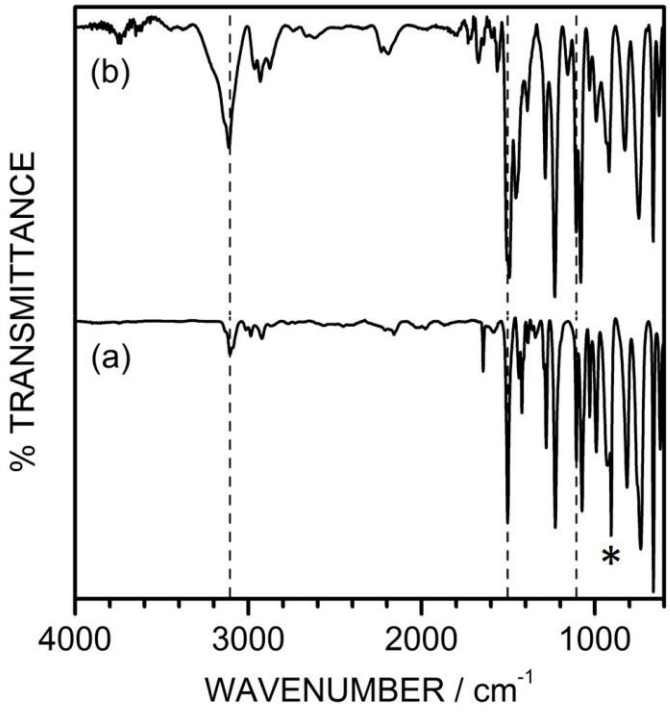

Figure 5.1: Infrared spectroscopy: (a) ATR of liquid 1-allylimidazole precursor; and (b) RAIRS of pulsed plasma poly(1-allylimidazole) deposited onto silicon wafer. * Denotes monoalkyl vinyl $=CH_2$ wag vibration at 906 cm^{-1} in 1-allylimidazole precursor. Dashed lines denote characteristic imidazole ring absorbances at 3107 cm^{-1}, 1504 cm^{-1} and 1107 cm^{-1}. Overall relative intensity differences between the two spectra are due to the use of ATR versus RAIRS infrared spectroscopic techniques.[48]

XPS analysis of pulsed plasma poly(1-allylimidazole) deposited onto silicon wafer detected only carbon, nitrogen, and low levels of oxygen (attributed to a small amount of water adsorption and adducts formed through carbon dioxide adsorption upon air

exposure[45,46]). The N(1s) binding envelope could be fitted to two different nitrogen environments at 398.7 eV and 400.5 eV corresponding to the imidazole ring C=N and C-N nitrogen centres respectively,[49] Figure 5.2. Their slight deviation in relative concentrations away from the expected theoretical 1 : 1 peak area ratio for the imidazole ring structure stems from a low level of precursor fragmentation occurring within the electrical discharge.[45]

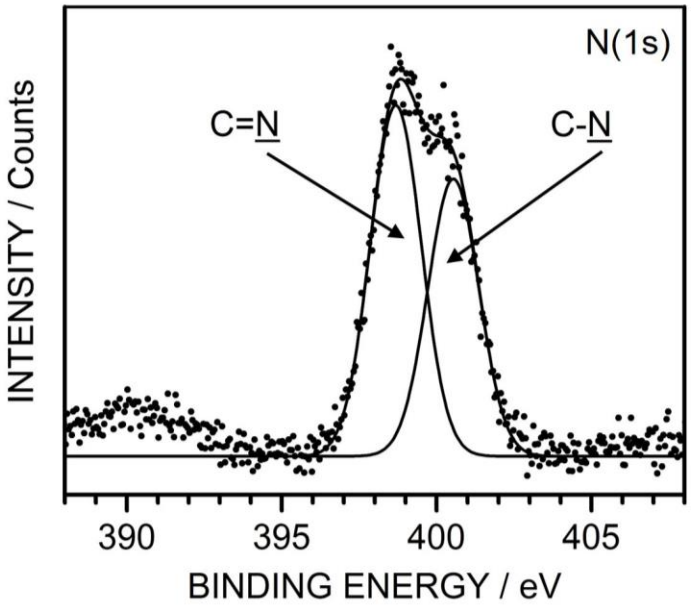

Figure 5.2: N(1s) XPS spectrum of pulsed plasma poly(1-allylimidazole) deposited onto silicon wafer.

5.3.2 Growth of MOF-508 Layers

The infrared spectrum of 200 layer MOF-508 grown by liquid phase epitaxy onto pulsed plasma poly(1-allylimidazole) coated silicon wafer contains two strong, broad absorbances between 1400–1700 cm^{-1}, which can be respectively attributed to the overlapping terephthalate $C\text{-}O^-$ deformation vibration (slightly shifted to lower wavenumbers from 1406 cm^{-1} in terephthalic acid for C-OH due to proton loss[50,51]) and carbonyl stretch vibration (the terephthalic acid 1673 cm^{-1} feature is shifted to 1670 cm^{-1} due to metal coordination[50,52]), Table 5.1 and Figure 5.3. Also, there are the 4,4'-bipyridine ring quadrant vibration (1593 cm^{-1} shifted to higher wavenumbers due to coordination relative to 1585 cm^{-1} for 4,4'-bipyridine[53,54]) and the 4,4'-bipyridine semicircle

stretch vibration (1408 cm^{-1})[53]. These infrared spectral features are consistent with the incorporation of both terephthalate and 4,4'-bipyridine organic linkers during the layered growth of MOF-508, Scheme 5.1. Additional lower intensity vibrations include C-O^- deformation mode (shifted to 1250 cm^{-1} compared to 1276 cm^{-1} for C-OH in terephthalic acid due to proton loss[50,51]), substituted benzene C-H deformation mode (1134 cm^{-1}) for the constituent terephthalate linker, and pyridine sextant out-of-plane bend vibration (748 cm^{-1}) for the constituent 4,4'-bipyridine linker unit.[50,53] The low intensity peak at 1017 cm^{-1} can be assigned to the antisymmetric C-O-C valence vibration of lattice incorporated tetrahydrofuran solvent molecules which is consistent with the formation of solvent-inclusive MOF-508a polymorph.[55]

Table 5.1: Infrared spectral assignments of MOF-508 constituent building units and 200 layer MOF-508 grown onto pulsed plasma deposited poly(1-allylimidazole).

Assignment	**Absorbance / cm^{-1}**			
	Zinc Acetate	**Terephthalic Acid**	**4,4'-Bipyridine**	**200 Layers of MOF-508**
Carbonyl symmetric stretch[56]	1443	-	-	~1430
Carbonyl asymmetric stretch[56]	1531	-	-	~1530
Substituted benzene C-H deformation[50]		1138		1134
Carboxylic acid C-OH / [C-O^-] deformation[50,51]	-	1276	-	[1250]
Carboxylic acid C-OH / [C-O^-] deformation[50,51]	-	1406	-	[~1400]
Carboxylic acid carbonyl stretch[50]	-	1673	-	~1670
Pyridine sextant out-of-plane bend[53]	-	-	734	748
Pyridine semicircle stretch[53]	-	-	1402	1408
Pyridine quadrant stretch[53,54]	-	-	1585	1593
Tetrahydrofuran solvent antisymmetric C-O-C vibration[55]				1017

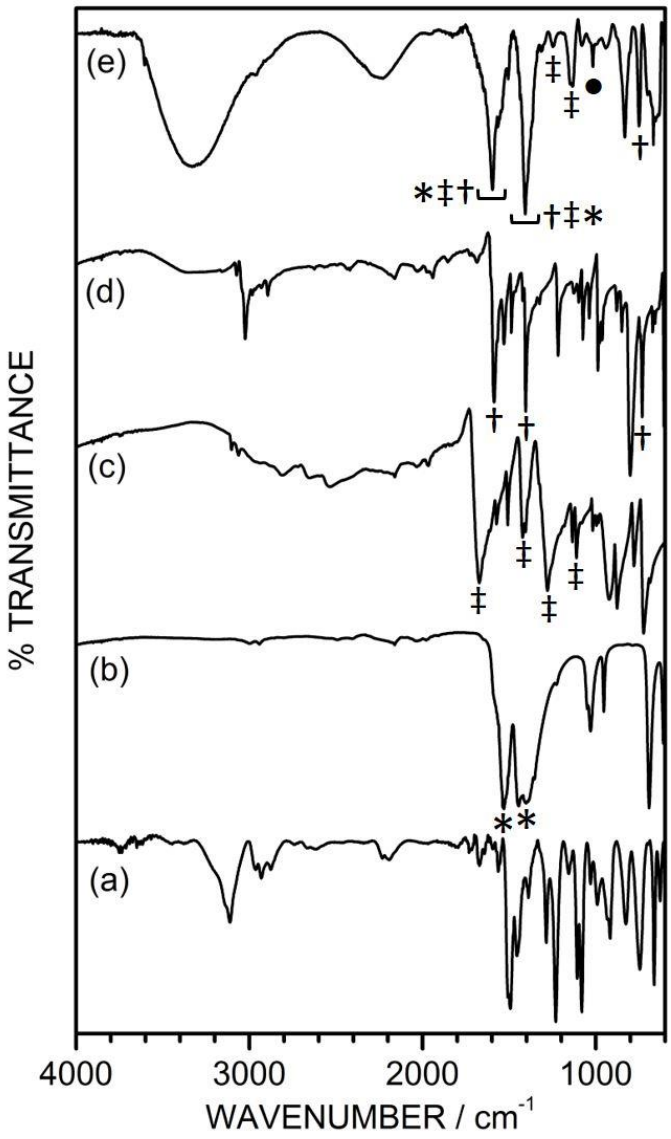

Figure 5.3: Infrared spectroscopy: (a) RAIRS of pulsed plasma poly(1-allylimidazole) deposited onto silicon wafer; (b) ATR of zinc acetate; (c) ATR of terephthalic acid; (d) ATR 4,4'-bipyridine; and (e) RAIRS of 200 layer MOF-508 grown onto pulsed plasma poly(1-allylimidazole) deposited onto silicon wafer. Fingerprint peaks: (*) zinc acetate; (‡) terephthalic acid; (†) 4,4'-bipyridine, and (•) tetrahydrofuran.

Powder X-ray diffractograms of 200 layer MOF-508 grown onto pulsed plasma poly(1-allylimidazole) coated silicon wafer showed two prominent peaks at low detector angles, which are consistent with an orientated large lattice constant material, Figure 5.4. These diffraction peaks at 6.3º and 12.5º are assigned to the (001) and (002) planes of the solvent-inclusive MOF (MOF-508a), with calculated lattice spacings of 14.0 Å and 7.1 Å respectively.[20,31] A lack of strong intensities for the (100) and (010) MOF-508a diffraction peaks indicates that the majority of the MOF crystallites have been templated (orientated) by the pulsed plasma deposited poly(1-allylimidazole) surface. Greater intensity of the (001) peak compared to the (002) peak supports an interpenetrated network of MOF-508a, which is caused by the incorporation of a second lattice.[20,57,58] This should be contrasted against non-interpenetrated MOF-508, which is reported to show the reverse (001) to (002) peak intensity ratio due to the absence of destructive interference effects.[20] Lower intensity 2θ peak values between 8º and 10º are attributable to a small amount of solvent-free MOF-508b and non-orientated solvent-inclusive MOF-508a.[20]

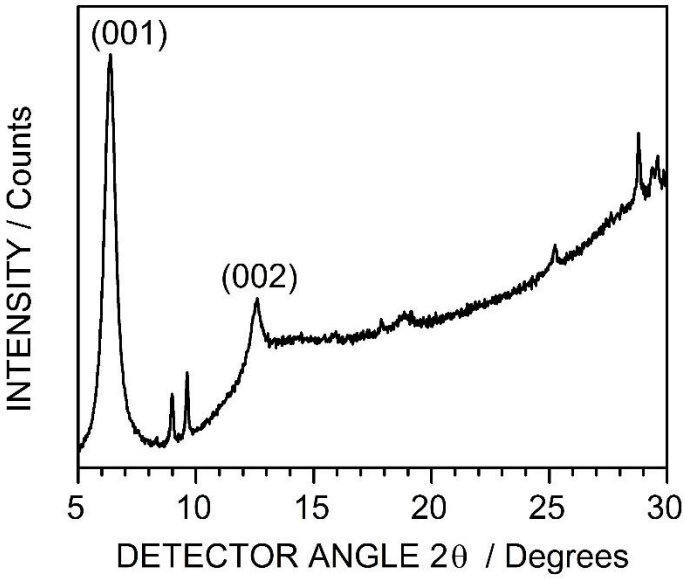

Figure 5.4: XRD of 200 layer MOF-508 grown onto pulsed plasma poly(1-allylimidazole) coated silicon wafer, collected by grazing incident XRD of the coated substrate. Peaks at 6.3º and 12.5º correspond to the (001) and (002) planes, as observed in the powder XRD of the free MOF. [XRD data collected by G. Oswald]

Scanning electron micrographs following 20 and 200 layer growth of MOF-508 onto pulsed plasma poly(1-allylimidazole) coated silicon wafer showed the presence of

individual crystallites on the surface, Figure 5.5. Upon reaching 200 layers of MOF-508 growth, a clear crystallite morphology is visible which is consistent with the bulk MOF-508 triclinic unit cell.[31] This confirms that imidazole linker group functionalised substrate surface provides seeding sites for the layer-by-layer growth of MOF-508 crystallites.

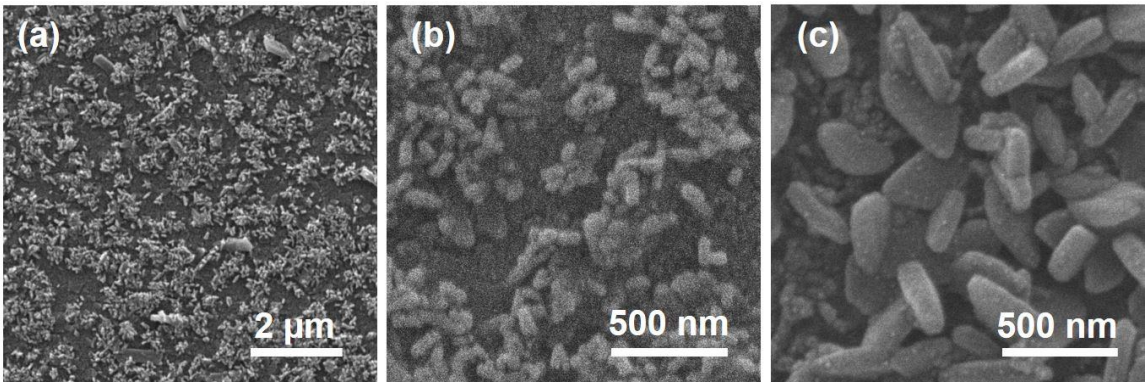

Figure 5.5: SEM micrographs of MOF-508 crystallite growth onto pulsed plasma poly(1-allylimidazole) coated silicon wafer substrate: (a–b) 20 layers; and (c) 200 layers.

5.3.3 CO_2 Gas Capture

MOF-508 layers grown onto pulsed plasma poly(1-allylimidazole) coated quartz crystal microbalance (QCM) discs were studied for CO_2 adsorption capacity at the equivalent of atmospheric CO_2 partial pressures (0.3 Torr CO_2 diluted in a 20:80 O_2:N_2 gas mixture to give 760 Torr total pressure)[59], Figure 5.6. Adsorption of CO_2 was rapid during the first 24 h, followed by a more gradual rise over the next 10 days. The overall capacity for CO_2 adsorption correlated to the number of MOF-508 layers grown, Figure 5.6. This is consistent with there being deposition of a single MOF-508 layer during each liquid phase epitaxial growth cycle. Saturation of gas adsorption was measured by using 760 Torr pressure of CO_2, and this showed that the maximum CO_2 adsorption capacity of the 20 layer MOF-508 was reached after 456 h, and this was only 10% greater than the amount of CO_2 adsorbed at 0.3 Torr CO_2 partial pressure (after 456 h), Figure 5.7. This relative insensitivity of CO_2 adsorption versus CO_2 partial pressure is consistent with earlier bulk MOF-508 studies,[31] and demonstrates the high affinity of the grown MOF-508 layers towards CO_2 gas capture across a wide range of partial pressures. Control experiments using pulsed plasma poly(1-allylimidazole) coated QCM discs showed a low level of CO_2 adsorption (due to adduct formation with imidazole centres),[46,47] Figure 5.6.

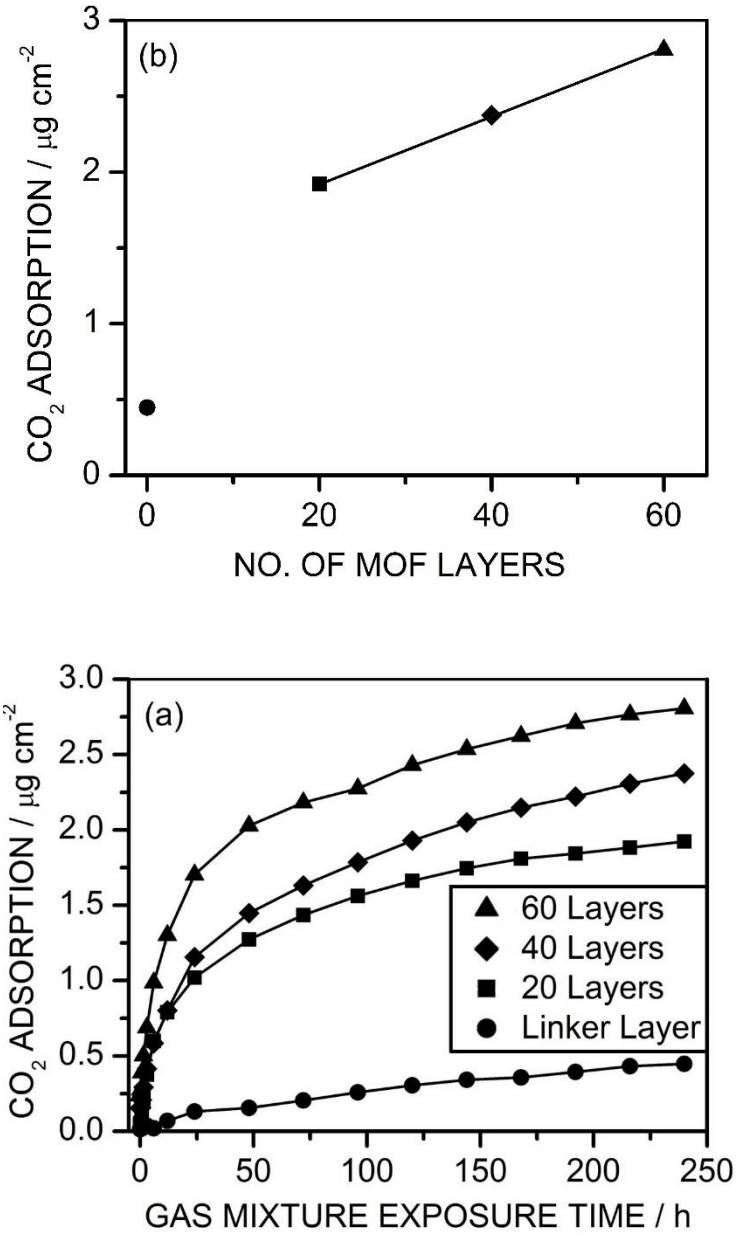

Figure 5.6: Quartz crystal microbalance CO_2 gas capture using 0.3 Torr partial pressure of CO_2 gas diluted in a 20:80 O_2:N_2 gas mixture to give 760 Torr total pressure as a function of: (a) gas mixture exposure time; and (b) number of MOF-508 layers grown onto pulsed plasma deposited poly(1-allylimidazole). Where cm^{-2} refers to the surface area of the quartz crystal monitor disk. [Linker layer sample prepared by S. N. Barrientos-Palomo, 20 layer epitaxial MOF growth conducted by P. C. Stevens, 40 and 60 layer epitaxial MOF growth conducted by N. L. Mitchell]

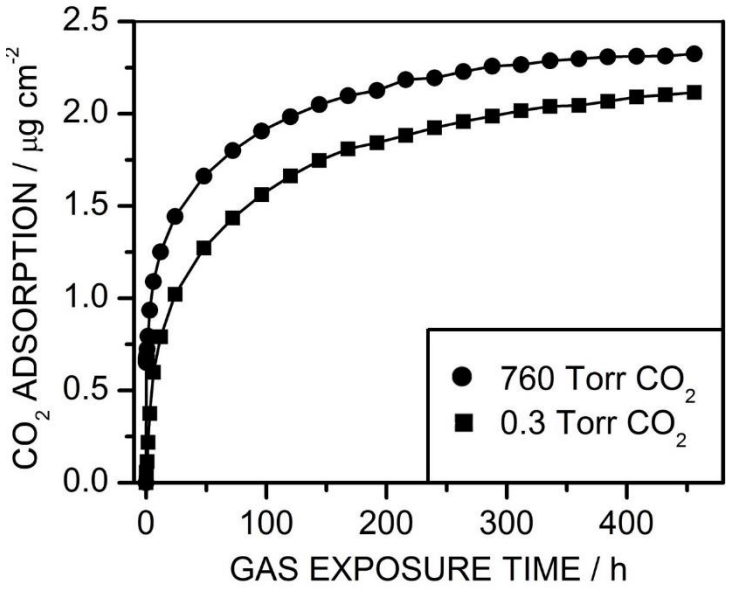

Figure 5.7: Quartz crystal microbalance CO_2 gas capture as a function of exposure time for 20 layer MOF-508 grown onto pulsed plasma deposited poly(1-allylimidazole) using: (■) 0.3 Torr partial pressure of CO_2 gas diluted in a 20:80 O_2:N_2 gas mixture to give 760 Torr total pressure; and (●) 760 Torr of CO_2 gas. [20 layer epitaxial MOF growth conducted by P. C. Stevens]

The practical viability of the described methodology for preparing CO_2 capture MOF materials supported on different types of substrate was demonstrated further by translating the developed methodology to flexible PTFE membrane films, Figure 5.8. PTFE supported 20 layer MOF-508 captured 148 μg cm^{-2} of CO_2 following 480 h of CO_2 gas exposure. The rate of CO_2 uptake over the first 12 h (starting from 2 min after the initial exposure) was 1.51 ± 0.10 μg cm^{-2} h^{-1} (which is significant given the ultrathin nature of the 20 layer MOF) compared to 0.51 ± 0.04 μg cm^{-2} h^{-1} for the uncoated PTFE membrane reference (no MOF or linker layer and just PTFE pore absorption[60]) — where cm^{-2} refers to the size of the piece of PTFE membrane substrate. Slower CO_2 gas adsorption was observed for these PTFE supported MOF-508 layers compared to their quartz crystal microbalance counterparts. This can be attributed to a combination of a lower starting pressure in the volumetric adsorption system (720 Torr compared to 760 Torr for QCM studies) in combination with a larger pressure drop over time due to the greater gas adsorption capacity of the PTFE membrane supported MOF-508 material, resulting in a longer period of time to reach equilibrium between $CO_{2(g)}$ versus $CO_{2(ads)}$,[61]

Figure 5.7 and Figure 5.8. The difference in adsorbed mass of CO_2 after 456 h between QCM and PTFE supported materials (2.1 μg cm^{-2} and 145 μg cm^{-2}, respectively) is due to the higher internal surface area of the porous PTFE membrane available for MOF crystallite growth.

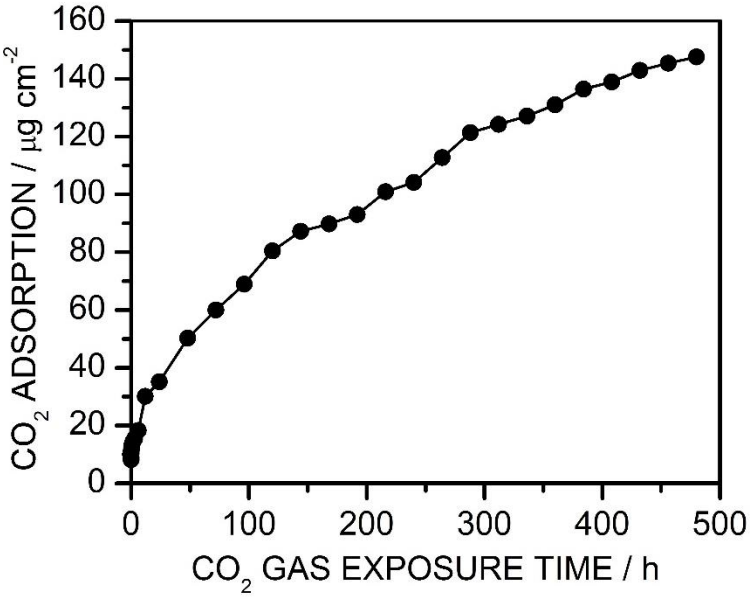

Figure 5.8: Mass of CO_2 gas adsorbed by 20 layer MOF-508 grown onto pulsed plasma deposited poly(1-allylimidazole) coated PTFE membrane in a sealed CO_2 atmosphere (initial pressure 720 Torr) as a function of exposure time (calculated from volumetric gas adsorption measurements). [Data collected in collaboration with S. N. Barrientos-Palomo]

5.4 Discussion

As discussed in Chapters 2, 3 and 5, pulsed plasmachemical functionalisation of solid surfaces using polymerisable functional precursors offers the advantage of substrate independent deposition and high levels of functional group retention,[62] making it well-suited for the deposition of functional groups onto both inorganic and organic substrates required for MOF templating. Infrared spectroscopy and XPS analyses have shown that there is a large degree of imidazole ring retention during pulsed plasma deposition of 1-allylimidazole precursor—which is a prerequisite for the epitaxial growth of MOF-508 layers, Figure 5.1 and Figure 5.2.

MOF-508a was found to grow selectively onto the pulsed plasma poly(1-allylimidazole) deposited layers, thereby confirming the substrate-independent nature of

the methodology. The crystallite morphology observed by SEM is consistent with other liquid phase epitaxial grown MOF layers (which display a Volmer–Weber island layer-by-layer growth mechanism[24]), Figure 5.5. This indicates that the surface energy of the crystal-solution interface is greater than that of the substrate-solution interface, which leads to the growth of three-dimensional islands on the surface (rather than Frank–van der Merwe uniform layer-by-layer growth across the whole substrate).[63]

In contrast to the previously reported growth of MOFs onto self-assembled monolayers (SAMs, which provide templating of non-interpenetrated MOF-508 lattice[20]), the pulsed plasma deposited layer approach gives rise to interpenetrated MOF-508 lattices (MOF-508a) providing added benefit of an appropriate pore size for selective CO_2 adsorption (4.0 Å diameter) and lack of water uptake from ambient humidity.[31,33,] Also, the Volmer–Weber island layer-by-layer growth mechanism provides relatively less compact packing of the MOF-508a crystallites (higher external surface area) providing guest CO_2 molecules greater access to MOF-508a crystallite pore openings from the (100) and (010) faces (which are blocked for both SAM-based close-packed unidirectional and perfect Frank–van der Merwe (001) layer-by-layer MOF film growth modes[64,65]). Such orientation specific gas adsorption behaviours have been documented for other MOF systems.[66]

Assuming complete coverage of an underlying flat substrate with a single unit cell thickness of interpenetrated MOF-508 layer during each epitaxial cycle, the maximum theoretical mass of MOF-508a grown onto the pulsed plasma deposited poly(1-allylimidazole) layer coated quartz crystal microbalance substrates is calculated to be 16.0 µg after 60 cycles (based on the MOF-508a unit cell dimensions measured by XRD and the QCM disc area). Using this value in conjunction with the experimental QCM CO_2 gas uptake measurements, the total amount of CO_2 captured per gram of MOF-508a is calculated to be 6 mmol g^{-1}—in fact, the incomplete layer-by-layer coverage of the substrate with MOF (due to Volmer–Weber island growth mechanism) means that this value is an underestimate. This CO_2 uptake value (6 mmol g^{-1}) is greater compared to previously reported surface supported CO_2 capture MOFs (1–4 mmol g^{-1}),[30,67] and is of the same order of magnitude as bulk MOF CO_2 capture materials (1–10 mmol g^{-1} at atmospheric pressure).[68] Furthermore, it appears to be on the same order of magnitude as theoretical maximum uptakes for other CO_2 sequestration technologies, such as alkali metal carbonates (9.4 mmol g^{-1})[69] and hyperbranched aminosilicas (5.5 mmol g^{-1}).[70] Based upon this saturated QCM CO_2 gas adsorption value of 6 mmol g^{-1}, the CO_2 : Zn(II)

ratio is calculated to be 2 : 1 for the MOF-508a film, with fast adsorption occurring up to 50% gas uptake attributable to the interaction of CO_2 with vacant Zn(II) lattice coordination sites.[71] Gas adsorption rate slows down beyond a CO_2 : Zn(II) stoichiometric ratio of 1:1, which is attributable to the participation of secondary weaker adsorption sites and CO_2-CO_2 interactions becoming dominant.[71]

The practical viability of the pulsed plasma deposited poly(1-allylimidazole) templated MOF-508a layers for CO_2 capture under atmospheric conditions (diluted CO_2 concentrations in O_2/N_2 carrier gas mixture) has been demonstrated by achieving gas uptake values close to those measured at the saturation adsorption limit for a pure CO_2 atmosphere, Figure 5.7. High affinity for the separation of CO_2 at atmospheric concentrations from air has been previously reported for sodium hydroxide,[72] zeolites,[73] and some bulk MOFs,[74] but not for surface-anchored MOFs. By combining the aforementioned CO_2 adsorption properties with a plasmachemical deposited flexible substrate linker layer, the described approach facilitates the application of MOF-508 to a wide variety of substrate materials and geometries (including membranes and fibres) and hence CO_2 capture applications (for example, carbon sequestration, industrial flue gas scrubbers, and recirculating breathing apparatus). This is something which is not easily feasible using other surface-templating methods such as self-assembled monolayers (SAMs), metals, and metal oxides due to their inherent substrate-specificities. Furthermore, apart from host–guest interactions, such growth of supported functional MOF layers could form the basis of physical or chemical responsive materials including phase transitions triggered by guest adsorption/desorption, or photochemical, thermal, and mechanical stimuli.[75]

5.5 Conclusions

Pulsed plasma deposited poly(1-allylimidazole) can be used for the substrate-independent epitaxial growth of microporous [Zn (benzene-1,4-dicarboxylate)-(4,4'-bipyridine)$_{0.5}$] (MOF-508) layers. Surface crystallite morphology is consistent with the Volmer–Weber island layer-by-layer epitaxial growth mechanism. High affinity for the separation of carbon dioxide at atmospheric concentrations in oxygen/nitrogen carrier gas mixtures is measured, and the total carbon dioxide capture capacity is found to correlate to the number of MOF-508 layers grown.

5.7 References

[1] Rosi, N. L.; Eckert, J.; Eddaoudi, M.; Vodak, D. T.; Kim, J.; O'Keeffe, M.; Yaghi, O. M. Hydrogen Storage in Microporous Metal-Organic Frameworks. *Science* **2003**, *300*, 1127–1129.

[2] Snurr, R. Q.; Hupp, J. T.; Nguyen, S. T. Prospects for Nanoporous Metal-Organic Materials in Advanced Separations Processes. *AICHE J*. **2004**, *50*, 1090–1095.

[3] Li, J.-R.; Sculley, J.; Zhou, H.-C. Metal-Organic Frameworks for Separations. *Chem. Rev*. **2012**, *112*, 869–932.

[4] Corma, A.; García, H.; Llabrés i Xamena, F. X. Engineering Metal Organic Frameworks for Heterogeneous Catalysis. *Chem. Rev*. **2010**, *110*, 4606–4655.

[5] Liu, J.; Chen, L.; Cui, H.; Zhang, J.; Zhang, Li.; Su, C.-Y. Applications of Metal–Organic Frameworks in Heterogeneous Supramolecular Catalysis. *Chem. Soc. Rev*. **2014**, *43*, 6011–6061.

[6] Sheberla, D.; Bachman, J. C.; Elias, J S..; Sun, C.-J.; Shao-Horn, Y.; Dincă, M. Conductive MOF Electrodes for Stable Supercapacitors with High Areal Capacitance. *Nat. Mater.* **2016**, *16*, 220−224.

[7] Du, L.; Lu, Z.; Zheng, K.; Wang, J.; Zheng, X.; Pan, Y.; You, X.; Bai, J. Fine-Tuning Pore Size by Shifting Coordination Sites of Ligands and Surface Polarization of Metal−Organic Frameworks To Sharply Enhance the Selectivity for CO_2. *J. Am. Chem. Soc.* **2013**, *135*, 562−565.

[8] Parkes, M. V.; Staiger, C. L.; Perry, J. L.; Allendorfc, M. D.; Greathouse, J. A. Screening Metal–Organic Frameworks for Selective Noble Gas Adsorption in Air: Effect of Pore Size and Framework Topology. *Phys. Chem. Chem. Phys*. **2013**, *15*, 9093–9106.

[9] Tanabe , K. K.; Cohen, S. M. Postsynthetic Modification of Metal–Organic Frameworks—a Progress Report. *Chem. Soc. Rev.* **2011**, *40*, 498–519.

[10] Li, J.-R.; Ma, Y.; McCarthy, M. C.; Sculley, J.; Yu, J.; Jeong, H.-K.; Balbuena, P. B.; Zhou, H.-C. Carbon Dioxide Capture-Related Gas Adsorption and Separation in Metal-Organic Frameworks. *Coord. Chem. Rev*. **2011**, *255*, 1791–1823.

[11] Wu, Y.-Y.; Yang, C.-X.; Yan, X.-P. Fabrication of Metal–Organic Framework MIL-88B Films on Stainless Steel Fibers for Solid-Phase Microextraction of Polychlorinated Biphenyls. *J. Chromatogr. A* **2014**, *1334*, 1–8.

[12] Zou, X.; Zhu, G.; Hewitt, I. L.; Sun F.; Qiu, S. Synthesis of a Metal–Organic Framework Film by Direct Conversion Technique for VOCs Sensing. *Dalton Trans*. **2009**, *16*, 3009–3013.

[13] Ameloot, R.; Pandey, L.; Van der Auweraer, M.; Alaerts, L.; Selsa, B. F.; De Vos, D. E. Patterned Film Growth of Metal-Organic Frameworks Based on Galvanic Displacement. *Chem. Commun*. **2010**, *46*, 3735–3737.

[14] Pan, C.; Nan, J.; Dong, X.; Ren, X.-M.; Jin, W. A Highly Thermally Stable Ferroelectric Metal-Organic Framework and Its Thin Film with Substrate Surface Nature Dependent Morphology. *J. Am. Chem. Soc*. **2011**, *133*, 12330–12333.

[15] Ahrenholtz, S. R.; Epley, C. C.; Morris, A. J. Solvothermal Preparation of an Electrocatalytic Metalloporphyrin MOF Thin Film and its Redox Hopping Charge-Transfer Mechanism*. J. Am. Chem. Soc*. **2014**, *136*, 2464−2472.

[16] Khaletskaya, K.; Turner, S.; Tu, M.; Wannapaiboon, S.; Schneemann, A.; Meyer, R.; Ludwig, A.; Van Tendeloo, G.; Fischer, R. A. Self-Directed Localization of ZIF-8 Thin Film Formation by Conversion of ZnO Nanolayers. *Adv. Funct. Mater*. **2014**, *24*, 4804–4811.

[17] Hashimoto, M.; Okajima, S.; Kondo, T.; Hara, K.; Chun, W.-J. Thin Film Structures of Metal-Organic Framework $[Cu_3(BTC)_2(H_2O)_3]_n$ on TiO_2(110). *Electrochemistry (Tokyo, Japan)* **2014**, *82*, 335–337.

[18] Abdollahian,Y.; Hauser, J. L.; Colinas, I. R.; Agustin, C.; Ichimura, A. S.; Oliver, S. R. J. IRMOF Thin Films Templated by Oriented Zinc Oxide Nanowires. *Cryst. Growth Des*. **2014**, *14*, 1506−1509.

[19] Yoo, Y.; Jeong, H.-K. Rapid Fabrication of Metal Organic Framework Thin Films Using Microwave-Induced Thermal Deposition*. Chem. Commun*. **2008**, *21*, 2441–2443.

[20] Shekhah, O.; Wang, H.; Paradinas, M.; Ocal, C.; Schüpbach, B.; Terfort, A.; Zacher, D.; Fischer, R. A.; Wöll, C. Controlling Interpenetration in Metal–Organic Frameworks by Liquid-Phase Epitaxy*. Nat. Mater.* **2009**, *8*, 481–484.

[21] Otsubo, K.; Haraguchi, T.; Sakata, O.; Fujiwara, A.; Kitagawa, H. Step-by-Step Fabrication of a Highly Oriented Crystalline Three-Dimensional Pillared-Layer-Type Metal−Organic Framework Thin Film Confirmed by Synchrotron X-ray Diffraction. *J. Am. Chem. Soc.* **2012**, *134*, 9605−9608.

[22] Hinterholzinger, F. M.; Wuttke, S.; Roy, P.; Preuße, T.; Schaate, A.; Behrens, P.; Godt, A.; Bein, T. Highly Oriented Surface-Growth and Covalent Dye Labelling of Mesoporous Metal–Organic Frameworks. *Dalton Trans.* **2012**, *41*, 3899–3901.

[23] Hanke, M.; Arslan, H. K.; Bauer, S.; Zybaylo, O.; Christophis, C.; Gliemann, H.; Rosenhahn, A.; Wöll, C. The Biocompatibility of Metal−Organic Framework Coatings: An Investigation on the Stability of SURMOFs with Regard to Water and Selected Cell Culture Media. *Langmuir* **2012**, *28*, 6877−6884.

[24] Ohnsorg, M. L.; Beaudoin, C. K.; Anderson, M. E. Fundamentals of MOF Thin Film Growth via Liquid-Phase Epitaxy: Investigating the Initiation of Deposition and the Influence of Temperature. *Langmuir* **2015**, *31*, 6114−6121.

[25] Mao, Y.; Li, J.; Cao, W.; Ying, Y.; Sun, L.; Peng, X. Pressure-Assisted Synthesis of HKUST-1 Thin Film on Polymer Hollow Fiber at Room Temperature toward Gas Separation. *ACS Appl. Mater. Interfaces* **2014**, *6*, 4473−4479.

[26] Lu, C.; Ben, T.; Xu, S.; Qiu, S. Electrochemical Synthesis of a Microporous Conductive Polymer Based on a Metal–Organic Framework Thin Film. *Angew. Chem. Int. Ed.* **2014**, *53*, 6454 –6458.

[27] Meilikhov M.; Yusenko, K.; Schollmeyer, E.; Mayer, C.; Buschmann, H-J.; Fischer, R. A. Stepwise Deposition of Metal Organic Frameworks on Flexible Synthetic Polymer Surfaces. *Dalton Trans.* **2011**, *40*, 4838–4841.

[28] Centrone, A.; Yang, Y.; Speakman, S.; Bromberg, L.; Rutledge, G. C.; Hatton, T. A. Growth of Metal-Organic Frameworks on Polymer Surfaces. *J. Am. Chem. Soc*. **2010**, *132*, 15687–15691.

[29] Zhou, M.; Li, J.; Zhang, M.; Wang, H.; Lan, Y.; Wu, Y.-N.; Li, F.; Li, G. A Polydopamine Layer as the Nucleation Center of MOF Deposition on ‘‘Inert’’ Polymer Surfaces to Fabricate Hierarchically Structured Porous Films. *Chem. Commun*. **2015***, 51*, 2706–2709.

[30] Benito, J.; Sorribas, S.; Lucas, I.; Coronas, J.; Gascon, I. Langmuir−Blodgett Films of the Metal−Organic Framework MIL-101(Cr): Preparation, Characterization, and CO_2 Adsorption Study Using a QCM-Based Setup. *ACS Appl. Mater. Interfaces* **2016**, *8*, 16486–16492.

[31] Chen, B.; Liang, C.; Yang, J.; Contreras, D. S.; Clancy, Y. L. Lobkovsky,E. B.; Yaghi, O. M.; Dai, S. A Microporous Metal–Organic Framework for Gas-Chromatographic Separation of Alkanes. *Angew. Chem. Int. Ed*. **2006**, *45*, 1390–1393.

[32] Bastin, L.; Bárcia, P. S.; Hurtado, E. J.; Silva, J. A. C.; Rodrigues, A. E.; Chen, B. A Microporous Metal-Organic Framework for Separation of CO_2/N_2 and CO_2/CH_4 by Fixed-Bed Adsorption. *J. Phys. Chem. C* **2008**, *112*, 1575–1581.

[33] Jasuja, H.; Walton, K. Effect of Catenation and Basicity of Pillared Ligands on the Water Stability of MOFs. *Dalton Transactions* **2013**, *42*, 15421–15426.

[34] Du, L.; Lu, Z.; Zheng, K.; Wang, J.; Zheng, X.; Pan, Yi.; You, X.; Bai, J. Fine-Tuning Pore Size by Shifting Coordination Sites of Ligands and Surface Polarization of Metal−Organic Frameworks to Sharply Enhance the Selectivity for CO_2. *J. Am. Chem. Soc.* **2013**, *135*, 562−565.

[35] Ehrlich, C. D.; Basford J. A. Recommended Practices for the Calibration and Use of Leaks. *J. Vac. Sci. Technol. A* **1992**, *10*, 1–17.

[36] Fonseca, J. L. C.; Apperley, D. C.; Badyal, J. P. S. Plasma Polymerization of Tetramethylsilane. *Chem. Mater.* **1993**, *5*, 1676–1682.

[37] Wood, T. J.; Schofield, W. C. E.; Lund, P.; Larsen, M. J.; Badyal, J. P. S. Highly Ion-Conducting Poly(Ionic Liquid) Layers. *Chem. Commun*. **2012**, *48*, 10201–10203.

[38] Scheel, H. J. Introduction to Liquid Phase Epitaxy. In *Liquid Phase Epitaxy of Electronic, Optical and Optoelectronic Materials*; Capper, P., Mauk, M., Eds.; John Wiley & Sons, Ltd.: Chichester, UK, **2007**; pp 1–19.

[39] Farha, O. K.; Hupp, J. T. Rational Design, Synthesis, Purification, and Activation of Metal-Organic Framework Materials. *Acc. Chem. Res*. **2010**, *43*, 1166–1175.

[40] Evans, J. F.; Gibson, J. H.; Moulder, J. F.; Hammond, J. S.; Goretzki, H. Angle Resolved ESCA Analysis of Plasma Modified Polystyrene*. Fresenius Z Anal. Chem*. **1984**, *319*, 841–844.

[41] Friedman, R. M.; Hudis, J.; Perlman, M. L. Chemical Effects on Linewidths Observed in Photoelectron Spectroscopy. *Phys. Rev. Lett.* **1972**, *29*, 692.

[42] Johansson, G.; Hedman, J.; Berndtsson, A.; Klasson, M.; Nilsson, R. Calibration of Electron Spectra. *J. Electron Spectrosc*. **1973**, *2*, 295–317.

[43] Kumagai, M.; Tsuchida, K.; Ogino, Y.; Hansen, J.; Ishida, H. Radical Copolymerization of 1-Vinylimidazole and Methacryl- or Styryl-Functional Silane Coupling Agents. *Polymer* **1995**, *36*, 3, 535–542

[44] Lin-Vien, D.; Colthup, N. B.; Fateley, W. G.; Grasselli, J. G. The Handbook of Infrared and Raman Characteristic Frequencies of Organic Molecules; Academic Press, Inc., 1250 Sixth Avenue, San Diego, CA 92101-4311, **1991**; pp 74.

[45] Han, L. M.; Timmons, R. B.; Bogdal, D.; Pielichowski, J. Ring Retention via Pulsed Plasma Polymerization of Heterocyclic Aromatic Compounds. *Chem. Mater.* **1998**, *10*, 1422–1429

[46] Battjes, K. P.; Barolo, A. M.; Dreyfuss, P. New Evidence Related to Reactions of Aminated Silane Coupling Agents with Carbon Dioxide. *J. Adhes. Sci. Technol*. **1991**, *5*, 10, 785–799

[47] Morris, W.; Leung, B.; Furukawa, H.; Yaghi, O. K.; He, N.; Hayashi, H.; Houndonougbo, Y.; Asta, M.; Laird, B. B.; Yaghi, O. M. A. A Combined Experimental-Computational Investigation of Carbon Dioxide Capture in a Series of Isoreticular Zeolitic Imidazolate Frameworks. *J. Am. Chem. Soc.* **2010**, *132*, 32, 11006–11008

[48] Zaera, F. New Advances in the Use of Infrared Absorption Spectroscopy for the Characterization of Heterogeneous Catalytic Reactions. *Chem. Soc. Rev.* **2014**, *43*, 7624–7663.

[49] Luo, X. F.; Goh, S. H.; Lee, S. Y.; Huan, C. H. A. Spectroscopic Studies of Interactions in Complexes of Poly(1-Vinylimidazole) with Poly(Styrenesulfonic Acid) or the Zinc Salt of Poly(Styrenesulfonate). *Macromol. Chem. Phys*. **1999**, *200*, 874–880.

[50] Lin-Vien, D.; Colthup, N. B.; Fateley, W. G.; Grasselli, J. G. The Handbook of Infrared and Raman Characteristic Frequencies of Organic Molecules; Academic Press, Inc., San Diego, **1991**.

[51] Yost, E. C.; Tejedor-Tejedor, M. I.; Anderson, M. A. In Situ CIR-FTIR Characterization of Salicylate Complexes at the Goethite/Aqueous Solution Interface. *Environ. Sci. Technol.* **1990**, *24*, 822–828.

[52] Tranchemontagne, D. J.; Hunt, J. R.; Yaghi, O. M. Room Temperature Synthesis of Metal-Organic Frameworks: MOF-5, MOF-74, MOF-177, MOF-199, and IRMOF-0. *Tetrahedron* **2008**, *64*, 8553–8557.

[53] Mistry, B. D. A Handbook of Spectroscopic Data: Chemistry; Oxford Book Company, Delhi, **2009**.

[54] Ruokolainen, J.; Tanner, J.; ten Brinke, G.; Ikkala, O.; Torkkeli, M.; Serimaa, R. Poly(4-vinyl pyridine)/Zinc Dodecyl Benzene Sulfonate Mesomorphic State Due to Coordination Complexation. *Macromolecules* **1995***, 28*, 7779–7784.

[55] Banh, H.; Gemel, C.; Seidel, R. W.; Fischer, R. A. A Solvated Zinc Analogue of the Calomel-Dication. *Chem. Commun*. **2015**, *51*, 2170–2172.

[56] Mereu, R. A.; Mesaros, A.; Petrisor, T. Jr.; Gabor, M.; Popa, M.; Ciontea, L.; Petrisor, T. Synthesis, Characterization and Thermal Decomposition Study of Zinc Propionate as a Precursor for ZnO Nano-Powders and Thin Films. *J. Anal. Appl. Pyrolysis* **2013**, *104*, 653–659.

[57] Perez, E. V.; Balkus K. J. Jr.; Ferraris, J. P.; Musselman, I. H. Mixed-Matrix Membranes Containing MOF-5 for Gas Separations*. J. Membr. Sci*. **2009**, *328*, 165–173.

[58] Ferguson, A.; Liu, L.; Tapperwijn, S. J.; Perl, D.; Coudert, F.-X.; Van Cleuvenbergen, S.; Verbiest, T.; van der Veen, M. A.; Telfer, S. G. Controlled Partial Interpenetration in Metal–Organic Frameworks. *Nat. Chem*. **2016**, *8*, 250–257.

[59] NOAA/ESRL Global Monitoring Division. https://www.esrl.noaa.gov/gmd/ccgg/trends/#mlo (accessed June 15, 2017).

[60] Chen, S.; Lin, S.; Chien, R.; Hsu, P. Effects of Shape, Porosity, and Operating Parameters on Carbon Dioxide Recovery in Polytetrafluoroethylene Membranes. *J. Hazard. Mater.* **2010**, *179*, 692–700.

[61] Low, M. J. D. Kinetics of Chemisorption of Gases on Solids. *Chem. Rev*. **1960**, *60*, 267–312.

[62] Badyal, J. P. S. Beyond the Surface. *Chem. Br.* **2001**, *37*, 45–46.

[63] Markov, I. V. Crystal Growth for Beginners: Fundamentals of Nucleation, Crystal Growth and Epitaxy; World Scientific Publishing Co. Pte. Ltd., Singapore, **2003**.

[64] Summerfield, A.; Cebula, I.; Schröder, M.; Beton, P. H. Nucleation and Early Stages of Layer-by-Layer Growth of Metal Organic Frameworks on Surfaces. *J. Phys. Chem. C* **2015**, *119*, 23544−23551.

[65] Stavila, V.; Volponi, J.; Katzenmeyer, A. M.; Dixon, M. C.; Allendorf, M. D. Kinetics and Mechanism of Metal−organic Framework Thin Film Growth: Systematic Investigation of HKUST- 1 Deposition on QCM Electrodes. *Chem. Sci.* **2012**, *3*, 1531−1540.

[66] Liu, B.; Tu, M.; Fischer, R. A. Metal-Organic Framework Thin Films: Crystallite Orientation Dependent Adsorption. *Angew. Chem. Int. Ed.* **2013**, *52*, 3402–3405.

[67] Lawson, S.; Hajari, A.; Rownaghi, A. A.; Rezaei, F. MOF Immobilization on the Surface of Polymer-Cordierite Composite Monoliths Through In-Situ Crystal Growth. *Sep. Purif. Technol.* **2017**, *183*, 173–180.

[68] Li, J.-R.; Ma, Y.; McCarthy, M. C.; Sculley, J.; Yu, J.; Jeong, H.-K.; Balbuena, P. B.; Zhou, H.-C. Carbon Dioxide Capture-Related Gas Adsorption and Separation in Metal-Organic Frameworks. *Coord*. *Chem. Rev.* **2011**, *255*, 1791–1823.

[69] Liang, Y.; Harrison, D. P.; Gupta, R. P.; Green D. A.; McMichael, W. J. Carbon Dioxide Capture Using Dry Sodium-Based Sorbents. *Energy Fuels*, **2004**, *18*, 569–575.

[70] Hicks, J. C.; Drese, J. H.; Fauth, D. J.; Gray, M. L.; Qi, G. G.; Jones, C. W. Designing Adsorbents for CO_2 Capture from Flue Gas-Hyperbranched Aminosilicas Capable of Capturing CO_2 Reversibly. *J. Am. Chem. Soc*. **2008**, *130*, 2902–2903.

[71] Simmons, J. M.; Wu, H.; Zhou, W.; Yildirim, T. Carbon Capture in Metal–Organic Frameworks—A Comparative Study. *Energy Environ. Sci.* **2011**, *4*, 2177–2185.

[72] Stolaroff, J. K.; Keith, D. W.; Lowry, G. V. Carbon Dioxide Capture from Atmospheric Air Using Sodium Hydroxide Spray. *Environ. Sci. Technol*. **2008**, *42*, 2728–2735.

[73] Stuckert, N. R.; Yang, R. T. CO_2 Capture from the Atmosphere and Simultaneous Concentration Using Zeolites and Amine-Grafted SBA-15. *Environ. Sci. Technol*. **2011**, *45*, 10257–10264.

[74] Shekhah, O.; Belmabkhout, Y.; Chen, Z.; Guillerm, V.; Cairns, A.; Adil, K.; Eddaoudi, M. Made-to-Order Metal-Organic Frameworks for Trace Carbon Dioxide Removal and Air Capture. *Nat. Commun*. **2014**, *5*, 1–7.

[75] Schneemann, A.; Bon, V.; Schwedler, I.; Senkovska, I.; Kaskel, S.; Fischer, R. A. Flexible Metal–Organic Frameworks. *Chem. Soc. Rev*. **2014**, *43*, 6062–6096.

Chapter 6 Magnetic Recyclable P25–TiO_2 Microcomposite Photocatalysts

6.1 Introduction

For industrialised countries, controlling emissions of greenhouse gases such as CO_2 is a vital step in environmentally sustainable industrial processes. However, for many countries a greater concern is access to clean drinking water, with approximately two billion people worldwide lacking this most basic resource.[1] In rural regions of developing countries, this is often due to surface or ground water being contaminated with agricultural run-off.[2,3] These pollutants include organic pesticides applied to arable land, travelling from point of application through waterways into river mouths.[4,5,6] Subsequent chronic ingestion can lead to fatal illnesses such as non-Hodgkin's lymphoma and Parkinson's disease.[7,8,9] In particular, children tend to be at high risk due to toxic dosages being as low as 1% advised for adults.[10] Industrialisation is another major source of organic molecule water contamination.[11] Often in developing countries, chloro and aromatic compounds are detected in textile factory effluents.[12,13,14] These environmental pollutants have been linked to mutagenic effects in mammals and aquatic vertebrates.[15,16,17,18]

One potential solution at the local village level (point of use) involves the UV illumination of semiconductor band gap materials (such as TiO_2) for the photocatalytic degradation of organic pesticide and dye pollutants,[19,20,21,22,23] alongside the inherent benefit of high UV bactericidal activity towards *E. coli* and other common waterborne health risks.[24,25,26,27] In particular, the use of TiO_2 nanoparticles has been widely reported for this purpose, despite such hydrophilic nanoparticles posing a risk to natural ecosystems due to their high levels of aqueous dispersity.[28,29] For instance, TiO_2 nanoparticles display biological toxicity towards living tissues sensitive to oxidative stress, such as those containing brain microglia and bronchial epithelial cells.[30,31] Furthermore, their small size makes them difficult to remove by physical means (e.g. filtration) because small pore membranes easily become blocked. Therefore, larger size, cheap, and easily separable photocatalytic particles are sought for sustainable water purification applications in developing countries.

TiO_2-coated magnetic core particles are promising candidates for magnetically recoverable photocatalysts. Previous examples for local production include: agglomerated TiO_2-coated sub-micron size iron oxide particles synthesised from ferric chloride (which is

toxic),[32,33] micron-sized magnetic Mn-Zn ferrite photocatalysts prepared from waste materials (which are a cheaper variant, however their synthesis requires an extensive number of wet chemical steps as well as the handling and disposal of waste sulphuric acid)[34], the combination of TiO_2 particles and a magnetic component within an organic matrix (such as chitosan,[35] poly(methyl methacrylate),[36] or poly(vinyl pyrrolidone))[37] to form micron-sized particles (these suffer from the organic host matrices themselves being vulnerable to photodegradation by the TiO_2 photocatalysts over extended periods of operation[38,39]), and the utilisation of inorganic matrices, such as reduced graphene oxide,[40] $SrFe_{12}O_{19}$ nanofibres, [41] or hydrotalcite clays,[42] (which add significant costs).

In this chapter, a simple, quick, and cheap strategy is described comprising the encapsulation of magnetically separable micron-sized steel filings with a sol-gel TiO_2 nanocomposite photocatalyst shell. Sol-gel chemistry is already widely employed for the large scale manufacture of silica and titania aerogels, nanopowders, and coatings.[43] Typically this involves acid hydrolysis of silica and titania precursors, followed by for example, substrate dipping, and a final thermal curing step.[44,45] This approach offers many advantages, including independent scope for fine tuning particle size,[43] pore size,[46] and film hardness, either by variation of the sol-gel synthesis conditions, or by mixing additional particles (such as photocatalytic P25 TiO_2 nanoparticles).[47] Herein, micron size magnetic steel particles are first encapsulated within a double sol-gel silica host matrix barrier layer to protect against corrosion, as well as help suppress electron-hole recombination and electron-hole transfer between the TiO_2 outer layer and the underlying steel particles .[48,49] These silica-steel microcomposite particles are then coated with a photocatalytic nanocomposite outer shell comprising photoactive TiO_2 (P25) nanoparticles incorporated within a TiO_2 sol-gel host matrix, Scheme 6.1. These silica-steel microcomposite core with TiO_2–P25 nanocomposite shell photocatalysts have been characterised by X-ray photoelectron spectroscopy (XPS), Raman microscopy, X-ray diffraction (XRD), UV-Vis diffuse reflectance spectroscopy, and BET surface area analysis. Photocatalytic degradation rates have been measured using aqueous methylene blue dye solution,[50,51] which is considered to be a good model pollutant for many organic pesticides and dyes which contain aromatic, heteroaromatic, and chloro groups.[6,52,53,54,55]

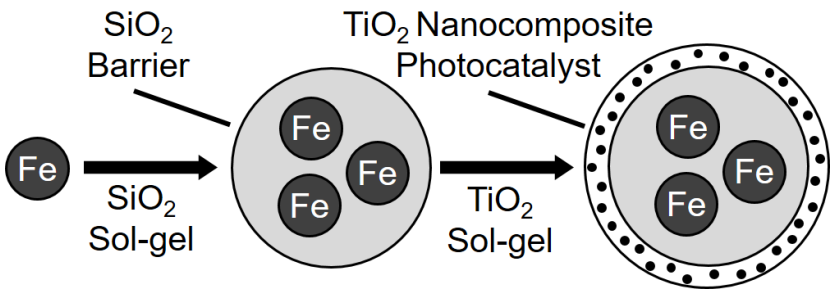

Scheme 6.1: Representation of sol-gel preparation of microcomposite silica-steel core with TiO_2 nanocomposite shell photocatalysts.

6.2 Experimental Section

6.2.1 Substrate Preparation

Quartz slides (23 mm x 10 mm x 2 mm, cut from a 75 mm diameter quartz window, UQG Ltd.) were cleaned with detergent and then sonicated in propan-2-ol (+99.5 wt%, Fisher Scientific UK Ltd.) for 15 min prior to use as control substrates.

Small pieces of sheet steel (10 mm x 10 mm x 1 mm, ECISS grade S275 (<0.25 wt% C, <1.60 wt% Mn, <0.04 wt% P, <0.05 wt% S, <0.05 wt% Si), SES Multi Metal Stock Ltd.) were used as model flat steel substrates. These were scrubbed with detergent followed by 15 min sonication in propan-2-ol. They were then rinsed with high purity water (BS 3978 Grade 1) and immersed in a 10 wt% solution of sodium hydroxide (99.2 wt%, Fisher Scientific UK Ltd.) in high purity water for 10 min. Next, the steel plates were rinsed in high purity water, and immersed in a solution comprising hydrochloric acid (32 wt% in water, Fisher Scientific UK Ltd.), nitric acid (70 wt% in water, Fisher Scientific UK Ltd.) and high purity water in a volume ratio of 1.0 : 2.0 : 17.0 for 10 min. This was followed by rinsing in high purity water, washing in acetone (+99.8 wt%, Fisher Scientific UK Ltd.), and final removal of surface contaminants by placing in a UV-Ozone cleaner (ProCleaner, BioForce Nanosciences Inc.) for 40 min, ready for coating.

Micron-sized steel particles were ground from a steel rod (ECISS grade S275 (<0.25 wt% C; <1.60 wt% Mn; <0.04 wt% P; <0.05 wt% S; <0.05 wt% Si), SES Multi Metal Stock Ltd.) using a horizontal belt finisher (Bandfacer, RJH Finishing Systems Ltd.,

running at 0.75 hp) fitted with a sanding belt (180 grit, 100 mm x 915 mm linishing belt, Deerfos Europe Sp. z.o.o.). The obtained coarse steel particles were magnetically separated from any residual non-magnetic particulates. Next, they were further ground manually under a 2 kg mass (with a cross-sectional area of 65 cm^2) for 30 min placed between two pieces of dry silicon carbide finishing paper (p400 grit, manufactured by Bibielle S.p.A., supplied by MSC Industrial Supply Co.), followed by grinding down between finer grade dry silicon carbide finishing paper (p1200 grit, Bibielle S.p.A., supplied by MSC Industrial Supply Co.) for 30 min, then magnetically separated and rinsed in acetone to yield a median particle size of 2.9 µm (upper and lower quartiles of 4.2 and 2.2 µm respectively, measured using a light microscope, Model BX40, Olympus Corp.).

A cylindrical glass plasma reactor (5.5 cm diameter, 475 cm^3 volume) housed within a Faraday cage was used for plasma cleaning of the steel particles. This was connected to a 30 L min^{-1} rotary pump via a liquid nitrogen cold trap (base pressure less than 2 x 10^{-3} mbar and air leak rate better than 6 x 10^{-9} mol s^{-1}).[56] A copper coil wound around the glass reactor (4 mm diameter, 11 turns, located 10 cm downstream from the gas inlet) was connected to a 13.56 MHz radio frequency (RF) power supply via an L-C matching network. Prior to loading each batch of steel particles, the whole apparatus was thoroughly scrubbed using detergent and hot water, rinsed with propan-2-ol, oven dried at 150 ºC, and further cleaned using a continuous wave 50 W air plasma at 0.2 mbar pressure for 30 min. Next, the steel particles were placed inside the chamber and plasma cleaned using the aforementioned electrical discharge parameters, ready for sol-gel coating application.

6.2.2 Silica Barrier Layer

A silica barrier layer was applied to the steel particles in order to protect against rusting, as well as suppressing electron-hole recombination, and electron-hole transfer from TiO_2 photocatalyst overlayer to the underlying steel particles.[48,49] A silica sol-gel was prepared by acid catalysed hydrolysis of tetraethyl orthosilicate (TEOS, +98 wt%, Sigma-Aldrich Co. LLC.) through mixing with ethanol (+99.8 wt%, Fisher Scientific UK Ltd.), high purity water, and hydrochloric acid (32 wt% in water, Fisher Scientific UK Ltd.) in a molar ratio of 1.0 : 3.8 : 7.3 : 5.4 × 10^{-3} respectively and magnetic stirring at 60 °C for 60 min. The extent of condensation increased with time, where the solution initially consisted of a sol and was followed by the formation of a gel network.[43] In order to produce uniform silica coatings,

the sol-gel solutions were used within 48 h of synthesis, whilst the sol-gel remained at its lowest viscosity (typically comprising particles in the nanometre size range).[43]

Coating of steel particles with one layer of silica entailed immersion in the sol-gel followed by vigorous manual agitation every 5 min over a 60 min period in order to ensure uniform particle dispersion throughout the growth phase of the coating. These coated steel particles were then magnetically separated, rinsed with ethanol, dried in air over a hot plate at 80 °C for 15 min, annealed at 150 °C under vacuum (<60 mbar) for 1 h, and finally any large agglomerates were mechanically separated using a ceramic pestle and mortar. Quartz slides and steel plates were also coated using this method (however vigorous agitation and magnetic separation were not necessary). The coated steel plates were analysed by X-ray photoelectron spectroscopy (XPS) in order to check for complete coverage of the steel substrate by the silica layer. Double silica barrier layers were built up by repeating the aforementioned procedure in order to ensure complete coverage of the substrate.

6.2.3 TiO_2 Coating

A TiO_2 sol-gel was prepared by stirring a solution of the following chemicals for 1 h prior to use: propan-2-ol, glacial acetic acid (+99 wt%, Fisher Scientific UK Ltd.), and titanium isopropoxide (+97 wt%, Sigma-Aldrich Co. LLC.) in a molar ratio of 45.0 : 6.0 : 1.0 respectively. In order to produce uniform coatings of TiO_2, the sol-gel solutions were used within 48 h of synthesis, whilst the sol-gel remained at its lowest viscosity (typically comprising particles in the nanometre size range).[43]

Quartz slides and steel plates precoated with a double silica barrier layer (to ensure complete coverage of the surface) were dip coated into the TiO_2 sol for 15 s and allowed to dry in air at 20 ºC for 30 min. This TiO_2 sol coating cycle was repeated three times for both substrates, in order to build up the layer, followed by air calcination at 500 °C for 30 min using a ramp rate of 5 °C min^{-1}.

500–600 mg batches of steel particles precoated with a double silica barrier layer were dip coated by immersion into 2 mL of the TiO_2 sol-gel, manually agitating for 15 s, followed by magnetic separation whilst decanting the excess solution. These TiO_2 sol-gel coated steel particles were then dried under N_2 (99.998 vol%, BOC Ltd.) flow at 20 ºC for 30 min, and any large agglomerates were mechanically separated using a ceramic pestle and mortar. This TiO_2 sol-gel coating cycle was repeated 8 times to build up a sufficiently

thick layer, and finally calcined at 500 °C for 30 min using a ramp rate of 5 °C min^{-1} under a dry (<60 ppm H_2O, Series 3 moisture monitor, GE Panametrics Ltd.) gas flow of O_2 (99.5 vol%, BOC Ltd., 20 cm^3 min^{-1}) and N_2. This is designated as one overall TiO_2 coating layer, Table 6.1. Calcination under gas flow was required due to the higher surface area of steel particle substrates compared to flat steel and quartz substrates. The use of a dry O_2/N_2 gas mixture was important in order to prevent rusting of the particles.

Table 6.1: TiO_2 coated substrates (all precoated with a double silica barrier layer).

Sample Code	Substrate	Outer Coating Matrix Material	Number of TiO_2 coating layers
TiO_2(Q)	Quartz Slide	Sol-Gel TiO_2	1
TiO_2(1)	Steel Particles	Sol-Gel TiO_2	1

6.2.4 Nanocomposite TiO_2 Coatings

3.6 wt% Aeroxide® P25 TiO_2 nanoparticles (anatase : rutile ratio 80 : 20 wt%, BET surface area 50 $m^2 g^{-1}$, Acros Organics)[57] were added to a freshly prepared TiO_2 sol-gel comprising a solution of propan-2-ol, glacial acetic acid and titanium isopropoxide in molar ratios of 45.0 : 6.0 : 1.0 respectively, which had been stirred for 1 h prior to use.

Quartz slides coated with a double silica barrier layer were dip coated into the TiO_2–P25 nanocomposite sol-gel for 15 s followed by drying in air at 20 ºC. This cycle was repeated three times followed by air calcination at 500 °C for 30 min, using a ramp rate of 5 °C min^{-1}.

500–600 mg batches of steel particles coated with a double silica barrier layer were dip coated by immersion into 2 mL of the TiO_2–P25 nanocomposite sol-gel and manually agitated for 15 s, followed by magnetic separation whilst decanting the excess solution. These TiO_2–P25 nanocomposite sol-gel coated steel particles were then dried under N_2 flow at 20 ºC for 30 min, and any large agglomerates were mechanically separated using a ceramic pestle and mortar. This TiO_2–P25 nanocomposite sol-gel coating cycle was repeated 8 times to build up a sufficiently thick layer, and finally calcined at 500 °C for 30 min using a ramp rate of 5 °C min^{-1} under a dry (<30 ppm H_2O) gas flow of O_2 (20 cm^3 min^{-1}) and N_2 (80 cm^3 min^{-1}). This is designated as one overall TiO_2–P25 nanocomposite coating layer, Table 6.2.

Table 6.2: TiO_2–P25 nanocomposite coated substrates (all precoated with a double silica barrier layer). Total coating thicknesses measured by: (†) optical microscopy; and (‡) Raman microscopy.

Sample Code	Substrate	Matrix Material	Filler Nanoparticles	Number of TiO_2–P25 Nanocomposite Coating Layers	Total Coating Thickness / µm
P25(Q)	Quartz Slide	Sol-Gel TiO_2	P25 TiO_2	1	$2.75 \pm 0.25^{\dagger}$
P25(1)	Steel Particles	Sol-Gel TiO_2	P25 TiO_2	1	$6 \pm 2^{\ddagger}$
P25(3)	Steel Particles	Sol-Gel TiO_2	P25 TiO_2	3	$10 \pm 4^{\ddagger}$
P25(5)	Steel Particles	Sol-Gel TiO_2	P25 TiO_2	5	$27 \pm 8^{\ddagger}$

6.2.5 Characterisation

Silica adhesion layer thicknesses on quartz slides were determined by cryo-fracturing coated slides using liquid nitrogen, and subsequent analysis by scanning electron microscopy (SEM, VEGA3 LMU, Tescan Orsay Holding, a.s.) at 25 kV, with sample cross sections orientated 10° from parallel to the beam path.

TiO_2 coating thickness on quartz slides was measured by confocal laser scanning microscopy (LSM 880 with Airyscan, Carl Zeiss AG) by analysing 22 µm x 22 µm areas of coating. Reflectance of the TiO_2 sol-gel and TiO_2–P25 nanocomposite sol-gel coatings under laser light (wavelength of 405 nm, transmitted by the quartz substrate and silica barrier layer) was captured in cross-sections parallel to the coating's surface. Image stack acquisition was started from above the surface of the coating and then moving in 0.29 µm steps along the direction perpendicular to the coating, using a 0.60 µm thickness optical section. Image stacks were rotated to yield the coating cross-section, and the average thickness of the film was then calculated by measuring the cross-sectional area (ImageJ, Java-based image processing program) and dividing it by the section length.

Surface elemental compositions were measured by X-ray photoelectron spectroscopy (XPS) using a VG ESCALAB II electron spectrometer equipped with a non-monochromated Mg K$\alpha_{1,2}$ X-ray source (1253.6 eV) and a concentric hemispherical analyser. Photoemitted electrons were collected at a take-off angle of 20° from the substrate normal, with electron detection in the constant analyser energy mode (CAE, pass energies of 20 and 50 eV for high resolution and survey spectra respectively). Experimentally determined instrument sensitivity factors were taken as C(1s) : O(1s) : Si(2p) : Fe(3d) equals 1.00 : 0.35 : 0.97 : 0.09 respectively.

Raman spectra were acquired on a confocal microscope laser Raman system (model Labram 1B, Instruments S. A. (UK) Ltd.) equipped with a 15 mW He-Ne laser (6328 Å) excitation source and an air-cooled CCD detector (model SpectrumOne CCD 2000). For Raman spectroscopy, coated steel and reference particle samples were compressed and levelled into a glass sample cell (10 mm diameter and 2 mm depth). Spectral background subtraction utilised a 6th degree polynomial. For Raman microscopy analysis, samples were set into epoxy resin (5 : 2 mixture of Epoxy resin L : Hardener S, R&G Faserverbundwerkstoffe GmbH Composite Technology) at 1 wt%, cured for 24 h at room temperature (20 °C), then cross sectioned using sequential polishing with dry silicon carbide finishing paper (p400 and p1200 grit, manufactured by Bibielle S.p.A., supplied by MSC Industrial Supply Co.) and alumina metal polish (Solvol®, Autosol LLC.). Raman microscopy spectra were taken at 1 µm intervals along a linear trace through the centre of each analysed particle using a 1800 g/mm grating; subsequently, Raman microscopy profiles were generated from the area of the anatase Eg TiO_2 (594–691 cm^{-1}) and haematite Fe_2O_3 (262–310 cm^{-1}) signals. A TiO_2 coating thickness for each analysed particle was calculated by averaging the distance measured between the outer and inner boundaries of the anatase Eg signal on each edge of the cross-sectioned particle.

X-Ray diffractograms were obtained across 5°–80° 2θ range with 0.02° step size using a powder diffractometer (model d8, Bruker Corp.). The copper anode X-ray source was operated at 40 kV and 40 mA emitting Cu Kα 1.5418 Å wavelength radiation.

UV-Vis absorbance spectra of coated quartz slides were acquired using a custom built centre-mount low density PTFE integrating sphere with an internal diameter of 100 mm. Illumination was provided from a deuterium tungsten-halogen fibre optic source (model DH-2000-S, Ocean Optics Inc., 215–2500 nm range), and the reflected light was

analysed by a fibre coupled CCD spectrophotometer (200–850 nm range, model USB-2000+, Ocean Optics Inc.).

Particle sizes were measured using a light microscope (Model BX40, Olympus Corp.). Particle surface area was determined using the BET method[58] (model BET-201 sorptometer, PMI Inc.). Prior to recording nitrogen adsorption isotherms, the samples (100–200 mg) were degassed under vacuum (<0.05 mbar) at 200 ºC for 3 h.

6.2.6 Photocatalytic Testing of Coated Steel Particles

TiO_2 photocatalyst coated silica-steel microcomposite core particles (solution concentration of 2.0 ± 0.3 mg mL^{-1}) were tested in a 100 mL volume cylindrical borosilicate glass reaction vessel (fitted with a quartz window for UV irradiation) filled with 90 mL of a 4.0 μM aqueous solution of methylene blue dye (+70 wt%, TCL UK Ltd.), Figure 6.1. Particles were agitated using a vertically mounted magnetic stirrer hot plate (IKAMAG RCT, IKA®-Werke GmbH & Co. KG) in contact with the back face of the reactor, and oxygen dissolution was maintained via a glass diffuser bubbling oxygen at a flow rate of 5 cm^3 min^{-1} at 1.5 Bar pressure. A Hg-Xe short arc lamp (model 6136, 200 W rated, operating at 26 V and 7 A, Oriel Newport Corp.) positioned 15 cm away from the reactor quartz window provided an incident UV flux of 7.4 ± 1.4 mW cm^{-2} onto the solution (measured with a thermopile and digital voltmeter, model 5300, Applied Photophysics Ltd.). A contact thermometer was used as part of a feedback loop to the stirrer hot plate in order to maintain the reaction vessel temperature at 28 ± 2 °C. Prior to UV irradiation, the photocatalyst coated steel particles were allowed to equilibrate in the methylene blue dye solution for 1 h in order to determine the extent of methylene blue dye adsorption onto the coated steel particles. 1 mL aliquots, filtered through a 0.22 μm polyethersulfone syringe filter (Gilson Scientific Ltd.), were taken prior to the addition of photocatalyst, and at 10 min intervals during UV illumination for UV-Vis absorption spectroscopy analysis of methylene blue dye concentrations at λ_{max} = 660 nm (model UV4, Unicam Lda.).[59] Dye photodegradation rate constants were calculated from absorbance readings taken over 1 h of UV exposure assuming first order kinetics (over this period dye degradation did not reach a point where mass transfer and other effects caused a deviation from linearity of the plots).[50,51] UV degradation of methylene blue dye in the absence of coated steel particles served as a control (the measured rate constant of 5.9 ± 1.5 x 10^{-3} min^{-1} was subtracted for each set of photocatalysis experiments). The calculated rate was then

normalised to the surface area of the photocatalyst coated steel particles. Finally, the ease of recycling was demonstrated by using a hand magnet to separate coated steel particles aqueous solution between consecutive photocatalytic cycles.

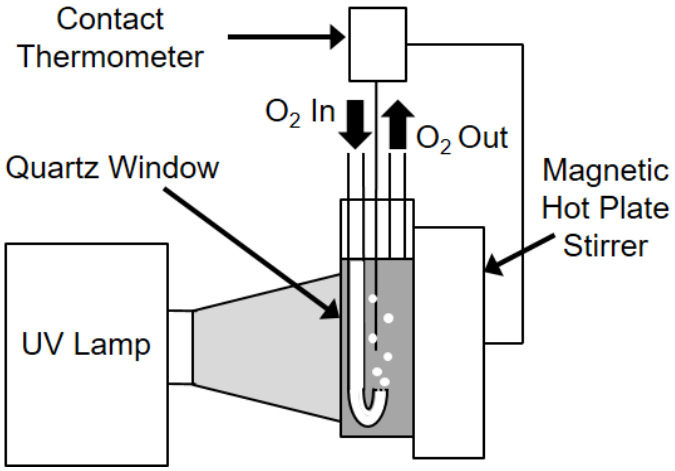

Figure 6.1: Schematic of borosilicate glass photoreactor fitted with a quartz front window and magnetic hot plate stirrer.

6.3 Results

6.3.1 Silica Barrier Layer

Wide scan XPS survey spectra of uncoated steel plates indicated the presence of only iron, oxygen, and carbon species at the surface (1–2 nm sampling depth),[60,61] Figure 6.2. The O(1s) envelope could be fitted to two different oxygen atom environments corresponding to bulk lattice Fe_2O_3 (530.7 ± 0.1 eV),[62,63] and surface hydroxyl groups (532.3 ± 0.1 eV), Figure 6.3.[62,64] Deposition of a double silica barrier layer was found to be necessary to achieve complete coverage of the steel substrate, as confirmed by the disappearance of the iron XPS features in conjunction with the emergence of signals from silicon-containing species. This included the appearance of a higher binding energy O(1s) component (533.1 ± 0.1 eV) characteristic of silica lattice and silanol groups.[65,66]

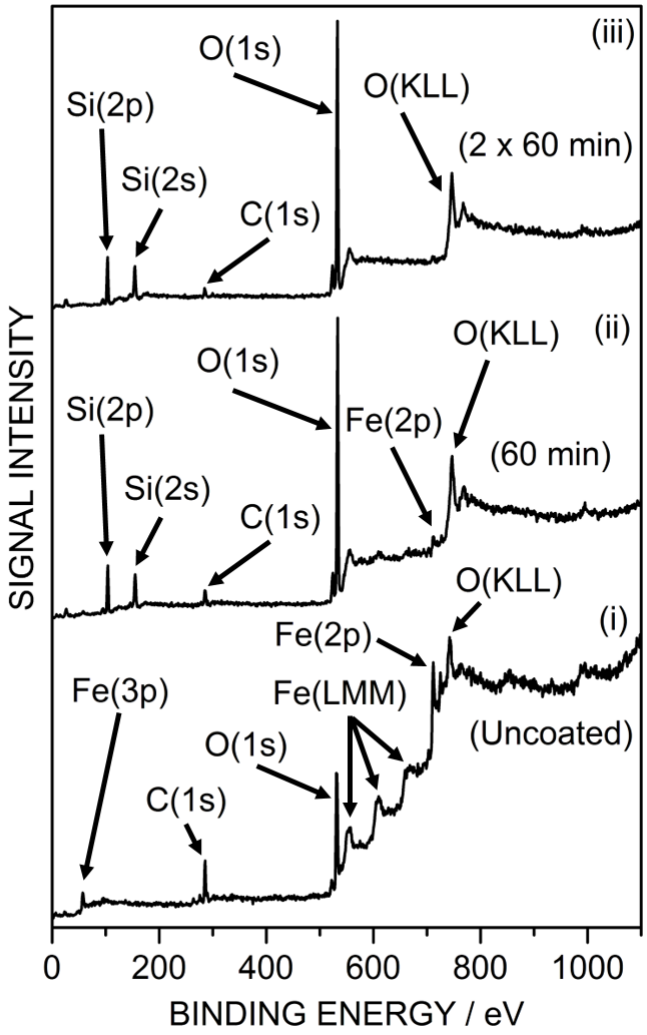

Figure 6.2: XPS wide scan survey spectra of: (i) clean uncoated steel plate; (ii) single silica barrier layer (60 min deposition) coated steel plate; and (iii) double silica barrier layer (2 x 60 min deposition) coated steel plate.

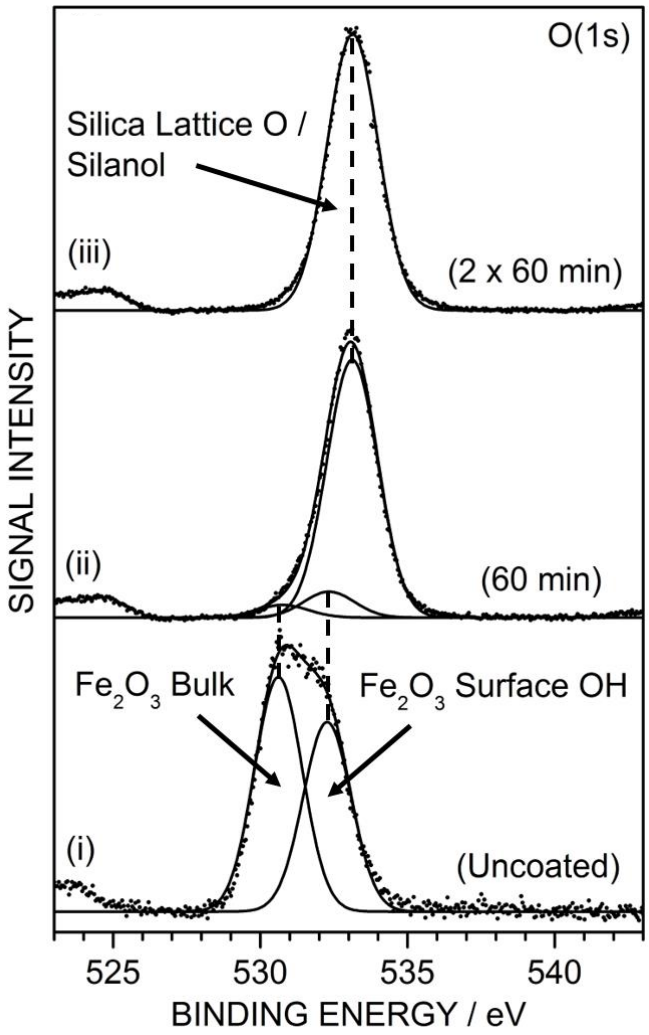

Figure 6.3: XPS O(1s) spectra of steel plates: (i) clean uncoated; (ii) single silica barrier layer (60 min deposition); and (iii) double silica barrier layer (2 x 60 min deposition).

Cross-section SEM analysis of the double silica barrier layer deposited onto quartz slides indicated a coating thickness of 92 ± 8 nm, Figure 6.4, whilst the particle size measured using an optical microscope after double silica barrier layer coating of steel particles (median 17.7 µm) was an order of magnitude larger compared to uncoated steel particles (median 2.9 µm). This is consistent with individual double silica barrier layer coated steel particles agglomerating to form larger (more easily handleable) composite particles, Scheme 6.1.

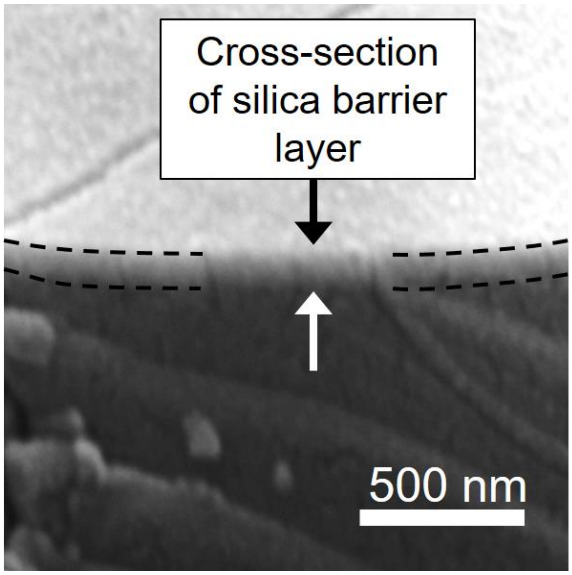

Figure 6.4: Cross sectional SEM micrograph of a quartz slide coated with a double silica barrier layer taken at 10° from parallel to the electron beam path.

The Raman spectrum of clean steel particles displayed signals characteristic of haematite (Fe_2O_3) and magnetite (Fe_3O_4),[67] Figure 6.5 and Table 6.3. An attenuation of these features was observed following application of the double silica barrier layer, accompanied by the emergence of silica peaks (993 cm^{-1}, 1353 cm^{-1}, and a broad band at around 3000 cm^{-1}).[68,69,70] The sampling depth of visible light Raman spectroscopy (which ranges from 3 µm for pure silicon to over 20 µm for some metal oxides)[71,72] is of the same magnitude as the double silica barrier layer-steel composite particle sizes (median 17.7 µm), resulting in both the silica coating and underlying steel particles being detected.

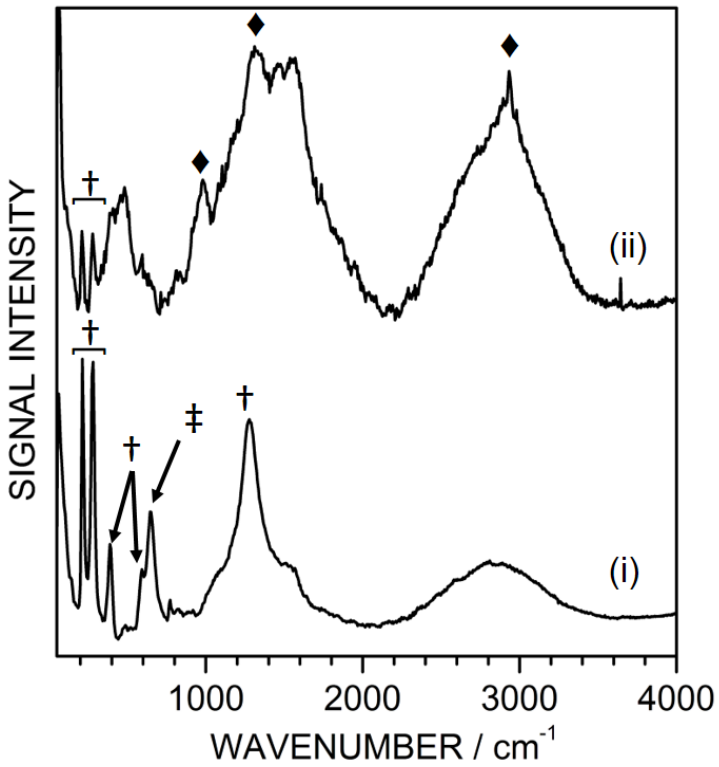

Figure 6.5: Raman spectra of steel particles: (i) uncoated; and (ii) double silica barrier layer coated. Significant peaks labelled: haematite Fe_2O_3 (†), magnetite Fe_3O_4 (‡), and silica (♦). For coating nomenclature see Table 6.1 and Table 6.2.

Table 6.3: Assignment of Raman bands for uncoated and coated steel particles.

Uncoated		**Silica Double Barrier Layer**	
Peak Position / cm^{-1}	**Assignment[73]**	**Peak Position / cm^{-1}**	**Assignment[73,74,75]**
213	Haematite Fe_2O_3	210	Haematite Fe_2O_3
281	Haematite Fe_2O_3	279	Haematite Fe_2O_3
395	Haematite Fe_2O_3	495	SiO_2 Defect peak
593	Haematite Fe_2O_3	1005	SiO_2
645	Magnetite Fe_3O_4	1365	SiO_2
1252	Haematite Fe_2O_3		
TiO_2(1)		**P25(5) Coated Steel Particles**	
Peak Position / cm^{-1}	**Assignment[73,76,77]**	**Peak Position / cm^{-1}**	**Assignment[76,77]**
141	Anatase Eg	148	Anatase Eg
291	Haematite Fe_2O_3	398	Anatase B_{1g}
397	Anatase B_{1g}	516	Anatase A_{1g} or B_{1g}
517	Anatase A_{1g} or B_{1g}	638	Anatase Eg
637	Anatase Eg		
P25 TiO_2 Nanoparticles			
Peak position / cm^{-1}	**Assignment[76,77]**		
148	Anatase Eg		
394	Anatase B_{1g}		
513	Anatase A_{1g} or B_{1g}		
636	Anatase Eg		

6.3.2 TiO_2 Coating

Prior to calcination of sol-gel coated TiO_2(1) silica-steel microcomposite core particles, Raman spectroscopy indicated that the coating was non-crystalline, with an absence of anatase or rutile Raman signals,[78,79,80,81] Figure 6.6. Following calcination of TiO_2(1) coated steel particles, Raman spectroscopy and powder XRD displayed strong anatase TiO_2 features,[78,79] Figure 6.7 and Figure 6.8. Rutile TiO_2 phase was not detected by XRD, which is consistent with the lack of asymmetry in the Raman B_{1g} at 386 cm^{-1} and E_g at 621 cm^{-1} anatase signals.[78,80,81] Optical particle size analysis showed that the TiO_2 coating steps did not lead to agglomeration.

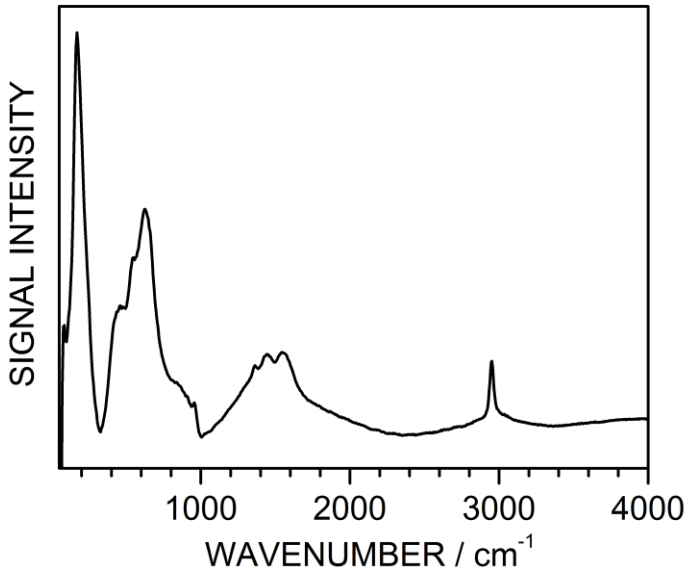

Figure 6.6: Raman spectra of uncalcined TiO_2(1) particles. The absorbance at 448 cm^{-1} can be assigned to disordered TiO_2,[82,83] (any adsorbed water librational bands typically appear around the 450 cm^{-1} region[84]). The peak at 182 cm^{-1} may be due to overlapping Raman active modes (including hydrogen bonded water vibrational bands at 175 cm^{-1},[84] and bridging hydroxyl group vibrational bands around 265 cm^{-1} in sheet silica[85]). The signal at 2966 cm^{-1} stems from residual acetic acid present in the film from the dip coating solution.[86]

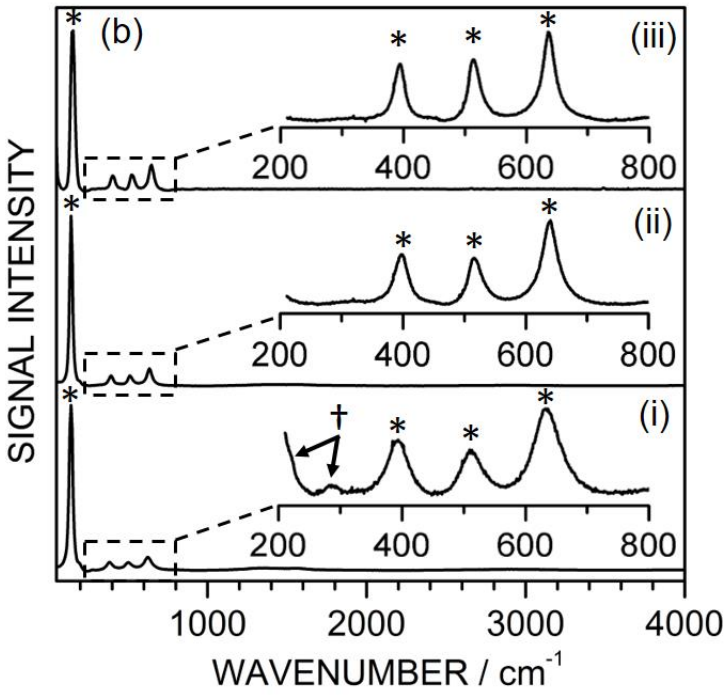

Figure 6.7: Raman spectra of: (i) TiO_2(1) coated silica-steel microcomposite core particles; (ii) P25(5) coated silica-steel microcomposite core particles; and (iii) P25 TiO_2 nanoparticles. Significant peaks labelled: haematite Fe_2O_3 (†), and anatase TiO_2 (*). Insets correspond to magnification of the 200–800 cm^{-1} region. For coating nomenclature see Table 6.1 and Table 6.2.

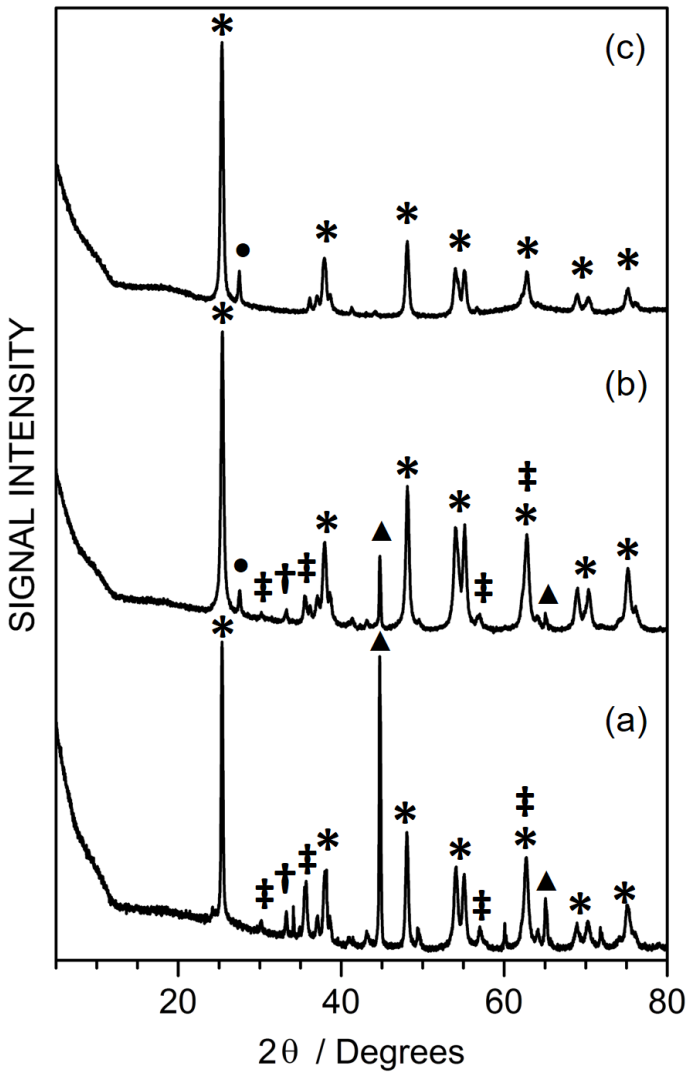

Figure 6.8: Powder XRD of: (a) TiO_2(1) coated silica-steel microcomposite core particles; (b) P25(5) coated silica-steel microcomposite core particles; and (c) P25 TiO_2 nanoparticles. Significant diffraction peaks labelled: α-Fe (▲); haematite Fe_2O_3 (†); magnetite Fe_3O_4 (‡); anatase TiO_2 (*); and rutile TiO_2 (•).

6.3.3 Nanocomposite TiO_2 Coatings

Powder XRD analysis of P25 TiO_2 nanoparticles showed anatase and rutile polymorph peaks at 2θ values of 25.3° (101) and 27.5° (110), respectively, Figure 6.8.[87,88] The [I_{Rutile}] / [$I_{Anatase}$] peak height intensity ratio of 0.10 (corrected for linear background subtraction) was used to calculate an anatase weight fraction ($W_{Anatase}$) of 0.86 using Equation 6.1,[89] which is comparable with the previously reported value of $W_{Anatase}$ = 0.8 for P25 TiO_2 material.[57] Additional lower intensity anatase peaks include 2θ values of: 37.8°, 48.0°, 53.9°, 62.7°, 68.7°, and 74.9°.[87,88] Powder XRD analysis of P25(5) coated silica-steel microcomposite core particles detected strong anatase TiO_2 peaks as well as weak signals from α-Fe, haematite (Fe_2O_3), magnetite (Fe_3O_4), and rutile TiO_2. [87,88,90,91] This is consistent with there being P25 TiO_2 nanoparticles embedded within the TiO_2(1) shell coating, Figure 6.8. For the P25(5) coated silica-steel microcomposite core particles, the sol-gel TiO_2 : P25 TiO_2 nanoparticle ratio is estimated to be 1.0 : 2.5, by calculating the remaining sol-gel TiO_2 contribution to [$I_{Anatase}$] after subtracting the P25 TiO_2 nanoparticle contribution (calculated by using the [I_{Rutile}] intensity, which is taken to be solely due to P25 TiO_2, in combination with the previously calculated anatase weight fraction ($W_{Anatase}$ = 0.86) for P25 TiO_2 nanoparticles).

$$W_{Anatase} = 1 / [1 + (1.26[I_{Rutile}] / [I_{Anatase}])] \quad \text{Eq. 6.1}$$

Raman spectroscopy of P25 TiO_2 nanoparticles displayed strong bands associated with anatase TiO_2 at 148 cm^{-1}, 394 cm^{-1}, 513 cm^{-1}, and 636 cm^{-1},[78,79] Figure 6.7 and Table 6.3. The lack of any TiO_2 rutile signal is consistent with previous Raman studies.[92,93] This is most likely due to the inherently low proportion of rutile (around 10 wt%, as shown by XRD) and the overlap of the Raman rutile E_g and A_{1g} peaks with the anatase B_{1g} and E_g peaks.[78,79,80,81] In the case of P25(5) nanocomposite coated silica-steel microcomposite particles, characteristic anatase TiO_2 Raman signals were observed, whilst the lack of any significant haematite Fe_2O_3 peaks,[67] corroborated a thicker coating compared to TiO_2(1), Figure 6.7 and Table 6.3. The absence of any TiO_2 rutile Raman signal for P25(5), is consistent with the aforementioned reference spectrum of P25 TiO_2 nanoparticles. However, powder XRD enabled a clear distinction to be made between the rutile and anatase phases for P25(5) nanocomposite coated silica-steel microcomposite core particles through the easily resolvable rutile diffraction peak at a 2θ value of 27.5º,

Figure 6.8. Raman microscopy of cross-sectioned silica-steel microcomposite core with TiO_2–P25 nanocomposite shell coating particles confirmed the presence of multiple (agglomerated) steel particles within the core silica host matrix, Figure 6.9. In contrast, to the earlier double silica barrier layer coating step of the steel particles (median 17.7 μm) which resulted in agglomeration, the sol-gel TiO_2 nanocomposite coating step did not cause agglomeration of the silica-steel microcomposite core particles, Figure 6.9.

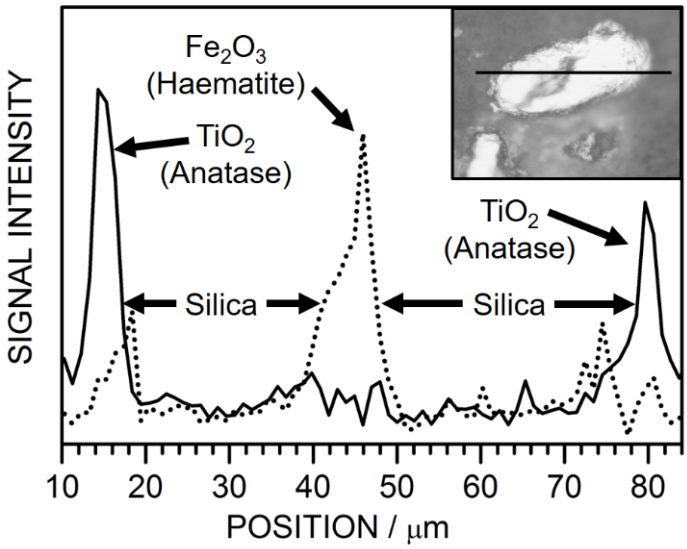

Figure 6.9: Raman microscopy signal across a cross-sectioned P25(1) coated silica-steel microcomposite core particle: anatase TiO_2 Eg signal (594–691 cm^{-1}, solid line); and haematite Fe_2O_3 signal (262–310 cm^{-1}, dotted line). Note haematite signal shows the incorporation of more than one steel particle within the silica-steel microcomposite core. Inset shows the optical micrograph of the particle analysed.

UV-Vis absorption spectra of TiO_2(Q) and P25(Q) coated quartz slides display distinct band gaps with negligible absorbance at wavelengths exceeding 400 nm into the visible region, Figure 6.10. The measured band gap of 3.15 eV (393 nm) for TiO_2(Q) coating is consistent with anatase TiO_2 phase (literature band gap of 3.15–3.20 eV).[87,94] In the case of P25(Q) coating, the lower band gap of 3.08 eV (402 nm) is in good agreement with previous reported values for P25 TiO_2 nanoparticles (3.1 eV),[87,95] which correlates to the larger rutile content measured by powder XRD analysis for P25(5) compared to TiO_2(1), Figure 6.8. Furthermore, this incorporation of P25 TiO_2

nanoparticles into TiO_2 sol-gel coatings (P25(Q)), enhances absorbance at shorter wavelengths (energies greater than the band gap), and slightly attenuates absorbance at longer wavelengths (energies below the band gap) compared to TiO_2(Q), Figure 6.10. The former can be attributed to a greater amount of absorbing species from a thicker TiO_2 layer (2.75 ± 0.25 μm for P25(Q) compared to 0.79 ± 0.08 μm for TiO_2(Q) measured by optical microscopy).[96] The latter may stem from differences in band tailing defect states.[97]

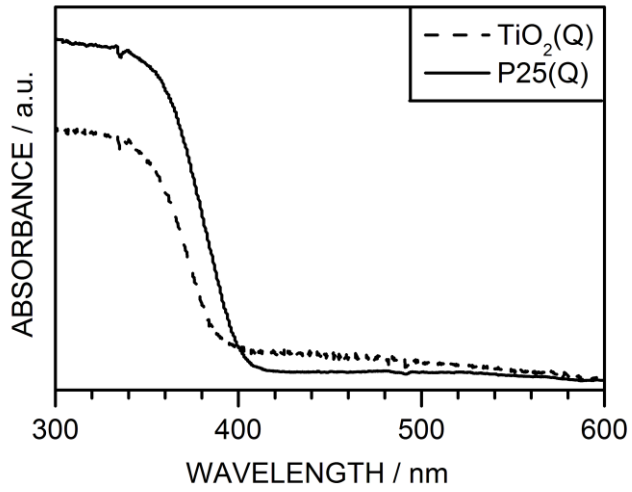

Figure 6.10: UV-Vis absorbance spectra of coated quartz slides: sol-gel TiO_2 coating (TiO_2(Q), dashed line); and sol-gel TiO_2 containing P25 nanoparticles (P25(Q), solid line).

The low surface area of 0.13 ± 0.02 m^2 g^{-1} measured for uncoated steel particles is in good agreement with the estimated theoretical surface area of 0.27 m^2 g^{-1} calculated from the optical particle size distribution (assuming spherical particles and an experimentally determined mild steel density of 7.53 ± 0.25 g m^{-3}), Table 6.4. TiO_2 sol-gel coating of the silica-steel microcomposite particles (TiO_2(1)) increased the overall surface area, whilst corresponding TiO_2–P25 nanocomposite shell coated steel-silica microcomposite particles yielded the highest values, with an enhancement factor of over 100 compared to uncoated steel particles being achieved for P25(3) and P25(5) variants, Table 6.4. This shows that the TiO_2 layer is porous.

Table 6.4: Coated steel particle TiO_2 shell thickness values measured by cross-section Raman microscopy and BET isotherm surface areas.

Steel Particle Coating	TiO_2 Coating Thickness / μm	Surface Area / m^2 g^{-1}
Uncoated	-	0.13 ± 0.02
TiO_2(1)	5 ± 6	4.39 ± 1.32
P25(1)	6 ± 2	10.3 ± 1.9
P25(3)	10 ± 4	14.7 ± 1.5
P25(5)	27 ± 8	16.3 ± 1.7

6.3.4 Magnetic Recycling

Following immersion of TiO_2 coated silica-steel microcomposite particles into solution, a preliminary drop in detected methylene blue dye concentration was observed in darkness, Figure 6.11. This can be attributed to surface adsorption of dye reaching a plateau over a period of about 1 h. Subsequent UV illumination led to photocatalytic dye degradation. For recycling studies, the TiO_2-silica-steel multicomposite particles were magnetically removed from the solution between each UV exposure cycle. For instance, the first order rate constant for UV photodegradation of the dye was measured to be 2.31 ± 0.14 x 10^{-2} min^{-1} for the P25(3) photocatalyst during its fifth UV exposure recycle run; this value dropped to 0.73 ± 0.23 x 10^{-2} min^{-1} following magnetic removal of the photocatalyst particles (which is the same within error as measured in the control experiment using no TiO_2-silica-steel multicomposite particles (0.59 ± 0.15 x 10^{-2} min^{-1}), thereby ruling out photocatalyst leaching into solution). No visible change or rust was seen on these samples (with the silica double barrier layer) after 5 cycles. Control experiments showed that uncoated steel particles display a photocatalytic dye degradation rate constant of 0.43 ± 0.15 x 10^{-2} min^{-1}, which lies within the error range of background UV photodegradation (rate constant of 0.59 ± 0.15 x 10^{-2} min^{-1} in the absence of any particles). Furthermore, TiO_2 or TiO_2–P25 nanocomposite shell coated silica-steel microcomposite photocatalysts prepared without the interfacial silica double barrier layer led to rapid delamination of the photocatalyst coating upon immersion into methylene blue dye solution, culminating in the formation of rust visible to the naked eye.

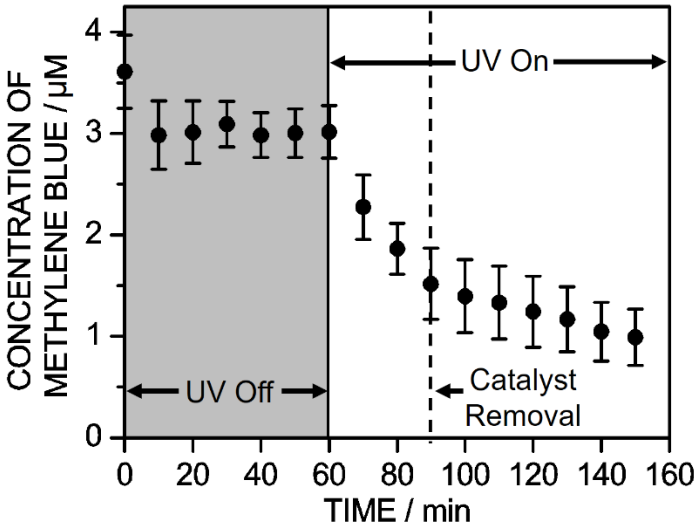

Figure 6.11: UV photocatalytic degradation profile of methylene blue dye solution (4 µM) using P25(3) coated silica-steel microcomposite particles (2.0 ± 0.3 mg mL^{-1} loading) during the fifth recycle run. Photocatalyst was magnetically removed after 30 min UV exposure, and the resulting methylene blue dye solution was exposed to UV for a further 60 min in the absence of photocatalyst. Error bars are the standard deviation of three repeat experiments.

First order rate constants (normalised to surface area) for the photodegradation of methylene blue dye solution during 1 h UV illumination were compared across the range of TiO_2 coated silica-steel microcomposite particle photocatalysts, Figure 6.12. TiO_2(1) shell coating displayed a lower rate constant compared to the TiO_2–P25 nanocomposite shell photocatalysts, with the highest rate constant being observed for triple coated sample (P25(3), 1.55 ± 0.25 x 10^{-2} min^{-1} m^{-2} leading to 92 ± 5% dye degradation after 1 h UV irradiation (82 ± 4% after 30 min)). Additional TiO_2–P25 nanocomposite coating layers led to no further gain in photocatalytic activities. This can be explained in terms of the limited penetration depth of UV photons into TiO_2 (140 nm),[98] which is significantly less than the coating thicknesses measured for all of the TiO_2–P25 nanocomposite shell photocatalysts, Table 6.4. The surface area normalised rate constants indicate that there is a definite enhancement in the photocatalytic activity through the incorporation of P(25) TiO_2 nanoparticles into the sol-gel TiO_2 shell coatings, whilst the total surface area appears to be the main factor contributing to dye photodegradation rates (within error) between the P25(1), P25(3), and P25(5) TiO_2 nanocomposite coatings, Table 6.4 and Figure 6.12.

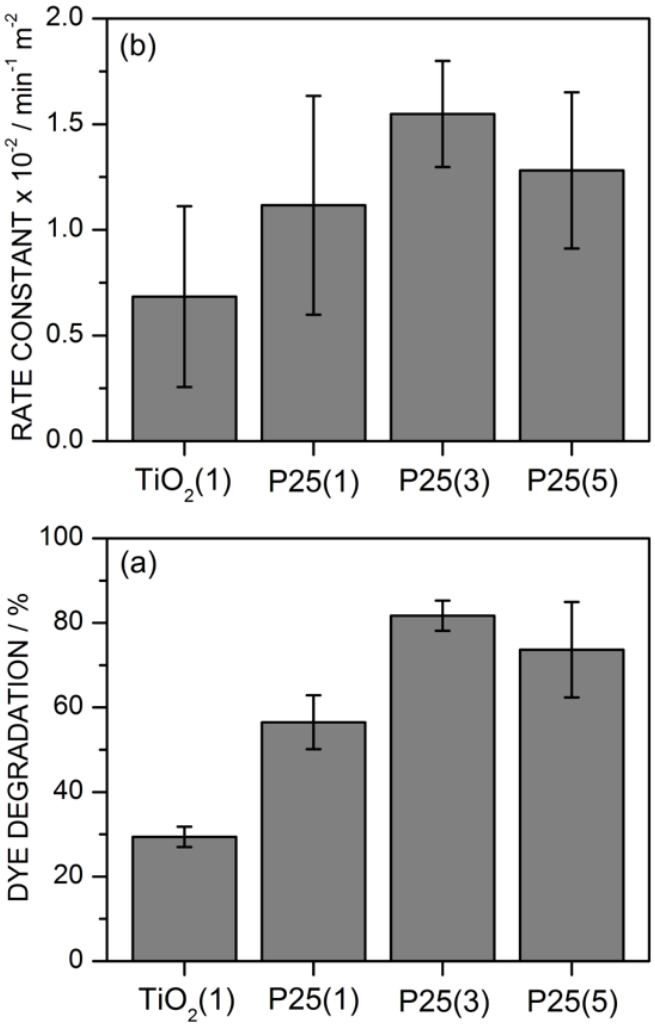

Figure 6.12: UV degradation of methylene blue dye solution (4 μM) using TiO_2 photocatalyst coated silica-steel microcomposite core particles (loadings of 2.0 ± 0.3 mg mL^{-1}): (a) percentage of dye degraded after 30 min continuous UV irradiation; and (b) dye degradation rate normalised to surface area (the large error values are due to propagation of error from surface area measurements). All photodegradation rates of the methylene blue dye solution were measured following an initial equilibration period in the dark for 1 h (see Figure 6.11). The background UV degradation rate (0.59 ± 0.15 x 10^{-2} min^{-1}) of methylene blue dye measured in the absence of any photocatalyst particles has been subtracted prior to surface area normalisation in all cases. For reference, dispersed P25 TiO_2 nanoparticles gave a surface area normalised dye photodegradation rate of 18.7 ± 2.0 x 10^{-2} min^{-1} m^{-2} (however, the use of P25 TiO_2 nanoparticles alone for water purification suffers from problems of environmental leaching and difficulty for reuse). Error bars are the standard deviation of three repeat experiments.

Magnetic separation recycling experiments were conducted on the most promising TiO_2 nanocomposite coated silica-steel microcomposite core particles (P25(3) and P25(5)). These did not display any change in photocatalytic activity (surface area corrected rate constant) over four recycle iterations, Figure 6.13. Percentage degradation of the methylene blue dye after 30 min of UV exposure for each photocatalyst during recycling displayed a similar trend. Thereby demonstrating the viability of these TiO_2–P25 nanocomposite coated silica-steel microcomposite core particles as magnetically recyclable photocatalysts.

6.4 Discussion

TiO_2 photocatalytic degradation of organic pollutants is widely understood to proceed via two predominant reaction pathways: firstly, by highly reactive hydroxyl radicals (originating from photoinduced lattice holes) reacting with pollutant molecules, and secondly by direct electron transfer between pollutant molecules and holes, Scheme 6.2. In competition with these photodegradative chemical processes, concurrent charge recombination and hydroxyl radical quenching to hydroxide anions takes place (e.g. by photogenerated electrons).[99,100] Adsorbed molecular oxygen also contributes to the overall photodegradation quantum yields.[101] This encompasses electron-hole pairs generated following the onset of UV illumination either undergoing recombination within the bulk, or electrons being trapped by defects and adsorbed surface species (such as molecular oxygen).[102,103,104] The hindering of surface charge recombination through electron trapping by adsorbed molecular oxygen increases hole formation, which in turn enhances reactive hydroxyl radical production.[99,105]

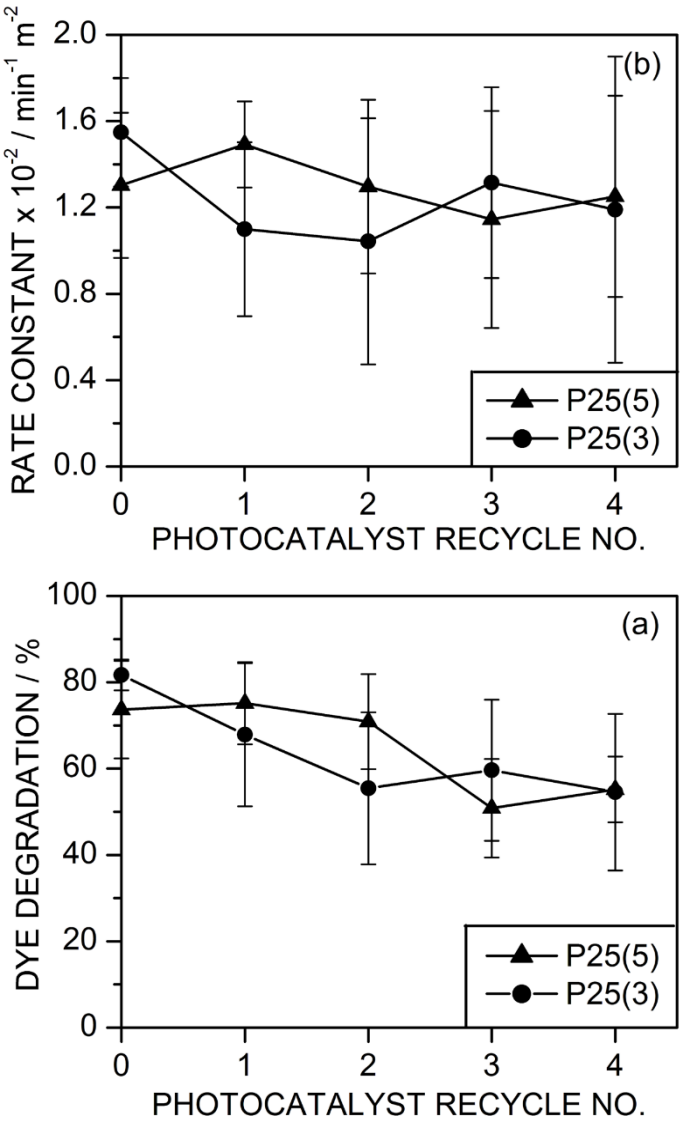

Figure 6.13: Magnetic separation recycling study using silica-steel microcomposite core with TiO_2–P25 nanocomposite shell photocatalyst particles (loading of 2.0 ± 0.3 mg mL^{-1}) for UV degradation of methylene blue dye solution (4 µM): (a) percentage of dye degraded after 30 min continuous UV irradiation; and (b) dye photodegradation rate normalised to surface area (the large error values are due to propagation of error from surface area measurements). All photodegradation rates of the methylene blue dye solution were measured following an initial equilibration period in the dark for 1 h (see Figure 6.11). The background UV degradation rate (0.59 ± 0.15 x 10^{-2} min^{-1}) of methylene blue dye measured in the absence of any photocatalyst particles has been subtracted prior to surface area normalisation in all cases. Error bars are the standard deviation of three repeat experiments.

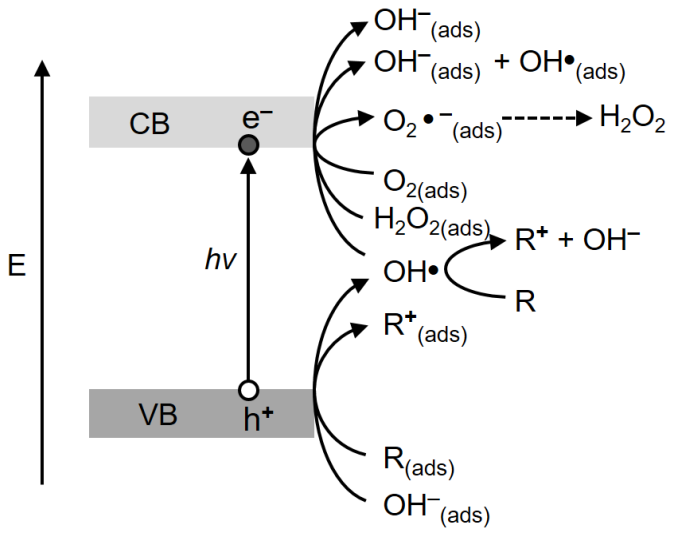

Scheme 6.2: Important reaction pathways during TiO_2 photocatalyst degradation of organic molecules (R).[106,107,108,109]

In the case of the present organic dye degradation study using silica-steel microcomposite core with TiO_2 shell photocatalyst, any direct interaction between steel particle surface iron oxides and the TiO_2 shell could potentially diminish photocatalytic activity in at least two ways. Firstly, by electron-hole recombination processes through transfer of photogenerated electrons and holes from the TiO_2 coating to the respective conduction and valence bands of the interfacial iron oxide (the smaller band gap of iron oxides compared to TiO_2 accelerates the recombination rate, and thus attenuates photocatalytic activity[49]).[110] Secondly, photogenerated electrons in the TiO_2 layer can migrate towards the underlying interface and reduce lattice Fe^{3+} ions to form the more soluble Fe^{2+} ions, thereby triggering photodissolution of TiO_2 coatings.[49] Such dissolved Fe^{2+} species are then able to react with hydroxyl radicals leading to a quenching of photocatalytic activity.[111] These unfavourable interactions between the steel particle iron oxide surface layer and the TiO_2 shell coating can be blocked by utilising a silica interfacial barrier layer.[48,49] A double silica barrier layer was found to be sufficient to block photocatalyst dissolution, as evidenced by the photocatalyst stability over extended magnetic recycling studies, Figure 6.13.

Despite rutile being the thermodynamically more stable bulk phase, sol-gel processing tends to favour the anatase phase.[112] This can be attributed to the lower surface energy of anatase driving its preferential formation due to the large surface area

to bulk volume ratio of the small particles typically formed during sol-gel processing.[113,114,115,116] Additional factors, such as the precursors employed and reaction conditions can also influence TiO_2 crystal growth.[117,118] The predominance of anatase TiO_2 in the sol-gel coatings employed in the present study (only a small amount of rutile polymorph found in P25(5)) is consistent with previous sol-gel TiO_2 calcination studies carried out at below 700 °C,[45] and TiO_2–P25 nanocomposite coatings deposited onto glass and flat steel substrates.[47,119]

The high photocatalytic activity reported for P25 TiO_2 nanoparticles is understood to be due to a combination of a large anatase (more photocatalytically active) to rutile ratio plus an inherent grain boundary structure.[120,121] This chapter describes the incorporation of P25 TiO_2 nanoparticles into the host TiO_2 sol-gel coating to form TiO_2–P25 nanocomposite shell coatings, which enhances photocatalytic activity for dye degradation, with the added benefit of easy magnetic separation and recycling, Figure 6.13. The measured high mass normalised dye degradation rates equal or exceed previously reported values for magnetically separable micron size photocatalytic particles tested under comparable reaction conditions.[33,34,36,37,40,42] Furthermore, the present magnetically separable photocatalysts are much cheaper, simpler to prepare, and readily scalable. All of these factors make them suitable for local manufacture and adoption in developing countries for sustainable water purification.

6.5 Conclusions

TiO_2 nanocomposite coated silica-steel microcomposite core particles have been synthesised by a cheap and easily scalable sol-gel method. These photocatalysts display high organic dye molecule degradation activities as well as ease of recyclability by magnetic separation from aqueous solution. A synergistic effect upon photocatalytic activity has been found involving level of TiO_2 nanoparticle loading and surface area of the TiO_2 nanocomposite shell coating.

6.7 References

[1] United Nations Water. http://www.unwater.org/statistics/statistics-detail/en/c/260727/ (accessed Feb 22, 2016).

[2] Almasri, M. N. Nitrate Contamination of Groundwater: A Conceptual Management Framework. *Environ. Impact Asses. Rev.* **2007**, *27*, 220–242.

[3] Jeevanandam, M.; Kannan, R.; Srinivasalu, S.; Rammohan, V. Hydrogeochemistry and Groundwater Quality Assessment of Lower Part of the Ponnaiyar River Basin, Cuddalore District, South India. *Environ. Monit. Assess.* **2007**, *132*, 263–274.

[4] Capel, P. D.; Larson, S. J.; Winterstein, T. A. The Behaviour of 39 Pesticides in Surface Waters as a Function of Scale. *Hydrol. Process.* **2001**, *15*, 1251–1269.

[5] Claver, A.; Ormad, P.; Rodríguez, L.; Ovelleiro, J. L. Study of the Presence of Pesticides in Surface Waters in the Ebro River Basin (Spain). *Chemosphere* **2006**, *64*, 1437–1443.

[6] Stehle, S.; Schulz, R. Agricultural Insecticides Threaten Surface Waters at the Global Scale. *Proc. Natl. Acad. Sci. USA* **2015**, *112*, 5750–5755.

[7] McDuffie, H. H.; Pahwa, P.; McLaughlin, J. R.; Spinelli, J. J.; Fincham, S.; Dosman, J. A.; Robson, D.; Skinnider, L. F.; Choi, N. W. Non-Hodgkin's Lymphoma and Specific Pesticide Exposures in Men: Cross-Canada Study of Pesticides and Health. *Cancer Epidemiol. Biomarkers Prev.* **2001**, *10*, 1155–1163.

[8] Betarbet, R.; Sherer, T. B.; MacKenzie, G.; Garcia-Osuna, M.; Panov, A. V.; Greenamyre, J. T. Chronic Systemic Pesticide Exposure Reproduces Features of Parkinson's Disease. *Nat. Neurosci.* **2000**, *3*, 1301–1306.

[9] Kamel, F.; Tanner, C. M.; Umbach, D. M.; Hoppin, J. A.; Alavanja, M. C. R.; Blair, A.; Comyns, K.; Goldman, S. M.; Korell, M.; Langston, J. W.; Ross, G. W.; Sandler, D. P. Pesticide Exposure and Self-Reported Parkinson's Disease in the Agricultural Health Study. *Am. J. Epidemiol.* **2007**, *165*, 364–374.

[10] Eskenazi, B.; Bradman, A.; Castorina, R. Exposures of Children to Organophosphate Pesticides and their Potential Adverse Health Effects. *Environ. Health Persp.* **1999**, *107*, 409–419.

[11] Brown, D. Effects of Colorants in the Aquatic Environment. *Ecotox. Environ. Safe.* **1987**, *13*, 139–147.

[12] Geenpeace. http://www.greenpeace.to/greenpeace/wp-content/uploads/2013/04/Technical-Report-02-2013.pdf (accessed Mar 1, 2016).

[13] Geenpeace. http://www.greenpeace.to/greenpeace/wp-content/uploads/2012/12/TechnicalReport-07-2012.pdf (accessed Mar 1, 2016).

[14] Geenpeace. http://www.greenpeace.to/greenpeace/wp-content/uploads/2012/03/Argentina-tanneries-Technical-Note-07-2011-final.pdf (accessed Mar 1, 2016).

[15] de Lima, R. O. A.; Bazo, A. P.; Salvadori, D. M. F.; Rech, C. M.; Oliveira, D. D.; Umbuzeiro, G. D. Mutagenic and Carcinogenic Potential of a Textile Azo Dye Processing Plant Effluent That Impacts a Drinking Water Source. *Mutat. Res-Gen. Tox. En.* **2007**, *626*, 53–60.

[16] Tsuboy, M. S.; Angeli, J. P. F.; Mantovani, M. S.; Knasmüller, S.; Umbuzeiro, G. A.; Ribeiro, L. R. Genotoxic, Mutagenic and Cytotoxic Effects of the Commercial Dye CI Disperse Blue 291 in the Human Hepatic Cell Line HepG2. *Toxicol. In Vitro* **2007**, *21*, 1650–1655.

[17] Sumathi, M.; Kalaiselvi, K.; Palanivel, M.; Rajaguru, P. Genotoxicity of Textile Dye Effluent on Fish (Cyprinus Carpio) Measured Using the Comet Assay. *Bull. Environ. Contam. Toxicol.* **2001**, *66*, 407–414.

[18] Birhanli, A.; Ozmen, M. Evaluation of the Toxicity and Teratogenity of Six Commercial Textile Dyes Using the Frog Embryo Teratogenesis Assay-Xenopus. *Drug Chem. Toxicol.* **2005**, *28*, 51–65.

[19] Matthews R. W.; Abdullah M.; Low G. K.-C. Photocatalytic Oxidation for Total Organic-Carbon Analysis. *Anal. Chim. Acta* **1990**, *233*, 171–179.

[20] Matthews R. W. Purification of Water with Near-UV Illuminated Suspensions of Titanium-Dioxide. *Water Res.* **1990**, *24*, 653–660.

[21] Low G. K.-C.; McEvoy S. R.; Matthews R. W. Formation of Ammonium and Nitrate Ions from Photocatalytic Oxidation of Ring Nitrogenous Compounds over Titanium Dioxide. *Chemosphere* **1989,** *19*, 1611–1621.

[22] Low G. K.-C.; McEvoy S. R.; Matthews R. W. Formation of Nitrate and Ammonium-Ions in Titanium-Dioxide Mediated Photocatalytic Degradation of Organic-Compounds Containing Nitrogen-Atoms. *Environ. Sci. Technol.* **1991**, *25*, 460–467.

[23] Augugliaro, V.; Palmisano, L.; Schiavello, M.; Sclafani, A.; Marchese, L.; Martra, G.; Miano, F. Photocatalytic Degradation of Nitrophenols in Aqueous Titanium-Dioxide Dispersion. *Appl. Catal.* **1991**, *69*, 323–340.

[24] Jacoby, W. A.; Maness, P. C.; Wolfrum, E. J.; Blake, D. M.; Fennell, J. A. Mineralization of Bacterial Cell Mass on a Photocatalytic Surface in Air. *Environ. Sci. Technol.* **1998**, *32*, 2650–2653.

[25] Ireland, J. C.; Klostermann, P.; Rice, E. W.; Clark, R. M. Inactivation of Escherichia Coli by Titanium-Dioxide Photocatalytic Oxidation. *Appl. Environ. Microbiol.* **1993**, *59*, 1668–1670.

[26] Saito, T.; Iwase, T.; Horie, J.; Morioka, T. Mode of Photocatalytic Bactericidal Action of Powdered Semiconductor TiO_2 on Mutans Streptococci. *J. Photochem. Photobiol. B: Biol.* **1992**, *14*, 369–379.

[27] Matsunaga, T.; Tomoda, R.; Nakajima, T.; Wake, H. Photoelectrochemical Sterilization of Microbial-Cells by Semiconductor Powders. *FEMS Microbiol. Lett.* **1985**, *29*, 211–214.

[28] Nel, A. E.; Mädler, L.; Velegol, D.; Xia, T.; Hoek, E. M. V.; Somasundaran, P.; Klaessig, F.; Castranova, V.; Thompson, M. Understanding Biophysicochemical Interactions at the Nano-Bio Interface. *Nat. Mater.* **2009**, *8*, 543–557.

[29] Bolis, V.; Busco, C.; Ciarletta, M.; Distasi, D.; Erriquez, J.; Fenoglio, I.; Livraghi, S.; Morel, S. Hydrophilic/Hydrophobic Features of TiO_2 Nanoparticles as a Function of Crystal Phase, Surface Area and Coating, in Relation to their Potential Toxicity in Peripheral Nervous System. *J. Colloid Interface Sci.* **2012**, *369*, 28–39.

[30] Long, T. C.; Saleh, N.; Tilton, R. D.; Lowry, G. V.; Veronesi, B. Titanium Dioxide (P25) Produces Reactive Oxygen Species in Immortalized Brain Microglia (BV2): Implications for Nanoparticle Neurotoxicity. *Environ. Sci. Technol.* **2006**, *40*, 4346–4352.

[31] Gurr, J.-R.; Wang, A. S. S.; Chen, C.-H.; Jan, K.-Y. Ultrafine Titanium Dioxide Particles in the Absence of Photoactivation can Induce Oxidative Damage to Human Bronchial Epithlial Cells. *Toxicology* **2005**, *213*, 66–73.

[32] Tawkaew, S.; Supothina, S. Preparation of Agglomerated Particles of TiO_2 and Silica-Coated Magnetic Particle. *Mater. Chem. Phys.* **2008**, *108*, 147–153

[33] Wang, Z.; Shen, L.; Zhu, S. Synthesis of Core-Shell Fe3O4@SiO2@TiO2 Microspheres and Their Application as Recyclable Photocatalysts. *Int. J. Photoenergy* [Online] **2012**, *2012,* Article ID 202519. http://www.hindawi.com/journals/ijp/2012/202519/cta/ (accessed Feb 22, 2016).

[34] Liu, R.; Wu, C. F.; Ger, M. D. Degradation of FBL Dye Wastewater by Magnetic Photocatalysts from Scraps. *J. Nanomater.* [Online] **2015**, *2015*, Article ID 651021. http://www.hindawi.com/journals/jnm/2015/651021/abs/ (accessed Feb 4, 2016).

[35] Chen, A.; Zeng, G.; Chen, G.; Hu, X.; Yan, M.; Guan, S.; Shang, C.; Lu, L.; Zou, Z.; Xie, G. Novel Thiourea-Modified Magnetic Ion-Imprinted Chitosan/TiO_2 Composite for Simultaneous Removal of Cadmium and 2,4-Dichlorophenol. *Chem. Eng. J.* **2012**, *191*, 85–94.

[36] Chen, Y.-H.; Liu, Y.-Y.; Lin, R.-H.; Yen, F.-S. Photocatalytic Degradation of p-Phenylenediamine with TiO_2-Coated Magnetic PMMA Microspheres in an Aqueous Solution. *J. Hazard. Mater.* **2009**, *163*, 973–981.

[37] Baiyila, D.; Wang, X.; Li, X.; Sharileaodu, B.; Li, X.; Xu, L.; Liu, Z.; Duan, L.; Liu, J. Electrospun TiO_2 Nanofibers Integrating Space-Separated Magnetic Nanoparticles and Heterostructures for Recoverable and Efficient Photocatalyst. *J. Mater. Chem. A* **2014**, *2*, 12304–12310.

[38] Horikoshi, S.; Serpone, N.; Hisamatsu, Y.; Hidaka, H. Photocatalyzed Degradation of Polymers in Aqueous Semiconductor Suspensions. 3. Photooxidation of a Solid Polymer: TiO2-Blended Poly(Vinyl Chloride) Film. *Environ. Sci. Technol.* **1998**, *32*, 4010–4016.

[39] Allen, N. S.; Bullen, D. J.; McKellar, J. F. Photooxidation of Commercial Polyethylene Containing Titanium-Dioxide (Rutile) - Antioxidant Systems. *J. Mater. Sci.* **1977**, *12*, 1320–1324.

[40] Li, Z.-Q.; Wang, H.-L.; Zi, L.-Y.; Zhang, J.-J.; Zhang, Y.-S. Preparation and Photocatalytic Performance of Magnetic TiO_2-Fe_3O_4/Graphene (RGO) Composites Under VIS-Light Irradiation. *Ceram. Int.* **2015**, *41*, 10634–10643.

[41] Li, C.-J.; Wang, J.-N.; Li, X.-Y.; Zhang, L.-L. Functionalization of Electrospun Magnetically Separable TiO2-Coated SrFe12O19 Nanofibers: Strongly Effective Photocatalyst and Magnetic Separation. *J. Mater. Sci.* **2011**, *46*, 2058–2063.

[42] Miranda, L. D. L.; Bellato, C. R.; Milagres, J. L.; Moura, L. G.; Mounteer, A. H.; de Almeida, M. F. Hydrotalcite-TiO2 Magnetic Iron Oxide Intercalated with the Anionic Surfactant Dodecylsulfate in the Photocatalytic Degradation of Methylene Blue Dye. *J. Environ. Manage.* **2015**, *156*, 225–235.

[43] Hench, L. L.; West, J. K. The Sol-Gel Process. *Chem. Rev.* **1990**, *90*, 33–72.

[44] Stober, W.; Fink, A.; Bohn, E. Controlled Growth of Monodisperse Silica Spheres in Micron Size Range. *J. Colloid Interface Sci.* **1968,** *26,* 62–69.

[45] Wang, C.-C.; Ying, J. Y. Sol−Gel Synthesis and Hydrothermal Processing of Anatase and Rutile Titania Nanocrystals. *Chem. Mater.* **1999**, *11*, 3113–3120.

[46] Nakanishi, K.; Takahashi, R.; Nagakane, T.; Kitayama, K.; Koheiya, N.; Shikata, H.; Soga, N. Formation of Hierarchical Pore Structure in Silica Gel. *J. Sol-Gel Sci. Technol.* **2000**, *17*, 191–210.

[47] Balasubramanian, G.; Dionysiou, D. D.; Suidan, M. T.; Subramanian, Y.; Baudin, I.; Laine, J.-M. Titania Powder Modified Sol-Gel Process for Photocatalytic Applications. *J. Mater. Sci.* **2003**, *38*, 823–831.

[48] Chen, F.; Zhao, J. Preparation and Photocatalytic Properties of a Novel Kind of Loaded Photocatalyst of TiO_2/SiO_2/γ-Fe_2O_3. *Catal. Lett.* **1999**, *58*, 245–247.

[49] Beydoun, D.; Amal, R.; Low, G.; McEvoy, S. Occurrence and Prevention of Photodissolution at the Phase Junction of Magnetite and Titanium Dioxide. *J. Mol. Catal. A: Chem.* **2002,** *180*, 193–200.

[50] Houas, A.; Lachheb, H.; Ksibi, M.; Elaloui, E.; Guillard, C.; Herrmann, J.-M. Photocatalytic Degradation Pathway of Methylene Blue in Water. *Appl. Catal. B: Environ.* **2001**, *31*, 145–157.

[51] Matthews, R. W. Photocatalytic Oxidation and Adsorption of Methylene Blue on Thin Films of Near-Ultraviolet-Illuminated TiO_2. *J. Chem. Soc., Faraday Trans. 1* **1989**, *85*, 1291–1302.

[52] Greenpeace. http://www.greenpeace.to/greenpeace/wp-content/uploads/2015/05/Pesticides-and-our-Health.pdf (accessed Mar 1, 2016).

[53] Barbeni, M.; Pramauro, E.; Pelizzetti, E.; Borgarello, E.; Serpone, N.; Jamieson, M. A. Photochemical Degradation of Chlorinated Dioxins, Biphenyls Phenols and Benzene on Semiconductor Dispersion. *Chemosphere* **1986**, *15*, 1913–1916.

[54] Barbeni, M.; Pramauro, E.; Pelizzetti, E.; Borgarello, E.; Serpone, N. Photodegradation of Pentachlorophenol Catalyzed by Semiconductor Particles. *Chemosphere* **1985**,*14*, 195–208.

[55] Matthews, R. W. Photooxidation of Organic Material in Aqueous Suspensions of Titanium-Dioxide. *Water Res.* **1986,** *20*, 569–578.

[56] Ehrlich, C. D.; Basford, J. A. Recommended Practices for the Calibration and Use of Leaks. *J. Vac. Sci. Technol. A* **1992**, *10,* 1–17.

[57] Evonik Industries. https://www.aerosil.com/sites/lists/IM/Documents/TI-1243-Titanium-Dioxide-as-Photocatalyst-EN.pdf (accessed Jul 8, 2015).

[58] Brunauer, S.; Emmett, P. H.; Teller, E. Adsorption of Gases in Multimolecular Layers. *J. Am. Chem. Soc.* **1938**, *60*, 309–319.

[59] Lewis, G. N.; Bigeleisen, J. Methylene Blue and Other Indicators in General Acids. The Acidity Function. *J. Am. Chem. Soc.* **1943**, *65*, 1144–1150.

[60] Tanuma, S.; Powell, C. J.; Penn, D. R. Calculations of Electron Inelastic Mean Free Paths. 3. Data for 15 Inorganic-Compounds Over the 50-2000-eV Range. *Surf. Interface Anal.* **1991**, *17*, 927–939.

[61] Cumpson, P. J.; Seah, M. P. Elastic Scattering Corrections in AES and XPS .2. Estimating Attenuation Lengths and Conditions Required for Their Valid Use in Overlayer/Substrate Experiments. *Surf. Interface Anal.* **1997**, *25*, 430–446.

[62] Gimzewski, J. K.; Padalia, B. D.; Affrossman, S.; Watson, L. M.; Fabian, D. J. Reaction of Oxygen and Water with Iron Films Studied by X-Ray Photoelectron Spectroscopy. *Surf. Sci.* **1977**, *62*, 386–396.

[63] Moulder, J. F.; Stickle, W. F.; Sobol, P. E.; Bomden, K. D. In *Handbook of X-ray Photoelectron Spectroscopy*; Chastain, J., Eds.; Perkin-Elmer Corporation: Minnesota, 1992; pp 45.

[64] Liu, P.; Kendelewicz, T.; Brown Jr., G. E.; Nelson, E. J.; Chambers, S. A. Reaction of Water Vapour with *α*-Al2O3(0001) and *α*-Fe2O3(0001) Surfaces: Synchrotron X-Ray Photoemission Studies and Thermodynamic Calculations. *Surf. Sci.* **1998**, *417*, 53–65.

[65] Görlich, E.; Haber, J.; Stoch, A.; Stoch, J. XPS Study of α-Quartz Surface. *J. Sol. State Chem.* **1980**, *33*, 121–124.

[66] Paparazzo, E.; Fanfoni, M.; Severini, E.; Priori, S. Evidence of Si-OH Species at the Surface of Aged Silica. In *J. Vac. Sci Technol. A*, 38th National Symposium of the American Vacuum Society, Seattle, WA, Nov 11–15, 1991; American Institute of Physics: New York, 1992; pp 2892–2896.

[67] Colomban, Ph.; Cherifi, S.; Despert, G. Raman Identification of Corrosion Products on Automotive Galvanized Steel Sheets. *J. Raman Spectrosc.* **2008**, *39*, 881–886.

[68] Colomban, Ph. Raman Studies of Inorganic Gels and of Their Sol-to-Gel, Gel-to-Glass and Glass-to-Ceramics Transformations. *J. Raman Spectrosc.* **1996**, *27*, 747–758.

[69] Kato, K. Transformation of Alkoxy-Derived SiO_2 Gels Without Catalysts to Glasses. *J. Mater. Sci.* **1991**, 2*6*, 6777–6781.

[70] Stolen, R. H.; Walrafen, G. E. Water and its Relation to Broken Bond Defects in Fused Silica. *J. Chem. Phys.* **1976**, *64*, 2623–2631.

[71] Horiba Application Note. http://www.horiba.com/fileadmin/uploads/Scientific/Documents/Raman/Semiconductors01.pdf (accessed Sep 14, 2016)

[72] Presser, V.; Keuper, M.; Berthold, C.; Nickel, K. G. Experimental Determination of the Raman Sampling Depth in Zirconia Ceramics. *Appl. Spectrosc.* **2009**, *63*, 1288–1292.

[73] Colomban, Ph.; Cherifi, S.; Despert, G. Raman Identification of Corrosion Products on Automotive Galvanized Steel Sheets. *J. Raman Spectrosc.* **2008**, *39*, 881–886.

[74] Kato, K. Transformation of Alkoxy-Derived SiO_2 Gels Without Catalysts to Glasses. *J. Mater. Sci.* **1991**, *26*, 6777–6781.

[75] Stolen, R. H.; Walrafen, G. E. Water and its Relation to Broken Bond Defects in Fused Silica. *J. Chem. Phys.* **1976**, *64*, 2623–2631.

[76] Beattie, I. R.; Gilson, T. R. Single Crystal Laser Raman Spectroscopy. *Proc. Roy. Soc. A.* **1968**, *307*, 407–429.

[77] Ohsaka, T.; Izumi, F.; Fujiki, Y. Raman-Spectrum of Anatase, TiO_2. *J. Raman Spec.* **1978**, *7*, 321–324.

[78] Beattie, I. R.; Gilson, T. R. Single Crystal Laser Raman Spectroscopy. *Proc. Roy. Soc. A.* **1968**, *307*, 407–429.

[79] Ohsaka, T.; Izumi, F.; Fujiki, Y. Raman-Spectrum of Anatase, TiO_2. *J. Raman Spec.* **1978**, *7*, 321–324.

[80] Narayanan, P. S. Raman Spectrum of Rutile: Polarisation Studies. *P. Indian Acad. Sci. A* **1953**, *37*, 411–414.

[81] Porto, S. P. S.; Fleury, P. A.; Damen, T. C. Raman Spectra of TiO_2, MgF_2, ZnF_2, FeF_2, and MnF_2. *Phys. Rev.* **1967**, *154*, 522–526.

[82] Hsu, L. S.; Rujkorakarn, R.; Sites, J. R.; She, C. Y. Thermally Induced Crystallization of Amorphous-Titania Films. *J. Appl. Phys.* **1986**, *59*, 3475–3480.

[83] Exarhos, G. J.; Hess, N. J. Phase Transformation Dynamics, Melting and Stress Evolution in Dielectric Films and at Surfaces. *J. Raman Spectrosc.* **1996**, *27*, 765–774.

[84] Walrafen, G. E. Raman Spectral Studies of Water Structure. *J. Chem. Phys.* **1964**, *40*, 3249–3256.

[85] Loh, E. Optical Vibrations in Sheet Silicates. *J. Phys. C. Solid State Phys.* **1973**, *6*, 1091–1104.

[86] Nakabayashi, T.; Kosugi, K.; Nishi, N. Liquid Structure of Acetic Acid Studied by Raman Spectroscopy and Ab Initio Molecular Orbital Calculations. *J. Phys. Chem*. *A* **1999**, 103, 8595–8603.

[87] Bickley, R. I.; Gonzalez-Carreno, T.; Lees, J. S.; Palmisano, L; Tilley, R. J. D. A Structural Investigation of Titanium-Dioxide Photocatalysts. *J. Solid State Chem.* **1991**, *92*, 178–190.

[88] Swanson, H. E.; McMurdie, H. F.; Morris, M. C.; Evans, E. H. *Standard X-Ray Diffraction Powder Patterns;* National Bureau of Standards Monograph 25 Section 7; National Bureau of Standards: Washington, DC, 1969; pp. 82–83.

[89] Spurr, R. A.; Myers, H. Quantitative Analysis of Anatase-Rutile Mixtures with an X-Ray Diffractometer. *Anal. Chem.* **1957**, *29*, 760–762.

[90] Swanson, H. E.; McMurdie, H. F.; Morris, M. C.; Evans, E. H. *Standard X-Ray Diffraction Powder Patterns;* National Bureau of Standards Monograph 25 Section 5; National Bureau of Standards: Washington, DC, 1969; pp. 31.

[91] Morris, M. C.; McMurdie, H. F.; Evans, E. H; Paretzkin, B.; Parker, H. S.; Panagiotopoulos, N. C. *Standard X-Ray Diffraction Powder Patterns;* National Bureau of Standards Monograph 25 Section 18; National Bureau of Standards: Washington, DC, 1969; pp. 37.

[92] Naldoni, A.; Allieta, M.; Santangelo, S.; Marelli, M; Fabbri, F.; Cappelli, S.; Bianchi, C. L.; Psaro, R.; Dal Santo, V. Effect of Nature and Location of Defects on Bandgap Narrowing in Black TiO2 Nanoparticles. *J. Am. Chem. Soc.* **2012**, *134*, 7600–7603.

[93] Knorr, F. J.; Zhang, D.; McHale, J. L. Influence of TiCl4 Treatment on Surface Defect Photoluminescence in Pure and Mixed-Phase Nanocrystalline TiO2. *Langmuir*, **2007**, *23*, 8686–8690.

[94] Tang, H.; Prasad, K.; Sanjinès, R.; Schmid, P. E.; Lévy, F. Electrical and Optical Properties of TiO2 Anatase Thin Films. *J. Appl. Phys.* **1994**, *75*, 2042–2047.

[95] Nagaveni, K.; Hegde, M. S.; Ravishankar, N.; Subbanna, G. N.; Madras, G. Synthesis and Structure of Nanocrystalline TiO2 with Lower Band Gap Showing High Photocatalytic Activity. *Langmuir* **2004**, *20*, 2900–2907.

[96] Murphy, A. B. Band-gap Determination from Diffuse Reflectance Measurements of Semiconductor Films, and Application to Photoelectrochemical Water-Splitting. *Sol. Energ. Mat. Sol. Cells* **2007**, *91*, 1326–1337.

[97] Chen, X.; Liu, L.; Yu, P. Y.; Mao, S. S. Increasing Solar Absorption for Photocatalysis with Black Hydrogenated Titanium Dioxide Nanocrystals. *Science* **2011**, *331*, 746–750.

[98] Tada, H.; Tanaka, M. Dependence of TiO_2 Photocatalytic Activity upon its Film Thickness. *Langmuir* **1997**, *13*, 360–364.

[99] Riegel G.; Bolton J. R. Photocatalytic Efficiency Variability in TiO_2 Particles. *J. Phys. Chem.* **1995**, *99*, 4215–4224.

[100] Munuera, G.; Rives-Arnau, V.; Saucedo, A. Photo-Adsorption and Photo-Desorption of Oxygen on Highly Hydroxylated TiO_2 Surfaces. Part 1. – Role of Hydroxyl Groups in Photo-Adsorption. *J. Chem. Soc., Faraday Trans.* **1979**, *75*, 736–747.

[101] Gerischer, H. Photoelectrochemical Catalysis of the Oxidation of Organic Molecules by Oxygen on Small Semiconductor Particles with TiO_2 as an Example. *Electrochim. Acta* **1993**, *38*, 3–9.

[102] Howe, R. F.; Grätzel, M. EPR Observation of Trapped Electrons in Colloidal Titanium Dioxide. *J. Phys. Chem.* **1985**, *89*, 4495–4499.

[103] Henderson, M. A.; Epling, W. S.; Peden, C. H. F. Perkins, C. L. Insights into Photoexcited Electron Scavenging Processes on TiO_2 Obtained from Studies of the Reaction of O_2 with OH Groups Adsorbed at Electronic Defects on TiO2(110). *J. Phys. Chem. B* **2003**, *107*, 534–545.

[104] Anpo, M.; Che, M; Fubini, B.; Garrone, E.; Giamello, E.; Paganini, M. C. Generation of Superoxide Ions at Oxide Surfaces. *Top. Catal.* **1999**, *8*, 189–198.

[105] Anpo, M.; Chiba, K.; Tomonari, M.; Coluccia, S.; Che, M.; Fox, M. A. Photocatalysis on Native and Platinum-Loaded TiO_2 and ZnO Catalysts — Origin of Different Reactivities on Wet and Dry Metal Oxides —. *Bull. Chem. Soc. Jpn*. **1991**, *64*, 543–551.

[106] Okamoto, K.; Yamamoto, Y.; Tanaka, H.; Itaya, A. Kinetics of Heterogeneous Photocatalytic Decomposition of Phenol over Anatase TiO_2 Powder. *Bull. Chem. Soc. Jpn.* **1985**, *58*, 2023–2028.

[107] Okamoto, K.; Yamamoto, Y.; Tanaka, H.; Tanaka, M.; Itaya, A. Heterogeneous Photocatalytic Decomposition of Phenol over TiO_2 Powder. *Bull. Chem. Soc. Jpn.* **1985**, *58*, 2015–2022.

[108] Turchi, C. S.; Ollis, D. F. Photocatalytic Degradation of Organic Water Contaminants: Mechanisms Involving Hydroxyl Radical Attack. *J. Catal.* **1990**, *112*, 178–192.

[109] Draper, R. B.; Fox, M. A. Titanium Dioxide Photosensitized Reactions Studied by Diffuse Reflectance Flash Photolysis in Aqueous Suspensions of TiO_2 Powder. *Langmuir* **1990**, *6*, 1396–1402.

[110] Beydoun, D.; Amal, R.; Low, G. K. C.; McEvoy, S. Novel Photocatalyst: Titania-Coated Magnetite. Activity and Photodissolution. *J. Phys. Chem. B* **2000,** *104*, 4387–4396.

[111] Narayani, H.; Arayapurath, H.; Shukla, S. Using Fenton-Reaction as a Novel Approach to Enhance the Photocatalytic Activity of TiO_2-γ-Fe_2O_3 Magnetic Photocatalyst Undergoing Photo-Dissolution Process without Silica Interlayer. *Catal. Lett.* **2013**, *143*, 807–816.

[112] Anderson, M. A.; Gieselmann, M. J.; Xu, Q. Titania and Alumina Ceramic Membranes. *J. Membr. Sci.* **1988**, *39*, 243–258.

[113] Zhang, H.; Banfield, J. F. Thermodynamic Analysis of Phase Stability of Nanocrystalline Titania. *J. Mater. Chem.* **1998**, *8*, 2073–2076.

[114] Zhang, H.; Banfield, J. K. Understanding Polymorphic Phase Transformation Behavior during Growth of Nanocrystalline Aggregates: Insights from TiO_2. *J. Phys. Chem. B* **2000**, *104*, 3481–3487.

[115] Naicker, P. K.; Cummings, P. T.; Zhang, H.; Banfield, J. F. Characterization of Titanium Dioxide Nanoparticles Using Molecular Dynamics Simulations. *J. Phys. Chem. B* **2005**, *109*, 15243–15249.

[116] Navrotsky, A. Energetics of Nanoparticle Oxides: Interplay Between Surface Energy and Polymorphism. *Geochem. Trans.* **2003**, *4*, 34–37.

[117] Yanagisawa, K.; Ovenstone, J. Crystallization of Anatase from Amorphous Titania Using the Hydrothermal Technique: Effects of Starting Material and Temperature. *J. Phys. Chem. B* **1999**, *103*, 7781–7787.

[118] Yanagisawa, K.; Yamamoto, Y.; Feng, Q.; Yamasaki, N. Formation Mechanism of Fine Anatase Crystals from Amorphous Titania under Hydrothermal Conditions *J. Mater. Res.* **1998**, *13*, 825–829.

[119] Chen, Y.; Dionysiou, D. D. TiO2 Photocatalytic Films on Stainless Steel: The Role of Degussa P-25 in Modified Sol–Gel Methods. *Appl. Catal. B: Environ.* **2006**, *62*, 255–264.

[120] Jing, L.; Li, S.; Song, S.; Xue, L.; Fu, H. Investigation on the Electron Transfer Between Anatase and Rutile in Nano-Sized TiO2 by Means of Surface Photovoltage Technique and its Effects on the Photocatalytic Activity. *Sol. Energ. Mat. Sol. Cells* **2008**, *92*, 1030–1036.

[121] Hurum, D. C.; Agrios, A. G.; Gray. K. A. ; Rajh, T.; Thurnauer, M. C. Explaining the Enhanced Photocatalytic Activity of Degussa P25 Mixed-Phase TiO_2 Using EPR. *J. Phys. Chem. B* **2003**, *107*, 4545–4549.

Chapter 7 Metal Oxide TiO_2 Photocatalytic Composite Macrospheres

7.1 Introduction

Water purification methods such as Solar Disinfection (SODIS)[1] and metal oxide photocatalytic purification has been demonstrated to be highly effective for the destruction of common water-borne pathogens.[2,3,4,5] As discussed in Chapters 1 and 6. one of the most common materials for photocatalytic purification is TiO_2,[6,7,8,9,,10] due to its band gap of 3.2 eV for anatase and 3.0 eV for rutile,[11] which is suited for the generation of hydroxyl radicals and oxidation of organic molecules. However, the absorption of TiO_2 is limited to the UV region of daylight, therefore only 3–5 % of sunlight can be utilised for photocatalysis.

To overcome this inefficiency, attempts have been made to decrease the band gap by doping with anions and transition metals. However, the latter has yet to show promise for significantly changing the band gap and typically suffers from thermal instability of the doped material.[12,13] Whilst many studies achieve band tailing resulting in a slight increase in photocatalytic efficiency, few achieve significant band gap modification. Experimental results show that nitrogen doping of TiO_2 can increase the absorption range to include visible light by reducing the band gap by 0.6 eV for rutile,[14] and 0.5 eV for anatase.[15] Urea, amine, hydrazine and thiourea are common sources of nitrogen for doping TiO_2,[16] however none provide a significant reduction in band gap.

Ammonia plasma treatment has proved to be one of the most successful methods for doping nitrogen, demonstrating band gap tuning from 3.10–1.52 eV, therefore absorbing light up to around 800 nm.[17] The reductions in band gap correlated well with an increase in nitrogen content in the film. Other successful methods have included ball milling,[18] oxidation of titanium nitride[19,20] and surface alloying of TiO_2 to stainless steel.[21]

Fluorine doping has been demonstrated to significantly increase the photocatalytic activity of TiO_2 due to promoted separation of photo-generated electrons and holes,[22] however the use of fluorine-containing reagents may reduce the widespread applicability of this method due to environmental concerns.[23] Sulphur has also showed potential for TiO_2 doping, however its large ionic radius hinders incorporation into the ionic lattice.[24,25]

Carbon doping has proved to be effective for band gap reduction, generated from titanium carbide and titanium metal-derived oxides, however the flame oxidation method tends to yield predominantly rutile phase, along with little controllability over morphology.[26,27] One of the benefits of using carbon doping is that the carbon source can be a titanium organic precursor, resulting in in situ doping, reducing the number of experimental steps. Chemical vapour deposition,[28] and templating on polymers and carbon black,[29,30,31] have all been demonstrated to show significant band gap reductions and visible light absorption through in-situ doping. Direct comparison of many of these materials is challenging as photocatalytic testing is carried out under a wide range of conditions.

Currently reported doping of TiO_2 is often focussed on nano or microscale particles, which require post reaction filtration. Whilst this may be practicable in an industrial scenario, for point of use drinking water purification simple catalyst separation is of vital importance. In addition, any material designed for this purpose must be low cost, with simple processing requirements and as few synthetic steps as possible. To this end, any doping of the TiO_2 photocatalyst must be carried out in situ with the synthesis steps.

Visible light photocatalytic TiO_2 has been prepared using intrinsic carbon within the alkoxide precursors of sol gels through calcinations,[32,33] as well as hydrolysis with bases.[34] Sol-gel chemistry is already widely employed for the large scale manufacture of silica and titania aerogels, nanopowders, and coatings.[35] Typically this involves acid hydrolysis of titania precursors, substrate coating via various methods including dip coating and followed by a final thermal curing step.[36] Chitosan has previously been used for improving the photocataytic activity of TiO_2,[37,38] as well as facilitating synthesis of pure TiO_2 spheres.[39,40,41]

In this chapter, a simple in situ synthesis of doped and undoped P25-TiO_2 composite macrospheres is described, comprising chitosan viscosity modulation of a TiO_2 sol-gel and loading of P25 filler powder before formation and curing of spherical particles. Synthesised macrospheres were then dried and calcined under different gas conditions to yield carbon doped and undoped photocatalysts. These P25-TiO_2 composite macrospheres have been characterised by BET surface area analysis, UV-Vis diffuse reflectance spectroscopy and Raman microscopy. Photocatalytic degradation rates under UV and visible light illumination and absorption properties have been measured using aqueous methylene blue dye solution.[42,43]

7.2 Experimental Section

7.2.1 Synthesis of P25-TiO_2 Composite Macrospheres

Composite macrospheres were synthesised using a modified sol-gel precipitation route. A TiO_2 sol-gel solution was prepared by stirring a solution of 33 wt% hydrochloric acid (32 wt% in water, Sigma-Aldrich Co. LLC.) in ethanol (+99.8 wt% Fisher Scientific UK Ltd.), followed by the addition of titanium isopropoxide (+97 wt%, Sigma-Aldrich Co. LLC.) in a molar ratio to ethanol of 1:5. Once mixed, 5 wt% of Aeroxide® P25 TiO_2 nanoparticles (anatase : rutile ratio 80 : 20 wt%, BET surface area 50 $m^2 g^{-1}$, Acros Organics)[44] was added and the solution was stirred for 1 h. The sol-gel solutions were used within 48 h of synthesis, whilst the sol-gel remained at its lowest inherent viscosity (typically comprising particles in the nanometre size range).[35] A separate solution comprising 1.9 wt% chitosan (medium molecular weight, Sigma-Aldrich Co. LLC.) in 5 vol% aqueous acetic acid (>99 wt%, Fisher Scientific UK Ltd., diluted in high purity water) was stirred for 1 h before use. The prepared TiO_2 sol-gel solution was added dropwise to the chitosan solution with continual stirring to prevent agglomeration, until the solution comprised 62 wt% TiO_2 sol-gel solution. The resultant solution was used immediately for macrosphere synthesis.

Gelation of the chitosan — TiO_2 sol-gel solution was carried out using an 80:20 (v:v) high purity water and ammonia solution (35 wt% in water, Fisher Scientific UK Ltd.). The viscous solution was added dropwise via a 50 mL plastic syringe to approximately 500 mL of ammonia solution at a height of 15 cm and a rate of one droplet per second. Upon contact with the ammonia solution, the external surface of the droplet gelled, retaining the spherical shape. The newly formed P25-TiO_2 composite macrospheres were allowed to gel for 1 h in the ammonia solution before draining and washing with high purity water. The wet spheres were dried for 16 h at room temperature, during which time their size reduced significantly. Further drying steps were carried out at 80 ºC in air followed by heating at 60 °C under vacuum (60 Torr) for 2 h.

Calcination of the P25-TiO_2 composite macrospheres was carried out in a cylindrical quartz tube furnace at 600 °C for 3 h using a ramp rate of 10 °C min^{-1} up to 450 °C and 5 °C min^{-1} up to 600 °C under a dry (<60 ppm H_2O, Series 3 moisture monitor, GE Panametrics Ltd.) gas flow of O_2 (99.5 vol%, BOC Ltd., 20 cm^3 min^{-1}) and N_2 (99.998 vol%, BOC Ltd., 80 cm^3 min^{-1}), herein referred to as MS(N_2/O_2). Alternatively, the calcination

was carried out under the same temperature conditions but under N_2 flow (100 cm^3 min^{-1}), herein referred to as MS(N_2).

7.2.2 Characterisation of P25-TiO_2 Composite Macrospheres

Particle sizes were measured using a light microscope (Model BX40, Olympus Corp.). Particle surface area was determined using the BET method[45] (model BET-201 sorptometer, PMI Inc.). Prior to recording nitrogen adsorption isotherms, the samples (100–200 mg) were degassed under vacuum (<0.05 mbar) at 200 ºC for 3 h.

UV-Vis absorbance spectra of coated quartz slides were acquired using a custom built centre-mount low density PTFE integrating sphere with an internal diameter of 100 mm. Illumination was provided from a deuterium tungsten-halogen fibre optic source (model DH-2000-S, Ocean Optics Inc., 215–2500 nm range), and the reflected light was analysed by a fibre coupled CCD spectrophotometer (200–850 nm range, model USB-2000+, Ocean Optics Inc.).

Raman spectra were acquired on a confocal microscope laser Raman system (model Labram 1B, Instruments S. A. (UK) Ltd.) equipped with a 15 mW He-Ne laser (6328 Å) excitation source and an air-cooled CCD detector (model SpectrumOne CCD 2000). Samples were set into epoxy resin (5 : 2 mixture of Epoxy resin L : Hardener S, R&G Faserverbundwerkstoffe GmbH Composite Technology) at 1 wt%, cured for 24 h at room temperature (20 °C), then cross sectioned using sequential polishing with dry silicon carbide finishing paper (p400 and p1200 grit, manufactured by Bibielle S.p.A., supplied by MSC Industrial Supply Co.) and alumina metal polish (Solvol®, Autosol LLC.).

7.2.3 Photocatalytic Testing

P25-TiO_2 composite macrospheres (solution concentration of 5.0 mg mL^{-1}) were tested under UV illumination in a 100 mL volume cylindrical borosilicate glass reaction vessel (fitted with a quartz window) filled with 90 mL of a 2.0 μM aqueous solution of methylene blue dye (+70 wt%, TCL UK Ltd.), Figure 7.1. Particles were agitated using a vertically mounted magnetic stirrer hot plate (IKAMAG RCT, IKA®-Werke GmbH & Co. KG) in contact with the back face of the reactor and stirrer bar. Oxygen dissolution was maintained via a glass diffuser bubbling oxygen at a flow rate of 5 cm^3 min^{-1} at 1.5 Bar pressure. A Hg-Xe short arc lamp (model 6136, 200 W rated, operating at 26 V and 7 A, Oriel Newport Corp.) positioned 15 cm away from the reactor quartz window provided an

incident UV flux of 7.4 ± 1.4 mW cm^{-2} onto the solution (measured with a thermopile and digital voltmeter, model 5300, Applied Photophysics Ltd.). A contact thermometer was used as part of a feedback loop to the stirrer hot plate in order to maintain the reaction vessel temperature at 28 ± 2 °C. Prior to UV irradiation, the P25-TiO_2 composite macrospheres were allowed to equilibrate in the methylene blue dye solution for 5 min in order to determine the extent of methylene blue dye adsorption onto the macrospheres. 1 mL aliquots, filtered through a 0.22 μm polyethersulfone syringe filter (Gilson Scientific Ltd.), were taken prior to the addition of photocatalyst, and at 10 min intervals during UV illumination for UV-Vis absorption spectroscopy analysis of methylene blue dye concentrations at λ_{max} = 660 nm (model UV4, Unicam Lda.).[46] Dye photodegradation rate constants were calculated from absorbance readings taken over 1 h of UV exposure assuming first order kinetics (over this period dye degradation did not reach a point where mass transfer and other effects caused a deviation from linearity of the plots).[47,48] UV degradation of methylene blue dye in the absence of macrospheres served as a control (the measured rate constant of 5.9 ± 1.5 x 10^{-3} min^{-1} was subtracted for each set of photocatalysis experiments).

Visible light irradiation was studied using a custom made horizontal bed continuous flow reactor, Figure 7.1, comprising a shallow cylindrical reaction chamber (100 x 20 mm) through which the methylene blue dye solution (20 μM, 400 mL) was pumped from a sump. The solution was separated by an overflow into a run-off tray and returned to the sump for recirculation. The solution was circulated through the system for 1 h prior to catalyst addition to equilibrate the adsorption onto the pump and reactor walls. Visible light illumination was provided by a halogen bulb with a similar spectral distribution to natural sunlight without the UV component (Decostar 51, 50 W, Osram GmbH), mounted 150 mm from the reactor quartz window with an incident flux of 0.8 mW cm^{-2} onto the solution (measured with a thermopile and digital voltmeter, model 5300, Applied Photophysics Ltd.) through an infrared filter (UQG Ltd.). Under flow, the macrospheres (0.50 g) were suspended in the dye solution providing even illumination of the catalyst. Dye degradation was measured in the same manner as for UV illumination studies, however samples were taken from the sump at 30 min intervals rather than 5 min.

.

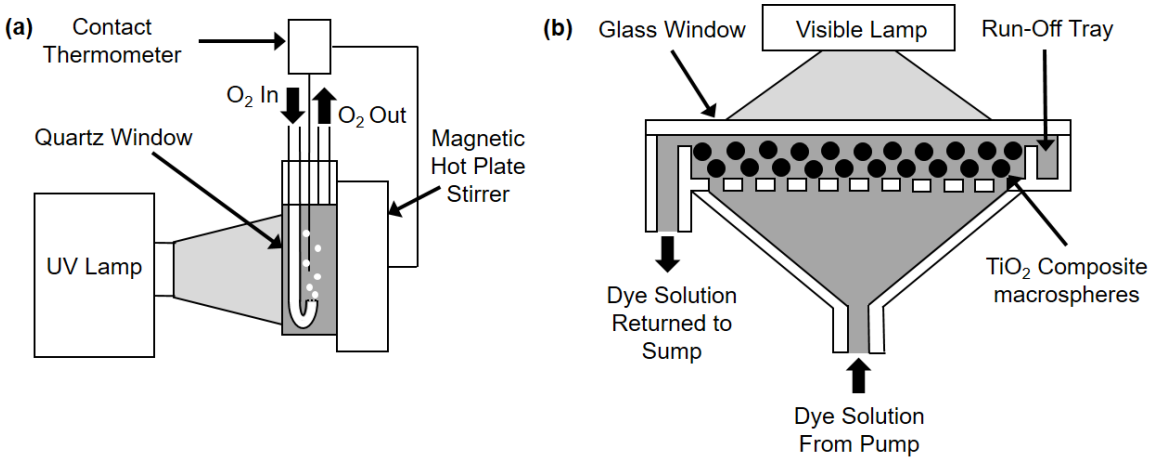

Figure 7.1: Schematic of: (a) borosilicate glass photoreactor fitted with a quartz front window and magnetic hot plate stirrer used for UV photodegradation studies; and (b) acrylic horizontal bed reactor fitted with a glass top window and recycling system used for degradation studies in the presence and absence of visible light.

7.3 Results

7.3.1 Synthesis of P25-TiO2 Composite Macrospheres

Particle size analysis on post-calcination P25-TiO_2 composite macrospheres shows that calcination environment did not affect the size of the spherical particles, Table 7.1. However, the BET surface area of the composite macrospheres varied significantly between the two calcination environments, with a pure nitrogen atmosphere resulting in a 4.3 times higher surface area. Synthesis of macrospheres without the addition of P25 TiO_2 resulted in a disruption of the spherical shape and poor mechanical properties of the calcined macrospheres.

Table 7.1: P25-TiO_2 composite macrosphere (MS) particle sizes and surface areas calcined under different gas flows (100 cm^3 min^{-1}).

Sample Code	Calcination Gas	Average Particle Size / mm	Surface Area / m^2 g^{-1}
MS(N_2/O_2)	80:20 N_2:O_2	1.0 ± 0.2	28 ± 1
MS(N_2)	N_2	0.9 ± 0.2	121 ± 5

The UV-Vis absorption spectrum of N_2/O_2 calcined P25-TiO_2 composite macrospheres displays a distinct band gap typical of a semiconductor material, with an uncharacteristic absorbance at wavelengths in the visible region, Figure 7.2. The measured band gap of 415 nm (2.98 eV) for N_2/O_2 calcined macrospheres is consistent with both measured and previous reported values for P25 TiO_2 nanoparticles (3.08 eV),[49,50] Figure 7.2. Tailing of the absorbance beyond the band gap is likely due to the incorporation of carbon from the organic precursors forming some band gap defect states.[51] Calcination with N_2 produced P25-TiO_2 composite macrospheres without a distinct band gap, absorbing light across the whole measured UV-Vis spectrum, Figure 7.2, indicating a high proportion of carbon within the macrospheres.

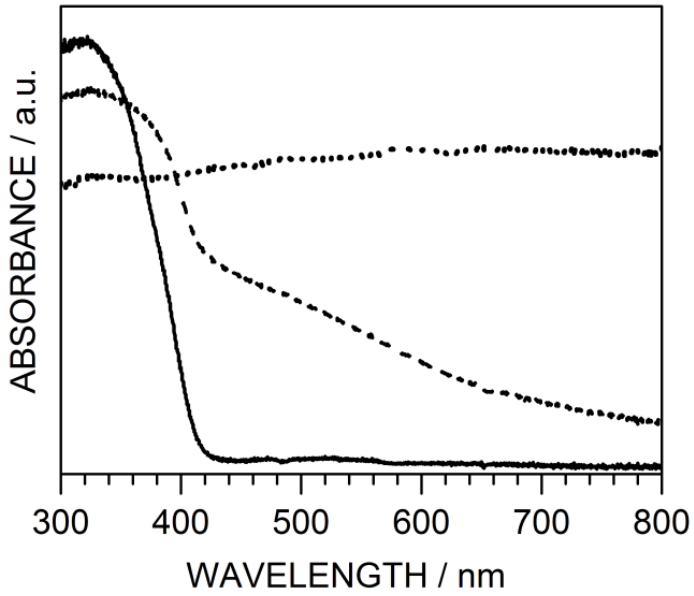

Figure 7.2: UV-Vis absorbance spectra of: P25 TiO_2 nanoparticles (solid line); MS(N_2/O_2) (dashed line); and MS(N_2) (dotted line).

Raman microscopy indicated that the N_2/O_2 calcined P25-TiO_2 composite macrospheres contained anatase TiO_2, with strong bands at 148 cm^{-1}, 394 cm^{-1}, 513 cm^{-1}, and 636 cm^{-1}, Figure 7.3.[52,53] Rutile Raman signals were not detected due to their overlapping Raman signals with anatase and the low proportion of rutile present in the P25 starting material.[54,55] Comparatively, the N_2 calcined P25-TiO_2 composite macrospheres showed only a weak anatase TiO_2 band at 148 cm^{-1}, consistent with the undetected band gap and strong visible absorbance measured by UV-Vis spectroscopy, Figure 7.2. A broad signal comprising the carbon D and carbon G Raman bands at 1340 cm^{-1} and 1580 cm^{-1} respectively is indicative of a mix of graphitic and amorphous carbon.[56]

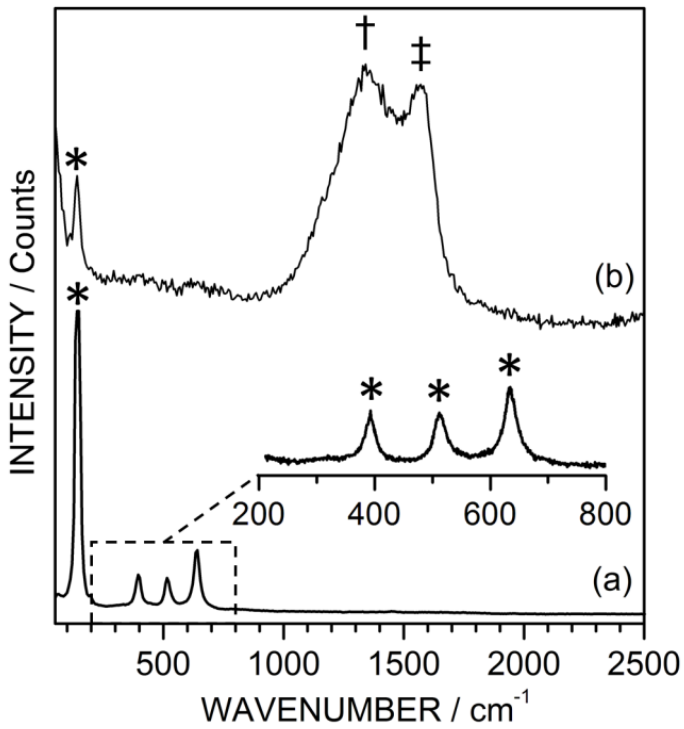

Figure 7.3: Raman spectra of: (a) MS(N_2/O_2); and (b) MS(N_2). Significant peaks labelled: anatase TiO_2 (*); carbon D line (†); and carbon G line (‡). Inset corresponds to the 200–800 cm^{-1} region.

7.3.2 Photocatalytic Testing

UV illumination of N_2/O_2 calcined P25-TiO_2 composite macrospheres in methylene blue solution led to photocatalytic dye degradation, with almost complete conversion after 30 min, Figure 7.4. Photocatalytic degradation rates displayed near first order kinetics, with a rate of 7.9 x 10^{-3} min^{-1} m^{-2} (compared to 1.9 ± 0.2 x 10^{-1} min^{-1} m^{-2} for dispersed P25 TiO_2 nanoparticles).

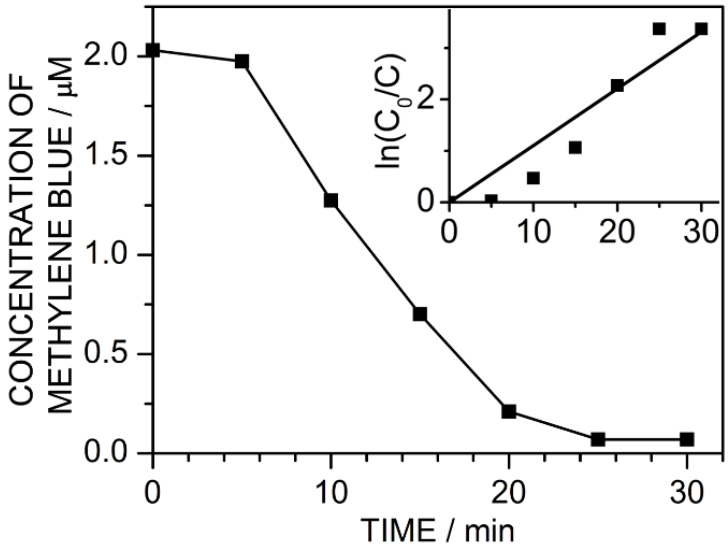

Figure 7.4: UV photodegradation profile of methylene blue dye solution (2 µM in high purity water, +70 wt%, TCL UK Ltd.) using MS(N_2/O_2) (5.6 ± 0.1 mg mL^{-1}), following an initial equilibration period in the dark for 5 min. Inset shows the pseudo first-order kinetic profile with linear best fit, with a calculated photodegradation rate of 7.9 x 10^{-3} min^{-1} m^{-2}.

Both N_2 and N_2/O_2 calcined macrospheres were tested for their photocatalytic activity under visible light illumination in a recirculating horizontal bed reactor. N_2/O_2 calcined macrospheres did not show any activity above the dark reference over the 8 h period of illumination, Figure 7.5. However, N_2 calcined macrospheres displayed activity for dye degradation both under illumination and in the dark reference, indicating a portion of the activity may be due to adsorption of the dye on the internal surface of the macrosphere. To study the degradation kinetics, the reaction of methylene blue over N_2 calcined macrospheres was plotted as a pseudo-first or pseudo-second order reactions, Figure 7.6. A good linear fit was found for the pseudo-first order reaction, whereas there was significant deviation from linearity in the case of the pseudo-second order fit.

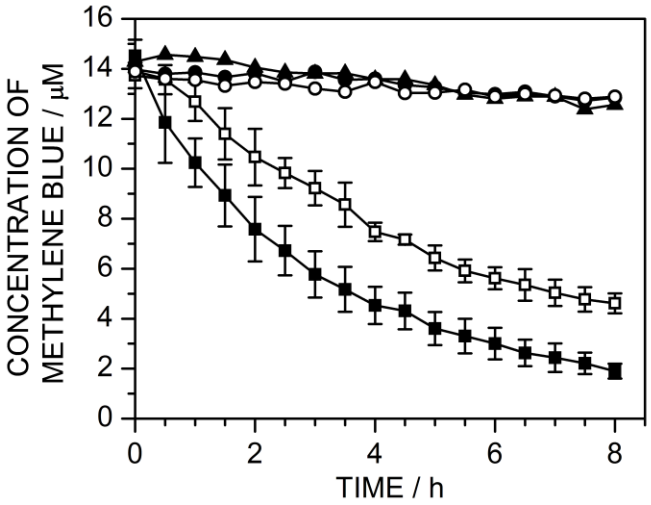

Figure 7.5: Degradation profiles of methylene blue dye solution (20 μM in high purity water, +70 wt%, TCL UK Ltd.): MS(N_2/O_2) in the presence of visible light (▲); MS(N_2) in the presence of visible light (■); MS(N_2) in the absence of visible light (□); in the presence of visible light without TiO_2 composite macrospheres (●); and in the absence of visible light without TiO_2 composite macrospheres (○). Macrosphere loadings when present were 12.5 ± 0.1 mg mL^{-1}. Error bars are the standard deviation of three repeat experiments. Tend lines have been added only as a guide.

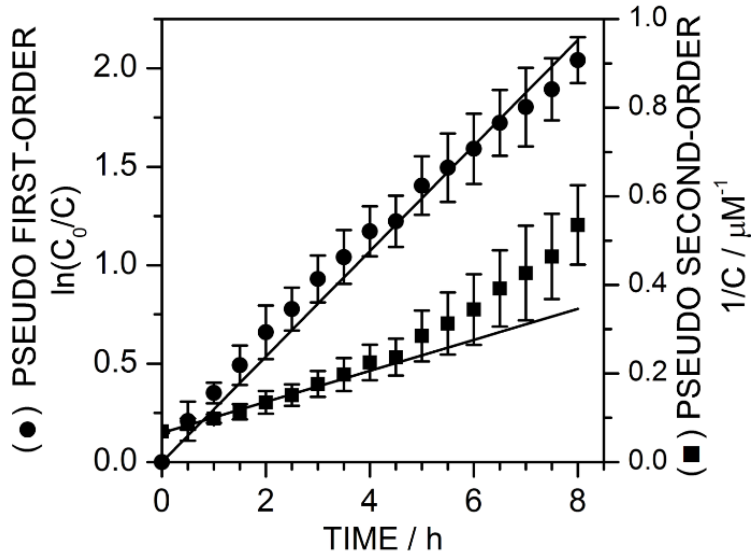

Figure 7.6: Visible light photodegradation of methylene blue dye solution by MS(N_2) kinetic profiles: pseudo first-order (●); and pseudo second-order (■). Error bars are the standard deviation of three repeat experiments. Trend lines have been added as a guide to show deviation from linearity.

Rate constants for the degradation of methylene blue over composite macrospheres show an almost twofold increase during upon illumination of the N_2 calcined macrospheres compared with the dark reference (0.22 to 0.43 h^{-1} m^{-2}), Figure 7.7. After 8 h of illumination, the N_2 calcined macrospheres removed 87% of the methylene blue dye (compared to 66% without illumination), indicating that visible light promoted degradation of the dye. Recycling studies of the N_2 calcined macrospheres with and without visible light showed that the additional activity in the presence of light was lost after the first use, with the subsequent 8 h period showing no improvement over the dye degradation in the dark, Figure 7.8. Therefore, whilst the N_2 calcined macrospheres displayed some visible light photocatalytic activity, it is quenched within the first 8 h of use.

7.4 Discussion

Synthesis of the N_2/O_2 calcined P25-TiO_2 composite macrospheres resulted in anatase TiO_2, consistent with previous sol-gel TiO_2 calcination studies carried out at below 700 °C,[57] and TiO_2–P25 nanocomposite coatings deposited onto glass and flat steel substrates.[58,59] Whilst rutile is the thermodynamically more stable bulk phase, sol-gel processing tends to favour the anatase phase.[60] This is attributed to the lower surface energy of anatase driving its preferential formation due to the large surface area to bulk volume ratio of the small particles typically formed during sol-gel processing.[61,62,63,64] Additional factors, such as the precursors employed and reaction conditions can also influence TiO_2 crystal growth.[65,66] The lack of any discernible rutile signal in the Raman spectrum is also consistent with the high weight fraction of anatase in the P25 TiO_2 filler material.[44]

Calcination under a nitrogen atmosphere resulted in a large amount of carbon present in the macrospheres, due to the lack of oxygen for combustion of the chitosan viscosity modifier. TiO_2 was present in the material in the form of anatase, but the high visible light absorbance by the carbon meant that a band gap was not detectable by UV-Vis diffuse reflectance spectroscopy. The high carbon content did not affect the physical properties of the spheres and they were used for photocatalysis as per the N_2/O_2 calcined macrospheres with no attrition.

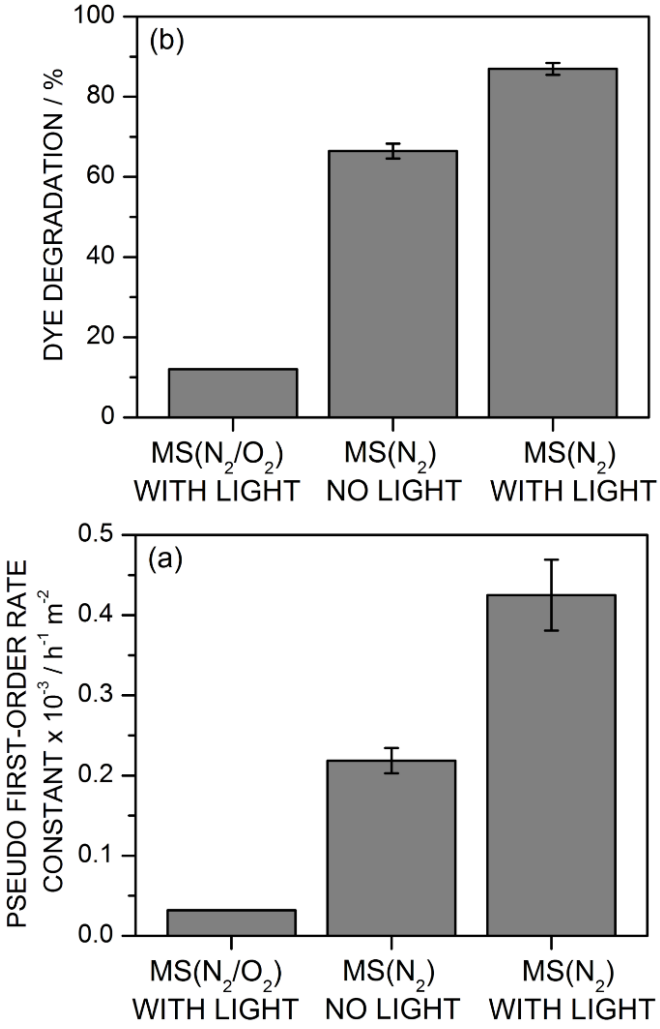

Figure 7.7: Degradation of methylene blue dye solution (20 µM in high purity water, +70 wt%, TCL UK Ltd.) using TiO_2 composite macrospheres (loadings of 12.5 ± 0.1 g L^{-1}) in the absence and presence of visible light: (a) degradation rate normalised to surface area; and (b) percentage of dye degraded after 8 h of contact with TiO_2 composite macrospheres. Error bars are the standard deviation of three repeat experiments.

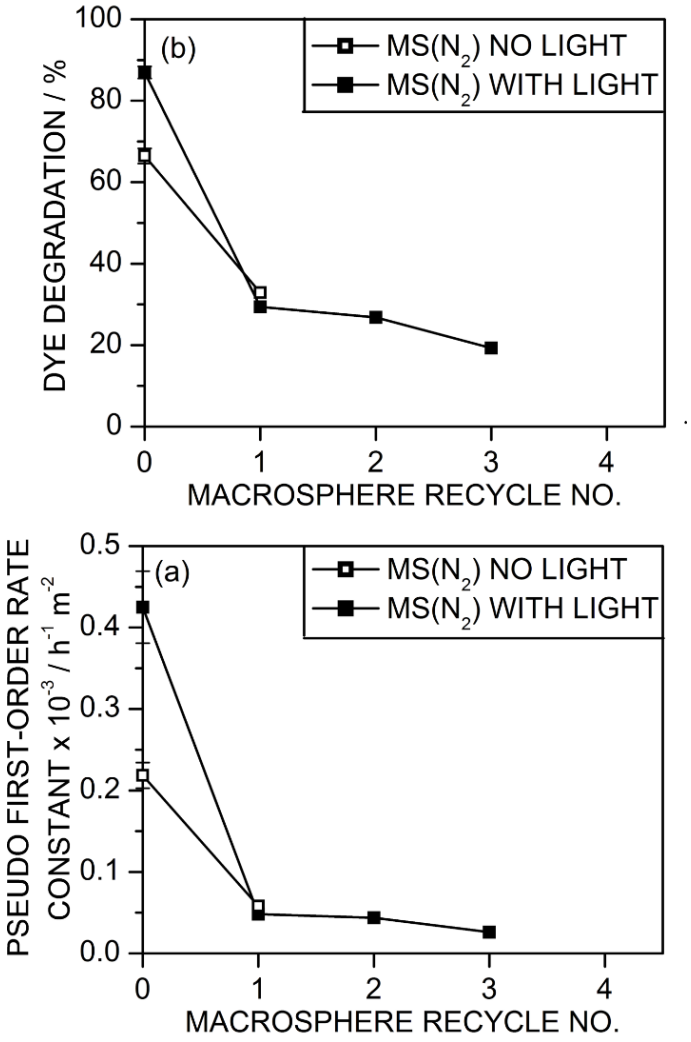

Figure 7.8: Recycling study for the degradation of methylene blue dye solution (20 µM in high purity water, +70 wt%, TCL UK Ltd.) using $MS(N_2)$ (loadings of 12.5 ± 0.1 g L^{-1}) in the absence and presence of visible light: (a) degradation rate normalised to surface area; and (b) percentage of dye degraded after 8 h of contact with TiO_2 composite macrospheres.

Photocatalytic activity of the N_2/O_2 calcined macrospheres under UV light was not as effective as P25 TiO_2 powder after surface area correction (7.9×10^{-3} min^{-1} m^{-2} compared to $1.9 \pm 0.2 \times 10^{-1}$ min^{-1} m^{-2}). This is not unexpected as the dispersion of P25 into the dye solution was considerable due to the small particle size increasing mass transfer to the active surface area. However, the macrospheres were easily separable by decanting the solution from the reactor. Visible light photocatalysis was not observed for the N_2/O_2 calcined macrospheres above the baseline degradation without any macropsheres, indicating that the slight tailing of the TiO_2 band edge observed in the UV-Vis diffuse reflectance did not transfer to absorption of light available for photocatalysis.

N_2 calcined macrospheres displayed good removal of the methylene blue dye under visible light, as well as removal with no illumination. This is indicative of carbon absorption due to the high carbon content and considerably increased surface area of the N_2 calcined macrospheres compared to the N_2/O_2 calcined samples. The increase in degradation under illumination indicates that the degradation is partly photocatalytic, with the material able to utilise the lower energy visible light compared to N_2/O_2 calcined macrospheres.

The enhanced visible light photocatalysis may be due to several factors. Given the high surface area of the macrospheres, it is possible that the methylene blue dye was adsorbed onto the surface in close proximity to the TiO_2, which allowed for a measurable rate of photocatalysis due to the increased surface area.[67] However, if this were the case, then the surface area corrected photocatalytic rates after background subtraction would be the same for N_2/O_2 and N_2 calcined macrospheres. As this is not the case, the enhanced photocatalytic activity cannot be purely a surface area affect.

Doping of the TiO_2 particles within the N_2/O_2 calcined macrospheres could occur through exchange of the lattice titanium atoms with carbon at the surface of the P25 TiO_2 nanoparticles, as well as more complete doping of TiO_2 formed from the sol-gel precursors.[67] Formation of carbonate type species has been suggested to occurr during carbon doping,[68] along with formation of substitutional anion and interstitial cation sites.[69] Any additional dopant levels in the band structure may result in either the formation of an increased number of radicals for photocatalytic destruction of the methylene blue dye,[38] or direct photooxidation by holes in the mid-band dopant levels.[32] High calcination temperatures tend to favour the formation of graphitic carbon,[70] therefore it is likely that some of the carbon is in this form; this is consistent with Raman microscopy results, Figure

7.3. Synergistic effects between carboxylic acid sites on activated carbon and electrons generated during photoexcitation of TiO_2 have been shown to enhance photocatalytic activity,[71] which may be another factor in the improved photocatalytic activity given the presence of both graphitic carbon and amorphous material. The large total carbon content present in the N_2/O_2 macrospheres made identification of the doped species and band structure impractical.

Recycling demonstrated that the N_2/O_2 calcined macrospheres were unstable under the reaction conditions, losing the photocatalytic benefit after a single use, Figure 7.8. It is likely that saturation of the surface due to adsorption of methylene blue by the carbonaceous material resulted in deactivation of the active sites. Further investigation involving washing, UV illumination and heat treatments may elucidate the mechanism for deactivation, along with highlighting a possible route for regeneration of the photocatalytic activity.

7.5 Conclusions

P25-TiO_2 composite macrospheres have been prepared from a chitosan modified sol gel and P25 TiO_2 nanoparticles for visible light removal and degradation of organic pollutants. Their size and shape allows for use in flat photocatalytic rectors with recycling systems, ideal for utilisation of sunlight, without the need for post use catalyst separation. Further work on optimising the photocatalytic activity through additional dopant materials and other filler materials aside from P25 may result in viable photocatalysts for point of use water purification.

7.7 References

[1] SODIS. http://www.sodis.ch/projekte/index_EN (accessed May 29, 2013)

[2] Jacoby, W. A.; Maness, P. C.; Wolfrum, E. J.; Blake, D. M.; Fennel, J. A. Mineralization of Bacterial Cell Mass on a Photocatalytic Surface in Air. *Environ. Sci. Technol.* **1998**, *32*, 2650–2653.

[3] Ireland, J. C.; Klostermann, P.; Rice, E. W.; Clark, R. M. Inactivation of Escherichia Coli by Titanium Dioxide Photocatalytic Oxidation. *Appl. Environ. Microbiol.* **1993**, *59*, 1668–1670.

[4] Saito, T.; Iwase, T.; Horie, J.; Morioka, T. Mode of Photocatalytic Bactericidal Action of Powdered Semiconductor TiO_2 on Mutans Streptococci. *J. Photochem. Photobiol. B.* **1992**, 14, 369–379.

[5] Matsunaga, T.; Tomoda, R.; Nakajima, T.; Wake, H. Photoelectrochemical Sterilization of Microbial Cells by Semiconductor Powders. *FEMS Microbiol. Lett.* **1985**, *29*, 211–214.

[6] Matthews, R. W.; Abdullah, M.; Low, G. K.-C. Photocatalytic Oxidation for Total Organic Carbon Analysis. *Anal. Chim. Acta.* **1990**, *223*, 171–179.

[7] Matthews, R. W. Purification of Water with Near—U.V. Illuminated Suspensions of Titanium Dioxide. *Water Res.* **1990**, *24*, 653–660.

[8] Low G. K.-C.; McEvoy S. R.; Matthews R. W. Formation of Ammonium and Nitrate Ions from Photocatalytic Oxidation of Ring Nitrogenous Compounds over Titanium Dioxide. *Chemosphere* **1989,** *19*, 1611–1621.

[9] Low G. K.-C.; McEvoy S. R.; Matthews R. W. Formation of Nitrate and Ammonium-Ions in Titanium-Dioxide Mediated Photocatalytic Degradation of Organic-Compounds Containing Nitrogen-Atoms. *Environ. Sci. Technol.* **1991**, *25*, 460–467

[10] Augugliaro, V.; Palmisano, L.; Schiavello, M.; Sclafani, A.; Marchese, L.; Martra, G.; Miano, F. Photocatalytic Degradation of Nitrophenols in Aqueous Titanium-Dioxide Dispersion. *Appl. Catal.* **1991**, *69*, 323–340.

[11] Tang, H.; Prasad, K.; Sanjinès, R.; Schmid, P. E.; Lévy, F. Electrical and Optical Properties of TiO_2 Anatase Thin Films. *J. Appl. Phys.* **1994**, *75*, 2042–2047.

[12] Ghosh, A. K.; Maruska, H. P. Photoelectrolysis of Water in Sunlight with Sensitized Semiconductor Electrodes. *J. Electroch. Soc.* **1977**, *124*, 1516–1522.

[13] Choi, W. Y.; Termin, A.; Hoffmann, M. R. The Role of Metal Ion Dopants in Quantum-Sized TiO2: Correlation between Photoreactivity and Charge Carrier Recombination Dynamics. *J. Phys. Chem.* **1994**, *98*, 13669–13679.

[14] Diwald, O.; Thompson, T. L.; Zubkov, T.; Goralski, E. G.; Walck, S. D.; Yates, J. T. Jr. Photochemical Activity of Nitrogen-Doped Rutile TiO_2(110) in Visible Light. *J. Phys. Chem. B* **2004**, *108*, 6004–6008.

[15] Sakthivel, S.; Janczarek, M.; Kisch, H. Visible Light Activity and Photoelectrochemical Properties of Nitrogen-Doped TiO2. J. Phys. Chem. B **2004**, *108*, 19384–19387.

[16] Cong, Y.; Zhang, J.; Chen, F.; Anpo, M. Synthesis and Characterization of Nitrogen-Doped TiO_2 Nanophotocatalyst with High Visible Light Activity. *J. Phys. Chem. C* **2007**, *111*, 6976–6982.

[17] Pulsipher, D. J. V.; Martin, I. T.; Fisher, E. R. Controlled Nitrogen Doping and Film Colorimetrics in Porous TiO_2 Materials Using Plasma Processing. *Acs Appl. Mater. Interfaces* **2010**, *2*, 1743–1753.

[18] Shifu, C.; Lei, C.: Shen, G.; Gengyu, C. The Preparation of Nitrogen-Doped Photocatalyst TiO2−xNx by Ball Milling. *Chem. Phys. Lett.* **2005**, *413*, 404–409.

[19] Asahi, R.; Morikawa, T.; Ohwaki, T.; Aoki, K.; Taga, Y. Visible-Light Photocatalysis in Nitrogen-Doped Titanium Oxides. *Science* **2001**, *294*, 269–271.

[20] Brudnik, A.; Bucko, M.; Radecka, M.; Trenczek-Zajac, A.; Zakrzewska, K. Microstructure and Optical Properties of Photoactive TiO_2:N Thin Films. *Vacuum*, **2008**, *82*, 936–941.

[21] Wang, H.-F.; Shu, X.-F.; Li, X.-Y.; Tang, B. Photocatalytic Activities of N Doped TiO2 Coatings on 316L Stainless Steel by Plasma Surface Alloying Technique. *Trans. Nonferrous Met. Soc. China* **2012**, *22*, 120–126.

[22] Yu, W.; Liu, X.; Pan, L.; Li, J.; Liu, J.; Zhang, J.; Li, P.; Chen, C.; Sun, Z. Enhanced Visible Light Photocatalytic Degradation of Methylene Blue by F-Doped TiO_2. *App. Surf. Sci.* **2014**, *319*, 107–112.

[23] Ricaud, P.; Lefèvre, F. Introduction to Fluorine and the Environment. In *Fluorine and the Environment: Atmospheric Chemistry, Emissions & Lithosphere*; Tressaud, A., Eds.; Elsevier: Amsterdam, 2006; pp 1–33.

[24] Morikawa, T.; Asahi, R.; Ohwaki, T.; Aoki, K.; Taga, Y. Band-Gap Narrowing of Titanium Dioxide by Nitrogen Doping. *Jpn. J. Appl. Phys. 2-Lett.* **2001**, *40*, L561–L563.

[25] Asahi, R.; Morikawa, T.; Ohwaki, T.; Aoki, K.; Taga, Y. Visible-Light Photocatalysis in Nitrogen-Doped Titanium Oxides. *Science* **2001**, *293*, 269–271.

[26] Shen, M.; Wu Z.; Hui, H.; Yukou, D.; Zhigang, Z.; Yang, P. Carbon-Doped Anatase TiO_2 Obtained from TiC for Photocatalysis Under Visible Light Irradiation. *Mater. Lett.* **2006**, *60*, 693–697.

[27] Khan, S. U. M.; Al-Shahry, M.; Ingler W. B. Jr. Efficient Photochemical Water Splitting by a Chemically Modified n-TiO_2. *Science*, **2002**, *297*, 2243–2245.

[28] Wu, G.; Nishikawa, T.; Ohtani, B.; Chen, A. Synthesis and Characterization of Carbon-Doped TiO_2 Nanostructures with Enhanced Visible Light Response. *Chem. Mater.* **2007**, *19*, 4530–4537.

[29] Zhang, Y.; Zhao, Z.; Chen, J.; Cheng, L.; Chang, J.; Sheng, W.; Huc, C.; Cao, S. C-Doped Hollow TiO_2 Spheres: In Situ Synthesis, Controlled Shell Thickness, and Superior Visible-Light Photocatalytic Activity. *Appl. Catal., B* **2015**, *165*, 715–722.

[30] Yin, H.-Y.; Wang, X.-L.; Wang, L.; Q.-L. N.; Zhao, H.-T. Self-Doped TiO_2 Hierarchical Hollow Spheres with Enhanced Visible-Light Photocatalytic Activity. *J. Alloys Compd.* **2015**, *640*, 68–74.

[31] Cong, Y.; Li, X.; Dong, Z.; Yuan, G.; Cui, Z.; Zhang, J. Core–Shell Structured Carbon Black@TiO_2 Microsphere with Enhanced Visible Light Photocatalytic Activity. *Mater. Lett.* **2015**, *138*, 200–203.

[32] Liu, J.; Zhang, Q.; Yang, J.; Ma, H.; Tade, M. O.; Wang, S.; Liu, J. Facile Synthesis of Carbon-Doped Mesoporous Anatase TiO_2 for the Enhanced Visible-Light Driven Photocatalysis. *Chem. Commun.* **2014**, *50*, 13971–13974.

[33] Park, Y.; Kim, W.; Park, H.; Tachikawa, T.; Majima, T.; Choi, W. Carbon-Doped TiO_2 Photocatalyst Synthesized Without Using an External Carbon Precursor and the Visible Light Activity. *Appl. Catal., B* **2009**, *91*, 355–361.

[34] Sakthivel, S.; Kisch, H. Daylight Photocatalysis by Carbon-ModifiedTitanium Dioxide. *Angew. Chem. Int. Ed.* **2003**, *42*, 4908–4911.

[35] Hench, L. L.; West, J. K. The Sol-Gel Process. *Chem. Rev.* **1990**, *90*, 33–72.

[36] Wang, C.-C.; Ying, J. Y. Sol−Gel Synthesis and Hydrothermal Processing of Anatase and Rutile Titania Nanocrystals. *Chem. Mater.* **1999**, *11*, 3113–3120.

[37] Sayilkan, F.; Emre, F. B. Characterization and Photocatalytic Properties of TiO2/Chitosan Nanocomposites Synthesized by Hydrothermal Process. *Turk. J. Chem.* **2016**, *40*, 28–37.

[38] Park, Y.; Kim, W.; Park, H.; Tachikawa, T.; Majima, T.; Choi, W. Investigation of Nitrogen Doped and Carbon Species Decorated TiO2 with Enhanced Visible Light Photocatalytic Activity by Using Chitosan. *Appl. Catal., B* **2015**, *179*, 344–351.

[39] Vega, A. A.; Keshmiri, M.; Mohseni, M. Composite Template-Free TiO_2 Photocatalyst: Synthesis, Characteristics and Photocatalytic Activity. *Appl. Catal. B* **2011**,*104*, 127–135.

[40] Kadib, A, E.; Molvinger, K.; Cacciaguerra, T.; Bousmina, M.; Brunel, D. Chitosan Templated Synthesis of Porous Metal Oxide Microspheres with Filamentary Nanostructures. *Micro. Meso. Mater.* **2011**, *142*, 301–307.

[41] Kimling, M. C.; Scales, N.; Hanley, T. L.; Caruso, R. A. Uranyl-Sorption Properties of Amorphous and Crystalline TiO_2/ZrO_2 Millimeter-Sized Hierarchically Porous Beads. *Environ. Sci. Technol*. **2012**, *46*, 7913–7920.

[42] Houas, A.; Lachheb, H.; Ksibi, M.; Elaloui, E.; Guillard, C.; Herrmann, J.-M. Photocatalytic Degradation Pathway of Methylene Blue in Water. *Appl. Catal. B: Environ.* **2001**, *31*, 145–157.

[43] Matthews, R. W. Photocatalytic Oxidation and Adsorption of Methylene Blue on Thin Films of Near-Ultraviolet-Illuminated TiO2. *J. Chem. Soc., Faraday Trans. 1* **1989**, *85*, 1291–1302.

[44] Evonik Industries. https://www.aerosil.com/sites/lists/IM/Documents/TI-1243-Titanium-Dioxide-as-Photocatalyst-EN.pdf (accessed Jul 8, 2015).

[45] Brunauer, S.; Emmett, P. H.; Teller, E. Adsorption of Gases in Multimolecular Layers. *J. Am. Chem. Soc.* **1938**, *60*, 309–319.

[46] Lewis, G. N.; Bigeleisen, J. Methylene Blue and Other Indicators in General Acids. The Acidity Function. *J. Am. Chem. Soc.* **1943**, *65*, 1144–1150.

[47] Houas, A.; Lachheb, H.; Ksibi, M.; Elaloui, E.; Guillard, C.; Herrmann, J.-M. Photocatalytic Degradation Pathway of Methylene Blue in Water. *Appl. Catal. B: Environ.* **2001**, *31*, 145–157.

[48] Matthews, R. W. Photocatalytic Oxidation and Adsorption of Methylene Blue on Thin Films of Near-Ultraviolet-Illuminated TiO_2. *J. Chem. Soc., Faraday Trans. 1* **1989**, *85*, 1291–1302.

[49] Bickley, R. I.; Gonzalez-Carreno, T.; Lees, J. S.; Palmisano, L; Tilley, R. J. D. A Structural Investigation of Titanium-Dioxide Photocatalysts. *J. Solid State Chem.* **1991**, *92*, 178–190.

[50] Nagaveni, K.; Hegde, M. S.; Ravishankar, N.; Subbanna, G. N.; Madras, G. Synthesis and Structure of Nanocrystalline TiO_2 with Lower Band Gap Showing High Photocatalytic Activity. *Langmuir* **2004**, *20*, 2900–2907.

[51] Chen, X.; Liu, L.; Yu, P. Y.; Mao, S. S. Increasing Solar Absorption for Photocatalysis with Black Hydrogenated Titanium Dioxide Nanocrystals. *Science* **2011**, *331*, 746–750.

[52] Beattie, I. R.; Gilson, T. R. Single Crystal Laser Raman Spectroscopy. *Proc. Roy. Soc. A.* **1968**, *307*, 407–429.

[53] Ohsaka, T.; Izumi, F.; Fujiki, Y. Raman-Spectrum of Anatase, TiO2. *J. Raman Spec.* **1978**, *7*, 321–324.

[54] Narayanan, P. S. Raman Spectrum of Rutile: Polarisation Studies. *P. Indian Acad. Sci. A* **1953**, *37*, 411–414.

[55] Porto, S. P. S.; Fleury, P. A.; Damen, T. C. Raman Spectra of TiO_2, MgF2, ZnF2, FeF2, and MnF2. *Phys. Rev.* **1967**, *154*, 522–526.

[56] Chu, P. K.; Li, L. Characterization of Amorphous and Nanocrystalline Carbon Films. *Mater. Chem. Phys.* **2005**, *96*, 253–277.

[57] Nakanishi, K.; Takahashi, R.; Nagakane, T.; Kitayama, K.; Koheiya, N.; Shikata, H.; Soga, N. Formation of Hierarchical Pore Structure in Silica Gel. *J. Sol-Gel Sci. Technol.* **2000**, *17*, 191–210.

[58] Balasubramanian, G.; Dionysiou, D. D.; Suidan, M. T.; Subramanian, Y.; Baudin, I.; Laine, J.-M. Titania Powder Modified Sol-Gel Process for Photocatalytic Applications. *J. Mater. Sci.* **2003**, *38*, 823–831.

[59] Chen, Y.; Dionysiou, D. D. TiO2 Photocatalytic Films on Stainless Steel: The Role of Degussa P-25 in Modified Sol–Gel Methods. *Appl. Catal. B: Environ.* **2006**, *62*, 255–264.

[60] Anderson, M. A.; Gieselmann, M. J.; Xu, Q. Titania and Alumina Ceramic Membranes. *J. Membr. Sci.* **1988**, *39*, 243–258.

[61] Zhang, H.; Banfield, J. F. Thermodynamic Analysis of Phase Stability of Nanocrystalline Titania. *J. Mater. Chem.* **1998**, *8*, 2073–2076.

[62] Zhang, H.; Banfield, J. K. Understanding Polymorphic Phase Transformation Behavior during Growth of Nanocrystalline Aggregates: Insights from TiO_2. *J. Phys. Chem. B* **2000**, *104*, 3481–3487.

[63] Naicker, P. K.; Cummings, P. T.; Zhang, H.; Banfield, J. F. Characterization of Titanium Dioxide Nanoparticles Using Molecular Dynamics Simulations. *J. Phys. Chem. B* **2005**, *109*, 15243–15249.

[64] Navrotsky, A. Energetics of Nanoparticle Oxides: Interplay Between Surface Energy and Polymorphism. *Geochem. Trans.* **2003**, *4*, 34–37.

[65] Yanagisawa, K.; Ovenstone, J. Crystallization of Anatase from Amorphous Titania Using the Hydrothermal Technique: Effects of Starting Material and Temperature. *J. Phys. Chem. B* **1999**, *103*, 7781–7787.

[66] Yanagisawa, K.; Yamamoto, Y.; Feng, Q.; Yamasaki, N. Formation Mechanism of Fine Anatase Crystals from Amorphous Titania under Hydrothermal Conditions *J. Mater. Res.* **1998**, *13*, 825–829.

[67] Ren, W.; Ai, Z.; Jia, F.; Zhang, L.; Fan, X.; Zou, Z. Low Temperature Preparation and Visible Light Photocatalytic Activity of Mesoporous Carbon-Doped Crystalline TiO2. *Appl. Catal., B* **2007**, *69*, 138–144.

[68] Kamisaka, H.; Adachi, T.; Yamashita, K. Theoretical Study of the Structure and Optical Properties of Carbon-Doped Rutile and Anatase Titanium Oxides. *J. Chem. Phys.* **2005**, *123*, 084704.

[69] Leary, R.; Westwood, A. Carbonaceous Nanomaterials for the Enhancement of TiO_2 Photocatalysis. *Carbon* **2011**, *49*, 741–772.

[70] Sullivan, J. A.; Neville, E. M.; Herron, R.; Thampi, K. R.; MacElroy, J. M. D. Routes to Visible Light Active C-Doped TiO_2 Photocatalysts Using Carbon Atoms from the Ti Precursors. *J. Photochem. Photobiol., A* **2014**, *289*, 60–65.

[71] Ocampo-Pérez, R.; Sánchez-Polo, M.; Rivera-Utrilla, J.; Leyva-Ramos, R. Enhancement of the Catalytic Activity of TiO_2 by Using Activated Carbon in the Photocatalytic Degradation of Cytarabine. *Appl. Catal., B* **2011**, *104*, 177–184.

Chapter 8 Conclusions and Future Work

Pulsed plasma deposition is a powerful tool for tailored surface functionalisation due to the retention of key monomeric functional groups. Chapters 3 and 4 demonstrate how this concept can be applied to making catalytic films through anchoring of active palladium centres to a plasma polymer. Poly(1-allylimidazole) is particularly effective due to the high density of nitrogen donors for association with palladium(II). As demonstrated in Chapter 3, surface bound palladium catalyses the formation of new carbon-carbon bonds via Suzuki, Sonogashira and Heck reactions with iodo-, bromo- and chloro- containing reagents. These reusable dip catalysts circumvent the problem of post reaction separation typical of homogeneous and powdered heterogeneous catalysts. The main advantage of pulsed plasma deposition is that it can be applied to a wide range of substrate materials. Therefore, development of these catalytic technologies can be envisaged thorough deposition of catalytically active films onto more complex reactor systems. Additionally, although some other palladium(II)-seeded plasma polymers were trialled for their catalytic activity, further design of the surface moieties using other polymers may allow for mimicry of ligand environments in specific homogeneous catalysts.

In Chapter 4, poly(vinylbenzyl chloride) was demonstrated for catalytic application as a quaternised imidazolium containing film. Palladium(II) coordination within the poly(ionic liquid) film yielded reusable catalytic surfaces on PTFE substrates. These were demonstrated for their use as catalytic membranes for room temperature sonochemical Suzuki coupling with in-situ separation of product from reaction solvent. The proof of concept work reported herein could be developed further to investigate the applicability to larger scale carbon-carbon coupling reactions and other metal catalysed reactions. In addition, deposition of different poly(ionic liquid) films is entirely possible given the wide range of polymerisable monomers and quaternisable functional groups. Further work on developing poly(ionic liquid) membranes may provide a variety of analogues to homogeneous catalysts which can be anchored to a permselective flow membrane.

Further demonstrating the flexibility of pulsed plasma deposited films, poly(1-allylimidazole) was also used for growth promotion and anchoring of metal organic frameworks (MOFs) to silicon, gold and PTFE substrates in Chapter 5. Using liquid phase epitaxy a MOF tailored for CO_2 capture comprising zinc, 4,4’-bipyridine and terephthalic acid was grown onto the pulsed plasma functionalised surfaces. This material was

successfully tested for CO_2 uptake at atmospheric concentrations (where more traditional materials have limited absorbances), demonstrating its applicability for CO_2 sequestration which could be used to reduce greenhouse gas emissions from indutrial processes. Increasing MOF film thickness increased the total CO_2 capture, indicating that the material could be improved further with increased deposition times. Tailoring of the MOF linkers may yield higher CO_2 uptake through additional free nitrogen moieties or metal centers. Although out of the scope of this work, it is envisaged that multifunctional surfaces are possible, which may provide capture of CO_2 alongside catalytic conversion to useful feedstocks such methanol and syngas.

CO_2 sequestration provides a potential solution for greenhouse gas emissions, which unless checked, are likely to rise with increased industrial growth. Such growth will undoubtedly place an even greater strain on freshwater resources in areas where there is currently insufficient clean drinking water. One potential solution is point of use photocataltyic water purification. To this end, photocatalytic materials were synthesised through two routes in Chapters 6 and 7. Firstly, a sol-gel of TiO_2 and P25 TiO_2 nanoparticles was used to coat steel particles that had been encapsulated with a silica barrier layer to form microcomposite particles. P25 TiO_2 remained primarily in the anatase polymorph, with complete coating of the steel particles, evidenced by repeated use without corrosion of the steel core. These microcomposite particles were catalytically active for the destruction of methylene blue dye under UV illumination and were separable and reusable due to their magnetic steel cores. It is envisaged that these particles could be used for point of use water purification as an enhancement to Solar Disinfection (SODIS) technology. An alternative method for preparation of separable photocatalysts is the synthesis of macrospheres, demonstrated in Chapter 7 through combination of a P25 TiO_2 sol-gel and a chitosan viscosity modifier. The synthesised macrospheres were active under UV illumination for the degradation of methylene blue when calcined in a synthetic air mix but gained visible light photoactivity when calcined under nitrogen. This was attributed to carbon from the chitosan, which produced a carbon doped TiO_2 material, as well as a high surface area for adsorption of the dye. Photocatalytic testing was carried out in a continuous flow reactor, which was illuminated using a daylight bulb. However, the system was designed for use under solar irradiation, which would be of interest going forward. In addition, further development of the calcination parameters to optimise the photocatalytic activity is possible.

Not included within this thesis is the investigation into plasma modification of TiO_2 photocatalysts. Some initial promising results were found however these did not transfer directly into enhanced photocatalytic activity. Despite this, doping of the TiO_2 surface using plasma may be possible; further work in this area may enhance the activity of the separable materials outlined in Chapters 6 and 7.

A fundamental study was started on the factors that govern the photocatalytic activity of P25 TiO_2, with the aim to use surface functionalisation to tune the catalytic sites on the surface. Some initial results are presented in Appendix 1. It was found that photocatalytic activity did not change linearly with calcination temperature and was not a function of the percentage anatase in the bulk of the crystallites. Elucidating the surface of P25 TiO_2 at different calcination temperatures would require a systematic study using ^1H solid state NMR to determine surface hydroxyls sites and TEM or a similar technique to map the distribution of crystal phases in the particles.

Throughout this thesis, it has been demonstrated that a functional surface approach can yield tailored catalytic materials for practical applications such as catalysis, photocatalysis and CO_2 sequestration. Emphasis has been placed on producing materials that are effective, reusable and cheap to manufacture to reduce the environmental impact of anthropogenic activities.

Appendix 1. P25 TiO_2 Photocatalysis

A1.1 Introduction

Inorganic oxides are used in a wide variety of applications, such as solid-state gas sensors,[1,2] memory applications,[3,4] photocleaning surfaces,[5] light emitting diodes and solar cells.[6,7,8] As with photocatalysis, many of these applications rely on energy generated from the harvesting of light, therefore increasing the efficiency of this process is paramount in developing new materials and enhancing productivity.

By far the most studied photocatalytic inorganic oxide is TiO_2. Possessing a wide band gap; 3.2 eV for anatase and 3.0 eV for rutile,[9] photoexcitation by UV light causes the formation of electron-hole pairs. The presence of adsorbed oxygen at the surface causes trapping of these photo excited electrons as $O_2^-{}_{(ads)}$ species;[10,11,12] resulting in an electrostatic repulsion between the surface and the remaining CB electrons, thus there is a self-limiting concentration of $O_2^-{}_{(ads)}$. The negatively charged surface attracts holes in the valence band, and the combination with $O_2^-{}_{(ads)}$ leads to dissociation of O_2 and formation of surface vacancies.[148,13,14] The equilibrium between dissociation and re-adsorption of O_2 dictates the concentration of electrons in the CB.[150]

Proceeding photoexcitation, the exact route to oxidation of organic compounds is widely debated. Two pathways for reactant oxidation are commonly accepted: one via hydroxide radicals generated from photoinduced holes, the second via direct electron transfer between reactant and hole.[15] Competing with these processes are not only charge recombination, but also quenching of the reactive hydroxide radicals by superoxide anions and directly by photogenerated electrons.[16] Adsorbed molecular oxygen plays a key role in determining the quantum yields from photodegradation.[17] During normal activity of a photocatalytic system, the concentration of hydroxide radicals reaches a steady-state, and the role of adsorbed molecular oxygen differs depending on whether the system is pre steady-state or steady-state.[16] Immediately after illumination, the formation of electron-hole pairs is followed by either recombination in the bulk or trapping of the electrons and holes.

There are still many questions to be answered relating to the exact nature of the oxidative species. Firstly, assuming hydroxide radicals are formed on the surface, can these radicals dissociate from the surface, or do they require the reactant molecules to also be bound to the surface for oxidation? If the latter is the case, then

does direct oxidation occur preferentially? More importantly, an understanding of the photocatalytic trends as a function of calcination temperature is required for studies on TiO_2 materials that involve a calcination step.

A1.2 Experimental Section

A1.2.1 Sample Preparation

Aeroxide P25 TiO_2 powder was supplied by Acros Organics, with a surface area of 35–65 $m^2\ g^{-1}$ and an average particle size of 21 nm. 0.25 g of as supplied P25 TiO_2 powder was loaded into a length of 12 mm quartz tubing, using quartz wool to aid loading of the powder. The furnace setup is schematically represented in Figure A1.1. N_2 and O_2 feed gases were passed through a sulphuric acid bubbler, P_2O_5 column and 3A molecular sieve column. System moisture content was monitored via a MCM hygrometer. Gas flow into the tube furnace was below 10 ppm by volume H_2O at all times. The quartz tubing was connected to the gas flow and a down-stream isolatable sample chamber. The whole system was purged for 15 minutes with heating of all exposed glassware to remove adsorbed water. Once purged, the sample chamber was isolated from the system. Heating rate was controlled to 10 °C min^{-1} in all cases. Different dwell temperatures were used spanning 200–800 °C at 1 h dwell times. All samples were calcined under a flow of 80 $cm^3\ min^{-1}$ N_2 and 20 $cm^3\ min^{-1}$ O_2.

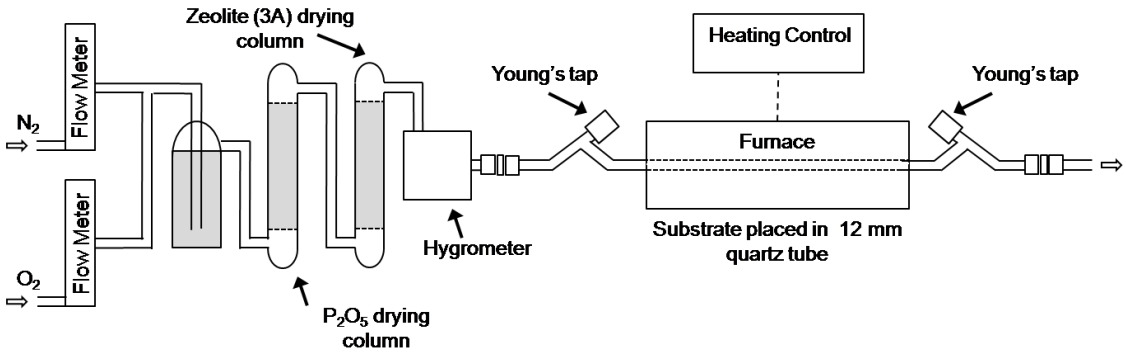

Figure A1.1: Schematic of calcination system.

A1.2.2 Sample Characterisation

X-Ray diffractograms were obtained across 5°–80° 2θ range with 0.02° step size using a powder diffractometer (model d8, Bruker Corp.). The copper anode X-ray source was operated at 40 kV and 40 mA emitting Cu Kα 1.5418 Å wavelength radiation.

A1.2.3 Photocatalytic Testing

TiO_2 photocatalysts were tested in a 100 mL volume cylindrical borosilicate glass reaction vessel (fitted with a quartz window for UV irradiation) filled with 90 mL of 34.5 ± 0.1 μM aqueous methylene blue dye solution (+70 wt%, TCL UK Ltd.), Figure 6.1. Powder was agitated using a vertically mounted magnetic stirrer hot plate (IKAMAG RCT, IKA®-Werke GmbH & Co. KG) in contact with the back face of the reactor, and oxygen dissolution was maintained via a glass diffuser bubbling oxygen at a flow rate of 5 cm^3 min^{-1} at 1.5 Bar pressure. A Hg-Xe short arc lamp (model 6136, 200 W rated, operating at 26 V and 7 A, Oriel Newport Corp.) was positioned at varying distance from the reactor. Flux was measured with a thermopile and digital voltmeter (model 5300, Applied Photophysics Ltd.). A contact thermometer was used as part of a feedback loop to the stirrer hot plate to maintain the reaction vessel temperature at 28 ± 2 °C. Prior to UV irradiation, the photocatalyst was allowed to equilibrate in the methylene blue dye solution for 10 min in order to determine the extent of methylene blue dye adsorption onto the nanopowder. 1 mL aliquots, filtered through a 0.22 μm polyethersulfone syringe filter (Gilson Scientific Ltd.), were taken prior to the addition of photocatalyst, and at 5 min intervals during UV illumination for UV-Vis absorption spectroscopy analysis of methylene blue dye concentrations at λ_{max} = 660 nm (model UV4, Unicam Lda.).[18] Dye photodegradation rate constants were calculated from absorbance readings taken over 30 min of UV exposure assuming first order kinetics.[50,51]

A1.3 Results

A1.3.1 Optimisation of Photocatalytic Conditions

The optimum distance between the arc lamp and reaction vessel was found to be 300 mm. Shorter distances resulted in complete degradation of the dye at timescales of less than 15 minutes, even at catalyst loadings of 5 mg. In addition, deviation from first

order kinetics was pronounced at a distance of 50 mm, but had no effect at 300 mm. The corresponding flux at 300 mm was 2.4 ± 0.2 mW cm^{-2}. Catalyst loadings were varied between 5 and 25 mg, with higher loading resulting in complete degradation at around 20 minutes. A linear trend was observed in rate constant as a function of catalyst loading, implying turbidity was not a contributing factor at the masses chosen. A mass of 10 mg was chosen for all further experimental as it did not degrade the dye fully over 30 minutes allowing for all data points to be utilised for rate calculation.

A1.3.2 Effect of Calcination Temperature

Rate constants for the degradation of methylene blue for samples calcined at different temperatures are given in Figure A1.2. There is a general decreasing trend observed as the calcination temperature increases, resulting in a 50% reduction in rate constant at 700 °C. Superimposed on this decreasing trend is an increase in rate constant at around 350 °C, although this is still within error of the uncalcined sample.

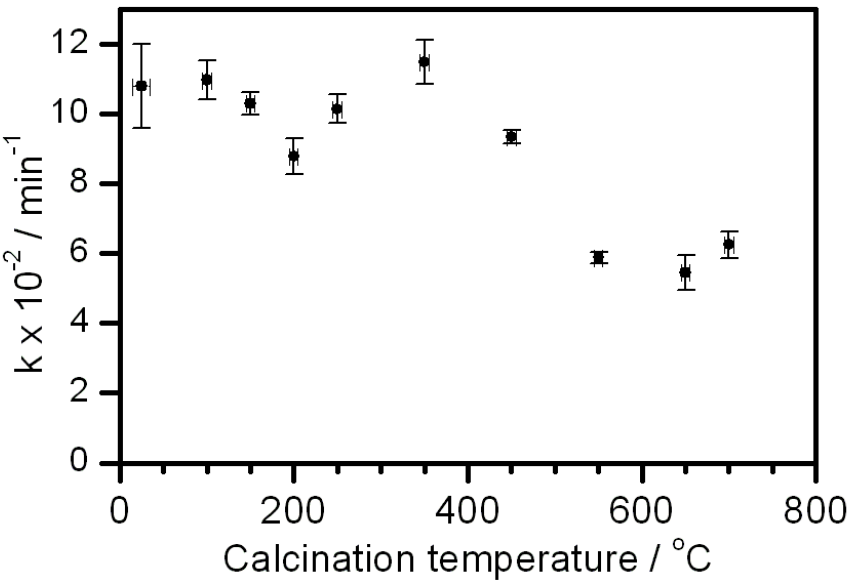

Figure A1.2 Effect of calcination temperature on the rate of methylene blue degradation. Error bars are the standard deviation of three repeat experiments. [Data collected in collaboration with J. Dawson]

A1.3.3 Bulk Analysis

The phase composition of the calcined samples was analysed by XRD. The characteristic peaks of anatase (101) at 2θ = 25.4° and rutile (110) at 2θ = 27.5° can be used to track the composition of the bulk TiO_2.[19,20] The intensity of each peak was

subtracted from the baseline to give the intensity ratio I_R/I_A. From this the weight fraction of anatase was then determined by Equation 6.1, which has proven to be accurate to within 4% (the majority of error arising due to instrumental error, approximately 2%).[20] Table A1.1 gives the proportion anatase at selected temperatures used for photocatalytic experiments. The decrease in anatase percentage is most pronounced above 550 ^oC and negligible below 350 ^oC. It is worth noting that this method does not consider amorphous TiO_2.

Table A1.1 Percentage composition of anatase derived from powder XRD.

Calcination temperature / ^oC	Proportion anatase / wt%
Uncalcined	86
200	87
350	86
550	84
700	39

A1.5 Conclusions and Future Work

The photocatalytic results provide an insight into the efficiency of the photocatalyst for waste water purification. The observed decreasing trend in rate constant occurred at lower calcination temperatures than the bulk phase change to rutile. This indicates that bulk phase has less of an impact on catalytic activity then is often suggested. In addition, a deviation from the decreasing trend was observed for samples calcined around 350 ^oC, indicating that a combination of factors affects the activity.

Further work is required to improve upon these initial results and to atudy the effects of the TiO_2 surface. Initial work on the hydroxyl environments was carried out using ^1H NMR, however substantial further work would be needed to determine if this is a contributing factor to the photocatalytic activity trends. HRTEM could be used to build a picture of the surface of the particles at different calcination temperatures and gas physisorption could be used to study the effects of surface area.

A1.6 References

[1] Eranna, G.; Joshi, B. C.; Runthala, D. P.; Gupta, R. P. Oxide Materials for Development of Integrated Gas Sensors—A Comprehensive Review. *Crit. Rev. Solid State* **2004**, *29*, 111–188.

[2] Mitra, P.; Chatterjee, A. P.; Maiti, H. S. Chemical Deposition of ZnO Films for Gas Sensors. *J. Mater. Sci.-Mater. El.* **1998**, *9*, 441–445.

[3] Beck, A.; Bednorz, J. G.; Gerber, C.; Rossel, C.; Widmer, D. Reproducible Switching Effect in Thin Oxide Films for Memory Applications. *App. Phys. Lett.* **2000**, *77*, 139–141.

[4] Somani, P. R.; Radhakrishnan, S. Electrochromic Materials and Devices: Present and Future. *Mater. Chem. Phys.* **2003**, *77*, 117–133.

[5] Wood, T. J.; Hurst, G. A.; Schofield, W. C. E.; Thompson, R. L.; Oswald, G.; Evans, J. S. O.; Sharples, G. J.; Pearson, G.; Petty, M. C.; Badyal, J. P. S. Electroless Deposition of Multi-Functional Zinc Oxide Surfaces Displaying Photoconductive, Superhydrophobic, Photowetting, and Antibacterial Properties *J. Mater. Chem.* **2012**, *22*, 3859.

[6] Bolink, H. J.; Brine, H.; Coronado, E.; Sessolo, M. Hybrid Organic-Inorganic Light Emitting Diodes: Effect of the Metal Oxide. *J. Mater. Chem.* **2010**, *20*, 4047–4049.

[7] Kim, S. Y.; Baik, J. M.; Yu, H. K.; Lee, J. L. Highly Efficient Organic Light-Emitting Diodes with Hole Injection Layer of Transition Metal Oxides. *J. Appl. Phys.* **2005**, *98*, 093707.

[8] Granqvist, C. G. Transparent Conductors as Solar Energy Materials: A Panoramic Review. *Sol. Enrerg. Mat. Sol. Cells* **2007**, *91*, 1529–1598.

[9] Ji, P. F.; Takeuchi, M.; Cuong, T. M.; Zhang, J. L.; Matsuoka, M.; Anpo, M. Recent Advances in Visible Light-Responsive Titanium Oxide-Based Photocatalysts. *Res. Chem. Intermediat.* **2010**, *36*, 327–347.

[10] Morrison, S. R. Surface Barrier Effects in Adsorption, Illustrated by Zinc Oxide. *Adv. Catal.* **1955**, *7*, 259–301.

[11] Tench, A. J.; Lawson T. Oxygen Species Adsorbed on Zinc Oxide. *Chem. Phys. Lett.* **1971**, *8*, 177.

[12] Thompson, T. L.; Yates, J. T. Jr. Surface Science Studies of the Photoactivation of TiO_2 - New Photochemical Processes. *Chem. Rev.* **2006**, *106*, 4428.

[13] Melnick, D. A. Zinc Oxide Photoconduction, an Oxygen Adsorption Process. *J. Chem. Phy.* **1957**, *26*, 1136.

[14] Barry, T. I.; Stone, F. S. The Reactions of Oxygen at Dark and Irradiated Zinc Oxide Surfaces. *Proc. R. Soc. London, Ser. A* **1960**, *255*, 124–144.

[15] Linsebigler, A. L.; Lu, G.; Yates, J. T. Photocatalysis on TiO_2 Surfaces: Principles, Mechanisms, and Selected Results. *Chem. Rev.* **1995**, *95*, 735–758.

[16] Riegel G.; Bolton J. R. Photocatalytic Efficiency Variability in TiO2 Particles. *J. Phys. Chem.* **1995**, *99*, 4215–4224

[17] Gerischer, H. Photoelectrochemical Catalysis of the Oxidation of Organic Molecules by Oxygen on Small Semiconductor Particles with TiO2 as an Example. *Electrochim. Acta* **1993**, *38*, 3–9.

[18] Lewis, G. N.; Bigeleisen, J. Methylene Blue and Other Indicators in General Acids. The Acidity Function. *J. Am. Chem. Soc.* **1943**, *65*, 1144–1150.

[19] Porter, J. F.; Li, Y.-G.; Chan, C. K. The Effect of Calcination on the Microstructural Characteristics and Photoreactivity of Degussa P-25 TiO_2. *J. Mater. Sci.* **1999**, *34*, 1523–1531.

[20] Spurr, R. A.; Myers, H. Quantitative Analysis of Anatase-Rutile Mixtures with an X-Ray Diffractometer. *Anal. Chem.* **1957**, *29*, 760–762.